Extreme Variables in Star Forming Regions

By
CARLOS EDUARDO CONTRERAS PEÑA

Thesis submitted to the University of Hertfordshire in partial fulfilment of the requirements of the degree of
Doctor of Philosophy

January, 2015.

Abstract

The notion that low- to intermediate-mass young stellar objects (YSOs) gain mass at a constant rate during the early stages of their evolution appears to be challenged by observations of YSOs suffering sudden increases of the rate at which they gain mass from their circumstellar discs. Also, this idea that stars spend most of their lifetime with a low accretion rate and gain most of their final mass during short-lived episodes of high accretion bursts, helps to solve some long-standing problems in stellar evolution.

The original classification of eruptive variables divides them in two separate subclasses known as FU Orionis stars (FUors) and EX Lupi stars (EXors). In this classical view FUors are at an early evolutionary stage and are still gaining mass from their parent envelopes, whilst EXors are thought to be older objects only surrounded by an accretion disc. The problem with this classical view is that it excludes younger protostars which have higher accretion rates but are too deeply embedded in circumstellar matter to be observed at optical wavelengths. Optically invisible protostars have been observed to display large variability in the near-infrared. These and some recent discoveries of new eruptive variables, show characteristics that can be attributed to both of the optically-defined subclasses of eruptive variables.

The new objects have been proposed to be part of a new class of eruptive variables. However, a more accepted scenario is that in fact the original classes only represent two extremes of the same phenomena. In this sense eruptive variability could be explained as arising from one physical mechanism, i.e. unsteady accretion, where a variation in the parameters of such mechanism can cause the different characteristics observed in the members of this class.

With the aim of studying the incidence of episodic accretion among young stellar objects, and to characterize the nature of these eruptive variables we searched for high amplitude variability in two multi-epoch infrared surveys: the UKIDSS Galactic Plane Survey (GPS) and the Vista Variables in the Via Lactea (VVV). In order to further investigate the nature of the selected variable stars, we use photometric information arising from public surveys at near- to far-infrared wavelengths. In addition we have performed spectroscopic and photometric follow-up for a large subset of the samples arising from GPS and VVV.

We analyse the widely separated two-epoch K-band photometry in the 5th, 7th and 8th data releases of the UKIDSS Galactic Plane Survey. We find 71 stars with $\Delta K > 1$ mag, including 2 previously known OH/IR stars and a Nova. Even though the mid-plane is mostly excluded from the dataset, we find the majority (66%) of our sample to be within known star forming regions (SFRs), with two large concentrations in the Serpens OB2 association (11 stars) and the Cygnus-X complex (27 stars). The analysis of the multi-epoch K-band photometry of 2010-2012 data from VVV covering the Galactic disc at $|b| < 1^{\circ}$ yields 816 high amplitude variables, which include known variables of different classes such as high mass X-ray binaries, Novae and eclipsing binaries among others. Remarkably, 65% of the sample are found concentrated towards areas of star formation, similar to the results from GPS. In both surveys, sources in SFRs show spectral energy distributions (SEDs) that support classification as YSOs. This indicates that YSOs dominate the Galactic population of high amplitude infrared variable stars at low luminosities

and therefore likely dominate the total high amplitude population.

Spectroscopic follow-up allows us to confirm the pre-main sequence nature of several GPS and VVV Objects. Most objects in both samples show spectroscopic signatures that can be attributed to YSOs undergoing high states of accretion, such as veiling of photospheric features and CO emission, or show FUor-like spectra. We also find a large fraction of objects with 2.12 μm H_2 emission that can be explained as arising from shock-excited emission caused by molecular outflows. Whether these molecular outflows are related to outbursts events cannot be confirmed from our data.

Adding the GPS and VVV spectroscopic results, we find that between 6 and 14 objects are new additions to the FUor class from their close resemblance to the near-infrared spectra of FUors, and at least 23 more objects are new additions to the eruptive variable class. For most of these we are unable to classify them into any of the original definitions for this variable class. In any case, we are adding up to 37 new stars to the eruptive variable class which would double the current number of known objects. We note that most objects are found to be deeply embedded optically invisible stars, thus increasing the number of objects belonging to this subclass by a much larger factor. In general, objects in our samples which are found to be likely eruptive variable stars show a mixture of characteristics that can be attributed to both of the optically-defined classes. This agrees well with the recent discoveries in the literature.

Finally, we are able to derive a first rough estimate on the incidence of episodic accretion among class I YSOs in the star-forming complex G305. We find that $\sim 9\%$ of such objects are in a state of high accretion. This number is in agreement with previous theoretical and observational estimates among class I YSOs.

Acknowledgments

Firstly I would like to thank my supervisor Dr. Phil Lucas for accepting me as a student and allowing me to continue to develop my interest in variable stars. Thank you for your patience, support and for making the effort to understand my English. I know that sometimes it was not easy to do. Also, thank you for helping me collect all of the data that was part of this PhD and for helping me with the observations in Chile. I would also like to thank my co-supervisor Dr Tim Gledhill and all of the staff at the Centre for Astrophysics Research (CAR) at the University of Hertfordshire.

A warm thanks to my former supervisors during my BSc and MSc degrees, Dr. Claus Tappert and Dr. Marcio Catelan, for helping me to get to this stage of my career, for being my friends and teaching me how to be a good researcher. I would also like to thank all of the people who inspired me through their teaching to love science: Hernan Chuaqui, Felipe Veloso, Dante Minitti, Marcelo Loewe and so many others at Universidad Catolica. Thanks to the people in the Plasma and Optics lab at Universidad Catolica for making me part of your group, David, Juan, don Dirk and Señora Cecilia. A especial thanks to my high school teacher Daniel Delgado, for being the best teacher and friend and for making every single one of his students believe that they could be better if they just worked hard.

To all of the people that helped me get through this PhD by being my friends at this University, Roberto, Kieran, James Canty, James Frith, Federico, Hywell, Liz, Ian, Silvia, Lissete, Andres, Angelo, Antoine and Ged. Thanks for all the laughs, football games and of course thank you for the amazing parties at 13 Horsa Gardens.

Also, thanks to the St Albans Romans Saturday league football team. Playing with you guys has been amazing, and I am sure we will be champions this year.

I would also like to acknowledge the biscuit companies of the United Kingdom, as well as to coffee producers from the whole world. Without the sugar rush and caffeine injections I would have never finished this PhD.

I would also like to thank the people in the Photonics department at Imperial College for accepting me every time I went to visit my wife, especially to Dr. Carl Paterson for allowing me to stay in the labs when I needed a desk to work. Also, thanks for letting me participate in the different BBQs, Christmas dinners, etc. Thank you Martin, Nick, David, Ian, Jack, Sunil, Judith and Marcia.

To my family and friends

- To all of the people in Chile who I am glad to call my friends, because even though we don't talk much I always know that I can count on you. To Alvaro, Fernanda, Joyce, Felipe, Jacuna, Tatiana, Fernando, Carlanga, Dario.

- To Jaime Gonzalez and Cristian Cepeda, Thanks for helping me get through high school, I know that I have not been the best friend during the last few years, but I cannot thank you enough for you friendship through those years. To Tomas Meneses, Luis Pacheco and

Cristian Martinez, thanks as well for your friendship and all of the beers and piscolas we shared so long ago.

- To the Riedel Family (Jim, Mary, Anna, Adam, Amy and Allison) and Robert Andersen in Monterey, USA. Your friendship, love and care during the year I stayed with you guys, helped me become a stronger and better person. I cannot thank you enough.

- To my aunts (Ana Maria, Raquel, Natalia), uncles (Luis, Victor, Italo) and cousins (so many, you know who you are), thanks for all of your support, love and for the great BBQs throughout the years.

- My parents Miguel and Patricia, without your support, care and love I would have not gotten this far. Thanks for all of the sacrifices you made to give us a good education and a good home to grow up in. Thank you for always believing in me, and for understanding my decision to come so far away to continue my career. And of course thank you for teaching me to be a good, honest person and to always work hard.

- To my sister Patricia and her husband Tom, you are a wonderful couple, thanks for accepting me and Noemi in Austria every year. It was always fun to see you guys, and I would always come back to work with more energy (and more wine as well).

- To my brother Miguel, thanks for always laughing with me at every stupid joke or thought that came to our minds (even when other people were looking at us like we were crazy, which we are not...I think), It was always good to see you and Anita when I travelled to Chile, specially the last time because I met my nephew Matias, he is a great kid, you should read this thesis to him whenever you want him to fall asleep.

- To my grandmother Lucy, gracias de todo corazón por estar siempre presente en los eventos mas importantes de mi vida, no sabe lo mucho que su cariño y apoyo han significado para mi. Gracias por todos los pisco sours que hemos compartido y por ser la mas prendida en nuestra fiesta de matrimonio.

- To the people who I am very happy to call my family as well, Manuel, Noemi, Manolo, Patty, abuelo Emilio. I am very thankful for all of the love and support you have given me through the years that I have been with Noemi. Abuela Julia even though you are not with us anymore...thank you for your sincere love towards me and for always being concerned about my well-being ... don't worry I will always take care of your muñeca.

- To Noemi, what else can I say that I haven't told you in person, I love you more than I ever thought I could have loved anyone. Through our years together you have made me a better and stronger person. Thanks for pushing me when I needed it and for being my friend throughout this PhD and our marriage. You are a strong, smart and beautiful woman and I am thankful and very lucky that you chose to be with me.

I would also like to acknowledge the different people, institutions and databases from which this work has benefited. I summarize this below

- This work is based on observations obtained in programme GN-2012B-Q-102 and GN-2013B-Q-47 at the Gemini Observatory, which is operated by the Association of Universities for Research in Astronomy Inc., under a cooperative agreement with the NSF on behalf of the Gemini partnership: The National Science Foundation (USA), the Science and Technology Facilities Council (UK), the National Research Council (Canada), CONICYT (Chile), the Australian Research Council (Australia). CNPq (Brazil) and CONICET (Argentina).

- This work is also based on observations taken as part of programme 085.C-0352(A) with the Very Large Telescope in Cerro Paranal, which is operated by the European Southern Observatory.

- This research has made use of the SIMBAD database, operated at CDS, Strasbourg, France.

- This research has made use of the NASA/ IPAC Infrared Science Archive, which is operated by the Jet Propulsion Laboratory, California Institute of Technology, under contract with the National Aeronautics and Space Administration.

- I would like to thank J. Najita for the very helpful discussions on some of our CO spectra and D. Steeghs for his assistance in providing the FAST data.

- I would like to thank D. Froebrich, C. Davis, N. Kumar, J. Drew, A. Adamson, G. Barentseen, N. Wright for all of the help and comments in the publication of the first paper from the GPS sample.

- Thanks to J. Goldstein, D. Barlow and R. Terzi, the summer students who helped with the visual inspection of variable star candidates arising from GPS and VVV.

- Finally, I have been supported by a University of Hertfordshire PhD studentship.

...Para el amor de mi vida, Noemí

Contents

List of Figures

List of Tables

Chapter 1

Introduction

The accepted model for the formation of low- and intermediate-mass stars is that they form from the collapse of dense cores in molecular clouds (Shu et al. 1987). This is usually explained as an inside-out collapse where the inner parts of the core collapse faster and become denser than the outer regions. Once the inner regions get dense enough they will become optically thick to their own radiation so the temperature rises, leading to the creation of a pressure-supported core surrounded by an infalling envelope. This stage marks the birth of the protostar (Lada 2005). The evolution of the protostar continues as it keeps gaining mass from the parent cloud, which occurs at nearly free fall velocities or at a constant rate of $\sim 10^{-5} \mathrm{M}_{\odot} \mathrm{yr}^{-1}$. Due to conservation of angular momentum and the fact that clouds have non-zero rotational velocities, a circumstellar accretion disc is expected to be formed. The material from the envelope feeds the disc, where the material is then accreted onto the star. In this picture the disc is able to transport the material at the same rate as the infall rate.

Once this accretion phase is over, the protostar becomes optically visible and continues its evolution towards the zero-age main sequence. Here the star is still not hot enough to burn hydrogen at its core, and the luminosity of the object arises from gravitational contraction. Stars in this later stage of evolution are known as pre-main-sequence (PMS) stars. Massive stars ($\mathrm{M}>8\mathrm{M}_{\odot}$) are expected to appear directly on the main sequence once the accretion phase is over (Shu et al. 1987).

Based on this simple model, several authors have tried to determine the evolutionary stage of young stellar objects (YSOs) according to their observed spectral energy distributions (SEDs). Lada (1987) defines different classes according to an infrared spectral index, α, determined from SEDs in the range $2 < \lambda < 20 \mu$m and where

$$\alpha = \frac{d \log(\lambda F_{\lambda})}{d \log \lambda} \tag{1.1}$$

In the definition of Lada (1987), the different classes can be divided as

- ***Class I*** These are objects with $\alpha > 0$, they are still deeply embedded within the infalling envelope and most of the system's luminosity is being radiated at near to far infrared wavelengths ($\lambda > 1 \mu$m), with flux increasing towards longer wavelengths. Stars in this

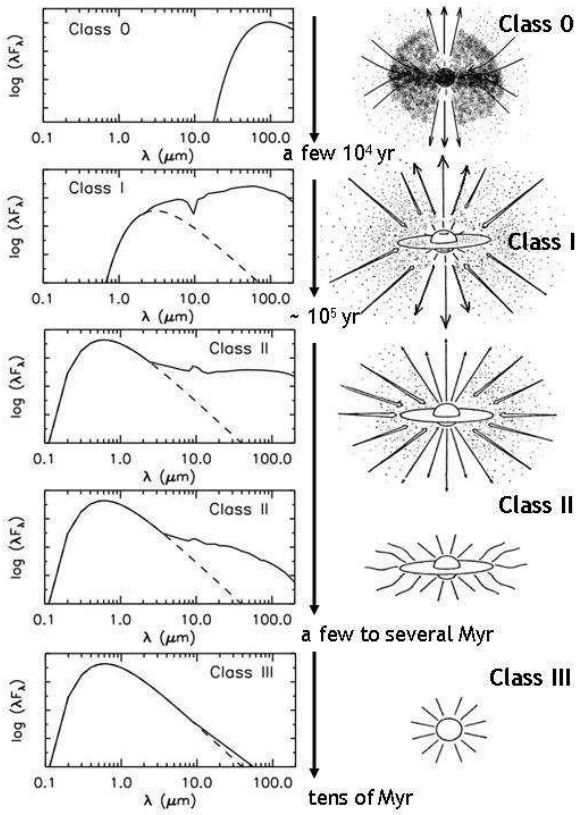

Figure 1.1: Diagram explaining the different SEDs and classification of YSOs. Figure adapted from Wilking (1989) by Elise Furlan (http://www.elisefurlan.com/Research.html)

stage are usually optically invisible.

- ***Class II*** Once the envelope has dissipated, the star becomes optically visible, but is still accreting material from a circumstellar disc (gaining a small percentage of its final mass during this stage, Lada 2005). Due to the latter, stars at this stage show near and mid infrared emission in excess of what is expected from a blackbody spectrum. These are known as class II objects and have a negative spectral index with $-2 < \alpha < 0$. Objects in this class are usually divided into classical T Tauri stars (CTTS Joy 1945), which have masses below $2M_\odot$ and spectral types later than F-type, and their more massive counterparts known as Herbig Ae/Be stars ($2M_\odot$ <M<$8M_\odot$ Herbig 1960).

- ***Class III*** The last stage, or class III stars, corresponds to the time where the star has a small but measurable infrared excess, arising from an optically thin accretion disk. Class III stars are also known as weak-lined T Tauri stars (WTTS).

Andre et al. (1993) and Greene et al. (1994) later add class 0 and "Flat-SED" objects to the groups of YSOs. The former are too deeply embedded to be detected in the near infrared, and are believed to be at a younger evolutionary stage than class I objects, being invisible even at near-infrared wavelengths, and with most of the flux of the stars being radiated at $\lambda > 10\mu$m.

Class	α
Class I	$\alpha > 0.3$
Flat	$-0.3 \leq \alpha \leq 0.3$
Class II	$-1.6 < \alpha < -0.3$
Class III	$\alpha \leq -1.6$

Table 1.1: Class definition according to the observed SED. Taken from Greene et al. (1994)

Flat-SED objects have $-0.3 < \alpha < 0.3$ and even though their nature is not clear, they are believed to be in transition stage between class I and II objects (see e.g. Dunham et al. 2014). Table 1.1 shows the class definition according to the spectral index α (taken from Greene et al. 1994). Figure 1.1 shows a schematic view of the SEDs for the different classes of YSOs

We note that because the classes are empirically defined and given the uncertainty caused by inclination or foreground reddening, researchers refer to stages 0 to 3 rather than classes 0 to 3, when they wish to be clear about the evolutionary status of a YSO (see e.g. Robitaille et al. 2006; Dunham et al. 2014).

During most of the stages of star formation, mass is accreted onto the central star via an accretion disc. During the infall phase the disc must be able to transport material at similar rates as the infall from the envelope to the disc, of approximately 10^{-5} $M_{\odot}yr^{-1}$. However, the observed protostellar luminosities are considerably lower than that expected from such high rates, this is the so-called "Luminosity problem" (see e.g Kenyon et al. 1990, and later on this chapter). This problem is resolved if the mechanism that transport mass and angular momentum through the disc is inefficient and most of the mass accumulates in the circumstellar disc, and it is later accreted onto the star in short-lived outburst events. Thus, the star will spend most of its lifetime in states of low accretion, being less luminous than expected from the high infall rates.

Works studying the physical mechanisms that likely transport material and angular momentum through the disc have shown that these mechanisms are unable to transport mass at the large rates expected from infall and are likely to produce outbursts of rapid accretion (see e.g Zhu et al. 2009; Dunham & Vorobyov 2012).

1.1 Episodic accretion

Observational support for the idea of episodic accretion arises from: 1) YSOs displaying sudden rises in luminosity, of up to 6 magnitudes, and that can last from months to $\sim$ 100 yr. This group of objects, known as eruptive variable stars, are usually divided into two sub-classes, FUors (named after the prototype FU Orionis) and EXors (after EX Lupi) (Herbig 1977, 1989; Hartmann & Kenyon 1996). 2) Observation of emission knots in jets from outflows of YSOs. These knots are separated by large distances and could be related to episodes of enhanced accretion onto the star (see e.g., Ioannidis & Froebrich 2012).

The widely accepted picture for young eruptive variables is that these objects correspond

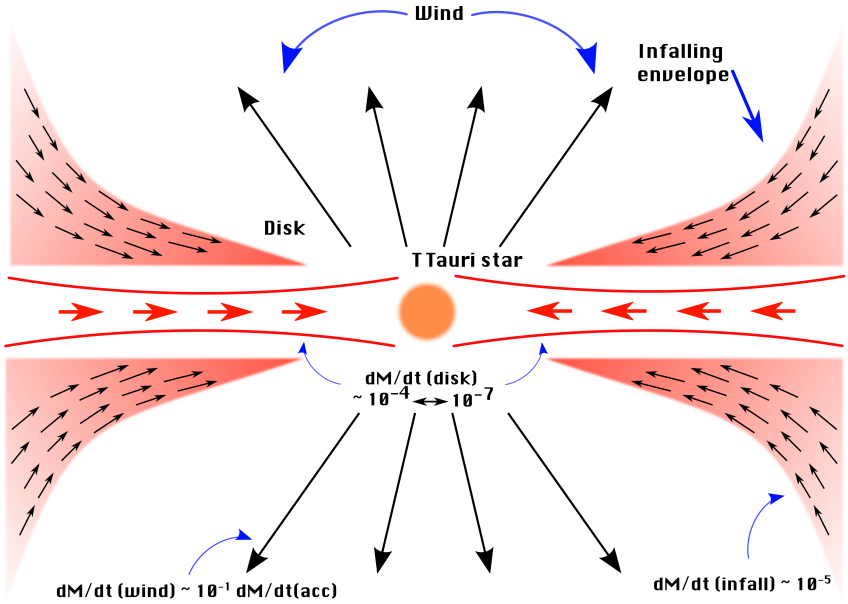

Figure 1.2: Schematic view of young eruptive variable of the FUor class. Figure adapted from Hartmann & Kenyon (1996)

to YSOs accreting material from a cirmcumstellar disc that suffer from episodic outbursts as a consequence of sudden and steep increase of the mass accretion rate onto the central star, going from typical rates of 10^{-7} $M_\odot$ yr^{-1} to reach up to 10^{-4} $M_\odot$ yr^{-1}, dumping as much as 0.01 $M_\odot$ into the central star in one outburst (see e.g Audard et al. 2014). As a consequence of the accretion event strong winds or even jets emerge from the system (many of these of objects are the sources of Herbig-Haro flows, see e.g. Reipurth & Aspin 1997) , which have a significant impact on the surrounding interstellar medium (ISM). These systems show infrared excesses that are consistent with them still possessing a protostellar envelope, from which material may still be falling onto the disc, providing the necessary material to replenish the disc between outburst episodes (Hartmann & Kenyon 1996). A schematic view of these young eruptive variables is shown in Fig. 1.2.

Both sub-classes show different photometric and spectral properties, which are summarized below

FUors

FU Orionis was observed to increase its luminosity by 6 magnitudes (in B) between 1936-37 and it was originally classified as a Nova outburst (see e.g McLaughlin 1945). However Herbig (1966) argued in favour of it being related to an early stellar evolution phenomenon rather than a Nova outburst. The classification did not become clear until the observations of outbursts in V1057 Cyg in 1970 and V1515 Cyg in 1974 (see Herbig 1977).

FUors share similar increase of 5-6 magnitudes over periods larger than 1 yr and decay times greater than 10 yrs (see figure 1.3). Stars belonging to this group are also spatially

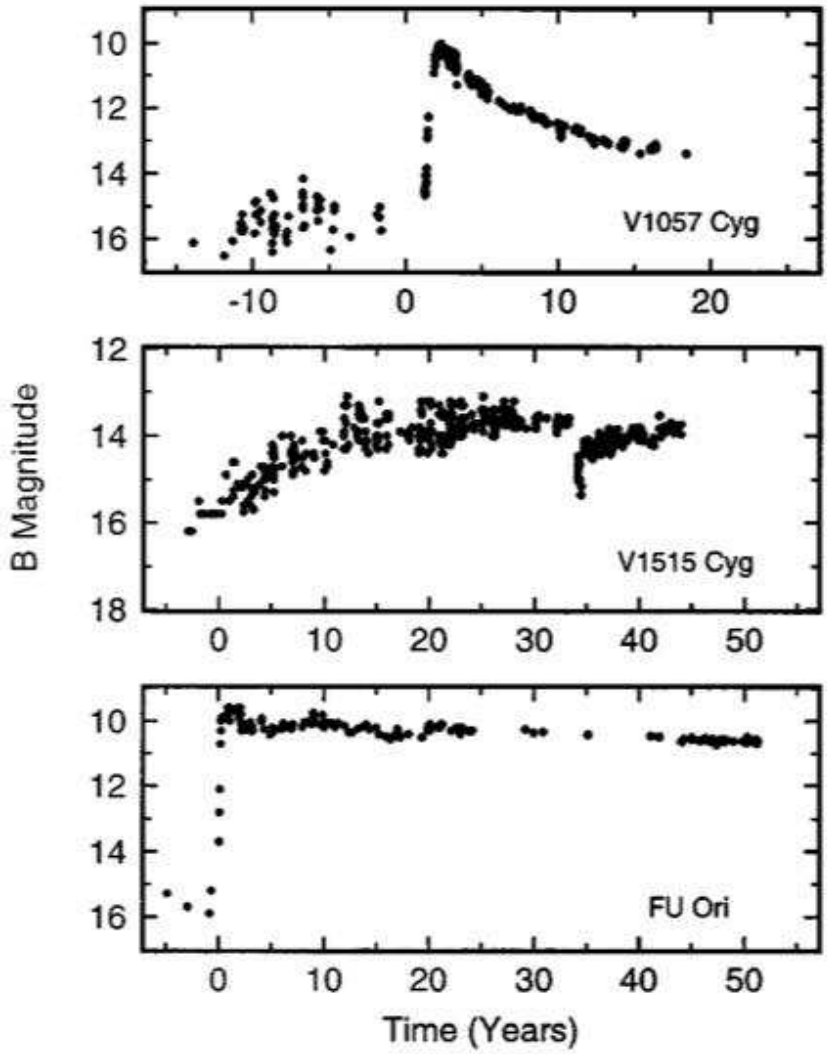

Figure 1.3: B light curves of classical FU Orionis stars. Figure taken from Hartmann & Kenyon (1996)

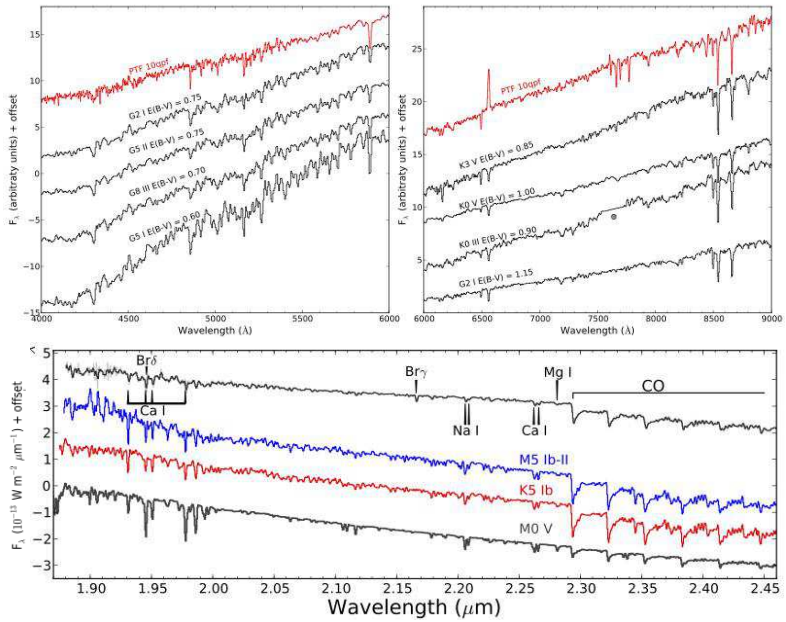

Figure 1.4: Figure taken from Miller et al. (2011) showing the optical (*top*) and near-infrared (*bottom*) spectrum of recent FUor object HBC722. In all graphs the spectrum of the star appears on the top, while the spectrum of stars of different spectral types are shown for comparison. Miller et al. (2011) find the stars resembles a G supergiant in the optical, whilst resembling a M giant in the near-infrared.

and kinematically associated with star forming regions. Many of these objects posses reflection nebulae and have also been linked to Herbig-Haro (HH) objects (Reipurth & Aspin 1997; Greene et al. 2008), with at least 50% of FUors being associated with HH flows (Reipurth & Aspin 1997).

The optical spectra of these objects, while in outburst, resemble those of stars with spectral types of late F to G supergiants. Hydrogen lines of the Balmer series are usually present, with Hα being the most prominent feature. This line is usually observed as a broad absoprtion feature blueshifted by several hundred km s^{-1}, where the emission component of the P Cygni profile is usually not present. The near-infrared spectrum shows strong CO absorption at 2.29 μm and from H_2O in the 1-2 μm region. The near-infrared features are inconsistent with optical spectra and in terms of stellar photospheres, resembles that of a K-M giant-supergiant (see figures 1.4 and 1.5). This change of spectral type with wavelength is one of the principal characteristics of the FUors class (Hartmann & Kenyon 1996).

Putative members of this class do not have recorded outbursts and are classified as FUors based only on the resemblance of their spectral characteristics to that of FU Orionis, specially the strength of the CO bands at 2.29 μm (e.g. Z CMa, BBW76, Parsamian 21, see Reipurth & Aspin 2010a, and references therein). These stars are usually referred as ***FUor-like stars***. Several other embedded (class I) stars have been found to be FUor-like given their spectral characteristics (e.g PP13S, AR6A+B, L1551IRS5, Aspin & Sandell 2001; Aspin & Reipurth 2003; Mundt et al. 1985). These are thought to be younger versions of FUors at a stage where

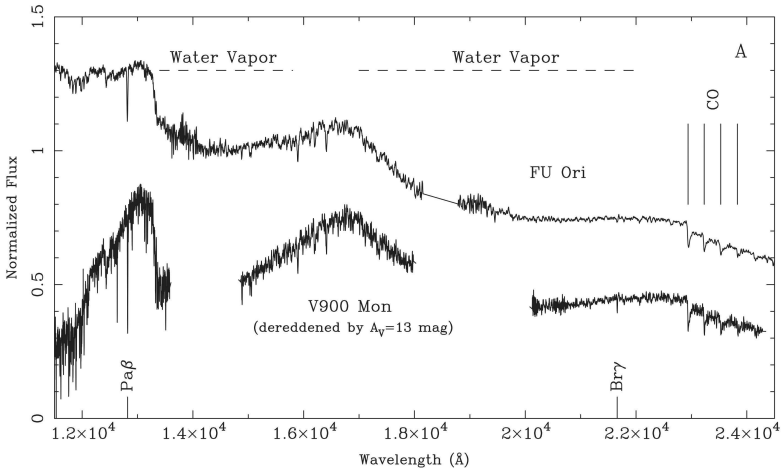

Figure 1.5: Near-infrared spectrum of the eruptive variable star V900 Mon (*bottom*) compared to that of FU Orionis (*top*). Figure from Reipurth et al. (2012)

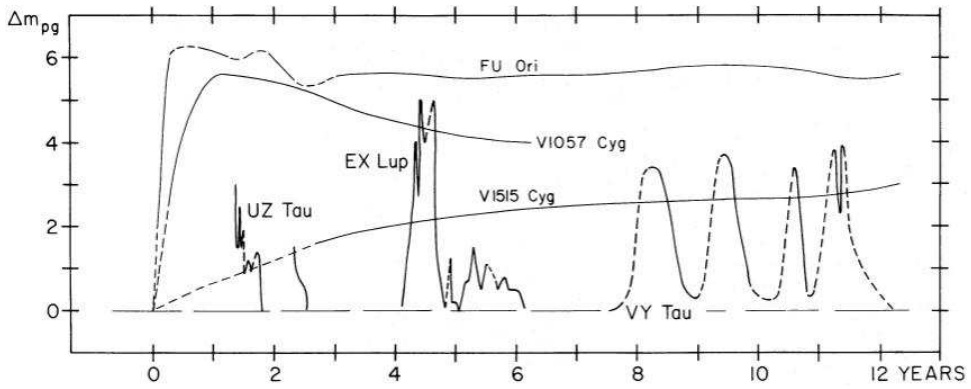

Figure 1.6: Light curves of some example classical EXors, EX Lupi, VY Tau and VZ Tau. Just as a comparison, light curves of classical FUors are also included in the picture. Figure taken from Herbig (1977)

stars are still accreting a significant portion of their final mass. In fact, we note that most of the objects classified as FUors or FUor-like objects are partially or fully embedded in molecular cloud cores.

EXors

EXors are thought to be the less dramatic counterparts of FUors as they show magnitude variation of 2-5 magnitudes in the optical, but with a higher recurrence of short-lived (less than $\sim$ 1 yr) outbursts superposed on longer quiescence periods of 5 to 10 years (e.g. Fedele et al. 2007; Lorenzetti et al. 2009a, see Fig. 1.6).

Their spectral characteristics also differ from FUors, as they show an emission line T Tauri spectrum in the optical when found at minimum light. The near-infrared spectrum shows strong Brγ emission and CO bandhead emission at 2.29 μm when the star is brightest, the latter being observed in absorption during quiescent states (see figure 1.7). A similar behaviour is observed

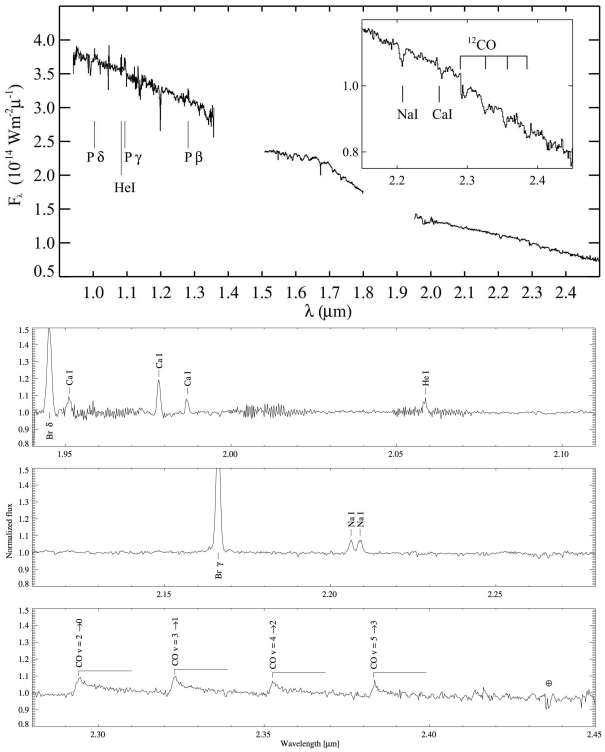

Figure 1.7: Near-infrared spectra of EXor prototype EX Lupi during a quiescent state (*top*, from Sipos et al. 2009), and during its 2008 outburst (*bottom* Kóspál et al. 2011a)

for atomic lines of Na I (2.206 μm) and Ca I (2.267 μm). During these quiescent periods the system's luminosity at this wavelength is dominated by the stellar flux, thus absorption from CO, Na I and Ca I arise from the stellar photosphere, whilst emission from these features are expected to arise from a hot inner disc during outburst (see e.g. Lorenzetti et al. 2009a).

1.1.1 FUors and EXors: related?

The different characteristics displayed by the two subclasses leads to the question: are these variable classes related? The classical view is that FUors are at an earlier evolutionary stage and belong to the transitional phase between Class I and Class II objects, whilst EXors are associated with instabilities in the discs of Class II objects. However, both classes of young eruptive variables were originally defined at optical wavelengths, which tends to exclude younger protostars which have higher accretion rates but are too deeply embedded in circumstellar matter to be observed at visible wavelengths.

Three optically invisible protostars have been confidently identified as eruptive variables, with K bandpass variability in excess of 2 magnitudes: OO Ser (Hodapp et al. 1996; Kóspál et al. 2007), [CTF93] 216-2 (V2775 Ori, Caratti o Garatti et al. 2011) and GM Cha (ISO-Cha I 192, Persi et al. 2007). These and other more recent discoveries show characteristics that can be attributed to both FUors and EXors. For example, the duration of the outburst of OO Ser of $\sim$ 10 years (Kóspál et al. 2007) is longer that expected for EXors but shorter

compared to classical FUors. In addition, the object shows a nearly featureless spectra lacking the characteristic deep CO absorption of FUors. V2775 Ori went into outburst in 2011, its near-infrared spectrum shows strong CO and H_2O absorption, typical of FUors, but its peak luminosity of $\sim$ 10 $L_\odot$ makes it one of the weakest outbursts in this class. In addition the duration of the outburst is also in between EXors and FUors (Caratti o Garatti et al. 2011).

Another example arises from V1647 Orionis. This object is a young eruptive star located in the L1630 cloud within the Orion B molecular cloud complex. It was observed to outburst in 2003, increasing its optical/infrared brightness by up to 6 mag. The outburst was covered over a wide range in wavelength and several authors have studied the behaviour of V1647 Ori (see Fedele et al. 2007; Reipurth & Aspin 2010a, and references therein). Its optical spectrum presented strong Hα in emission with blueshifted absorption, whilst in the near-infrared showed strong CO bands in emission with Na I and Brγ also in emission. After one year the star had returned to its pre-outburst magnitude but was observed to re-brighten in late 2008 (Aspin et al. 2009b) showing different spectral characteristics in the near-infrared, without CO in emission, and resembling the high-resolution spectral characteristics of FUors in Aspin et al. (2009a). Thus, V1647 Orionis presents characteristics that can be associated with both FUors (amplitude, Hα P Cygni profile) or EXors (near-infrared spectrum, duration of outbursts) as noted by several authors (e.g. Fedele et al. 2007; Gibb et al. 2006).

Given the peculiar characteristics of the recent discoveries, it has been proposed that they represent a new type of eruptive variables (Kóspál et al. 2007). However, a more accepted scenario is that, if we think of the outburst phenomena as a continuum, these objects may instead represent a "connection" between FUors and EXors , with FUors representing one extreme (long duration) and EXors being the short duration end of the same phenomenon. In this sense the different types of outbursts are produced by variations of one or more of the parameters involved in the instabilities that give rise to the outburst. This scenario has already been presented by previous studies of young eruptive variables (Gibb et al. 2006; Fedele et al. 2007; Aspin et al. 2009a).

1.1.2 Physical Mechanism

The mechanism in which an outburst occurs for this kind of star is not completely clear and different models have been proposed, with the vast majority of them proposing that some kind of disc instability must drive the sudden changes in the mass accretion rate onto the star. It is unlikely that a single model is able to explain the outburst behaviour in all of the members of the class of eruptive variables. Instead, the outbursts could be triggered by different mechanisms which would give rise to the mixture of characteristics observed in eruptive variables. Figure 1.9 shows the timescales of the outburst generated by some of the different models that will be explained below.

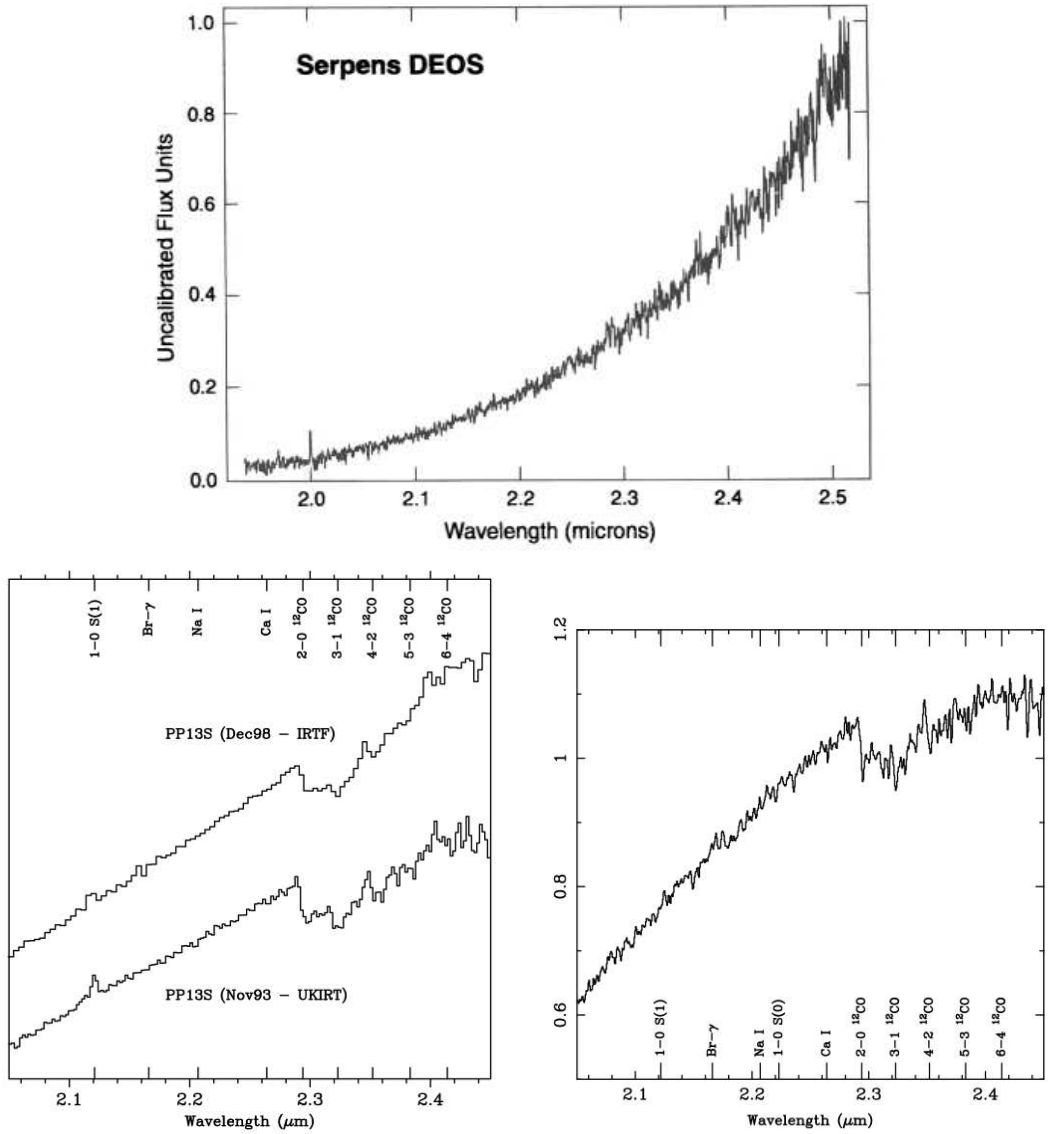

Figure 1.8: K-band spectra of three embedded sources (*top*) OO Ser (from Hodapp et al. 1996), (*bottom left*) PP13S (from Aspin & Sandell 2001) and (*bottom right*) AR6B (from Aspin & Reipurth 2003)

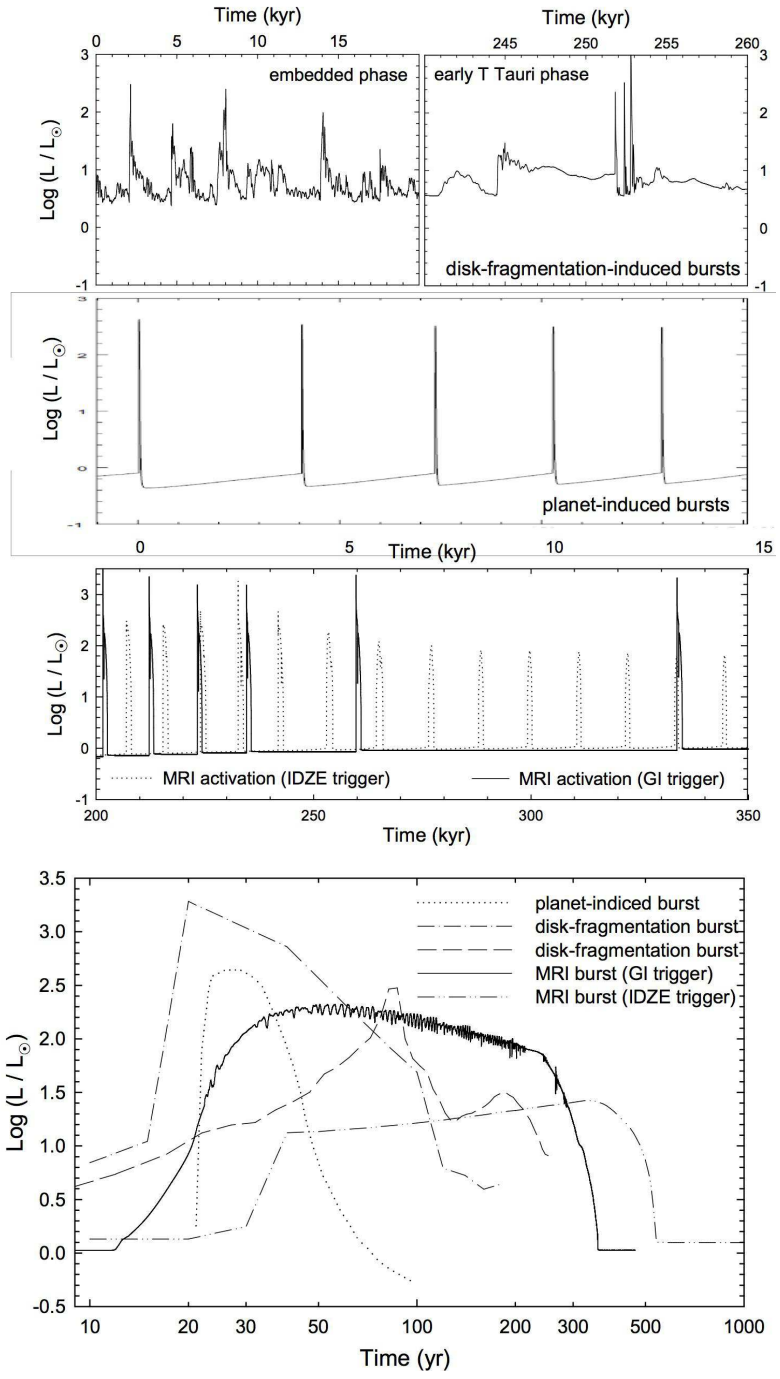

Figure 1.9: Variability produced by different models that trigger outbursts in YSOs and which are summarized in the text. These are shown over long timescales during the evolution of the star (*top*) and over a single outburst (*bottom*). Taken from Audard et al. (2014).

Rapid Rotation of a PMS star

This mechanism states that the change in the luminosity of FU Ori stars is due to processes in the star itself rather than occurring in an accretion disc. The original model is proposed by Larson (1980), as the authors neglect a possible effect from a circumstellar disc, given the scarce evidence present at the time for the existence of such discs in YSOs.

Larson (1980) proposes that the gravitational energy during contraction of a PMS star is converted to rotational energy, spinning up the star, which could explain the large broadening of absorption lines in these type of variable stars. The large velocities would lead to bar-like instabilities in the equatorial regions, which would create shocks and turbulence that would convert a large fraction of the rotational energy of the star into heating of these outer layers, which accounts for the flare-up and consequent mass-loss (Herbig et al. 2003).

Petrov & Herbig (1992); Herbig et al. (2003) are able to reproduce the optical spectrum of FUor objects V1057 Cyg, and FU Ori as arising from a rapidly rotating star with a GIII spectral type. However, this model fails to account for several other characteristics of FUor objects, such as the dependence of $v \sin(i)$ on wavelength, as well as the observed M-type spectrum at near-infrared wavelengths.

Binary Interaction

In this scenario the gravitational force of a companion star may perturb the disc and thus enhance accretion (Bonnell & Bastien 1992), this idea is supported by the fact that a number of known eruptive variables are members of binary systems (see e.g., Reipurth & Aspin 2010a; Fedele et al. 2007, and references therein). In some of these, both stars in the system are found to have FUor-like characteristics (AR6A+B, RNO1B/C Aspin & Reipurth 2003). Reipurth & Aspin (2010a) claim that is very unlikely that two YSOs in a binary system go through episodic events independently, so whatever mechanism is producing the outburst in one star is likely responsible for the episodic accretion in the companion star. However, these systems have large separations of a few thousand AU, which implies a few thousand years before periastron passage, and outbursts are unlikely to have such long duration. Also, this would require large eccentricities of the binary orbit in order to obtain the periastron distances required to perturb the discs (d$\sim$10 AU, which are unlikely in wide binary systems, Reipurth & Aspin 2010a).

The timescale and eccentricity problem in this scenario is solved by invoking the formation of a multiple system (Reipurth & Aspin 2004b, 2010a). A tightly bound, eccentric binary is expected to form from an initial unstable, non-hierarchical triple system, where the third original member has escaped from the system. The new binary is still surrounded by circumstellar material. Interaction with the latter leads to quick shrinkage of the orbit and as the stars spiral inward, more perturbations of the disc and thus outbursts are expected to occur (Bonnell & Bastien 1992; Reipurth 2000; Reipurth & Aspin 2004b). This could explain the fact that FU Orionis itself is a binary system (Reipurth & Aspin 2004b).

In this case, episodic accretion is a natural result from the evolution of a multiple system. However, this does not imply that other sources of instabilities might not be able to explain the

sudden outbursts observed in YSOs.

Thermal Instabilities

The transport of angular momentum in accretion discs is not well understood, and it is usually assumed that some form of viscosity induced by instabilities in the disc is able to allow this transport (this is usually described by the standard α-disc model Shakura & Sunyaev 1973).

The standard mechanism invoked to explain what triggers outburst events in FU Orionis stars is the thermal instability of the accretion disc, a mechanism that has also been used to explain outbursts in accretion discs of binary systems such as cataclysmic and symbiotic variables (see e.g. Bell & Lin 1994; Bell et al. 1995; Hartmann & Kenyon 1996). In this scenario, in order to maintain thermal equilibrium, the energy generated in a viscous disc must balance radiative losses. This is possible if the opacity κ of the disc changes slowly with temperature. When the disc reaches the hydrogen ionization temperature (T$\sim$5000 K), the opacity changes abruptly with temperature, $\kappa \propto T^{10}$, thus a slight change in temperature will increase the amount energy trapped in the disc, leading to a thermal runaway which ends when the disc is fully ionized. The high temperature at the end of the thermal runaway can lead to a high accretion rate on the viscous disc, given the dependence of the viscosity, ν, with temperature

$$\nu = \frac{\alpha c_s^2}{\Omega} \propto \frac{\alpha T}{\Omega}, \tag{1.2}$$

where c_s, Ω and α correspond to the speed of sound, the angular velocity and the viscosity parameter respectively (with $0 < \alpha \leq 1$ Shakura & Sunyaev 1973).

Given the high temperatures required to ionize hydrogen, the instability will proceed in an inside-out fashion, decelerating as it propagates (Bell et al. 1995). This will lead to slow rising times, contrary to what is usually observed in FU Ori-like outbursts. However, a perturbation in the outer edge of the disc can lead to thermal instabilities that will propagate inwards, producing the observed fast rise times of eruptive variable stars (Bell et al. 1995).

- **Thermal instabilities induced by a planet** Lodato & Clarke (2004) propose that the interaction of a massive planet with the disc can trigger thermal instabilities in the outer disc. In this scenario, the migration of the planet opens up a gap in the disc, and the inner disc is emptied out. Due to the tidal effect induced by the planet, material will pile up at larger radii. When the density reaches a critical value, thermal instabilities are triggered. The sudden increase of the accretion rate will overcome the tidal effects of the planet and the gas moves to the inner disc triggering the outburst. Lodato & Clarke (2004) find that this planet-triggered outside-in outburst is able to reproduce the fast rising times and peak luminosity expected for FUor objects, as compared to an inside-out model where no interaction is present. However, their models are not able to produce outbursts with durations longer than 50 years.

  It is worth noticing that other mechanisms that will be discussed later can also trigger thermal instabilities for an outside-in outburst.

MRI+GI instabilities

Accretion discs where the gas is coupled to a weak magnetic field are subject to magnetohydrodynamic instabilities that lead to turbulences which allow the transport of angular momentum (Armitage et al. 2001; Lodato & Rice 2004; Turner et al. 2014). In order for this magneto-rotational instabilities (MRI) to efficiently transport angular momentum, a large fraction of the disc must be ionized. In regions at $r < 1$ AU this fraction is usually large due to thermal ionization (Gammie 1996). However, at larger radii the ionization fraction is low and MRI is suppressed. In this zone the midplane of the disc is cold enough and turbulence free whilst X-ray and far ultraviolet radiation from the star or incident cosmic rays, can ionize the upper disc layer, which will be coupled to the magnetic field, thus allowing MRI to transport angular momentum (Gammie 1996). The latter process is known as layered accretion. Zhu et al. (2009) establish that this layered accretion is unlikely to transport mass at r of a few AU at protostellar infall rates of $\sim 10^{-5}$ $M_{\odot}yr^{-1}$.

A second mechanism must be responsible of the mass transport at larger r in protoplanetary discs. This is usually ascribed to gravitational instabilities (see e.g. Vorobyov & Basu 2005, 2006). If MRI is inefficient at these large radii, then mass will accumulate until the disc becomes gravitationally unstable. This will occur when the Toomre parameter Q (Toomre 1964)

$$Q \approx \frac{c_s \Omega}{\pi G \Sigma}, \tag{1.3}$$

becomes lower than a critical value Q_{cr} (usually $Q_{cr} \sim 1$, see e.g., Zhu et al. 2009). In the above, Σ corresponds to the disc surface density at a given r. This instability results in the formation of spiral arms through which mass can be rapidly transported. Given this compression into spiral arms, discs are likely to heat up, which will tend to suppress this instability. However, if the disc can cool efficiently it can again become unstable. This self regulating state can persist for several orbital periods if the cooling rate is longer than a few dynamical timescales (see Audard et al. 2014, and references therein). The fast transport of mass to smaller r will trigger GI in the inner disc. However, GI becomes inefficient at $r < 1$ AU. This is because at this distance temperatures (which relate to c_s) and angular velocities (Ω) are much higher, so in order to fulfil $Q < Q_{cr}$, Σ must attain values that are higher than has been observed in YSOs (Zhu et al. 2009, estimates that the inner disc must have a mass of at least 0.5-0.6 $M_{\odot}$).

During the protostellar phase where infall rates are high, accretion is not expected to a be steady process (Armitage et al. 2001; Zhu et al. 2009). GI in the outer disc can transport mass at the high infall rates, this will lead to an eventual triggering of MRI at $r \sim 1 - 2$AU due to thermal ionization. Triggering of MRI will lead to outburst as observed in FU Ori stars (Armitage et al. 2001; Zhu et al. 2009; Audard et al. 2014). Zhu et al. find that for lower infall rates of Class II objects, layered MRI turbulence might be able to accumulate mass and trigger the MRI outbursts (Audard et al. 2014, and references therein).

Disc Fragmentation

From the section 1.1.2 we see that accretion discs can transport mass due to GI during the protostellar phase, where the disc self regulates to maintain Q close to Q_{cr}. However, for cooling times shorter than the dynamical timescale, disc pressure is not able to support the collapsing gas against its own gravity, leading to disc fragmentation (see e.g., Vorobyov & Basu 2005; Machida et al. 2011). Vorobyov & Basu (2010) find that high initial rotational velocities of the collapsing molecular cloud lead to the formation of more massive and extended discs, where GI and disc fragmentation are more likely to occur.

The fragments are later transported to the inner disc via gravitational interactions with the spiral arms (Machida et al. 2011), and are likely to trigger mass accretion bursts (Vorobyov & Basu 2010). The interaction of the substellar mass fragments might also induced episodic accretion via perturbations to the inner disc (Machida et al. 2011). The accretion during the protostellar phase due to this process is highly variable, with short duration bursts followed by long quiescent periods. Mass accretion outburst might occur during the Class II phase if some of these fragments survive the embedded stage (see Audard et al. 2014, and references therein).

1.2 Importance of Episodic accretion on Low Mass Star Formation

Hartmann & Kenyon (1996) conclude that if all low-mass stars go through periods of enhanced accretion, then every star goes through at least 10 outbursts during its formation. In addition they estimate that stars must spend $\sim 5\%$ of their lifetime in high states of accretion to gain their final mass during the infall phase. Enoch et al. (2009) and Evans et al. (2009) find that 5-7% of class I stars in their sample are at high accretion states. Giving the growing evidence for episodic accretion, it has been brought forward to help solve long-standing problems in young stellar evolution.

1.2.1 Protostellar Luminosity Problem

During the protostellar phase, the luminosity of the star+envelope system is given by:

$$L_s = L_{phot} + f_{acc}\frac{GM\dot{M}}{r}, \tag{1.4}$$

where L_{phot} corresponds to the luminosity arising from the stellar photosphere, which is generated by deuterium burning and gravitational contraction, M and r are the stellar mass and radius, respectively, f_{acc} is the fraction of energy radiated away in the accretion shock and $\dot{M}$ is the accretion rate (Dunham et al. 2014). The accretion rate in this phase of the evolution arises from gravitational collapse and is in the order of $\dot{M} \approx 10^{-5}$ $M_{\odot}yr^{-1}$. Kenyon et al. (1990), in their study of the Taurus-Auriga molecular cloud, find that the typical luminosities of YSOs is lower than the expected L_s. This problem has been exacerbated in more recent years. Luminosities of protostars from the *Spitzer* "From Molecular Cores to Planets Forming

discs" survey (c2d Evans et al. 2003) show that the L_s distribution is strongly skewed towards lower luminosities and indicates that for most stars $\dot{M} \leq 10^{-6}\mathrm{M}_{\odot}\mathrm{yr}^{-1}$ (Enoch et al. 2009; Evans et al. 2009)

A possible solution to the so called "Luminosity Problem" is that a large population of stars are at present in a quiescent state of accretion, thus having low luminosity, with only a few percent of them being on high-accretion states. Stars will then gain most of their final mass during these periods of enhanced accretion (Kenyon et al. 1990; Evans et al. 2009; Caratti o Garatti et al. 2012).

1.2.2 Luminosity spread in Hertsprung-Russel Diagrams of low-mass YSO clusters.

The Hertzsprung-Russell (HR) Diagrams of low-mass YSO clusters are known to display a large spread of the luminosities of the stars belonging to individual clusters (Hartmann 2001; Hillenbrand 2009; Weights et al. 2009). This scatter is usually explained as an age spread within the cluster (of ∼10 Myr), although it is uncertain whether such age differences are real or if the spread can be explained by observational uncertainties or unknown physical processes (Hillenbrand 2009).

Stellar ages and masses are estimated from HR diagrams by comparing L–T_{eff} with theoretical models of non-accreting PMS stars evolving through Hayashi tracks. However, Baraffe et al. (2009, 2012) argues that the observed spread can be explained by including episodic accretion during the protostellar phase. The final location of an individual star in the HR diagram, strongly depends on its accretion history. The implications of this is that stellar masses determined through HR diagrams may be overestimated, with Baraffe et al. (2012) finding that stellar masses determined by comparing to non-accreting models can be overestimated by as high as $\sim 40\%$.

1.2.3 Effect on the formation of low mass stars and Brown Dwarfs

Stamatellos & Whitworth (2009) determines that low-mass hydrogen burning stars ($0.08 - 0.2\mathrm{M}_{\odot}$), brown dwarfs (BDs, $0.012 - 0.08\mathrm{M}_{\odot}$) and planetary-mass objects ($\leq 0.012\mathrm{M}_{\odot}$) can form via gravitational fragmentation of the accretion disc and end up bound to the primary star or ejected from the system. This mechanism is able to explain properties of low mass stars, such as the observed binary fraction and the BD desert (Burgasser et al. 2007).

However, strong radiative feedback from the star can heat up the disc, stabilizing it and thus suppressing its ability to fragment (Stamatellos et al. 2011, and references therein). The standard model of low mass star formation predicts that the accretion to the star, and thus radiative feedback, is constant. Then, episodic accretion can play a major role for gravitational fragmentation. Stamatellos et al. (2011) argues that during periods of enhanced accretion, radiative feedback will be strong enough to suppress disc fragmentation. However, the long quiescent states expected after outburst, would allow sufficient time for the disc to cool, enhancing its ability to fragment and produce low mass star companions.

1.3 Motivation

The idea that mass accretion is not constant but rather episodic during the formation for all low- to intermediate-mass stars would help solve several standing problems in stellar evolution.

It is the motivation of this Thesis to study and characterize eruptive variability in areas of star formation and possibly estimate the incidence of episodic accretion in young stellar objects.

With this goal in mind we have searched for high amplitude variability in near-infrared multiepoch surveys of the Galactic Plane. We have also used ancillary data from near- to far-infrared public surveys to support our investigation on the nature of these objects. Additional spectroscopic follow-up were also obtained for a subset of high amplitude variables in order to clarify their nature as possible YSOs. With this information in hand we are able to address the following points:

- How rare is high-amplitude variability ($\Delta K > 1$ magnitudes) among stars in areas of star formation?
- Are these large variations in YSOs being driven by outbursts of accretion?
- Can we classify objects showing characteristics of eruptive variables into the classical definition for these objects? Or are the new additions more in line with more recent discoveries of eruptive variables?
- And finally, what is the incidence of eruptive variability among YSOs?

Although in this last point we are only providing an initial rough estimate, this work surely represents and advancement towards providing a definite answer to that question.

This work is divided in the following chapters. Chapter 2 describes the mechanisms that usually explain the spectroscopic and photometric characteristics that are observed in YSOs. In chapter 3 we describe the surveys and the selection methods that were used to search for high amplitude variables. A brief summary of the characteristics of different near- to far-infrared surveys used as support information during this thesis is also given. In the same chapter we provide the description of telescopes and instruments used for spectroscopic and photometric follow-up of GPS and VVV objects. Chapter 4 presents the results of the analysis GPS objects arising from the searches in data releases DR5 and DR7 of GPS, with a detailed discussion on the spectroscopic follow up of DR5 objects. Chapter 5 provides the results of the search in data release DR8 of GPS as well as the general discussion of the spectroscopic follow up of DR7 and DR8 objects. Chapter 6 present similar discussion, but for the results of the search in the 2010-2012 database of VVV. Finally, summary, conclusions and future work are presented in chapter 7 of the thesis.

Chapter 2

Spectroscopic and photometric characteristics of YSOs

In this chapter we will discuss the typical spectroscopic signatures and photometric variability observed in YSOs and the physical mechanisms that are brought forward to explain these characteristics. The photometric variability and spectroscopic signatures of these objects can be explained by processes occurring in the stellar photosphere, the accretion discs or in winds/molecular outflows.

This chapter is motivated by the fact that identification of eruptive variables is done via the photometric light curves and the spectroscopic features observed in these objects. Some of these features can be unique to the class, such as the broad 2.3 μm CO first-overtone band head absorption observed in FUor and FUor-like stars, but many of them can also be observed in non-eruptive young stars.

One of the main characteristics of YSOs is that they are variable stars. These are usually of low-level variability driven by several physical mechanisms, which are not comparable with the large variations observed in eruptive YSOs. However, some of these mechanisms could still drive large variations that could explain the light curves in our sample of YSOs.

In the following, I will summarize the information on typical emission/absorption lines observed in the spectra of YSOs as well as the common physical mechanisms that produce variability in YSOs. The main focus will be on the signatures observed at near-infrared wavelengths.

2.1 Spectroscopic signatures

2.1.1 Hydrogen recombination lines.

It is accepted that in low and intermediate mass YSOs the accretion onto the star occurs via a process known as magnetospheric accretion (see e.g. Muzerolle et al. 1998a, 2001, 2004). In this model the disc is truncated at a radius, R_T, where the pressure from magnetic field lines from the star balances the ram pressure of the accretion disc. Material at R_T is then guided onto the

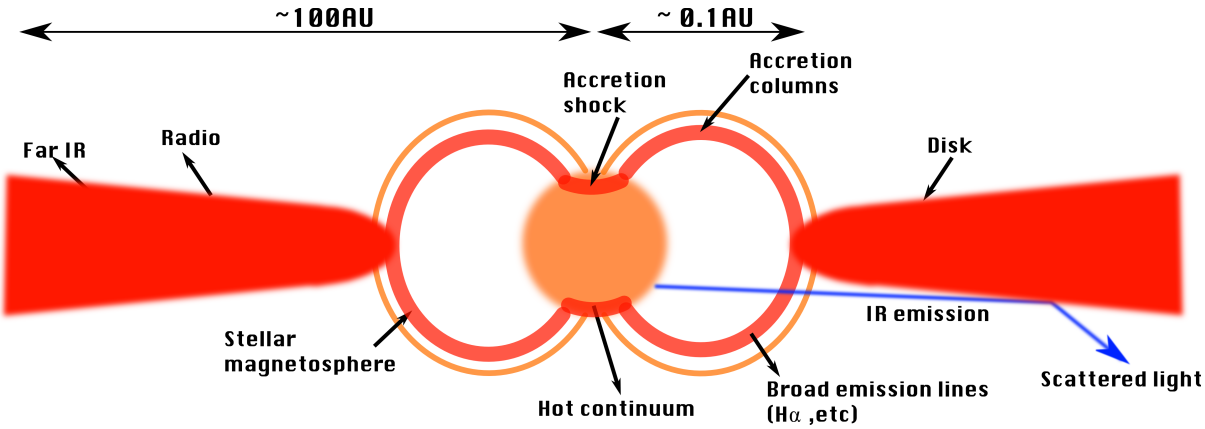

Figure 2.1: Schematic view of the magnetospheric accretion model. Figure adapted from Hartmann (2000)

star through magnetic channels (or also called accretion columns). The gas travels along the accretion columns at approximately free-fall velocities, which is approximately 200-300 km s^{-1} for typical parameters of class II YSOs (Muzerolle et al. 2001), and terminates at the stellar surface, producing an accretion shock that is able to explain the UV/blue continuum excess observed in CTTS (see e.g. Hartmann et al. 1994). Before and after reaching the stellar surface, the gas is heated and ionized, and the H I emission lines result from recombining and accreting hydrogen gas in these magnetic channels (see Beck et al. 2010, and references therein). Figure 2.1, shows a schematic view of the magnetospheric accretion model.

The most prominent feature from H I in CTTS corresponds to emission from the Hα($n = 3-2$) transition of the Balmer series. This emission feature has been used to divide between weak-lined T Tauri stars (WTTS), which shows equivalent widths (EW) of this line of EW$<$ 10Å and CTTS (EW$>$ 10Å). WTTS are considered to be more evolved counterparts of CTTS, with little or no circumstellar emission, but not yet in the main sequence, thus can be considered as class III objects. Hα has also been found to be strongly correlated with the mass accretion rate (Muzerolle et al. 1998a).

The Hα emission in these YSOs is characterized by displaying a mixture of profiles, with 25% of objects having single-peaked symmetric profiles, 54% with blueshifted absorption features (P Cygni profiles) and 21% had redshfited absorption or inverse P Cygni profiles in the work of Reipurth et al. (1996). P Cygni and Inverse P Cygni profiles are signposts of outflow and infall of material respectively. In the former, the cool outflowing gas absorbs emission from the system. In the case of redshifted absorption, the gas falling through accretion columns absorbs emission arising from the hot accretion shock (Davis et al. 2001; Beck et al. 2010).

In the near-infrared, the $n = 7 - 4$ transition of the Brackett series of hydrogen (Brγ) has been found to be strongly correlated to the mass accretion rate (see Muzerolle et al. 1998b)[1] and it serves as a surrogate for Hα as signpost of circumstellar accretion (Najita et al. 1996b). This emission line can be used to study reddened class II objects or class I stars that are usually

[1]Although these authors note that such tight correlation is not expected from their models as other parameters such as the size of the magnetospehre or temperature have a stronger effect on the line flux.

too deeply embedded to be observed at optical wavelengths.

The majority of YSOs usually show a Brγ line with a broad (FHWM $\sim$ 200 km s^{-1}) single-peaked symmetric profile (see e.g. Davis et al. 2001), with 20% of YSOs in Folha & Emerson (2001) displaying redshifted absorption as expected from infall from accretion. Davis et al. (2001) determined that the observed Brγ profiles in their sample are in agreement with the expected profile from the magnestospheric accretion scenario. Beck et al. (2010) shows that for young protostars a non-negligible component arising from outflows can contribute to the line emission ($\sim$ 10% of the flux).

One of the main characteristics of FU Orionis stars during high accretion states is the strong CO absorption in excess of photospheric values and lack of any other features in the K band. From the tight correlation found by Muzerolle et al. (1998b), it would be expected that FUors would show strong emission from Brγ. The lack of this feature in the spectra of FUors has been explained as a break of magnetospheric accretion (or "crushing of the magnetosphere"). The radius at which the disc is truncated by magnetic field lines depends on the accretion rate as $R_T \approx \dot{M}^{-2/7}$ for a constant mass, radius and stellar magnetic field (see Fischer et al. 2012). Thus for sufficiently large accretion rates, as expected for FUors, the truncation radius can become the stellar radius, thus suppressing the accretion flows and the mechanism from which H I lines are expected to arise.

2.1.2 Carbon Monoxide.

The ^{12}CO first-overtone ro-vibrational $\nu = 2-0$, $3-1$, $4-2$, $5-3$, $6-4$ bandhead absorption, spanning the wavelength range $2.293-2.415\mu m$ is a common signature of the cool atmospheres of stars with spectral type later than G0 (see e.g Wallace & Hinkle 1997). The strength of the CO absorption at these wavelengths is greater in giant and supergiant stars, and the presence of this signature was considered to be associated with field stars rather that YSOs in the study of molecular clouds (Elias 1978). However, YSOs were later discovered to have such absorption features, and were recognized to arise from the stellar photosphere of CTTS (see e.g. Casali & Matthews 1992). The lack of such features in the K-band spectra of Class I YSOs can be explained by the features being heavily veiled by a emission from the hot circumstellar dust (see e.g Connelley & Greene 2010).

CO first-overtone emission in YSOs was first detected by (Scoville et al. 1979) in their study of the Becklin-Neugaber object. Further studies by Scoville et al. (1983) showed that the required vibrational temperatures to produce the observed intensities, were in the order of $T \sim 3500$ K. In addition the size of the emitting region had to be confined to within 1 AU of the central star. Calvet et al. (1991) and Najita et al. (1996a) model this emission as arising from the inner parts of a Keplerian disc, where a temperature inversion in the the disc gives rise to the emission. Carr (1989) shows that CO emission can be explained as arising from a neutral stellar wind ($v \sim$ 100-300 km s^{-1}, T$\sim$ 3000 K). However, this wind model requires high mass-loss rates in order to maintain the required densities for overtone emission (Najita et al. 1996a). Martin (1997) proposed that CO emission arises from the accretion flows, similar

to the mechanism that gives rise to Brγ emission. However, Connelley & Greene (2014) find no correlation between the variability of Brγ and CO in a sample of class I objects, as would be expected if both lines have similar origin. Their observations are found to be in agreement with CO arising from a hot inner disc. Rovibrational bandhead emission has been observed in a considerable fraction of YSOs of different masses, with 20%, 22% and 17% of low-mass, intermediate-mass and massive YSOs, respectively, showing this feature (see Cooper et al. 2013, and references therein).

Calvet et al. (1991) studies the effect of stellar irradiation on the atmosphere of optically thick accretion discs of YSOs. The effect of stellar irradiation is to increase the temperature of the disc's upper layers, above what would be expected from viscous heating alone. For a given stellar temperature (that of T Tauri stars, T$\sim$4000 K) and low mass accretion rates, the disc's upper layers will have a higher temperature than the mid-plane, which gives rise to CO emission. However, for the case of low accretion rates, the flux from the system is dominated by the stellar flux, thus the spectrum will show CO absorption, but weaker than photospheric values due to veiling from the hot inner disc. As the mass accretion rate increases (for the same stellar temperature), the mid-plane of the disc will become hotter than the upper layers due to viscous heating. In this case the flux is dominated by the disc, which is much cooler than the stellar photosphere so strong CO absorption will be observed in the spectrum of the system. This would explain the near-infrared spectrum of FU Orionis stars.

In the case of EXors, during outbursts the accretion rates are higher, given this UV radiation from the accretion shocks will increase. The latter increase will raise the temperature of the inner disk, leading to the observed CO emission (see e.g. Kóspál et al. 2011a).

The models of Calvet et al. (1991) also show that for higher stellar temperatures, CO will be observed in emission even for high mass accretion rates of 10^{-5} $M_\odot$ yr^{-1} (see figure 2.2).

2.1.3 Molecular Hydrogen.

Protostellar jets and outflows are a common signature of the early stages of star formation and they appear to be closely related to accretion processes, although the mechanisms that connect accretion with jets is not completely understood (see e.g. Ferreira et al. 2006). The interaction of the outflow with the circumstellar medium gives rise to shock-excited emission from transitions across a wide range in wavelength (like [SII], Hα, [FeII] and H_2.) These shock-excited nebulae were first discovered near T Tauri stars and more evolved class I objects at optical wavelengths as traced by their [SII] and Hα emission. These emission knots are known as Herbig-Haro objects (see Bally et al. 1996; Reipurth & Bally 2001). Evidence of shock-excited emission has been discovered in younger, optically invisible protostars, by detection of emission from [Fe II] (1.64 μm) and H_2 (Davis et al. 2006; Antoniucci et al. 2008; Caratti o Garatti et al. 2009).

Molecular hydrogen emission in YSOs is usually explained as arising from collisional excitation in the warm postshock gas with T$\sim 2000 - 3000K$ and $n \sim 10^4 cm^{-3}$ (Wolfire & Konigl 1991; Smith 1995). In this scenario only the lower vibrational states of the ground electronic

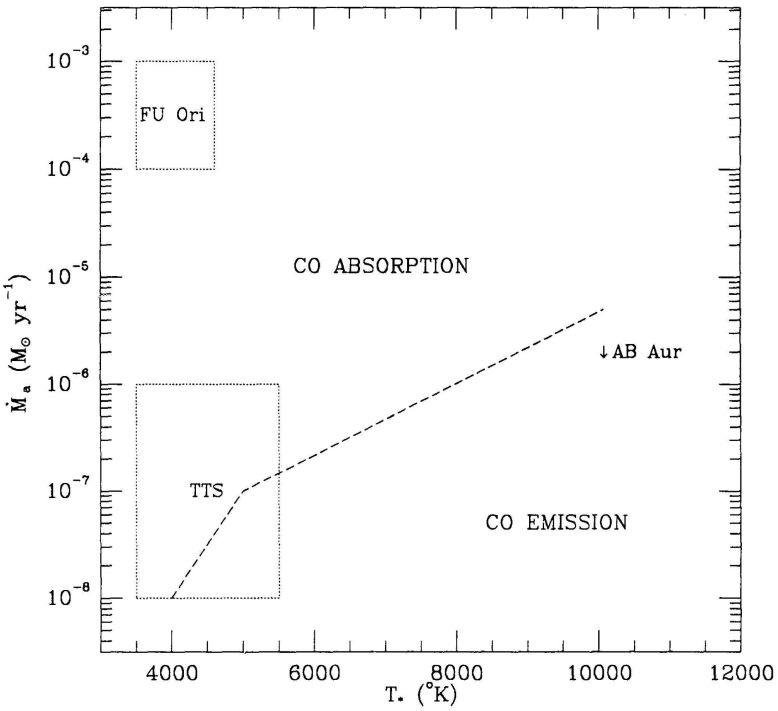

Figure 2.2: Stellar effective temperature vs Mass accretion rate diagram from Calvet et al. (1991). The diagram is used to illustrate the expected behaviour of CO according to the stellar effective temperature and mass accretion rate used in their models. In the figure Calvet et al. (1991) mark the expected location for T Tauri stars and FU Orionis objects. In addition, the Herbig Ae star AB Aur is also marked in the diagram.

state are excited in a non-dissociative shock. The molecule then decays to lower vibrational transitions through permitted rotational transitions of $\Delta J = 0, 2, -2$, with the most common transition corresponding to $\nu = 1, J = 3 \rightarrow \nu = 0, J = 1$ or the 1-0 S(1), which occurs at 2.1218 μm. Shock-excited emission models are characterized by the high 1-0 S(1)/2-1 S(1) ratios (4-5 see e.g Wolfire & Konigl 1991; Smith 1995).

Molecular hydrogen can also result by the excitation from UV photons. In this scenario an UV photon can excite the molecule into a higher electronic state. In about 10% of the cases this will result in the dissociation of the H_2 molecule, whilst in the remaining cases the molecule will decay in a cascade populating higher rovibrational levels, which will give rise to a rich emission spectrum from these higher transitions. In this model the 1-0 S(1)/2-1 S(1) ratio is expected to be equal to 1-2 (Wolfire & Konigl 1991; Beck et al. 2008). Beck et al. (2008) shows that from a sample of T Tauri stars driving HH jets, the H_2 emission is explained as arising from shocks from molecular outflows, but could also have a contribution from emission from quiescent molecular gas in the circumstellar disc being stimulated by UV radiation.

One of the main characteristics of jets from YSOs is the appearance of knots along the jet which have large proper motions (Reipurth & Bally 2001). These knots are separated by large distances and could be related to episodes of enhanced accretion onto the star (see e.g., Ioannidis & Froebrich 2012). Reipurth & Aspin (1997) studied a sample of Herbig-Haro energy sources, finding that at least 50% presented near-infrared spectra similar to FU Orionis objects, leading to the idea that HH objects are related to outburst events. A direct connection between outburst and molecular outflow has not been established properly. However, Magakian et al. (2013) find such a connection in the FUor object V2494 Cyg.

2.2 Photometric Variability

One of the main characteristics of YSOs is their photometric variability, with classical T Tauri stars first being identified as variable stars (Joy 1945). This variability occurs over a wide range in wavelength and with a variety of timescales. The flux variations are thought to arise from several physical processes. Herbst et al. (1994) studies the photometric variability of these objects and classifies it according to the physical processes involved. Type I variability is defined as periodic variations occurring due to the presence of cold spots in the photospheres of weak-lined T Tauri stars, with irregular and periodic variation in CTTs associated with the presence of hot spots due to accretion (type II). A final class are early type T Tauri stars, or ETTS, which corresponds to T Tauri stars with spectral types K0 and earlier (this class includes Herbig Ae/Be stars) and are classified with type III variability. Type III objects, also known as UX Ori stars, show variations of 0.8-3 magnitudes in V which are usually explained by obscuration events from circumstellar material, given that when becoming fainter, these objects become redder and the degree of linear polarisation rises. Herbst & Shevchenko (1999) invoke an alternative scenario, where unsteady accretion is the process that drives the photometric variability in UX Ori objects. Herbst & Shevchenko (1999) explain the rise in linear polarisation in this scenario as possibly arising from electron scattering from an optically thin, geometrically flattened shell,

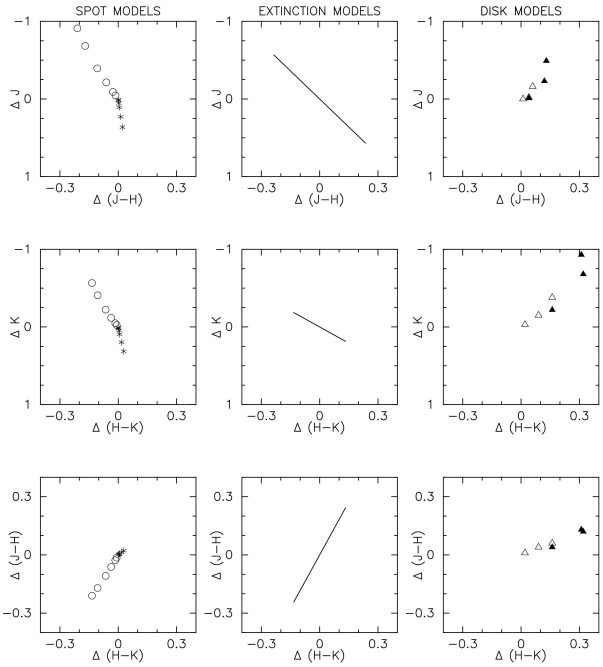

Figure 2.3: ΔJ vs $J-H$, ΔK_s vs $H-K_s$ and $J-H$ vs $H-K$ diagrams showing the expected variability arising from spot, extinction and disc models from Carpenter et al. (2001). The *left* diagrams show spot modelss calculated for a stellar temperature of 4000 K, spot temperatures T_{cool} of 2000 K (*asterisks*) and T_{hot} of 8000 K (*circles*) and for spot coverages of 1%, 2%, 5%, 10%, 20%, 30%. The *centre* diagrams show extinction models for $\Delta A_V = \pm 2$ magnitudes. Finally, the *right* plots show the expected variability from changes in disc properties, for mass accretion rates of $10^{-8.5}$ $M_\odot yr^{-1}$ (*open triangles*) and $10^{-7.0}$ $M_\odot yr^{-1}$ (*filled triangles*), with varying inner holes sizes of 1, 2 and 4 $R_\odot$.

similar to what is observed in classical Be stars. However, the degree of linear polarisation from this mechanism would not agree with that observed in Herbig Ae/Be stars.

Most PMS stars have been observed to show a low level near-infrared variability due to the various physical processes presented above (see e.g. Lamm et al. 2004; Parihar et al. 2009), but with a mean peak-to-trough variability of 0.15-0.17 mag in the K band (see e.g. Carpenter et al. 2001; Alves de Oliveira & Casali 2008; Scholz 2012; Dörr et al. 2013), with variations only very rarely exceeding 1 mag in K. YSOs are also known to vary at mid-infrared wavelengths (see e.g Vijh et al. 2009) and the same physical processes are not expected to produce variability larger than 0.6 mag, whereas variations larger than 1 mag are usually associated with eruptive variability (see Scholz et al. 2013, and references therein)

In the following I briefly explain some of the physical processes that drive common photometric variability in YSOs.

2.2.1 Hot and Cool Spots

.

The interaction of stellar magnetic fields with the gas in the photosphere leads to the presence

of spots, similar to what is observed in the Sun. If the spots are asymmetrically distributed, flux variations modulated by the rotation period of the star will be observed (see e.g. Carpenter et al. 2001; Scholz et al. 2009). The surface covered by these spots is in the range of 0-40% of the surface of the star (Herbst et al. 1994), whilst the temperature difference between the spots and the stellar photosphere is of 10-30% (Bouvier et al. 1995; Scholz et al. 2009).

The presence of hot spots is a consequence of magnetospheric accretion onto the star. These will be produced in regions where the material that is being accreted along magnetic field lines impacts the star. The fraction of the stellar surface that is being covered by these kind of spots can vary between 2-40%. Temperatures in these regions cover the range 5000-12000 K (Scholz et al. 2009).

The timescales of the variability caused by either of these mechanisms is similar to the stellar rotation period and is in the order of $\sim$10 days (Herbst et al. 1994; Carpenter et al. 2001; Scholz et al. 2009). Cool spots can be persistent and stable features that can last over time-scales of years, whilst hot spots only last over a period of days or weeks, and can disappear and reappear, thus making the observed variability due to this process highly irregular.

The amplitude of the variability due to both processes is expected to be larger at optical wavelengths. In order to estimate the amplitude due to spot coverage in the near-infrared Carpenter et al. (2001) presents a simplified model, where it is assumed that both hot and cool spots covering a fraction f of a star with effective temperature T_*, can be characterized by a single-temperature blackbody, T_{spot}. Carpenter, Hillenbrand, & Skrutskie (2001) notes that this simplified model ignores effects such as limb darkening or inclination effects, the model also assumes that all of the spots covering the stellar surface have the same temperature. The model can be expressed as

$$\Delta m(\lambda) = -2.5 \log\{1 - f[1 - B_\lambda(T_{spot})/B_\lambda(T_*)]\} \tag{2.1}$$

Figure 2.3 shows the expected change in J, H and K_s as well as changes in J$-$H and H-K_s colours estimated by Carpenter et al. (2001), for a star with T_{eff} = 4000 K, and for $T_{spot,cool}$ = 2000 K, $T_{spot,hot}$ = 8000 K and covering factors $f = 1 - 30\%$. For low covering fractions, both hot and cool spots produce small changes in near-infrared amplitudes. However, a combination of increasing values of f and larger $T_{spot,hot}$ could produce changes larger than 1 magnitude in K_s (although such large changes are not observed in Scholz et al. 2009), whilst variations due to cools spots do not exceed 0.4 mag at this wavelength. We note that hotspots do not seem to cover large areas of the stellar surfaces ($f < 10\%$ according to Herbst et al. 1994), compared to the large fractions covered by cool spots ($f \sim 40\%$ Bouvier et al. 1993; Carpenter et al. 2001). Both processes can also be distinguished by the observed changes in colours, where variation due to cool spots are nearly constant, compared to changes of 0.1-0.4 mag due to hot spots.

2.2.2 Variable Extinction

Temporal changes in the absorbing material along the line of sight can lead to variability in young stars. These are produced by inhomogeneities in the circumstellar environment or in the surrounding molecular cloud that moves across the line of sight. The timescale for this type of variability ranges from days to years.

In the case that the inhomogeneity is located in the ambient cloud, the timescale will depend on the size of this structure and on the velocity field of the cloud. Carpenter et al. (2001) establishes that a point in the Orion molecular cloud would take approximately $\sim$ 12 days to transit a stellar diameter of $3R_{\odot}$, or the typical diameter for a 0.5 $M_{\odot}$, 1 Myr old star.

If these inhomogeneities are located within the inner circumstellar material, the timescale of the variability can range from days to years, depending on the location and the extension of the instability within the disc. Inhomogeneities can be produced by several mechanisms, among these are:

- Interaction of the stellar magnetic field with the inner disc. An inclined magnetic dipole can produce a warped inner disc with a scale heights of up to $h = 0.3r$, with r the distance from the star to the inner disc edge (see e.g Romanova et al. 2013).
- Accretion driven wind and outflow. In this scenario, dust at larger radii can be uplifted from the disc by a centrifugally driven wind, thus enhancing the extinction along the line of sight (see e.g Bans & Königl 2012; Bouvier et al. 2013).
- Azimuthal disc asymmetry. These can be produced by the interaction of a planetary mass companion embedded within the disc (Bouvier et al. 2013, and references therein)

It is noted that edge-on geometries of the disc are required in order to observe flux variability, if the scaleheights associated with these inhomogeneities are small. Variability in these cases should then not be observed for face-on geometries (Scholz 2012). However, Natta & Whitney (2000) explain the variability of UX Ori objects as arising from obscuration from dust clouds floating above the disk. In this case, the variability is observed for a wide range of disc inclinations.

A good example of variable extinction is given by the YSO, AA Tau. The object presents periodic variability ($\Delta V = 1.5$ mag, $P \sim 8.2d$) that has been explained by the presence of a warped inner disc (Bouvier et al. 1999). The light curve of this object has remained stable over a monitoring period of $\sim$24 years. However, the object suffered a sudden fading of $\sim$ 2 mag. in 2011 and has remained at a faint state ever since (Bouvier et al. 2013). The extra 3-4 mags of extinction along the line of sight have been proposed to arise at distances of $r > 7.7$ AU by Bouvier et al. (2013), possible by asymmetries due to the interaction of a planetary companion with the accretion disc. The duration of the minima implies that the inhomogeneity covers at least 30° of the disc at these large distances. Figure 2.4 shows the historical light curve for this object.

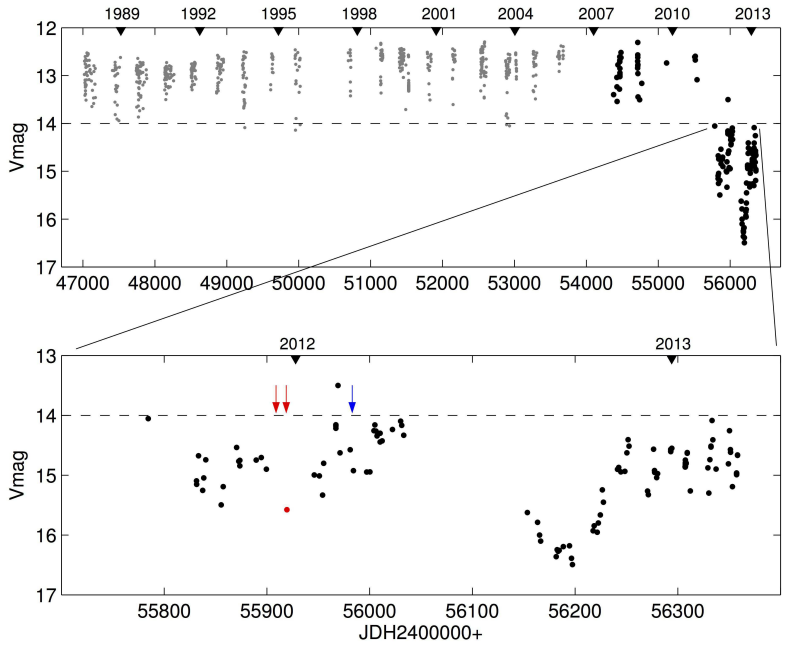

Figure 2.4: Historic light curve of YSO AA Tau from Bouvier et al. (2013). The light curve shows the periodic fading due to the warped disc and the additional fading of ~ 2 magnitudes from 2011.

2.2.3 Variable Disc emission

The near-infrared excess emission that is observed in young stars is explained by the presence of a circumstellar accretion disc. The latter contributes to the emission at these wavelengths via a) reprocessed radiation from the inner disc and b) the release of energy when material is transported through a viscous, optically thick accretion disc. In the first case the amount of excess emission depends on the distance of the inner disc to the star and how hot it becomes. In the latter case the amount of energy release depends on the rate at which material is being accreted onto the star (see e.g. Meyer et al. 1997; Carpenter et al. 2001, and references therein)
.

Meyer et al. (1997) concludes that the observed near-infrared colour distribution of CTTS can be explained by circumstellar discs with a range of accretions rates ($10^{-8} < \dot{M} < 10^{-6}$ $M_{\odot}yr^{-1}$), inner disc holes ($1-6R_{*}$), and a random distribution of inclination angles (the so-called T Tauri locus, see figure 2.5). Thus any changes in these parameters are expected to produce photometric variability (see figure 2.3). Carpenter et al. (2001) argues that the amplitude due this type of variability can reach up to $\Delta K = 1$ mag or higher. However, the authors claim that changes in these parameters are speculative and it is unlikely to expect for such changes to occur in periods of days.

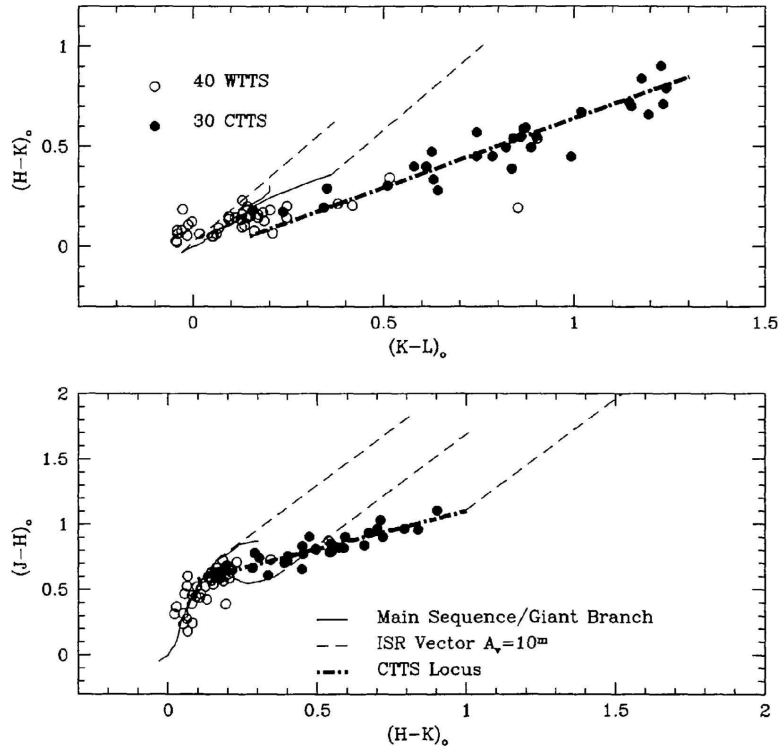

Figure 2.5: Dereddened $H-K$, $K-L$ and $J-H$,$H-K$ colour-colour diagrams showing the T Tauri locus from Meyer et al. (1997).

Chapter 3

Surveys and follow-up

Some sections in this chapter are based on the publication "Extreme infrared variables from UKIDSS - I. A concentration in star-forming regions"

Contreras Peña et al. 2014, 2014MNRAS.439.1829C

Synoptic optical surveys such as OGLE (Udalski et al. 1992) and the 2 epochs of the photographical digital sky survey (DSS) have been successful in finding a large population of variable stars in the past, such as a large population of RR Lyrae, Mira variables, Type II Cepheids, eclipsing binaries, planetary transits, among others. These surveys have covered a small area with a high cadence. However, given the high interstellar extinction towards the Galactic plane they are unable to detect very red, Population I stars. Therefore a large population of such stars, and of course some other interesting type of very red variable stars are expected to arise from infrared surveys.

During the course of my PhD project I have worked with data arising from two near infrared surveys: 1) the Galactic Plane Survey (GPS) at the UKIRT Infrared Deep Sky Survey (UKIDSS) (Lawrence et al. 2007; Lucas et al. 2008) and 2) the VISTA Variables in the Via Lactea (VVV, Minniti et al. 2010) survey. A brief description of both surveys is presented below

3.1 UKIDSS GPS

UKIDSS is not a single survey but it is in fact composed of five survey components of complementary combinations of depth and area.

The data for the survey is collected by the Wide-Field Camera (WFCAM) on the 3.8m United Kingdom Infra-Red Telescope (UKIRT). The camera has a field of view of 0.21 deg^2 and a 0."4 pixel size. The five surveys employ up to 5 broadband filters, ZYHJK, covering 0.8 $< \lambda <$ 2.37 μm and extended over high and low Galactic latitudes.

The Galactic Plane Survey (Lucas et al. 2008) is part of the UKIRT Infrared Deep Sky

Survey. The GPS has covered the entire northern and equatorial Galactic plane that is accessible to UKIRT, surveying 1868 deg^2 and providing JHK photometry for $\sim$1 billion stars. Single-epoch observations are made in J, H and K with total integration times of 80, 80 and 40 s respectively. The median approximate 5σ depths (from data release DR2, Warren et al. 2007) are of J=19.8, H=19.0, K=18.1. The survey includes an additional epoch of K band photometry, with the aims of (1) finding examples of brief and rarely observed phases of stellar evolution via detection of high amplitude variability and (2) providing a proper motion catalogue.

3.1.1 Selection Method

We searched the GPS for high amplitude infrared variables identified via the two epochs of K band photometry, which provide a minimium time baseline of 2 years. We used SQL queries of the WFCAM Science Archive (WSA, Hambly et al. 2008). The GPS catalogues contain a large number of parameters which provide photometric, astrometric, morphological and quality information of the sources in the catalogue. Among these we are interested in the following

- *mergedClass* indicates the most probable morphological classification for the source. This parameter can have discrete values of -1, +1, 0, -2 and -9 corresponding to stellar, non-stellar, noise, borderline stellar and saturated sources respectively. The data reduction pipeline generates a curve-of-growth from the flux at different aperture sizes and for each object. This is compared to a locus of stellar sources. This information along with the ellipticity of the source is used to generate a morphological classification for the star (see Irwin et al. 2004, for more details on the WFCAM catalogue generation).

- $K_{1,2}ppErrBits$ contain the quality error information for each source. Objects with values below a threshold of 256 have information that can be considered as harmless, such as a deblended source or known bad pixel being located within the aperture diameter. Higher values contain more severe warnings, such as sources close to saturation or with unreliable photometry.

- $K_{1,2}AperMag3$ the default 2" diameter aperture photometry in K for the two epochs.

- $K_{1,2}Ell$ ellipticity of the source

- $K_{1,2}Xi, K_{1,2}Eta$ correspond to the east/west and north/south offset with respect to the master position of the catalogue for each epoch. The master position is obtained at the shortest wavelength at which the object is detected, usually corresponding to J-band for GPS data.

For the purposes of our analysis, we selected stars (objects with image profile classifier *mergedClass=-1*) that varied by $\Delta K \geq 1$ mag, having $K < 16$ mag in at least one epoch and for which no serious post-processing photometric errors are found ($K_{1,2}ppErrBits < 256$). The magnitude cut was designed to reduce the number of false positives, given that the faintest

stars in crowded fields are the most likely to have incorrectly deblended fluxes. The cut used "apermag3", the default 2" diameter aperture.

In order to further decrease the number of contaminant sources we also made additional cuts on the ellipticity of the detections ($K_{1,2}Ell < 0.3$) and in astrometric offsets between the observations (the detection in both epochs were required to be within 0.5" from each other). The queries returned a large number of candidates and in order to remove false positives, images of each candidate were inspected visually (an example is shown in figure 3.1). Most false positives arose from bad pixels, diffraction spikes from bright stars or a small number of fields with bad astrometry. [1]

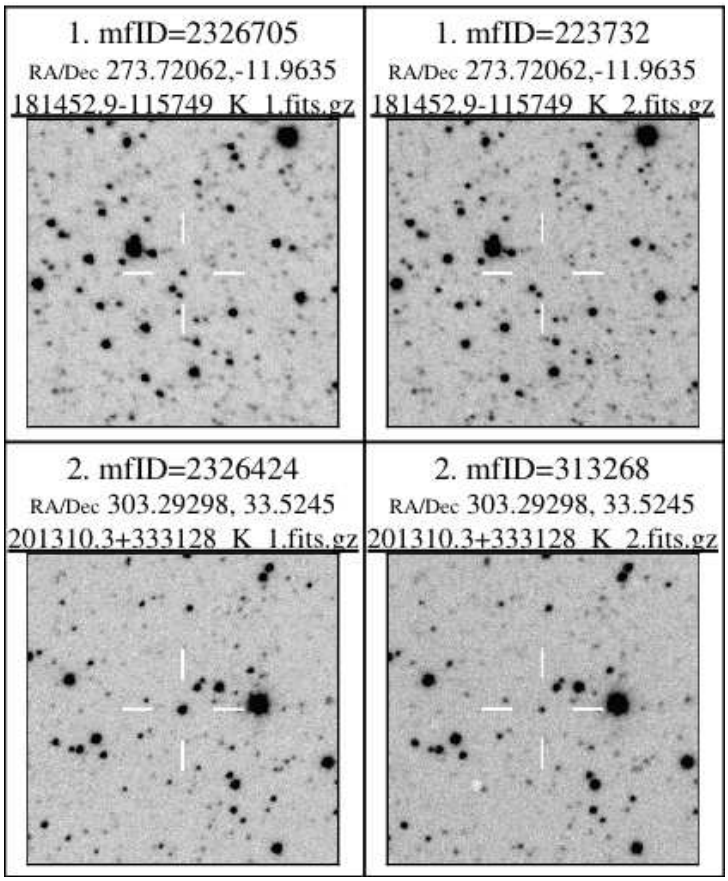

Figure 3.1: Examples of the images used for visual inspection of the variable star candidates. Both images are of real high amplitude variables. In these cases the large change is already apparent from the images.

We note that the amplitude of the variations are always observed to be much larger than individual errors. The amplitudes observed at 2.2 μm are also larger than the expected difference that arises from comparing different photometric passbands, e.g. UKIDSS K vs 2MASS K_s, when ancillary data is available for the stars.

[1] These fields with bad astrometry were corrected for the 8th Data Release and the pipeline has now been made more robust against such errors.

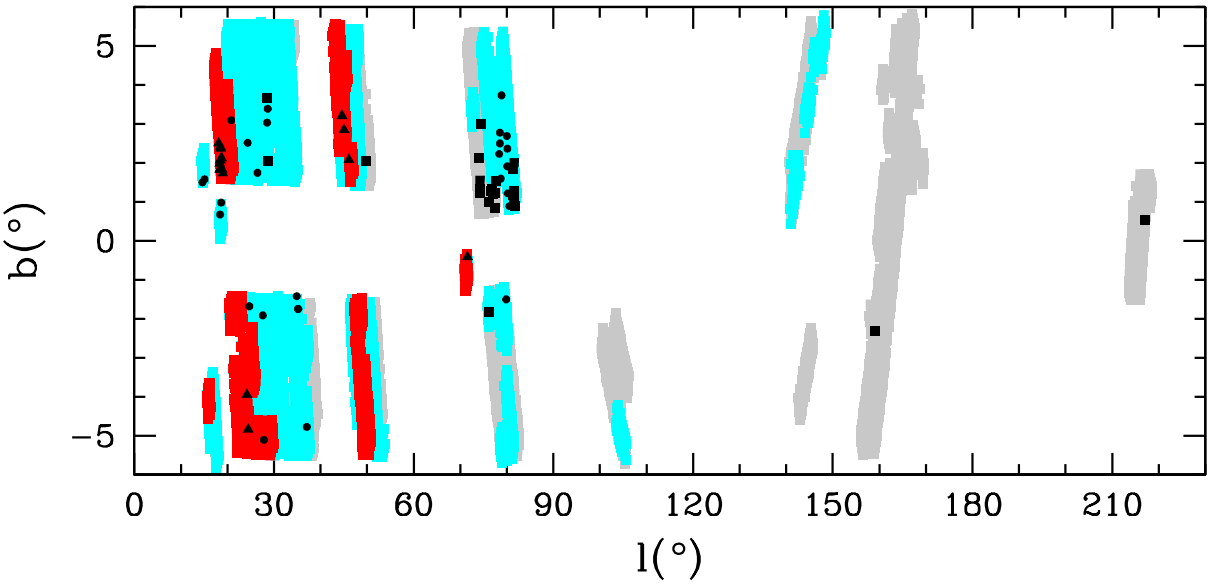

Figure 3.2: UKIDSS GPS two epochs K band photometry coverage up to DR8 (*grey*), with areas covered in DR5 and DR7 shown in red and cyan colours respectively. The locations of the 71 high-amplitude variables found in our searches are marked with black squares (DR8 search), circles (DR7 search) and triangles (DR5 search). The higher concentration towards Serpens OB2 ($l \sim 18°$) and the Cygnus-X complex ($l \sim 78° - 80°$) is already apparent.

Just to emphasize how rare these events are within the surveyed area of the Galactic plane, we consider the number of real variables from our searches compared to the total number of stars, considering data up to DR7. Adding the results from the DR5 and DR7 searches yields a total of 45 high amplitude infrared variables. When excluding the $\Delta K > 1$ mag condition in our searches, $\sim$ 11.8 million stars are selected from the DR7 catalogue (which includes the DR5 release). This implies that high amplitude variability occurs in $\sim$ 1 out of 262000 stars in GPS.

Two epoch data were only available for a small proportion of the Galactic plane at the time of the searches, as indicated in Figure 3.2. The figure shows that the area covered is mostly located at Galactic latitudes $1° < |b| < 6°$. In other words, two epoch data for the mid-plane were largely excluded from the available data releases. This is for historical scheduling reasons. This spatial bias in the initial results reported here will be eliminated in future searches as the dataset becomes more complete. The fact that the mid-plane is not covered, implies that relatively few star formation regions or young stellar populations with similarly small scale heights will be included in our search. To be more specific, most star formation regions at heliocentric distances, d>3 kpc will be excluded, assuming a scale height of $\sim$ 67 pc for molecular clouds located near R=R_0 (e.g. Knapp 1987). In addition, massive OB associations are also excluded (OB stars scale height of $\sim 30 - 50$ pc, e.g. Reed 2000; Elias, Cabrera-Caño, & Alfaro 2006).

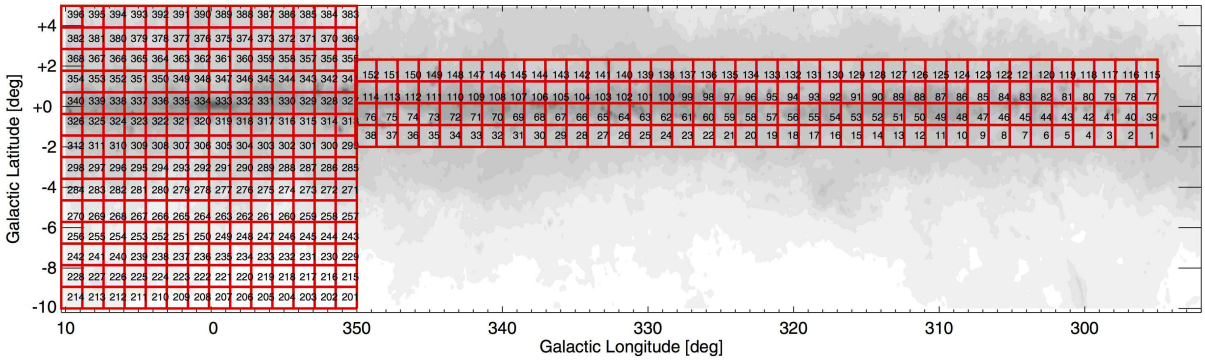

Figure 3.3: Map of the area to be surveyed by VVV. Figure taken from Minniti et al. (2010)

3.2 VVV

The VVV survey plans to map a 520 deg^2 area containing $\sim 10^9$ point sources with multi-epoch near-infrared photometry. The surveyed area includes the Milky Way bulge and an adjacent section of the mid plane. The final product of the survey will consist of a deep near-infrared Atlas in five bandpasses and a catalogue of more than 10^6 variable sources, mainly composed by RR Lyrae stars.

One of the main scientific goals, expected to arise from the final product of VVV is the finding of rare variable sources such as Cataclysmic Variables, RS CVn stars, eclipsing binary RR Lyrae, among others. Most importantly for our project, is the possibility of finding FU Orionis-like protostars undergoing unstable accretion. I note that the higher cadence of observations of VVV will favour the detection of eruptive variables at early stages of outburst episodes.

The regions covered by the survey comprise a Bulge region within $-10° < l < +10°$ and $-10° < b < +5°$ and the plane region in $295° < l < 350°$ and $-2° < b < +2°$. The surveyed area can be seen in Figure 3.3.

The data is collected by the Visible and Infrared Survey Telescope for Astronomy (VISTA). This is a 4m telescope located in Cerro Paranal Observatory in Chile and is designed to conduct large-scale surveys of the southern sky at near-infrared wavelengths, covering $0.9 < \lambda < 2.5$ μm. The telescope is equipped with a near-infrared camera consisting of an array of 16 2048×2048 pix detectors, with a typical pixel scale of 0.”339, with each detector covering 694×694 arcsec^2. The detectors are set in a 4×4 array and have large spacing along the X and Y axis. Therefore a single pointing, called a “pawprint”, covers 0.59° giving partial coverage of a particular field of view. A continuous coverage of a particular field is achieved by combining six single pointing with appropriate offsets. This combined image is called a tile. The instrument has five broad-band filters ZYJHK$_s$ available and two narrow filters at 0.98 and 1.18 μm. VVV uses all 5 broadband filters.

The images are combined and processed at the Cambridge Astronomical Survey Unit (CASU). The tile catalogues are produced from the image resulting from combining six pawprints. The catalogues provide parameters such as positions and fluxes from different aperture sizes. A flag

indicating the most probable morphological classification is also provided, with "-1" indicating stellar sources, "-2" borderline stellar, "1" non-stellar , "0" noise, "-7" indicating sources containing bad pixels and finally class=-9 related to saturation (for more details on all of the above, see Saito et al. 2012).

Quality control (QC) grades are also given by ESO according to requirements provided by the observer. These include constrains on parameters such as airmass, sky transparency, moon distance, seeing and ellipticity of the observations. According to whether observations fulfil the constrains established by the observer, these are classified as fully satisified (QC A), almost satisfied, where for example only 10% of the constrains are violated (QC B) and finally not satisfied (QC C)

3.2.1 Selection Method

In order to search for variable stars we used the multiepoch database of VVV comprising the observations of disc tiles with $|b| \leq 1^{\circ}$ taken between 2010 and 2012. The catalogues were requested and downloaded from the CASU. We used catalogues of observations with QC grades A, B or C. Catalogues with QC grades C are still considered in order to increase the number of epochs. Some of them were still useful for our purposes. However, a small number of catalogues still presented some issues (e.g. zero point errors, bad seeing) making them useless, and as such were eliminated from the analysis. The number of catalogues in each tile varied from 14 to 23 epochs, with a median of 17 epochs per tile.

For each tile, the individual catalogues are merged into a single master catalogue. The first catalogue to be used as a reference was selected as the catalogue with the highest number of sources on it. In every case this turns out to correspond to the catalogue of the deepest K_s observation from VVV ($t_{exp} \sim 80$s). This step was taken to ensure that variability was searched for in the higher number of sources possible.

Variable star candidates are selected from the master catalogue from stars which fulfilled the following criteria

- Classified as a star (class= -1) in every available epoch.
- Ellipticity with ell<0.3 in every epoch.
- The absolute difference (ΔK_s) between the brightest ($K_{s,max}$) and faintest point ($K_{s,min}$) in the light curve of the source to be larger than 1 magnitude.

  This was the original classification scheme. However, we observed that for each tile we were selecting a large number of sources as variable star candidates. Figure 3.4 shows the average K_s magnitude vs ΔK_s for variable stars in one of the VVV tiles. The figure shows that the majority of stars selected in the original classification scheme are located at the bright and faint ends of the distribution. The latter arise due to unreliable photometry at this faintest part. The VISTA detectors become increasingly non-linear when reaching the saturation level. This non-linearity is corrected for in the creation of the catalogues,

but differences between the magnitudes of the same object can still be observed, even for objects classified as stellar sources (Saito et al. 2012). Figure 3.5 shows the comparison of the K_s magnitudes of stellar sources found in overlapping regions of adjacent disc tiles, where stars found at the brighter end show an increasing difference in magnitude (an effect also observed in Cioni et al. 2011; Gonzalez et al. 2011). This effect would explain the large differences observed at the brighter end of figure 3.4. This part of the distribution also shows marked "finger-like" sequences. Each of the sequences can be explained by the fact that the VISTA detectors have different saturation levels. In order to minimize these effects we applied an additional cut

- We separated the average K_s distribution of figure 3.4 into bins of 0.5 magnitudes and derived the mean and standard deviation, σ, on ΔK_s for each bin. In order to select an object as a candidate variable star we required its ΔK_s to be 3σ above the mean ΔK_s at the corresponding magnitude level. This 3σ line is shown in red in figure 3.4 where we can see that it is able to account for the unreliable photometry and non-linearity effects at the faint and bright ends of the distribution respectively.

  This additional constraint reduced the number of variable stars candidates by a large factor. The original requirements yield 158478 stars, the additional cut reduced this to 5085 stars.

The effect of requiring a stellar classification in every epoch is still being studied, as we are bound to lose real variable stars, especially eruptive variables that might not show up in some epochs if they are faint, but appear once they go into outburst.

A case of this selection effect is found in a variable star that showed a large variation ($\Delta \mathrm{K}_s >$ 1 magnitude) in the analysis of an early release of 2010 data. However, the star does not show up as a variable star candidate in the analysis described above. Inspection of the master catalogue for the respective tile shows that the star has a classification different from stellar in 3 out of 18 epochs available for tile d090. This star is included in the final list of VVV high-amplitude variables and is also part of the sample that has follow up spectroscopic observations.

After the initial selection, for each star we constructed images of a size of $1' \times 1'$ around the star, and for every available epoch. Variable stars were confirmed as real through visual inspection of the individual images (an example is shown in figure 3.6). The most common causes for the appearance of false positives were, bad pixels in the images, saturation of bright sources, diffraction spikes and stars that were found on the edge of tiles.

This selection method yields a total of 837 real variable stars. However, 22 of them are found twice as they are covered by adjacent tiles in VVV. The final list of VVV high-amplitude infrared variables consists of 816 stars, which includes the variable star found to show large variability in 2010 (described above). The latter is assigned as VVVv815. In addition, a true variable star in tile d046 was left out of an initial final list. This error was not recognized until recently and we have rectified it adding the star as VVVv816.

We note that photometry from 2013 and 2014 (when available) VVV catalogues has been

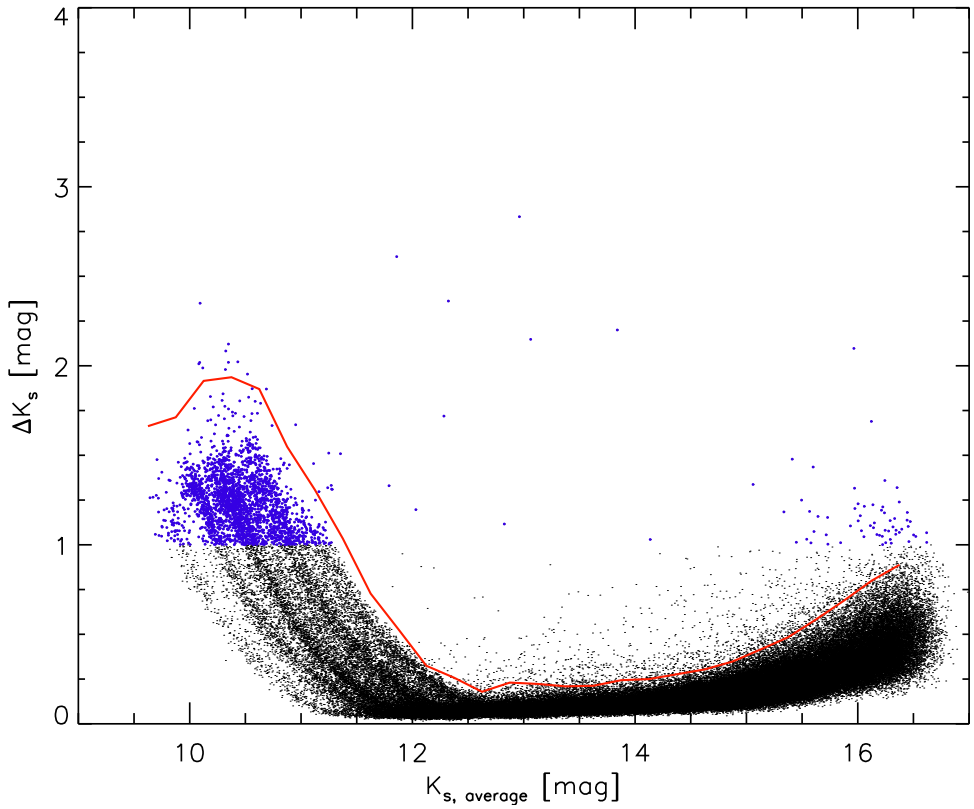

Figure 3.4: K_s vs ΔK_s for one of the VVV tiles studied in this work, showing stars with class= -1 and ellipticity < 0.3 in every epoch (black circles). Variable star candidates which fulfil the condition $\Delta K_s > 1$ magnitude are shown as blue circles. The red solid line marks the additional 3σ cut applied to the objects as explained in the text. Stars above this line are selected for subsequent visual inspection.

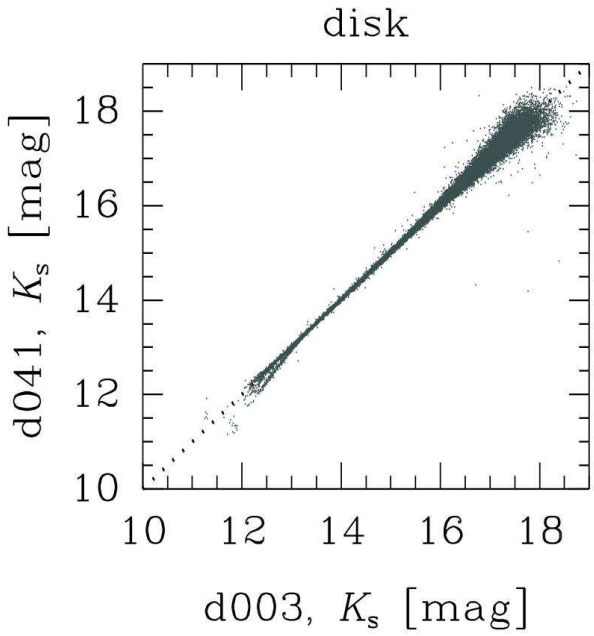

Figure 3.5: K_s photometry of the overlapping region between disc tiles d003 and d041. Figure taken from Saito et al. (2012)

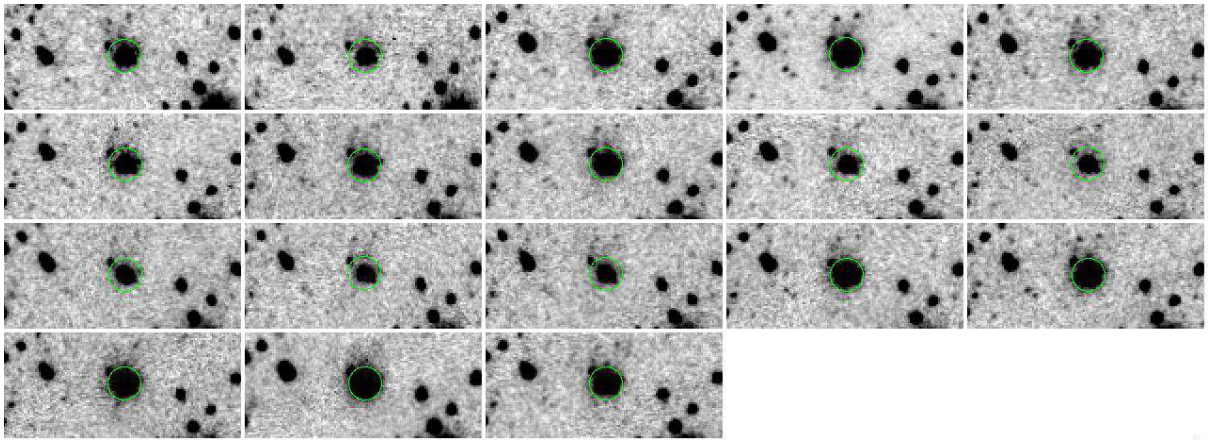

Figure 3.6: Example of the images used to visually inspect variable star candidates.

added to the light curves of every object in the list. In these cases we have added the data points without concern on the morphological classification of the object in individual catalogues.

The number of stars in the analysed VVV area that fulfil items 1 and 2 above is 12 789 000 stars. Considering the number of real variable stars we see that high-amplitude infrared variability occurs in approximately 1 out of 15000 stars in VVV.

3.3 Additional Data sets

Additional data sets arising from public photometric and near-, mid- and far-IR surveys, that overlap with either GPS or VVV or with each other, will be used to i) construct SEDs for our sources to confirm them as YSOs and ii) provide additional epochs in different filters to confirm the variable nature of our candidates. Below I present a brief description of such surveys.

3.3.1 IPHAS, VPHAS+

The Isaac Newton Telescope(INT) Photometric Hα Survey of the Northern Galactic Plane (IPHAS, Drew et al. 2005) searches for emission line objects (Hα) in the northern Galactic plane covering an area of 1800 deg^2 within the region $-5^\circ < b < +5^\circ$, $30^\circ < l < 215^\circ$. The survey uses the WFC imager mounted on the 2.5m INT taking images in the Hα narrow-band and sloan $r^{'}$ and $i^{'}$ broad-band filters, reaching down to point source magnitudes of $r^{'} \sim 20$. It provides an optical counterpart of GPS.

The VLT Survey Telescope Photometric Hα Survey of the Southern Galactic Plane (VPHAS+) will survey the southern Galactic plane within the $-5^\circ < b < +5^\circ$ region. In addition it will survey the Galactic bulge within $-10^\circ < b < +10^\circ$, providing an optical counterpart to VVV, in the Sloan $u^{'}$ and $g^{'}$, $r^{'}$ and $i^{'}$ broad band and Hα narrow-band filters. The survey is expected to reach a 10σ magnitude limit of 21-22 in all of the filters.

3.3.2 2MASS, DENIS

The Two-Micron All Sky Survey (2MASS, Skrutskie et al. 2006) mapped 99% of the sky between 1997 and 2001 using three near-infrared bandpasses, namely J (1.25 μm), H (1.65 μm) and K_s (2.12 μm). The observations were carried with two 1.3m telescopes located in Mount Hopkins, Arizona and Cerro Tololo, Chile. The survey obtained a 5σ detection level of 17, 16.3 and 15.5 magnitudes for J, H and K_s respectively.

The Deep Near Infrared Survey of the Southern Sky survey the whole sky at declinations $-88^\circ < d < -2^\circ$ in the $gunnI$ (0.86 μm), J (1.25 μm) and K_s (2.15 μm) filters, using the ESO 1m telescope at La Silla observatory, with limiting magnitudes of 18.5, 16.5 and 14.5 magnitudes for the respective filters.

3.3.3 All Sky mid- to far- IR Surveys

The Infrared Astronomical Satellite (IRAS, Neugebauer et al. 1984) was the first extensive mid-to far infrared survey of the sky; launched in 1983 it mapped $\sim 87\%$ of the sky in four photometric bands 12,25,60,100 μm, with a low angular resolution of 33". This survey pioneered various new fields of astronomy. A decade later the Midcourse Space Experiment (MSX, Price et al. 2001), a multi-discipline experiment sponsored by the Ballistic Missile Defence Organisation, surveyed the Galactic plane and the regions missed by IRAS or where the sensitivity of IRAS was degraded by confusion noise. MSX surveyed the sky in five mid-IR wavelengths, 4.29, 435, 8.3, 12.13, 14.65 and 21.34 μm, with a spatial resolution of 18" at 8.3 μm.

The AKARI satellite (Murakami et al. 2007) was launched in 2006, and its main purpose is to provide a second generation of infrared catalogues of the entire sky, with a better sensitivity, spatial resolution and wider infrared coverage than IRAS. AKARI is equipped with a cryogenically cooled, 68.5 cm aperture telescope and two scientific instruments, the far-infrared surveyor (FIS) and the infrared camera (IRC). This mission surveyed the entire sky in six infrared wavelengths, 9, 18, 65, 90, 140 and 160 μm, with a spatial resolution of 10" at 9 and 18 μm.

The Wide Infrared Survey Explorer (WISE, Wright et al. 2010) maps the whole sky in four infrared bands, $w1, w2, w3, w4$ centred at 3.4, 4.6, 12 and 22 μm respectively using a 40 cm telescope. WISE is achieving a sensitivity 100 times better than IRAS at 12 μm, and with a spatial resolution of 6".

3.3.4 Mid- to Far-IR Surveys of the Galactic Plane

The Galactic Legacy Infrared Midplane Survey Extraordinaire (GLIMPSE, Benjamin et al. 2003) survey used the Spitzer telescope Infrared Array Camera (IRAC) to map the Galactic plane in four different filters centred at 3.6, 4.5, 5.8, 8.0 μm. The survey is comprised of four different programs, each mapping a different region of the Milky Way, these are

- *GLIMPSE I* Covered the region within $|b| < 1^\circ$, $|l| = 10 - 65^\circ$.

- *GLIMPSE II* The programme mapped longitudes $\pm 10^\circ$ of the central region of the galaxy. The latitude coverage is $\pm 1^\circ$ from $|l| = 10 - 5^\circ$, $\pm 1.5^\circ$ from $|l| = 5 - 2^\circ$ and $\pm 2^\circ$ from $|l| = 2 - 0^\circ$.

- *GLIMPSE 3D* Adds vertical extensions, generally to $|b| < 3^\circ$ but up to $|b| < 4.2^\circ$ in the centre of the galaxy.

- *GLIMPSE 360* Is a warm Spitzer mission, i.e. only uses the 3.6 and 4.5 μm filters of IRAC, that is mapping the remaining 187 degrees of longitude of the Galactic plane that have not been mapped by previous Spitzer Galactic plane surveys (GLIMPSE I, II, 3D, Cygnus-X, SMOG, Vela Carina), thus covering the regions $l = 65 - 76^\circ, 82 - 102^\circ, 109 - 265^\circ$, whilst the latitude range covers about 2.8° with its centre following the Galactic warp.

The Mid Infrared Photometer for Spitzer Galactic Plane Survey (MIPSGAL, Carey et al. 2009) uses the MIPS camera on board of Spitzer to map the regions $|l| = 5 - 63^\circ, |b| < 1^\circ$ and $|l| < 5^\circ, |b| < 3^\circ$ in 24 μm and 70 μm with a resolution of 6" and 18" respectively. The programme overlaps with GLIMPSE I/II/3D.

The CYGNUS-X Programme (Hora et al. 2007) aims to survey the CYGNUS-X complex, home of a rich concentration of massive protostars and large OB associations, with IRAC (3.6,4.5,5.8,8.0 μm) and MIPS (24, 70 μm).

The Herschel Infrared Galactic Plane (Hi-GAL, Molinari et al. 2010) uses the Herschel Space Telescope photometric cameras PACS and SPIRES to deliver maps at five different wavelengths, 70 and 170 μm (PACS) and 250, 350 and 500 μm (SPIRES), covering the region $-60^\circ < l < 60^\circ$, $|b| < 1^\circ$, which contains most of the star formation of the galaxy.

We obtained Hi-Gal information for our VVV selected variable stars using the band-merged catalogue that was kindly provided by Dr. Mark Thompson. The merging process is described in Elia et al. (2010).

3.4 Spectroscopic and Photometric follow-up

In order to identify the nature of the high-amplitude variable stars selected in the aforementioned surveys, we have performed near-infrared spectroscopic and photometric follow up of a large sample of the objects arising from GPS and VVV. The data was obtained prior to and during the duration of this PhD, using several instruments from different telescopes located in Chile and USA.

The time allocated for observations was limited and did not allow us to observe every object in our sample. The selection made for follow-up can be considered arbitrary since we did not have a strict requirement for the objects to be selected for such purposes. Only the 2010 VLT/ISAAC follow up of the DR5 sample included the majority of the objects obtained in the search for high amplitude variables. In general, objects were selected based on their light curves, SEDs and/or their association with SFR, which would make them strong candidates

to be eruptive variables. In addition objects has to be bright enough to obtain a high signal-to-noise ratio in the K band (S/N $\sim$ 30, usually we required $K < 14.5$ magnitudes). A brief explanation of the selections is shown in the following.

- *VLT/ISAAC* The first follow up campaign of this PhD project included 15 out of the 17 objects selected in the analysis of GPS DR5. Follow-up of the whole sample allow us to characterize high amplitude variable stars, regardless of their possible nature as YSOs.

- *Gemini/NIFS* The campaigns of 2012 and 2013 included the 4 DR5 objects that were found likely to be eruptive variables from VLT/ISAAC data. Sixteen more objects from the DR7 and DR8 analysis were also observed with this instrument. Their selection was based on the observed amplitude of variability (preferentially showing $\Delta K > 1.5$ magnitudes) and/or association with a SFR.

- *Magellan/FIRE low resolution* Three objects were observed at low resolution with FIRE at the Magellan Baade Telescope in Chile in 2012. The observing time was kindly provided by Dr Ben Burningham and preference was given to the two DR5 objects that were likely embedded FUors from the DR5 analysis. The third object, VVVv815, was observed as a target of opportunity during a short gap in Dr Burningham's schedule.

- *Magellan/FIRE high resolution* Objects arising from VVV were observed in 2013 and 2014. The 2013 observations included objects that were associated with SFRs but also showed $\Delta K > 2$ magnitudes and the full sample of objects within the SFR G305 that showed $\Delta K > 1.4$ magnitudes. The $\Delta K > 2$ magnitudes constraint was not applied to objects observed in 2014. This sample included two objects observed in 2013 and that had strong characteristics of eruptive variables.

3.4.1 VLT/ISAAC

Spectroscopic and photometric follow-up observations of 15 of the DR5 candidates were obtained in visitor mode during two consecutive nights in June 30th/July 1st 2010. The data were acquired at the Very Large Telescope (VLT) in Cerro Paranal, Chile with the ISAAC imager and spectrograph.

Observations were carried out with the short-wavelength (1-2.5 μm) arm of ISAAC, equipped with a Hawaii Rockwell 1024×1024 array The imaging mode has a scale of 0.147"/px with a field of view of 152"×152".

Low-resolution (0.8" slit, R=$\lambda/\Delta\lambda \sim 700$) K_s spectra were obtained in two different positions along the direction of the slit (positions A and B), in an ABBA sequence with individual integration times of 120 s.

In order to remove telluric lines, main sequence F-type stars were observed consecutively at similar airmass with the same instrumental setup. Filament lamp images were taken for purposes of flat-fielding of the data, while Xenon-Argon lamp images were acquired for wavelength

Object	Instrument	R	T_{exp} (s)	Airmass	N_{exp}	Date
GPSV1	ISAAC	700	120	1.1	10	30 June 2010
GPSV2	ISAAC	700	120	1.2	10	30 June 2010
GPSV3	ISAAC	700	120	1.1	4	30 June 2010
GPSV3	FIRE	300	148	1.1	4	8 May 2012
GPSV3	NIFS	5000	480	1.2	2	13 September 2012
GPSV4	ISAAC	700	120	1.3	20	30 June 2010
GPSV5	ISAAC	700	120	1.2	20	1 July 2010
GPSV6	ISAAC	700	120	1.1	20	1 July 2010
GPSV7	ISAAC	700	120	1.2	10	30 June 2010
GPSV8	ISAAC	700	120	1.1	4	30 June 2010
GPSV8	NIFS	5000	480	1.2	2	4 September 2012
GPSV9	ISAAC	700	120	1.2	20	1 July 2010
GPSV10	ISAAC	700	120	1.2	10	1 July 2010
GPSV11	ISAAC	700	120	1.1	20	30 June 2010
GPSV12	ISAAC	700	120	1.2	14	30 June 2010
GPSV13	ISAAC	700	120	1.1	4	30 June 2010
GPSV15	ISAAC	700	120	1.1	4	30 June 2010
GPSV15	FIRE	300	148	1.4	4	8 May 2012
GPSV15	NIFS	5000	480	1.2	2	4 September 2012
GPSV16	ISAAC	700	120	1.2	10	1 July 2010
GPSV16	NIFS	5000	480	1.2	4	3 August 2012
GPSV19	NIFS	5000	480	1.1	4	26 August 2012
GPSV22	NIFS	5000	480	1.1	4	26 August 2012
GPSV24	NIFS	5000	480	1.1	4	21 September 2012
GPSV25	NIFS	5000	480	1.1	4	3 September 2012
GPSV26	NIFS	5000	480	1.1	4	27 August 2012
GPSV28	NIFS	5000	480	1.2	2	27 August 2012
GPSV30	NIFS	5000	480	1.1	4	10 August 2012
GPSV34	NIFS	5000	480	1.1	2	26 August 2012
GPSV46	NIFS	5000	480	1.4	2	2 August 2013
GPSV47	NIFS	5000	480	1.3	4	29 September 2013
GPSV49	NIFS	5000	480	1.2	2	6 October 2013
GPSV53	NIFS	5000	480	1.2	2	11 October 2013
GPSV62	NIFS	5000	480	1.1	2	9 October 2013
GPSV63	NIFS	5000	480	1.3	2	11 October 2013
GPSV64	NIFS	5000	480	1.1	2	22 October 2013
GPSV65	NIFS	5000	480	1.1	4	22 October 2013

Table 3.1: Spectroscopic observations of GPS objects.

calibration and to model the slit curvature. In addition a set of 12 STARTRACE images were downloaded from the ESO archive to correct for the tilt of ISAAC spectra.

Flat-fielding, wavelength calibration, tilt correction and extraction of the spectrum for each object and the corresponding F-type calibrator were performed with the usual tasks in the NOAO/TWODSPEC package in IRAF. The intrinsic H I Brγ absorption of the telluric star was removed using SPLOT in IRAF. Finally, the calibrator spectrum was divided by a blackbody curve of similar temperature to that of the star and used to correct the target spectrum.

Photometric observations for each target consisted of 12 images in J_s, H and K_s with typical exposure times of 5 s. Each image was observed in a different position within a 15" wide jitter box. The seeing at K_s varied between 0.65-1.1" for the first night and 1.0-2.04" for the second night of observations.

Dark images and sky-flats were obtained for bias subtraction and to correct for pixel-to-pixel variations in the detector response. The latter consisted of $\sim$ 10-15 images in filters J_s and H with exposure times of 5 s. K_s images were not taken for this project so suitable images were acquired from the ESO archive, taking care to select images that were observed with the same instrumental setup, exposure times and a similar observing date. Source magnitudes were obtained through aperture photometry, performed on final sky-subtracted images, using APPHOT in IRAF. The calibration of the final magnitudes was obtained with the process described below.

Photometric Calibration

Firstly, a set of 180 local standards from the IRAF aperture photometry results were selected, corresponding to bright stars, with low photometric errors, no processing errors and with no close companions. Cross-match with the UKIDSS GPS catalog of the same area covered by ISAAC, yielded typically $\sim$ 60-100 matches.

By taking the average (after removal of outlying sources) of $\Delta m = M_{UKIDSS} - m_{ISAAC}$, we obtain the offset that will be applied to the ISAAC instrumental magnitudes. This process is sufficiently accurate for both J_s and H, given the similar $\Delta\lambda$ and λ_c for the UKIDSS and ISAAC filters, however, $K_{s,ISAAC}$ differs from K_{UKIDSS}, being similar to 2MASS K_s filter profile.

To study the differences between UKIDSS and 2MASS K, we cross-matched our local standards with the 2MASS catalog for the same area, finding around 20-40 stars. The differences between UKIDSS and 2MASS are plotted in Fig. 3.7, here it can be seen that magnitudes are similar in both systems, especially for brighter sources. Thus the selection of either system for the calibration would not have a severe effect on the calibrated magnitudes. This was found to be true for each of our objects. Given the greater number of UKIDSS stars found, and the greater precision of UKIDSS magnitudes for the fainter stars, we decide to use UKIDSS photometry for the K_s calibration. A magnitude correction, however, needs to be applied for our sample, especially the case of the reddest stars where most of its flux falls in the K-band. Using the reduced spectrum of the object, a correction factor was derived by comparing the ratio of the total flux of the star in UKIDSS and ISAAC K filters, to the same ratio for a

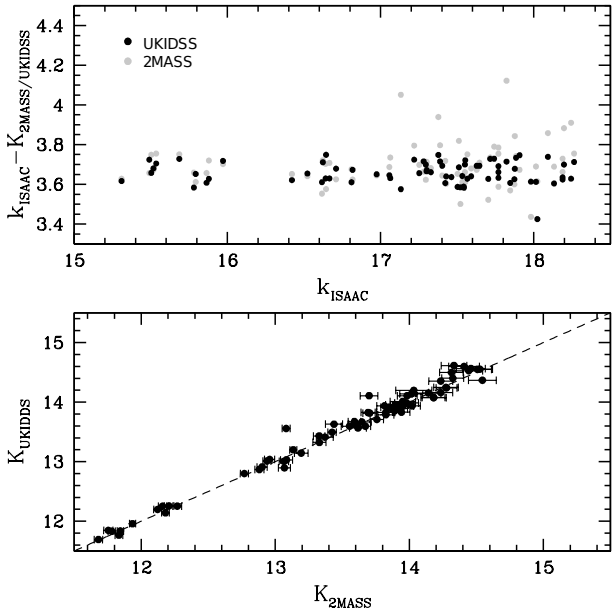

Figure 3.7: Comparison of 2MASS and UKIDSS K for a set of local standards in the field of view centered on GPSV3, as explained in the text (*bottom*), the dashed line represents the identity line. The *top* graph shows the offset between ISAAC instrumental magnitudes and UKIDSS (*black filled circles*) and 2MASS (*grey filled circles*) photometry.

blackbody spectrum at T = 9700 K (which is appropriate for these Vega-based magnitudes). The correction factor is then given by

$$\Delta K = -2.5 \times \log \frac{F_{\star,UKIDSS}/F_{\star,ISAAC}}{F_{bb,UKIDSS}/F_{bb,ISAAC}} \tag{3.1}$$

This correction was largest for the reddest stars in our sample but never exceeded 0.05 mag.

3.4.2 Gemini North/NIFS

K-band spectroscopic data of twenty GPS variables, were acquired in 2012 and 2013 using the Near-infrared Integral Field Spectrometer (NIFS) of Gemini North telescope, Mauna Kea, Hawaii. The instrument has a field of view of 3"×3" with a pixel scale of 0.1" across image slices and 0.04" within image slices and a resolving power $R \sim 5300$ at 2.2 μm.

The observations are part of the queue mode programmes GN-2012B-Q-102 and GN-2013B-Q-47. The date of the observations, integration times and observing sequences for the GPS objects are shown in Table 3.1. Main sequence F-type stars were also observed for telluric correction and relative flux calibration. For each object a standard set of calibration data were acquired, consisting of flat images, XeAr lamp and its corresponding dark images and Ronchi calibration mask to correct for the spatial distortion of integral field unit.

Data reduction was performed in the standard way using the tasks of the GEMINI/NIFS package in IRAF. For every object we had to perform an additional removal of skylines and cosmic rays using an IDL+IRAF script. In addition, before performing the telluric correction,

the intrinsic absorption line of Brγ was removed from the telluric spectrum using SPLOT in IRAF.

3.4.3 UKIRT/WFCAM

With the aim of investigating the presence of molecular outflows around eruptive variables candidates in Serpens OB2, near-infrared K band and 2.12 μm (1-0)S(1) H_2 narrow band imaging data were obtained on August 7th 2012 using the Wide Field Camera (WFCAM, Casali et al. 2007) mounted on UKIRT. The instrument has four Rockwell Hawaii II arrays (2048×2048 pixels) separated by 90% of a detector width, with a pixel scale of 0.4"/pixel. The standard 2×2 tiling pattern was used to cover a continuous $0.9^\circ \times 0.9^\circ$ region containing 10 of the 11 eruptive variables candidates in the Serpens OB2 association. The total integration times were 2 minutes in K and 25 minutes at 2.12 μm. The observations consisted of 24 images in K, with exposure times of 5 s (K) and 20 images at 2.12 μm, with 75 s exposures. A 2×2 microstepping pattern was used to fully sample the spatial resolution in both filters, yielding a 0.2" pixel scale in the reduced images. Data reduction and photometry were done by the Cambridge Astronomical Survey Unit (CASU) using the standard reduction pipeline.

Difference ($H_2 - K$) images are built in order to reveal emission line regions possibly associated with H_2 jets and outflows. The continuum subtracted images are built with the standard procedure (see e.g. Ioannidis & Froebrich 2012).

3.4.4 VST/OmegaCam VPHAS+

VPHAS+ (Drew et al, in prep.) is an ESO public survey, collecting u', g', r', i' and narrowband $H\alpha$ photometry of the southern Galactic Plane and Bulge. It is in execution on the VLT Survey Telescope (VST), using the 1 square-degree imager, OmegaCam. The camera is constructed around a 4×8 mosaic of 2k×4k CCDs. The pixel size projects to 0.21" on the sky, permitting good sampling of the 0.8-1.0" point-spread function achieved. The exposure times for the data used here were u': 150 s, g': 30 s, r',i': 25 s, and $H\alpha$ 120 s.

To ensure more uniform seeing conditions, finally, across the full filter set, u', g', r' exposures are obtained as a contemporaneous group, separately from r, i and $H\alpha$ exposures. At each field pointing, each filter is exposed twice (or three times, in $H\alpha$) at different offsets to compensate for gaps between the CCDs making up the mosaic. The data are reduced and calibrated by the Cambridge Astronomical Survey Unit (CASU), on the basis of nightly standards. In principle this should yield an accuracy of ±0.03 magnitudes. The scale set should be regarded as provisional, as it is too early to establish a global calibration. All magnitudes and colours are referred to Vega as the zero-magnitude, zero-colour reference object.

The Serpens OB2 region, relevant to this study, was observed as part of VPHAS+ on the nights of June 10th 2012 (r', i' and $H\alpha$) and November 11th 2012 (u', g', r').

Object	Instrument	R	T_{exp}	airmass	N_{exp}	Date
VVVv20	FIRE	6000	253.6	1.4	4	11 May 2014
VVVv25	FIRE	6000	253.6	1.2	4	10 May 2014
VVVv32	FIRE	6000	253.6	1.2	8	10 May 2014
VVVv42	FIRE	6000	253.6	1.4	4	22 April 2013
VVVv45	FIRE	6000	253.6	1.2	4	22 April 2013
VVVv63	FIRE	6000	253.6	1.4	4	11 May 2014
VVVv65	FIRE	6000	158.5	1.3	4	11 May 2014
VVVv94	FIRE	6000	253.6	1.2	4	10 May 2014
VVVv118	FIRE	6000	253.6	1.2	4	22 April 2013
VVVv193	FIRE	6000	158.5	1.1	4	11 May 2014
VVVv202	FIRE	6000	158.5	1.1	2	11 May 2014
VVVv229	FIRE	6000	158.5	1.1	4	22 April 2013
VVVv235	FIRE	6000	158.5	1.1	2	11 May 2014
VVVv240	FIRE	6000	253.6	1.2	4	10 May 2014
VVVv270	FIRE	6000	158.6	1.2	4	11 May 2014
VVVv322	FIRE	6000	158.5	1.3	4	11 May 2014
VVVv322	FIRE	6000	253.6	1.1	4	22 April 2013
VVVv374	FIRE	6000	253.6	1.1	4	10 May 2014
VVVv405	FIRE	6000	158.5	1.3	4	11 May 2014
VVVv406	FIRE	6000	158.5	1.4	4	11 May 2014
VVVv452	FIRE	6000	253.6	1.2	8	10 May 2014
VVVv473	FIRE	6000	253.6	1.2	4	22 April 2013
VVVv480	FIRE	6000	253.6	1.25	12	22 April 2013
VVVv514	FIRE	6000	158.5	1.2	4	11 May 2014
VVVv562	FIRE	6000	253.6	1.3	4	11 May 2014
VVVv625	FIRE	6000	158.5	1.2	4	11 May 2014
VVVv628	FIRE	6000	253.6	1.1	4	11 May 2014
VVVv630	FIRE	6000	158.5	1.2	4	11 May 2014
VVVv631	FIRE	6000	253.6	1.1	4	10 May 2014
VVVv632	FIRE	6000	253.6	1.2	4	10 May 2014
VVVv662	FIRE	6000	158.5	1.2	4	11 May 2014
VVVv665	FIRE	6000	158.5	1.1	4	11 May 2014
VVVv699	FIRE	6000	158.5	1.1	4	11 May 2014
VVVv699	FIRE	6000	253.6	1.1	4	22 April 2013
VVVv717	FIRE	6000	253.6	1.1	4	22 April 2013
VVVv721	FIRE	6000	158.6	1.2	4	11 May 2014
VVVv796	FIRE	6000	253.6	1.3	4	10 May 2014
VVVv800	FIRE	6000	253.6	1.2	4	10 May 2014
VVVv815	FIRE	6000	253.6	1.2	4	22 April 2013
VVVv815	FIRE	300	148	1.3	4	8 May 2012

Table 3.2: Spectroscopic observations of VVV objects.

3.4.5 Magellan Baade/FIRE

Low Resolution spectroscopy

Follow up of the two reddest objects in the DR5 sample, GPSV3 and GPSV15, and VVV object VVVv815 was performed on May 8th, 2012 with the FIRE spectrograph mounted on the Magellan Baade Telescope at Las Campanas Observatory, Chile. The observations were carried out in the high-throughput prism mode which provides a continuous coverage from $0.8-2.5\ \mu m$ at low resolution of $R \sim 250-350$ with a 0.6" slit.

The objects were observed in the usual ABBA pattern along the slit, with individual exposures of 148 s and at airmasses of 1.1 and 1.4 for GPSV3 and GPSV15 respectively. Observations of spectroscopic calibrators were carried out for purposes of telluric correction and flux calibration; the calibrators were observed at similar airmass as the objects and with the same instrumental setup. Quartz lamp images were obtained for flat fielding of the data, they consisted of high-voltage (2.2V) images that provide data for the z/J bands but saturate the red end of the spectrum, and low-voltage(1.1V) that generate counts in H/K but are too faint for the blue end. Additionally, NeNeAr arc lamp images were acquired for wavelength calibration.

The images were reduced using the longslit package of the FIREHOSE software. Using the NeNeAr lamp image FIREHOSE generates an arc solution, which had typical uncertainties of 0.4 pixels or $\sim$ 2.7 Å. The second step consisted of creating a flat image; this is done by combining the 2.2V (blue) and 1.1V (red) with a smooth weighting function spread over $\sim$ 150 pixels centered on a transition pixel defined by the user. Finally the software traces and extracts the spectrum of the object. Telluric correction and flux calibration were performed in the standard mode using NOAO/TWODSPEC package in IRAF, in a similar process to that described in section 3.4.1.

Unfortunately, the selected exposure times saturated part of the K-band data of GPS objects, more noticeably in GPSV15. However, the data still provide useful information for our analysis, particularly at the shorter wavelengths not covered by the ISAAC or Gemini NIFS spectra.

High Resolution.

We performed follow up observations of 37 high-amplitude variables from VVV. The observations were carried out with the high-resolution echellete mode, which provides coverage from $0.8-2.5\ \mu m$ using echelle grating orders 11-32, and at high resolution of $R \sim 6000$ with a 0.6" slit. The spectrograph provides a spatial resolution of 0.18" pixel^{-1}. The observations were carried out over a total of 3 nights, on April 19th 2013 and May 10th-11th 2014.

The majority of the objects were observed in the typical ABBA pattern along the slit, with exposures times between 158-260 s, and at airmasses in the range 1-1.4. Immediately after the objects, we observed ThAr lamps for wavelength calibration, and F-type and A0 main sequence stars for relative flux calibration purposes. These were also done in an AB pattern and with exposure times between 10-60 s. Sky and Qh lamp flats were acquired at the beginning/end of each night to determine the pixel-to-pixel response calibration. Table 3.2 shows the date,

exposure time and number of exposures for all of the VVV objects.

Data reduction was performed using the echelle mode of the FIREHOSE data reduction software. The latter determines the boundaries of each order in the image, constructs a master Qh flat, a slit illumination function from the sky twilight flats and determines the tilt of the slit in the detector from a wavelength calibration frame. The software then generates the wavelength solution and traces the object in each order. The profile of the object and background sky residuals are fitted using an iterative procedure, where a bspline function is used for orders with high signal-to-noise, whilst a Gaussian profile is assumed for low signal-to-noise orders. It then performs an optimally-weighted extraction of the object using the profile determined before.

In the case of the extraction of the telluric, the software follows a different procedure and uses a boxcar extraction, which just adds the counts of the target within a box of a pre-determined size.

It was found that the different extraction methods for the object and calibrator yielded odd results for the final spectrum of the object after telluric calibration, i.e. the objects had bluer spectra than expected from their near-infrared colours. This problem was solved by forcing FIREHOSE to perform optimal extraction to the telluric images.

The software removes intrinsic absorption features of H I from the telluric objects following the methods of Vacca et al. (2003). This procedure is only suitable for A0V stars and it was used for telluric standards observed in the 2014 run. For the 11 objects observed in 2013, intrinsic features from the F-type calibrator were removed manually for each order using SPLOT in IRAF.

The final relative flux calibration and merging of individual orders were performed using the ONEDSPEC tasks TELLURIC and SCOMBINE respectively.

During the second half of the first night of the 2014 observing run, we observed telluric standards with higher airmasses than those of the respective object. Given this, some of the telluric features are not properly corrected from the spectrum of the object and would appear as emission line features. Five stars in our sample suffer from this error in the observations.

The TELLURIC task of ONEDSPEC in IRAF allows to scale the standard spectrum to that of the object spectrum in order to match the intensities of the telluric features to be removed. This effectively performs a correct removal of such features, but at the same time changes the shape of the continuum in the final spectrum of the object. We divided the original relative flux calibrated spectrum (image A) by the spectrum that results from matching the intensities of the tellurci features (image B). This new spectrum, or image C, only contains the telluric features that were not properly removed in the original image. The next step was to create a continuum normalized spectrum of image C, or image D. Finally dividing image A by image D yields the final spectrum of the object, effectively removing telluric features without affecting the shape of the continuum.

Chapter 4

GPS

This chapter is based on the publication "Extreme infrared variables from UKIDSS - I. A concentration in star-forming regions"

Contreras Peña et al. 2014, 2014MNRAS.439.1829C

4.1 Search results

Table 4.1 presents the parameters for the variables selected in the searches of DR5 and DR7 described in section 3.1.1. Column 1 gives the source number sorted by ascending right ascension of the objects. Column 2 presents the original designation given to the sources by the authors. This designation is maintained throughout the remainder of this work. Column 3 corresponds to the full UKIDSS GPS designation for the source. Coordinates for the objects are given in Columns 4 and 5. The K band magnitude of the source is presented in Column 6, where K_1 represents the K band epoch with contemporaneous J and H photometry[1]. The corresponding $J-K$ and $H-K$ colours are given in columns 7 and 8 respectively. Column 9 gives the K band magnitude difference between the 2 GPS epochs, $K_2 - K_1$. Column 10 presents ΔK_{all}, the absolute value of the peak-to-trough difference when using all of the available data from this work and the literature. Finally, the number of epochs used in the calculation of the latter, N_K, is given in column 11, whilst the data release from which the objects arise is given in column 12.

Figure 4.1 shows the ΔK distribution of the 45 stars found in this analysis as well as the mean K distribution of the sample.

The colours and magnitudes of the 45 stars found in the analysis are shown in Figures 4.2 and 4.3, and listed in Table 4.1. Two of the 17 variables in DR5 show blue colours. One of them was identified via SIMBAD as Nova Sct 2003 (Nakano et al. 2003) corresponding to GPSV17 in Table 4.1. The other 16 stars from DR5 are unknown in the literature, except GPSV13,

[1]For the sources in this sample K_2 represents the earlier epoch, but this is not true for all GPS sources.

n°	Object ID	GPS Designation	α (J2000)	δ (J2000)	K_1 (mag)	$J-K_1$ (mag)	$H-K_1$ (mag)	K_2-K_1 (mag)	ΔK_{all} (mag)	N_K	DR
1	GPSV36	UGPS J181140.3−152954.2	18:11:40.30	-15:29:54.27	12.20(0.02)	2.56(0.02)	1.05(0.02)	1.43	1.76	4	DR7
2	GPSV37	UGPS J181219.4−150304.3	18:12:19.43	-15:03:04.30	15.80(0.04)	1.14(0.04)	0.30(0.04)	1.14	1.14	2	DR7
3	GPSV1	UGPS J181452.9−115748.7	18:14:52.94	-11:57:48.77	15.11(0.02)	2.72(0.04)	1.21(0.03)	3.75	3.75	3	DR5
4	GPSV8	UGPS J181556.9−114113.8	18:15:56.91	-11:41:13.82	12.79(0.02)	1.94(0.02)	0.75(0.02)	-1.07	1.17	6	DR5
5	GPSV10	UGPS J181612.8−113809.1	18:16:12.83	-11:38:09.17	13.99(0.02)	3.36(0.03)	1.56(0.02)	-1.28	1.50	6	DR5
6	GPSV7	UGPS J181707.1−115142.5	18:17:07.12	-11:51:42.55	14.15(0.02)	2.71(0.02)	1.29(0.02)	-1.00	1.00	4	DR5
7	GPSV9	UGPS J181717.3−115854.3	18:17:17.38	-11:58:54.30	16.43(0.05)	>2.30	>2.56	-1.16	1.16	4	DR5
8	GPSV5	UGPS J181727.1−113531.4	18:17:27.11	-11:35:31.49	15.53(0.02)	2.08(0.04)	0.77(0.03)	1.05	1.05	4	DR5
9	GPSV4	UGPS J181753.5−120116.6	18:17:53.51	-12:01:16.61	15.53(0.02)	2.01(0.04)	0.95(0.04)	1.07	1.07	4	DR5
10	GPSV38	UGPS J181758.5−091831.4	18:17:58.57	-09:18:31.40	14.38(0.02)	>5.43	>4.62	-2.68	2.68	4	DR7
11	GPSV11	UGPS J181802.1−115424.8	18:18:02.14	-11:54:24.85	15.84(0.03)	3.55(0.18)	1.69(0.07)	-1.34	2.62	5	DR5
12	GPSV6	UGPS J181809.2−115519.6	18:18:09.24	-11:55:19.61	16.37(0.05)	1.88(0.08)	0.67(0.07)	-1.00	1.00	4	DR5
13	GPSV3	UGPS J181844.7−113651.9	18:18:44.74	-11:36:51.92	12.47(0.02)	>7.00	3.56(0.02)	1.28	1.72	6	DR5
14	GPSV2	UGPS J181933.6−112800.8	18:19:33.64	-11:28:00.80	14.47(0.02)	1.95(0.02)	0.72(0.02)	1.94	2.45	6	DR5
15	GPSV39	UGPS J182126.3−121224.7	18:21:26.31	-12:12:24.75	15.12(0.02)	1.03(0.02)	0.35(0.03)	1.11	1.11	2	DR7
16	GPSV40	UGPS J182206.7−123254.9	18:22:06.71	-12:32:54.95	16.67(0.09)	3.39(0.32)	1.78(0.21)	-1.10	1.10	2	DR7
17	GPSV41	UGPS J182642.1−062747.3	18:26:42.18	-06:27:47.30	17.31(0.11)	1.28(0.13)	0.38(0.14)	-1.34	1.34	2	DR7
18	GPSV42	UGPS J183135.3−021424.2	18:31:35.31	-02:14:24.21	13.99(0.02)	3.55(0.02)	1.30(0.02)	1.45	1.45	3	DR7
19	GPSV43[a]	UGPS J183237.6−023102.7	18:32:37.67	-02:31:02.70	14.60(0.02)	>2.06	1.90(0.02)	-1.06	1.18	4	DR7
20	GPSV44	UGPS J183321.4−045726.0	18:33:21.45	-04:57:26.06	13.46(0.02)	4.66(0.04)	2.18(0.02)	2.30	2.30	2	DR7
21	GPSV45	UGPS J184221.9−080459.6	18:42:21.94	-08:04:59.68	11.37(0.02)	7.78(0.16)	5.11(0.03)	2.01	2.01	4	DR7
22	GPSV18	UGPS J184834.5−053518.3	18:48:34.53	-05:35:18.36	15.18(0.02)	1.83(0.02)	0.60(0.02)	-1.10	1.10	2	DR7
23	GPSV17	UGPS J184937.6−093350.9	18:49:37.60	-09:33:50.94	17.77(0.16)	0.36(0.17)	0.10(0.18)	-2.35	2.35	2	DR5
24	GPSV12	UGPS J185318.8−094329.1	18:53:18.82	-09:43:29.15	15.77(0.03)	0.78(0.03)	0.16(0.03)	1.10	1.29	3	DR5
25	GPSV19	UGPS J190003.3+010528.7	19:00:03.34	01:05:28.73	14.19(0.02)	5.27(0.18)	2.27(0.03)	2.08	2.08	2	DR7
26	GPSV20	UGPS J190028.0−064918.7	19:00:28.02	-06:49:18.77	13.52(0.02)	0.54(0.02)	0.16(0.02)	1.04	1.04	4	DR7
27	GPSV13	UGPS J190122.5+115203.2	19:01:22.50	11:52:03.24	12.92(0.02)	0.29(0.02)	0.14(0.02)	-1.02	1.23	4	DR5
28	GPSV21	UGPS J190146.8+011349.3	19:01:46.89	01:13:49.37	17.27(0.09)	>2.53	1.86(0.18)	-1.81	1.81	2	DR7
29	GPSV22	UGPS J190147.0.021228.0	19:01:47.07	01:12:28.08	13.40(0.02)	4.89(0.04)	1.86(0.02)	1.72	1.72	2	DR7
30	GPSV15	UGPS J190332.1+120557.2	19:03:32.11	12:05:57.25	11.21(0.02)	6.23(0.02)	2.93(0.02)	1.03	1.38	4	DR5
31	GPSV14	UGPS J190815.0+124021.4	19:08:15.06	12:40:21.44	15.98(0.03)	0.88(0.03)	0.25(0.03)	2.08	2.08	2	DR5
32	GPSV23	UGPS J191557.0.022906.7	19:15:57.05	01:29:06.77	15.78(0.02)	0.61(0.02)	0.16(0.02)	1.01	1.63	3	DR7
33	GPSV16	UGPS J201310.3+333128.1	20:13:10.31	33:31:28.17	13.46(0.02)	3.20(0.02)	1.47(0.02)	2.21	2.21	3	DR5
34	GPSV24	UGPS J201613.5+415436.5	20:16:13.50	41:54:36.51	14.83(0.02)	2.73(0.02)	0.99(0.02)	1.07	1.07	2	DR7
35	GPSV25	UGPS J201924.8+410503.0	20:19:24.83	41:05:03.07	14.82(0.02)	2.33(0.02)	0.97(0.02)	1.22	1.22	2	DR7
36	GPSV26	UGPS J202038.9+405606.8	20:20:38.91	40:56:06.86	14.48(0.02)	3.13(0.02)	1.19(0.02)	1.36	1.48	3	DR7
37	GPSV27	UGPS J202117.2+403825.1	20:21:17.28	40:38:25.18	15.73(0.02)	3.28(0.08)	1.15(0.03)	1.14	1.14	3	DR7
38	GPSV28	UGPS J202421.3+421605.6	20:24:21.37	42:16:05.63	11.88(0.02)	>7.92	2.62(0.02)	1.00	1.56	3	DR7
39	GPSV29	UGPS J202504.2+403332.6	20:25:04.23	40:33:32.63	15.76(0.02)	1.14(0.02)	0.38(0.02)	1.42	1.42	2	DR7
40	GPSV30	UGPS J202605.3+420932.9	20:26:05.36	42:09:32.94	15.38(0.02)	>4.42	2.86(0.11)	1.51	1.51	2	DR7
41	GPSV31	UGPS J202759.3+415255.7	20:27:59.34	41:52:55.79	16.60(0.05)	>3.20	1.37(0.09)	-1.16	1.16	2	DR7
42	GPSV32	UGPS J203117.5+413242.5	20:31:17.58	41:32:42.52	15.87(0.03)	2.86(0.10)	1.06(0.04)	-1.00	1.00	2	DR7
43	GPSV33	UGPS J203352.9+413844.9	20:33:52.90	41:38:44.94	16.41(0.04)	2.59(0.14)	0.81(0.07)	-1.13	1.13	2	DR7
44	GPSV34	UGPS J203427.1+421353.3	20:34:27.13	42:13:53.31	11.48(0.02)	4.58(0.02)	1.82(0.02)	1.74	2.11	3	DR7
45	GPSV35	UGPS J204142.0+393852.0	20:41:42.01	39:38:52.03	16.84(0.05)	>2.96	>2.16	-1.79	2.79	3	DR7

[a] For GPSV43 the J band image is not contemporaneous to H and K_1. Given the red H-K_1 colour we regard the J-K_1 colour as a lower limit.

Table 4.1: Parameters of the high-amplitude variables from UKIDSS GPS. For the description of the columns see section 4.1

which is listed in the Witham et al. (2008) catalogue of Hα emission line stars. Also, some have previous detections in the Deep Near Infrared Survey of the Southern Sky (DENIS) or the 2 Micron All Sky Survey (2MASS). Two stars arising from DR7, GPSV38 and GPSV45, present exceptionally red $H-K$ colours and $\Delta K > 2$ mag. These correspond to the known OH/IR stars, GLMP755 (Jiménez-Esteban et al. 2006) and IRAS 18396-0807 (Hashimoto 1994). OH/IR stars typically represent the most extreme oxygen-rich Asymptotic Giant Branch (AGB) stars, with mass loss rates greater than 10^{-5} $M_{\odot}yr^{-1}$. They are thought to be the extension towards longer periods and higher luminosities of Mira variables (Whitelock et al. 1991), being more evolved and in some cases perhaps in the process of becoming planetary nebulae. Given the higher mass loss rate, these objects are deeply embedded, being only detectable towards near-infrared wavelengths. Thus these stars will likely be a source of "contamination" in our search for eruptive PMS variables (see discussion below). However, these are still interesting objects. The mid-infrared colours of two sources detected here put them at the red end of the sequence of colours predicted for O-rich AGB stars with increasing mass loss (Bedijn 1987) in the work of Jiménez-Esteban et al. (2006), implying that these stars are about to leave the sequence to become planetary nebulae.

4.1.1 YSOs?

From the DR5 sample, eight of the stars appear very red in colour-magnitude diagrams (CMD, see left panel of Fig. 4.2), i.e. redder than the giant branch plotted for stars in the vicinity. Five of the remaining stars also appear quite red, being projected against the giant branch. These 13 "red" stars have colours indicating a K band excess due to hot dust in our colour-colour diagrams, a common property of pre-main-sequence (PMS) stars with accretion discs. In fact, most of them are consistent with being reddened T Tauri stars (Fig. 4.3). We note that 4 of these are located in the boundary between reddened T Tauri and main sequence stars, however some of their properties favour the T Tauri interpretation. Three of them (GPSV9, GPSV3 and GPSV15) have larger K-band excesses, which could point to the objects being Class I YSOs. The results of the DR7 search are similar to those of DR5, in that most of the variables have redder (J-K) colours than normal dwarf branch or giant branch stars in a 6×6 arcmin field centered on the variable objects (see Fig. 4.2). There are some extreme cases: GPSV28 is extremely red and it may correspond to IRAS source IRAS 20226+4206. Gemini NIFS spectroscopy also shows that the object has a spatially extended H_2 outflow (Contreras Peña et al., in prep.). Figure 4.3 shows the near-infrared colours of the selected candidates. Many of the objects fall in the region dominated by disc emission, i.e. between the reddened sequence of main sequence stars and the T Tauri locus of Meyer et al. (1997). Some candidates show a larger excess, which would usually suggest classification as a Class I YSO, i.e. a disc + envelope system.

Strong evidence to support the YSO interpretation is given by the apparent high concentration of our sample towards SFRs. We performed the search for a possible association of the sources using SIMBAD and the Avedisova (2002) catalog of SFRs. The main condition for the

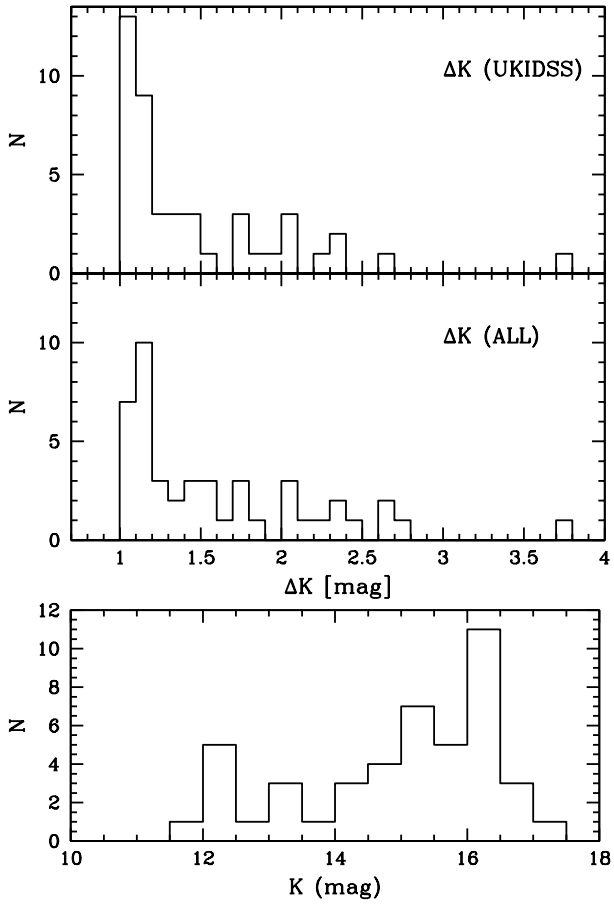

Figure 4.1: Histogram of the absolute K band magnitude difference from GPS (top) and when taking into account all of the available data (middle). The middle graph shows an increase of the observed amplitude of the variability when more epochs over an extended baseline are available. (bottom) Mean GPS K magnitude distribution for the 45 objects in our sample.

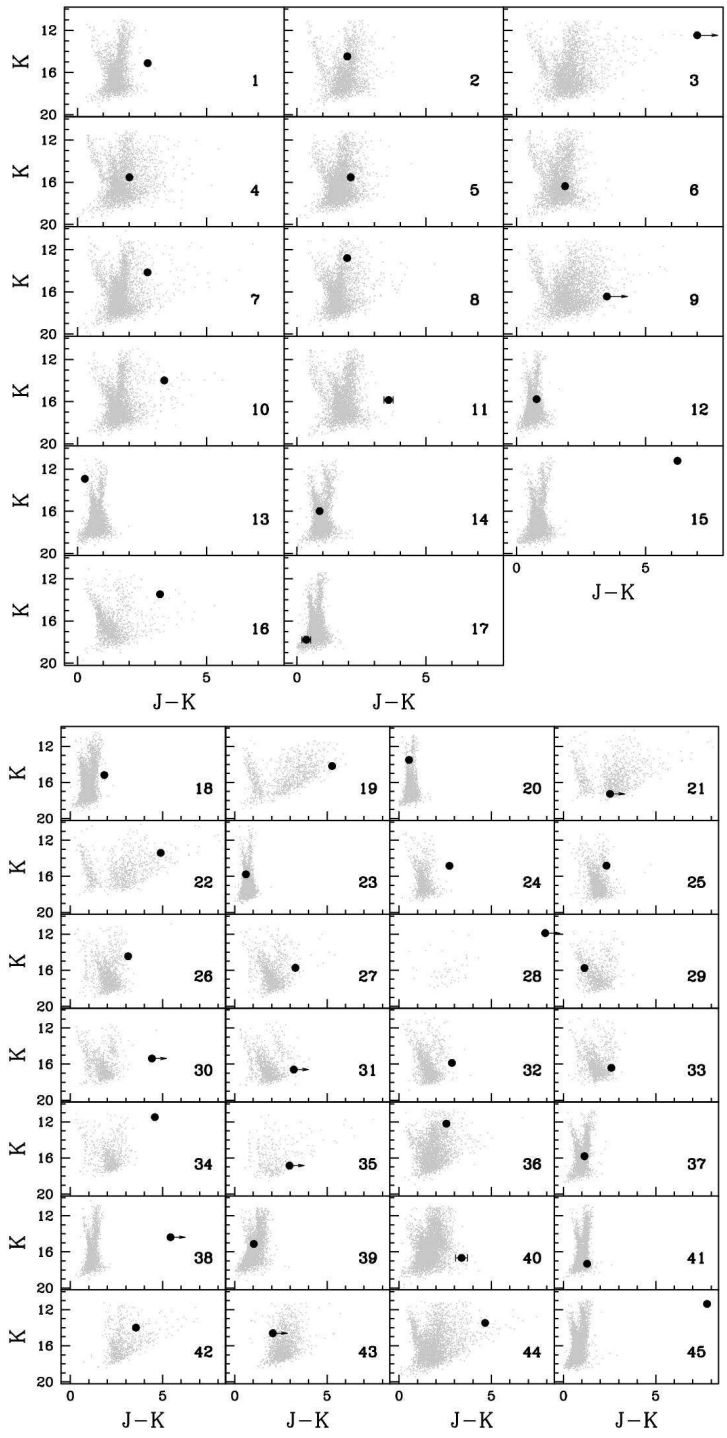

Figure 4.2: Colour-magnitude diagrams of $6' \times 6'$ regions centered on each of the variable candidates. This is presented for candidates in DR5 (top) and DR7 (bottom). The arrow marks candidates for which *J-K* colours represent lower limits. Numbers relate to the original designation of the objects given by the authors in column 2 of table 4.1. Errors are plotted only for objects that present significant uncertainties on their measurements.

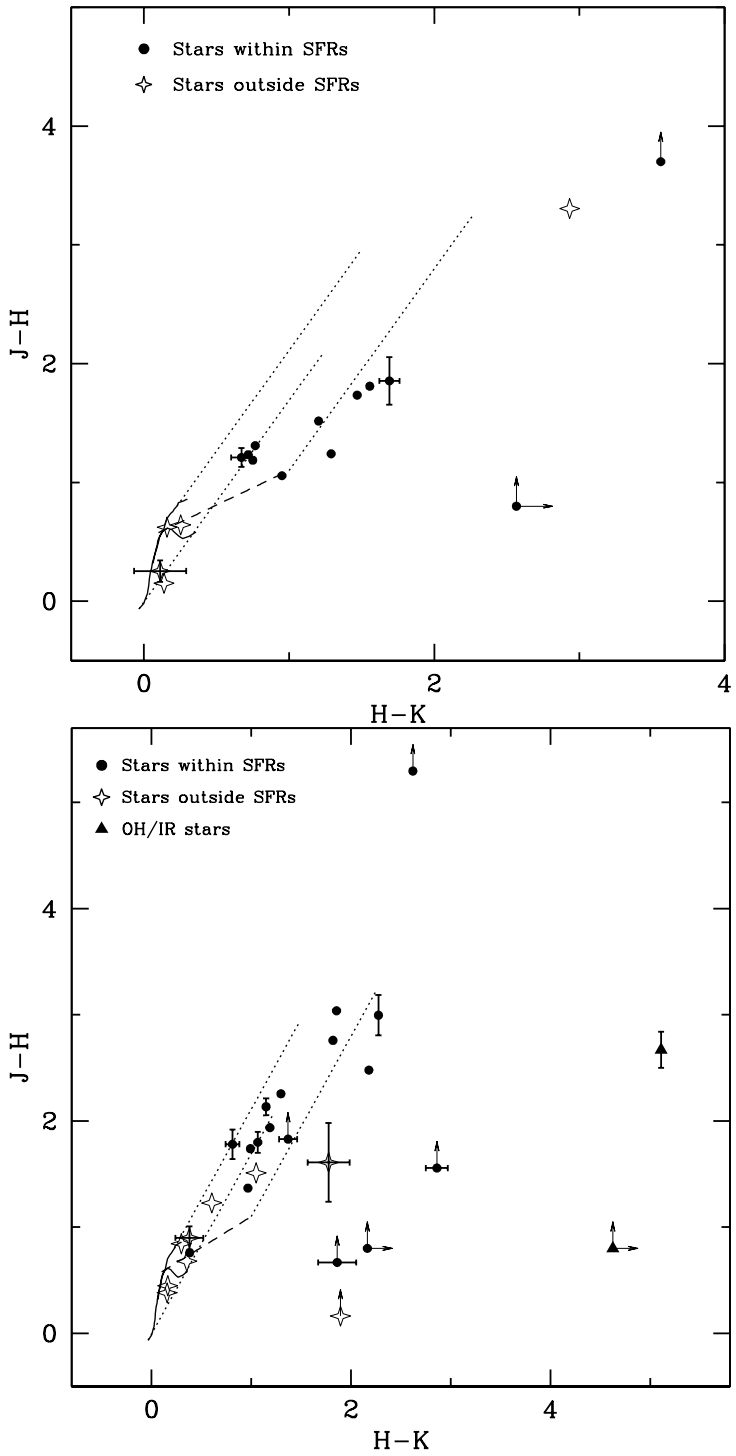

Figure 4.3: Colour-colour diagram for GPS-selected candidates in DR5 (top) and DR7 (bottom). The objects are divided between those associated with SFRs as described in the text (filled circles) and objects not found within such areas (open diamonds). The two OH/IR stars found in the DR7 sample are marked with filled triangles. The classical T Tauri locus of Meyer, Calvet, & Hillenbrand (1997) is presented (long-dashed line) along with intrinsic colours of dwarf and giants (solid lines) from Bessell & Brett (1988). Reddening vectors of $A_V = 20$ mag are shown as dotted lines. The arrows mark stars for which colours represent lower limits. Errors are plotted only for objects that present significant uncertainties on their measurements.

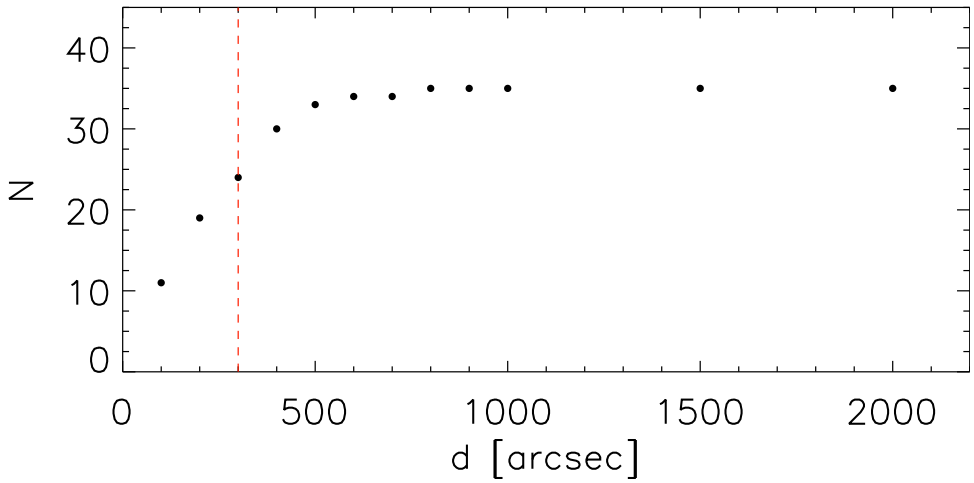

Figure 4.4: Cumulative distribution of variable stars from DR5 and DR7 flagged as likely associated with areas of star formations when using different radii for searches in SIMBAD and the Avedisova catalog of SFRs. The dashed red line marks the 300" radius used in this work.

stars to be flagged as likely associated with a SFR was that evidence of star formation would show up in a 300" radius search, centred on the star, in SIMBAD (i.e. PMS stars, dark clouds, HII regions) and the Avedisova (2002) catalog.

The use of a radius of 300" arises from previous statistical studies of PMS stars using GPS data. In figure 4.4 we show the cumulative distribution of variable stars from DR5 and DR7 which are flagged as likely associated with SFRs when using different radii for the searches. We observe a rise in the number of stars associated with SFRs with increasing radius reaching a maximum between 400" and 500"and having a nearly constant value at $d > 500$". In the plot, the 300" radius represents the point where the slope of the curve changes, i.e. at larger radii we will more likely flag stars as associated with SFRs which are probably just chance selections given the large radius used in the search, whilst we are likely to lose stars in SFRs at lower radii. We note that a 300" radius is used as a first condition on the likeliness of the variable stars to be associated with an area of star formation and other characteristics of the objects are also taken into account (see below). In addition, later in this section we estimate that only 10% of the objects from the DR5 and DR7 analysis which are found to be associated with SFRs are likely to be chance selections when using this radius. This percentage will be larger when analysing the data from VVV as we are studying the Galactic disc mid-plane which is rich in areas of star formation and many objects which can be are flagged as associated with SFRs are likely to be located at larger distances than the SFRs and be selected just due to projection effects.

Four stars failed this main condition but are still flagged as likely associated with SFRs for the following reasons:

- GPSV5 and GPSV10 are within the large concentration of high amplitude variables in an area of 1 deg^2 that is coincident with the Serpens OB2 association (see below) and have colours consistent with a T Tauri interpretation (see Fig. 3). In addition GPSV5 is close

to a bright 8 μm emission feature in Figure 4.5. GPSV10 (discussed in more detail in Section 4.3.4) also shows an SED that is consistent with a YSO classification.

- GPSV26 is part of the sample that is within the Cygnus X star forming complex (see below). Its near infrared colours and SED are also consistent with a YSO interpretation (see figure 4.6).

- GPSV19 is only 318" from SFR G35.20-1.75 in the Avedisova (2002) catalog (see below). Its colour is consistent with a YSO classification and it is an unusually red object compared to its local $6\times6'$ field. The lack of mid-infrared data for the object does not allow us to confirm this interpretation through its SED. However, the spectrum of the object shows H_2 emission at 2.12 μm, probably associated with a molecular outflow, and Brγ emission, both of which support a YSO classification (see Section 5.1).

Using our search criteria, it was found that 12 of the 17 DR5 variables present an apparent spatial association with known star forming regions. GPSV1 through 11 are located in an area of 1 deg^2 that is coincident with the Serpens OB2 association, a loose association of PMS stars located $\sim$2 kpc away (Forbes 2000) and which contains several molecular clouds. The candidates do not appear to be located in the regions of most recent massive star formation that can be identified by the bright 8 μm emission in Figure 4.5. Two objects, GPSV3 and GPSV9, are actually within the 8 μm nebulosity and they have the reddest near-infrared colours of the Serpens OB2 objects. However, they do not seem to be Class I objects (see Section 4.3.3). The variable object GPSV16 is found to be within $\sim$ 170" of the SFR listed as G71.52-0.39 (Scoville et al. 1987) in the Avedisova (2002) catalog (Fig.4.5).

We find 17/28 DR7 variables likely associated with a known SFR. Three stars (GPSV19, GPSV21 and GPSV22) are likely associated with SFR G35.20-1.75 (Zhang et al. 2009), GPSV42 is in SFR G26.35+1.83 (Hunter et al. 1990) and GPSV44 in SFR G28.96+3.54 (Crutcher & Chu 1982). Twelve of our candidates are distributed along the Cygnus X star forming complex (Fig. 4.5), which is known to contain several rich and complex SFRs. The presence of FUor outbursts would not be new for this region (see e.g. Rice et al. 2012; Magakian et al. 2013).

We note that 4 other stars fall in the YSO region in colour-colour plots but lack a spatial association with known SFRs. These are GPSV15, 36, 40 and 43. As discussed in section 4.3.3, GPSV15 displays several characteristics associated with eruptive YSOs, and DR7 objects GPSV36 and 43 show SEDs similar to YSOs (see section 4.1.1). GPSV40 is a faint object, and very red in its local CMD. However, mid-infrared data are not available to confirm its YSO nature.

In order to verify the significance of this spatial association with SFRs, we performed a Monte Carlo selection of many samples of 45 real GPS sources in the 2 epoch area, using the same cuts as the variable star selection, except for $\Delta K > 1$ mag. We find that only 10% of randomly chosen sources would be within 300" of a known star forming region, i.e. 4-5 stars in our sample would be near SFRs by chance. However, as noted above, 4 stars in our sample have characteristics of YSOs but are not spatially associated with known SFRs. This indicates

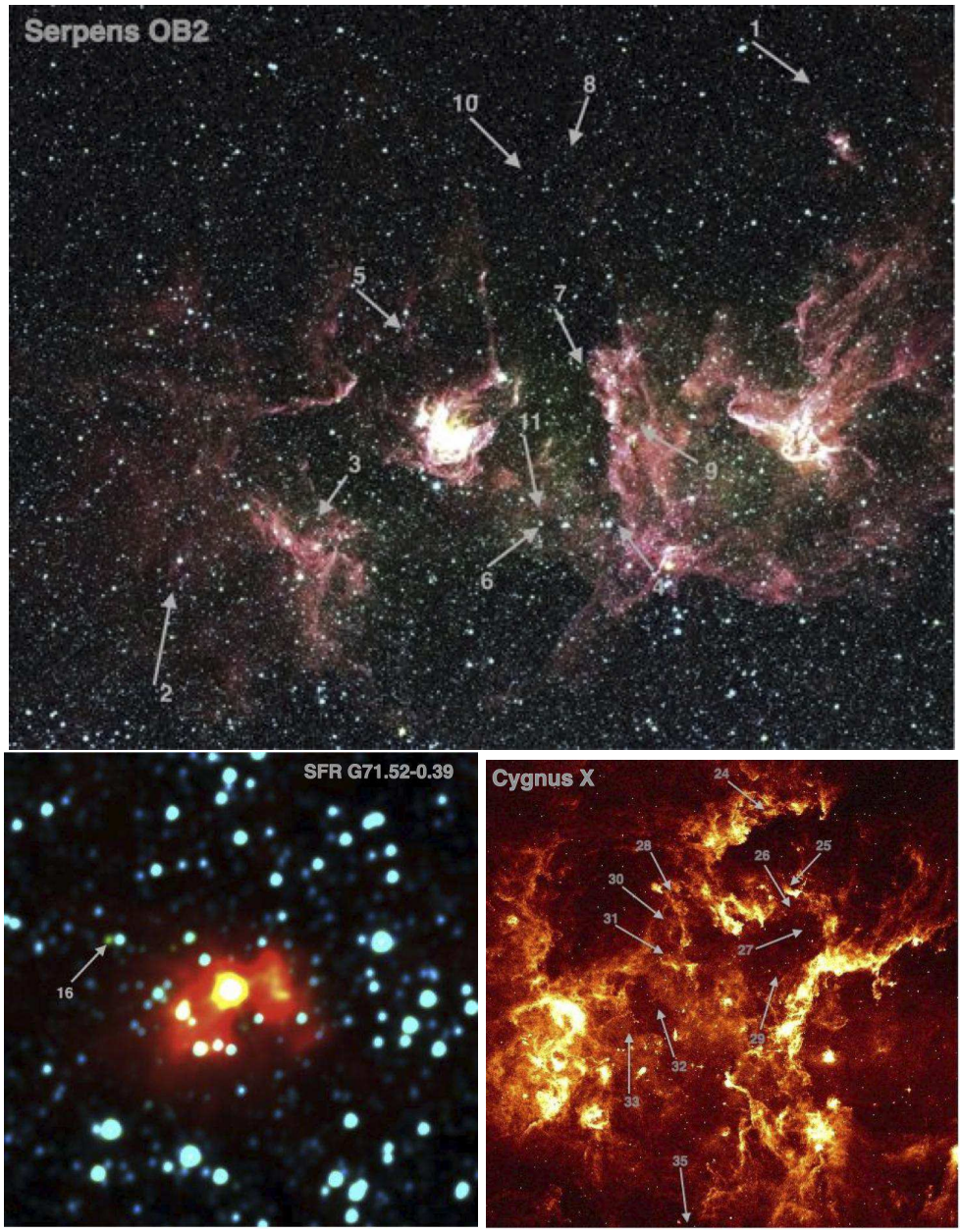

Figure 4.5: (top) False colour Spitzer GLIMPSE3D image (blue=3.6 μm, green=4.5μm, red=8.0μm) of the Serpens OB2 association. The projected location of 11 candidates found within this region are marked by the arrows with the corresponding source number from Table 4.1. (bottom left) False colour WISE image (blue=3.5 μm, green=4.6 μm, red=12 μm), the arrow marks the position of GPSV16; SFR G71.52-0.39 from Avedisova (2002) catalog is clearly observed at the centre of the image.(bottom right) MSX6C 8 μm image of the Cygnus-X star forming complex. Projected location of 12 sources found within this area are marked by arrows with their corresponding GPSV designations.

that chance associations have little effect on the proportion of variables (29/45) that would be classified as YSOs primarily on the basis of spatial association. In view of this, we believe that the strong concentration of high amplitude variables in SFRs found in our study is sufficient evidence on its own that most of the high amplitude variables are YSOs. Confirmation for the majority of the DR5 objects (based on SEDs and spectra) is discussed at length in section 4.3.

SEDs of DR7 objects in SFRs

The spectral energy distributions for the 17 objects from DR7 associated with SFRs (see above) are presented in figure 4.6. In addition we present the SEDs for the three objects that have similar characteristics to YSOs in colour-colour plots but are not located near a known star formation region. These are GPSV36, 40 and 43. The SEDs are constructed using the 2 epoch UKIDSS GPS DR7 information (2005,2008) and public data, when available, from the Spitzer legacy survey, Cygnus-X (2007-2008 observations), and/or WISE (2010 observations). Some of the objects that lack mid-infrared data, or for which an infrared excess is not clear, are compared to an M5V (3240 K) Castelli & Kurucz model atmosphere, and the same model reddened to A_V=10 and 20 mag. A_V=20 is near the upper end of the possible interstellar extinction column values for any of the variables (determined in §2.2 using the local CMD for the field around each source).

The fact that the near- and mid-infrared observations are not contemporaneous does not allow to clearly classify some of the objects as YSOs. This is observed in GPSV32 where if we only take into account the first epoch of GPS and the Spitzer data, its SED resembles that of an M-dwarf with $A_V = 20$ mag of extinction. This changes if we take the second GPS epoch and Spitzer data, where the SED would point to an infrared excess. The same issue arises in GPSV29.

It is also difficult to classify as YSOs in our sample without mid-infrared data. In every case, these objects could point to either infrared excess (not being observed) or correspond to highly obscured M-dwarfs. As an example we compare the object GPSV34 with the same Castelli & Kurucz model atmospheres in figure 4.6. We see that the near infrared data from the second GPS epoch is well fitted by a M-dwarf with $A_V = 20$ mag of extinction. However, the mid-infrared data allows us to confirm its probable YSO nature. Two of the objects with GPS data only are confirmed via its spectra in the analysis to be presented in section 5.1, these are GPSV19 and GPSV22.

Objects GPSV36 and GPSV43 have no association with a star forming region (see above). However, their SEDs show a clear infrared excess that suggests a YSO classification.

Even though we cannot confirm every object in SFR as a YSO, the SEDs shown here and the spectral characteristics for a sample of them (section 5.1) point to such classification for the majority of them. This supports our conclusion that finding high amplitude variables close to areas of star formation is sufficient evidence that most of these stars are YSOs.

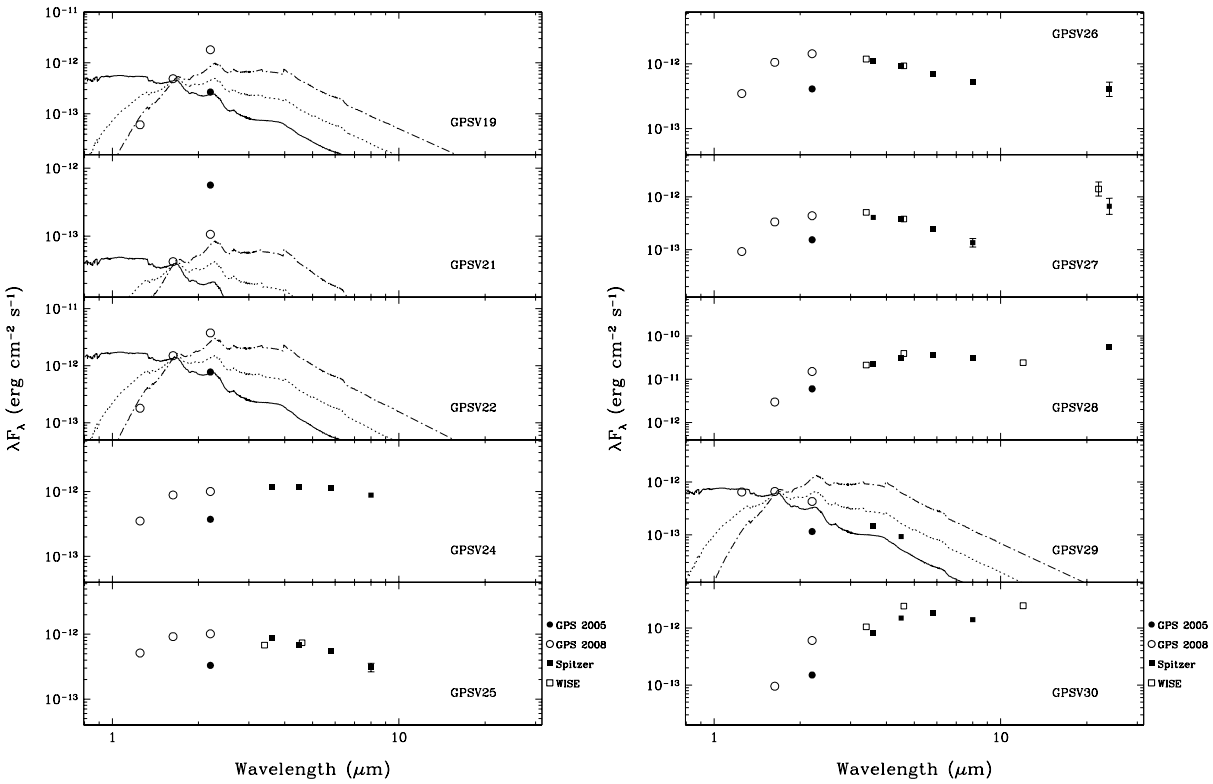

Figure 4.6: Spectral energy distributions of DR7 objects in SFRs, including three objects with YSO characteristics which are not found within SFRs. Data for some of the objects are compared to a M5V (3240 K) Castelli & Kurucz model atmosphere (solid line) and the same model reddened to $A_V = 10$ mag (dotted line) and $A_V = 20$ mag (dashed-dotted line). Fluxes of the model where arbitrarily set to match the 2008-2009 H observations of GPS. The models are reddened using the Cardelli et al. (1989) extinction law for wavelengths in the range $0.3\mu\text{m} < \lambda < 3.3\mu\text{m}$. Extinction towards the wavelengths of the *Spitzer* bands is derived following Chapman et al. (2009).

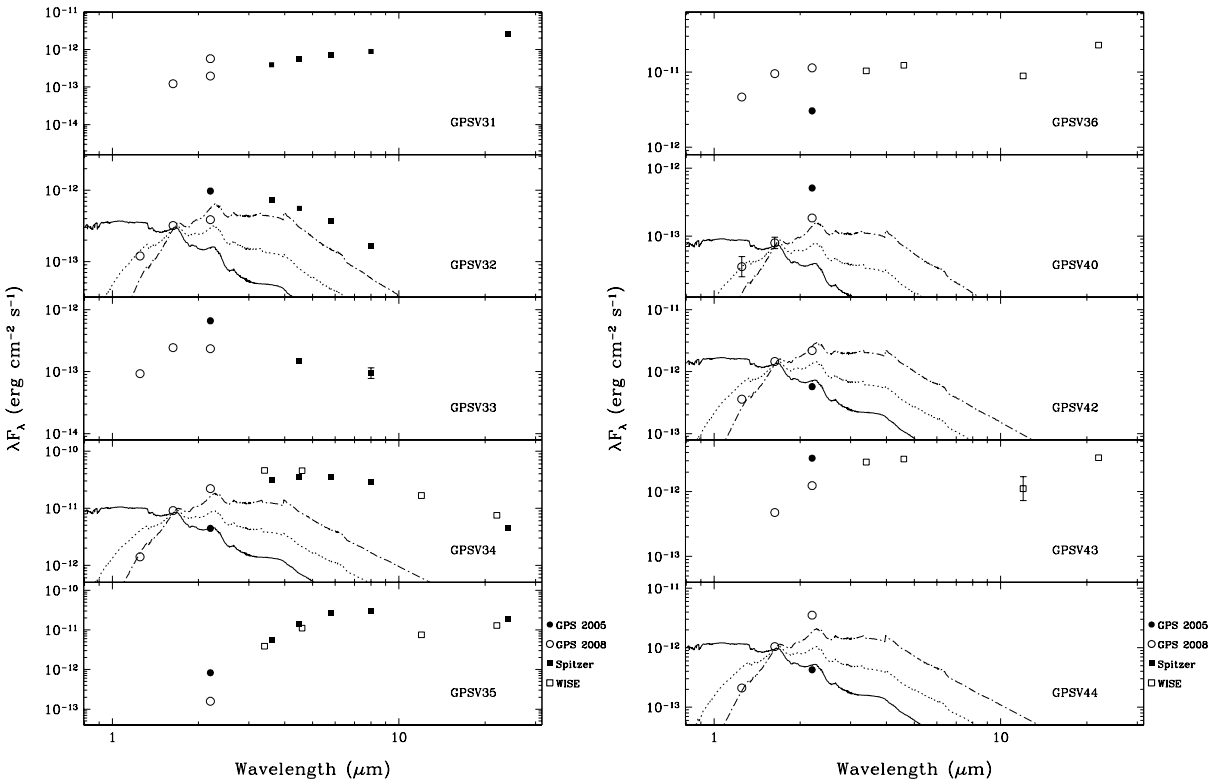

Figure 4.7: Spectral energy distributions of DR7 objects in SFRs, including three objects with YSO characteristics which are not found within SFRs. Data for some of the objects are compared to a M5V (3240 K) Castelli & Kurucz model atmosphere (solid line) and the same model reddened to $A_V = 10$ mag (dotted line) and $A_V = 20$ mag (dashed-dotted line). Fluxes of the model were arbitrarily set to match the 2008-2009 H observations of GPS. The models are reddened using the Cardelli et al. (1989) extinction law for wavelengths in the range $0.3\mu\text{m} < \lambda < 3.3\mu\text{m}$. Extinction towards the wavelengths of the *Spitzer* bands is derived following Chapman et al. (2009).

4.1.2 Different high-amplitude variable classes

Despite the strong evidence that the sample is dominated by YSOs, we still need to discuss other classes of high amplitude variable stars that could have the observed red colours and may account for those objects which are not in known SFRs.

The faint K band magnitudes of the stars in our sample suggests that they are too faint to be R Cor Bor variables or luminous AGB stars, such as Mira-type variables. To verify this, we first derive the approximate extinction towards background objects in the local CMD of each of our sources. To do this, we noted the typical $J-K$ colour of the reddest sources in the local field (excluding any extreme outliers) and then calculated an estimate of the maximum extinction that they could have by assuming that they have the intrinsic colours of -0.1, corresponding to early B type stars. We then derive the distance at which a typical AGB star (Assuming typical $M_K = -7.25$ mag, $(J-K) = 1.25$ mag, Whitelock, Feast, & van Leeuwen 2008) would have to be located in order to have the apparent magnitude of the individual variable source being considered (using the local A_V estimated before). In each case a typical AGB star would have to be located well beyond the Galactic disc edge at Galactocentric radius $R_G = 14$ kpc (see e.g. Minniti et al. 2011), indicating that there are no typical Mira variables in the sample.

AGB stars with high mass loss rates, such as OH/IR stars or extreme carbon stars (see e.g. Volk, Kwok, & Langill 1992), are deeply embedded in circumstellar material and can suffer high extinction. These stars may only be observable at near-infrared wavelengths and appear fainter than typical AGB stars (see e.g., van Loon et al. 1997). Therefore they can show up in our sample and in fact two of them are present in the DR7 sample, as discussed above. Olivier, Whitelock, & Marang (2001) study a complete sample of nearby dust-obscured AGB stars, spread over $\sim 3/4$ of the sky, that are undergoing heavy mass loss ($\dot{M} > 10^{-6}$ $M_{\odot}yr^{-1}$). They find 30 stars within 1 kpc from the sun (the completeness limit of the study) with a scale height of 236 pc. This implies a space density of 9.35 kpc^{-3}. Most AGB stars are located at R_G <10 kpc (Ishihara et al.2011). For a typical inner disc sight line at $l = 45^{\circ}$ this corresponds to a maximum heliocentric distance, $d \approx 14$ kpc. (Beyond this distance, the Galactic latitudes of our survey ($|b| \approx 1.5 - 5.5^{\circ}$) would place most sources a few scale heights above the plane, so very few AGB stars should be found). An area of 1 deg^2 along this $l = 45^{\circ}$ sightline encompasses a conical volume of 1.1 kpc^3 out to d=14 kpc. After allowing for the effect of scale height on the source density this is equivalent to an effective volume of 0.12 kpc^3 in the mid-plane. Then, 1.12 dust-enshrouded AGB stars deg^{-2} should be contained in this volume. However, we expect to detect only a small fraction of them in a 2-epoch survey. In fact, we find that only 27% should be detected, based on a Monte Carlo analysis using a large sample of randomly generated sinusoidal curves with different amplitudes and periods, similar to the sample of Olivier et al. (2001), when randomly selecting two epochs separated by 3 years. In addition, only 2/30 stars in the Olivier et al. sample would have similar magnitudes to the brightest stars in our GPS sample, if they are located at R_G <10 kpc (the remaining stars would almost certainly saturate in UKIDSS even at these large distances). These two stars correspond to the first and third highest mass losing AGB stars in the Olivier et al. sample ($\dot{M} > 10^{-4.8}$ $M_{\odot}yr^{-1}$). AGB stars with this

extremely high mass loss rate, such as the OH/IR stars in the DR7 sample and the extreme carbon stars in Volk et al. (1992), show a steep rise of their SEDs towards the mid-infrared, characterised by a very red $K - [12]$ colour, displaying $K - [12] > 9$ mag.

When we apply the expected detection ratio (0.27) and the fraction of AGB stars with high mass loss rates that would show up in our survey (2/30) we end up with 3.1 dust-enshrouded AGB stars in the area covered by our study. This number is remarkably close to our actual detection of two OH/IR stars in DR7. Only two objects from the remainder of the sample have $K - [12]$ colours similar to extreme AGB stars (GPSV3 and GPSV15) but we are confident that they are YSOs rather than AGB stars, see section 4.3.3. Despite this, it is reasonable to expect that we will find more very red AGB stars in future data releases, some of which may be previously unknown objects.

Symbiotic variable stars can be located in the same area as most of our variable stars in the JHK colour-colour diagram (see Figure 2 in Corradi et al. 2008). The D-type symbiotic stars in particular have the fairly red *(H−K)* colours found among most of our sample. However, D-type symbiotic stars have AGB star companions, most of which can be expected to saturate in the GPS K band data (see the earlier discussion in this section). Corradi et al. (2010) note that the space density of symbiotic stars is very uncertain but it is clear that they are a small Galactic population. As an illustration of their rarity, Corradi et al. (2008) selected a large number of possible symbiotic stars based on an Hα and broad bandpass colour selection. Spectroscopic follow up (Corradi et al. 2010) showed that most of their candidates were in fact T Tauri stars, despite their attempt to reduce contamination by avoiding spatially clustered candidates (Symbiotic variables, like AGB stars are expected to be found in isolation). It is unlikely therefore that there are many symbiotic stars in our sample but it is conceivable that some of the isolated objects with bluer *(H−K)* colours (after allowing for extinction) might be S-type symbiotic stars.

Active Galactic Nuclei (AGN) can also show up in our searches as point sources, with a wide range of near infrared colours. Maddox et al. (2008) finds an expected density of ~ 40 quasars down to $K = 16$ mag in their study of 12.5 deg^2 of the early data release of the UKIDSS Large Area survey (LAS, Dye et al. 2006), which implies ~ 470 quasars in the area covered in our study. However, the fraction of high-amplitude ($\Delta K > 1$ mag) variable AGNs appears to be much lower than 1%. For example, none of the 116 quasars in the sample of Cioni et al. (2013) displays $\Delta K > 1$ mag. Kouzuma & Yamaoka (2012) searched for near-infrared counterparts of AGNs in the UKIDSS Large Area Survey (DR6, covering ~ 1850 deg^2) and 2MASS catalogues. They identified 1920 AGN via K band variability between the two epochs (UKIDSS and 2MASS), using several catalogue data quality cuts to remove most erroneous variables. Their sample included 15 candidate high amplitude AGNs ($\Delta K > 1$ mag) and they provided the coordinates to us at our request. Only 9 of these 15 have a point source profile-classification ($mergedclass = -1$) in UKIDSS, and visual inspection reveals that only 6 of these 9 are real. The approximate completeness limit of their study only reaches to about $K = 15.2$ mag (although some objects are still detected at fainter magnitudes). To compare

with our GPS sample, we must first correct for the fact that the Kouzuma & Yamaoka (2012) high amplitude variable sample will not include most AGN that were fainter at the less sensitive 2MASS epoch and then allow for our fainter magnitude limit. We find a factor of 1.6 for the first correction (using the proportion of highly variable AGN that were fainter in UKIDSS rather than in 2MASS) and we conservatively estimate a factor of 4 more quasars arises from our $K = 16$ mag limit, using Table 7 of Maddox et al. (2008). After applying these corrections and scaling to our survey area we find that we should expect $\sim 3 - 4$ high-amplitude AGNs in the area covered in DR7. We note that the LAS covers areas of low extinction, so if we allow for the higher extinction in the Galactic plane (typically 0 to 1 mag in the K band) then this estimate should be considered an upper limit.

4.2 Concentration of extreme variables in SFRs

When we add the results of our searches of DR5 and DR7, we find that 29 out of 45 variables are likely associated with SFRs, thus representing ∼66% of our sample. As discussed above, 4 other stars show characteristics of YSOs but do not seem to be associated with a known star forming region (a discussion on this point is presented below). Thus, the fraction of variables in SFRs could increase.

In view of the spatial bias against star formation regions in the mid-plane in this initial sample (see Section 3.1.1) it is clear that YSOs must dominate the Galactic population of high amplitude infrared variables with $\Delta K > 1$ mag, at least in the magnitude range that this search has explored ($K \approx 11.5$ to 16 mag). The question then arises as to whether YSOs dominate the total population of high amplitude infrared variables. Inspection of the General Catalogue of Variable Stars (GCVS, Samus et al. 2010) shows that Mira-type variables are the commonest type at bright magnitudes. These very luminous stars are generally saturated in the GPS, except for a tiny minority with exceptionally high extinction and mass loss rate, such as the two OH/IR stars in our DR7 sample. We note that the high variability OH/IR phase is only expected to last 1700 yr (Lewis 2000), thus we do not expect to find many of these type of variables. The GCVS data indicate that 67% of Miras have $\Delta K > 1$ mag. (Note that the K to V amplitude ratio has an average value of 0.2, see Lebzelter & Wood (2005); Soszynski et al. (2005)). Ortiz & Maciel (1996) calculated a space density of 265 kpc^{-3} for a complete sample of AGB stars within 1 kpc of the Sun, with a scale height of 330 pc. Ishihara et al. (2011) performed the search for AGB stars complete out to 8 kpc and they found a similar space density for sources located at Galactocentric radii $3 < R_G < 8$ kpc, after correcting for colour-based incompleteness (see figure 9 of that work). They also showed that most O-rich AGB stars, which dominate the numbers at $l < 90°$, are located at Galactocentric radii R_G <10 kpc. A typical inner disc sight line at $l = 45°$ with an area of 1 deg^2 encompasses a volume of 1.11 kpc^{-3} at R_G <10 kpc. After allowing for the effect of scale height, the effective volume comes to 0.21 kpc^{-3} at these distances. This volume should contain ≈50 AGB stars deg^{-2}.

Only a small fraction of AGB stars are expected to be Mira variables, which are at the end of the thermally pulsating phase of their evolution. Cioni et al. (2001) give the fraction as 8%.

Combining this with the 67% fraction of Miras with $\Delta K > 1$ mag then implies a source density of $\approx$2.7 deg^{-2} for typical sight lines in quadrants 1 and 4 of the Milky Way. This is broadly consistent with an estimate of ≈ 0.5 deg^{-2} in the Galactic plane obtained from inspection of the GCVS: the GCVS only includes Mira variables with known periods so we expect it to provide a somewhat smaller space density.

The 29 YSOs imply a source density of $29/155 = 0.19$ deg^{-2}. However, the true number is higher because: (1) with only two epochs most high amplitude variables will be missed; (2) the source density rises towards our magnitude cut (see Fig. 4.1), indicating that most distant, low luminosity PMS variables will be undetected; and (3) the present dataset excludes the mid-plane and is therefore strongly biased against SFRs (see Section 3.1.1). The Avedisova (2002) catalogue indicates that item (3) excludes 60% of Galactic SFRs (and the true fraction is undoubtedly higher since the catalogue is incomplete for distant SFRs in the mid-plane). The effect of item (2) cannot be reliably quantified, but it is likely to raise the source density by at least an order of magnitude. E.g. typical members of our sample with $K = 14.8$ mag, d=1.4 to 2 kpc (sources in Cygnus X or Serpens OB2) would be below our K=16 magnitude cut at $d > 3.4$ kpc. The overwhelming majority of Galactic SFRs lie at greater distances than this. The study of the spiral structure in the Galaxy by Russeil (2003) is said to be complete for star forming complexes with excitation parameters, U, brighter than 60 pc cm^{-2}. We find that 85% of these are found to be at $d > 3.4$ kpc. Also, most PMS stars are less luminous than those in our sample but presumably can still have high amplitude variability, judging by the rising incidence to faint magnitudes. Finally, item (1) is believed to cause approximately 75% incompleteness: our analysis of high-amplitude variables arising from the 2010-2012 VVV data (with at least 14 epochs of K band observations for each variable) reveals that only $\sim$ 25% of such variables would be detected when comparing the magnitudes of two epochs separated by $\sim$ 2 years. Adopting factors of 4, 6.7 and 2.5 for items 1, 2 and 3 respectively, our observed surface density of 0.19 deg^{-2} rises to 12.7 deg^{-2}. If we assume that 5 YSOs in our sample are actually chance spatial associations of other types of variable (see §2.2), and also remove the 4 stars that did not pass our 300" criterion for SFR association but were still included, the surface density still remains high at 8.7 deg^{-2}. This figure is of course highly uncertain, and the figure of 2.7 deg^{-2} for Miras in quadrant 1 sight lines is also quite uncertain (by perhaps a factor of two given that the space density of AGB stars has a $\sim$50% uncertainty in Ishihara et al.(2011) and the error on the 8% fraction of AGB stars that are Mira variables is not clear in the literature). Nonetheless, we conclude that PMS high amplitude infrared variables are likely to be the commonest type of high amplitude infrared variable in most parts of the Milky Way, except in the Bulge where AGB stars have higher densities. The true incidence will no doubt be established more precisely in the near future using data from VVV (Minniti et al. 2010).

Optical surveys have been used effectively to identify low mass PMS stars even in regions where molecular gas, a common tracer for SFRs, has dissipated (Briceño et al. 2005). Although the near-infrared variability of such objects has been less thoroughly studied, previous surveys show that the majority of YSOs are variable at these wavelengths due to different physical

processes (see e.g. Rice et al. 2012). However, peak to peak amplitudes have been found to be low, with a mean of 0.17 mag in the work of e.g. Carpenter et al. (2001). Only a small fraction show larger amplitudes, e.g. only $\sim 3\%$ of stars with discs show $\Delta K > 0.5$ mag in the sample of Scholz (2012). The fraction seems remarkably higher ($\sim 50\%$) in the recent time series study of Class I protostars (Rice et al. 2012) which suggests that infrared variability surveys can most easily pick out the parts of molecular clouds where star formation has occurred very recently. Scholz (2012) also shows that the fraction of high-amplitude variables increases with extending time baselines.

It is possible then that high-amplitude variability in the infrared, studied over a long baseline such as the one in GPS, can also effectively trace low mass PMS stars and thus evidence of star formation. This could be supported by the finding of the four objects with YSO colours that are not associated with known SFRs. Only marginal and inconclusive evidence for any association with star formation could be found for three of these sources. The projected location of GPSV15 is at the edge of the dark cloud LDN 667 (Lynds 1962; Dutra & Bica 2002), GPSV36 is within 2 arcmin of reflection Nebula GN 18.08.8 (Magakian 2003) and GPSV43 is located in a highly reddened field near the edge of the W40 HII region (Quireza et al. 2006). A search for low-amplitude near-infrared variability in the GPS near these sources does not reveal the presence of a PMS association, however a more statistically thorough study is necessary to firmly discard the presence of such an association.

4.3 Results

4.3.1 Near- and mid-infrared photometry

Table 4.2 shows the results of the 2010 ISAAC and 2012 UKIRT photometry, along with the magnitudes found for targets in other near- and mid-IR surveys. The errors are typically small (≤ 0.08 mag), although given the faintness of some of our objects and significant source confusion in some fields, some of the detections in 2MASS, and WISE have moderate to poor signal to noise ratios (SNR). Detections with SNR < 10 or errors larger than the typical values are marked with ":" in Table 4.2. We also note that even though errors in DENIS photometry are in the range $0.07 - 0.24$ mag, the photometric quality flag had a value of 100 for all of the detections in Table 4.2 and are considered to be reliable measurements. Only one measurement is left out of the table and it corresponds to a VPHAS+ g' detection of GPSV8 with $g' = 22.84 \pm 0.15$ mag.

Spitzer GLIMPSE detections yield more evidence that most of our objects are PMS stars. Figure 4.8 shows the location of our sample on colour-colour diagrams often used for YSO classification when only near-infrared and IRAC 3.6-8.0 μm fluxes are available (see e.g. Hartmann et al. 2005). For comparison we show the sample of YSOs in young stellar clusters of Gutermuth et al. (2009), the classification scheme shown in the diagrams is the same as the one used by these authors. Due to the high variability of our sample, the location of the objects will be affected in the two lower panels, which use H and K photometry. The latter are not contemporary with GLIMPSE3D ($\sim$ 2006), GLIMPSE360 ($\sim$ 2010-2012) nor WISE ($\sim$ 2010). Therefore

we use the closest epoch with simultaneous observations in these two bands, i.e. GPS H and K_1 ($\sim$ 2008) for the Serpens objects, and VLT/ISAAC H and K (2010) for both GPSV15 and GPSV16.

Figure 4.8 shows that most of our objects fall in what appears to be an area of transition between class I to class II objects, especially on the diagrams based purely on *Spitzer* photometry. Two sources stand out as they are located in the region where Class I objects are found: these are GPSV3 and GPSV15. However, the latter is not covered by *Spitzer* surveys and filters $W1$ and $W2$ of WISE are used instead. The use of these filters should not have much effect on location in the diagrams as differences between WISE and IRAC filters are only observed for $W1 \geq 14$ magnitudes and $W2 > 13$ magnitudes (Cutri & et al. 2012), which is fainter than the measured magnitudes for GPSV15.

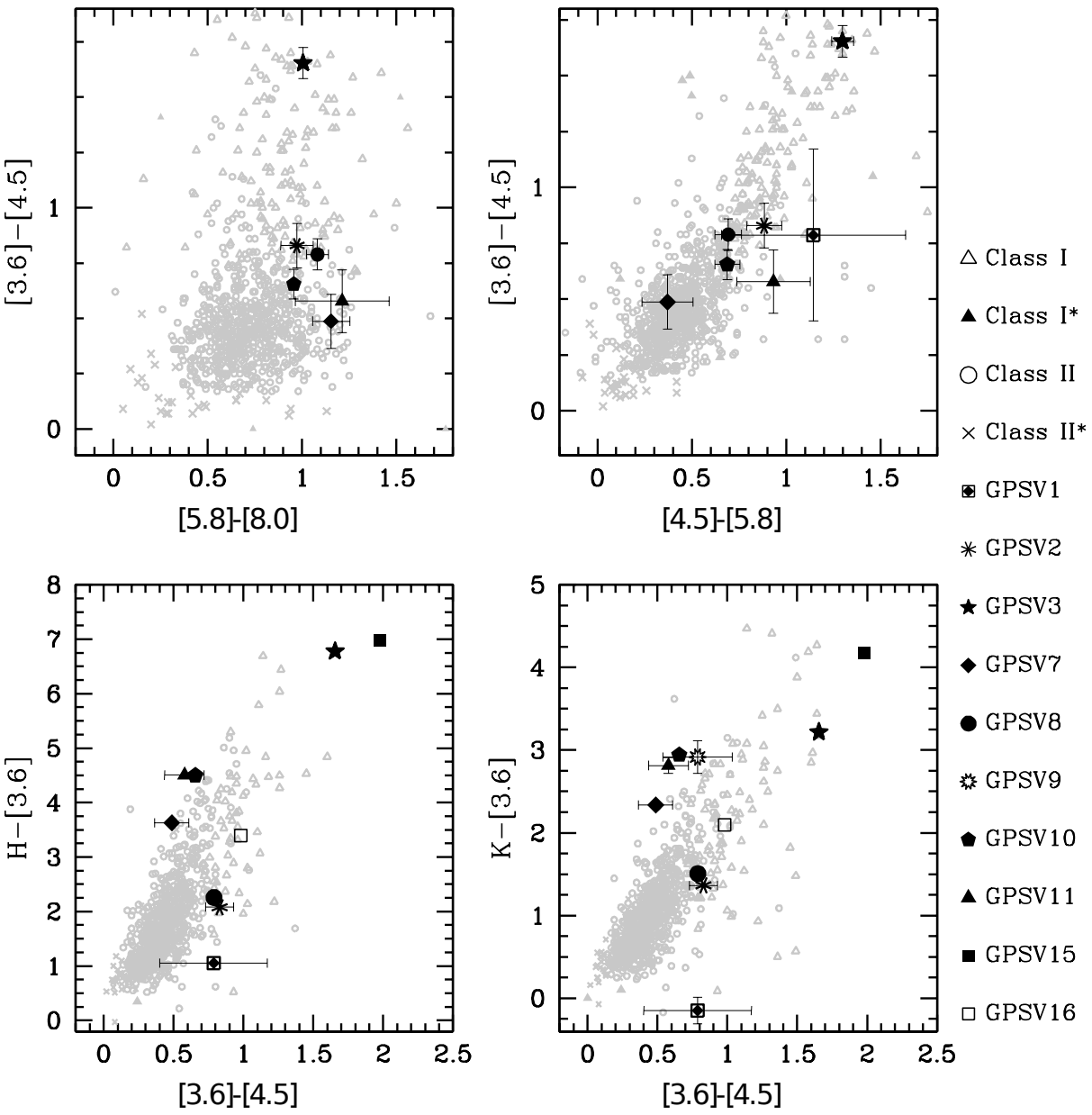

Figure 4.8: Colour-colour diagrams of GPS candidates based on *Spitzer* and UKIDSS photometry. Young stellar objects from Gutermuth et al. (2009) are shown for comparison. The latter are divided in: protostars with infalling envelopes (Class I, open triangles), pre-main-sequence stars with optically thick discs (Class II, open circles), deeply embedded sources (Class I*, filled triangles) and transition disc candidates (Class II*, crosses). Objects GPSV3 and GPSV15 are located in the Class I region of the two bottom graphs, however SEDs of the sources show a flatter distribution than expected for Class I objects (see Figure 4.10). Errors are plotted only for objects that present significant uncertainties on their measurements.

Dataset	IPHAS/VPHAS+			DENIS			2MASS			GPS				VLT/ISAAC			UKIRT		Spitzer/IRAC				WISE				MSX6C			Akari	
filter	r′	i′	Hα	I	J	K_s	J	H	K_s	J^a	H^a	K_1^a	K_2^b	J	H	K_s	K	[2.12]	[3.6]	[4.5]	[5.8]	[8.0]	[3.4]	[4.6]	[12]	[22]	[8.28]	[12.13]	[14.65]	[9.0]	[18.0]
	(mag)	(mag)	(mag)	(mag)	(mag)	(mag)	(mag)	(mag)	(mag)	(mag)	(mag)	(mag)	(mag)	(mag)	(mag)	(mag)	(mag)	(mag)	(mag)	(mag)	(mag)	(mag)	(mag)	(mag)	(mag)	(mag)	(mag)	(mag)	(mag)	(mag)	(mag)
5σ Limit	*21.8*	*21*	*20.8*	*18.5*	*16.5*	*14.5*	*17*	*16.3*	*15.5*	*19.8*	*19*	*18.1*	*18.1*	*21*	*19.9*	*19.5*	*17.3*	*17.4*	*15.4*	*14.9*	*13.6*	*13*	*16.6*	*15.6*	*11.3*	*8.0*	*6.9*	*3.5*	*3.3*	*7.4*	*4.2*
GPSV1	*nd*	*nd*	*nd*	*nd*	*nd*	*nd*	*nd*	*nd*	*nd*	17.83	16.32	15.11	18.86:	17.98	16.49	15.38	*nc*	*nc*	15.26:	14.47:	13.33:	*nd*	*nd*	*nd*	*nd*	*nd*	*nd*	*nd*	*nd*	*nd*	*nd*
	–	–	–	–	–	–	–	–	–	(0.04)	(0.02)	(0.02)	(0.55)	(0.05)	(0.03)	(0.04)	–	–	(0.16)	(0.35)	(0.34)	–	–	–	–	–	–	–	–	–	–
GPSV2	20.92:	19.06	20.04:	18.14	16.06	13.98	15.72	14.59	13.96	16.43	15.19	14.47	16.41	17.79	16.06	15.08	14.30	14.28	13.11	12.28	11.40	10.42	13.61	11.53	7.92	6.00:	*nd*	*nd*	*nd*	*nd*	*nd*
	(0.10)	(0.04)	(0.12)	(0.18)	(0.24)	(0.22)	(0.08)	(0.07)	(0.06)	(0.02)	(0.02)	(0.02)	(0.06)	(0.05)	(0.03)	(0.04)	(0.02)	(0.02)	(0.08)	(0.06)	(0.07)	(0.05)	(0.07)	(0.04)	(0.05)	(0.18)	–	–	–	–	–
GPSV3	*nd*	*nd*	*nd*	*nd*	*nd*	12.28	>16.62	>16.39	13.28	*nd*	16.03	12.47	13.75	*nd*	17.24	13.81	12.09	12.51	9.25	7.60	6.30	5.30	9.27	7.02	4.44	3.29:	4.32	3.43:	3.39:	4.77	3.39
	–	–	–	–	–	(0.13)	–	–	(0.04)	–	(0.02)	(0.02)	(0.02)	–	(0.04)	(0.05)	(0.02)	(0.02)	(0.05)	(0.05)	(0.03)	(0.03)	(0.03)	(0.02)	(0.04)	(0.16)	(0.11)	(0.18)	(0.20)	(0.47)	(0.11)
GPSV4	*nd*	*nd*	*nd*	*nd*	*nd*	*nd*	*nd*	*nd*	*nd*	17.54	16.48	15.53	16.60	17.80	16.87	16.26	16.42	16.42	*nd*	*nd*	*nd*	*nd*	*nd*	*nd*	*nd*	*nd*	*nd*	*nd*	*nd*	*nd*	*nd*
	–	–	–	–	–	–	–	–	–	(0.04)	(0.03)	(0.02)	(0.07)	(0.06)	(0.04)	(0.06)	(0.02)	(0.04)	–	–	–	–	–	–	–	–	–	–	–	–	–
GPSV5	*nd*	*nd*	*nd*	*nd*	*nd*	*nd*	*nd*	*nd*	*nd*	17.61	16.30	15.53	16.58	18.19	16.85	15.97	15.55	15.62	*nd*	*nd*	*nd*	*nd*	*nd*	*nd*	*nd*	*nd*	*nd*	*nd*	*nd*	*nd*	*nd*
	–	–	–	–	–	–	–	–	–	(0.03)	(0.02)	(0.03)	(0.07)	(0.05)	(0.04)	(0.05)	(0.02)	(0.02)	–	–	–	–	–	–	–	–	–	–	–	–	–
GPSV6	*nd*	*nd*	*nd*	*nd*	*nd*	*nd*	*nd*	*nd*	*nd*	18.25	17.04	16.37	15.36	17.98	16.89	16.18	15.77	15.80	*nd*	*nd*	*nd*	*nd*	*nd*	*nd*	*nd*	*nd*	*nd*	*nd*	*nd*	*nd*	*nd*
	–	–	–	–	–	–	–	–	–	(0.07)	(0.04)	(0.05)	(0.03)	(0.04)	(0.03)	(0.04)	(0.02)	(0.02)	–	–	–	–	–	–	–	–	–	–	–	–	–
GPSV7	*nd*	*nd*	*nd*	*nd*	*nd*	*nd*	*nd*	*nd*	*nd*	16.86	15.44	14.15	13.15	16.53	15.00	13.82	13.30	13.48	11.82	11.33	10.96	9.80	11.20	10.71	8.42	>5.20	*nd*	*nd*	*nd*	*nd*	*nd*
	–	–	–	–	–	–	–	–	–	(0.02)	(0.02)	(0.02)	(0.02)	(0.04)	(0.03)	(0.04)	(0.02)	(0.02)	(0.07)	(0.10)	(0.09)	(0.04)	(0.03)	(0.03)	(0.08)		–	–	–	–	–
GPSV8	19.85	18.16	18.85	16.70	14.29	12.03	14.59	13.12	12.11	14.72	13.54	12.79	11.72	14.71	13.53	12.89	12.88	12.96	11.28	10.49	9.80	8.72	12.06	11.08	7.87	5.62:	*nd*	*nd*	*nd*	*nd*	*nd*
	(0.04)	(0.02)	(0.04)	(0.11)	(0.11)	(0.10)	(0.04)	(0.03)	(0.03)	(0.02)	(0.02)	(0.02)	(0.02)	(0.04)	(0.03)	(0.04)	(0.02)	(0.02)	(0.05)	(0.05)	(0.05)	(0.03)	(0.04)	(0.03)	(0.06)	(0.47)	–	–	–	–	–
GPSV9	*nd*	*nd*	*nd*	*nd*	*nd*	*nd*	*nd*	*nd*	*nd*	*nd*	*nd*	16.43	15.28	*nd*	*nd*	16.19	15.77	16.08	13.52:	12.73:	*nd*	*nd*	*nd*	*nd*	*nd*	*nd*	*nd*	*nd*	*nd*	*nd*	*nd*
	–	–	–	–	–	–	–	–	–	–	–	(0.05)	(0.02)	–	–	(0.05)	(0.02)	(0.03)	(0.19)	(0.16)	–	–	–	–	–	–	–	–	–	–	–
GPSV10	*nd*	*nd*	*nd*	*nd*	*nd*	13.04	>16.56	14.60	13.10	17.36	15.55	13.99	12.71	17.15	15.39	14.01	14.21	14.36	11.05	10.40	9.71	8.75	12.16	10.78	8.52	4.16	*nd*	*nd*	*nd*	*nd*	*nd*
	–	–	–	–	–	(0.16)	–	(0.08)	(0.05)	(0.03)	(0.02)	(0.02)	(0.02)	(0.04)	(0.03)	(0.04)	(0.02)	(0.02)	(0.03)	(0.06)	(0.03)	(0.03)	(0.04)	(0.03)	(0.10)	(0.08)	–	–	–	–	–
GPSV11	*nd*	*nd*	*nd*	*nd*	16.06	*nd*	16.05	14.80	14.39	19.38:	17.53	15.84	14.49	20.28:	18.31:	16.99	14.37	14.40	13.02	12.45	11.51:	10.30:	*nd*	*nd*	*nd*	*nd*	*nd*	*nd*	*nd*	*nd*	*nd*
	–	–	–	–	(0.24)	–	(0.13)	(0.13)	(0.13)	(0.18)	(0.06)	(0.03)	(0.02)	(0.2)	(0.12)	(0.08)	(0.02)	(0.02)	(0.09)	(0.11)	(0.16)	(0.19)	(0.08)	(0.06)	(0.15)	–	–	–	–	–	–
GPSV12	*nc*	*nc*	*nc*	*nd*	*nd*	*nd*	16.26:	>16.75	>16.36	16.55	15.93	15.77	16.87	16.32	15.77	15.58	*nc*	*nc*	*nc*	*nc*	*nc*	*nc*	*nd*	*nd*	*nd*	*nd*	*nd*	*nd*	*nd*	*nd*	*nd*
	–	–	–	–	–	–	(0.12)	–	–	(0.02)	(0.02)	(0.03)	(0.08)	(0.04)	(0.03)	(0.04)	–	–	–	–	–	–	–	–	–	–	–	–	–	–	–
GPSV13	13.98	13.38	13.45	*nc*	*nc*	*nc*	12.46	12.13	11.90	13.21	13.06	12.92	11.90	13.33	13.21	13.12	*nc*	*nc*	*nc*	*nc*	*nc*	*nc*	13.23	13.29	>12.30	>8.66	*nd*	*nd*	*nd*	*nd*	*nd*
	(0.02)	(0.02)	(0.02)	–	–	–	(0.02)	(0.02)	(0.02)	(0.02)	(0.02)	(0.02)	(0.02)	(0.03)	(0.02)	(0.04)	–	–	–	–	–	–	(0.03)	(0.04)	–	–	–	–	–	–	–
GPSV14	*nd*	*nd*	*nd*	*nc*	*nc*	*nc*	*nd*	*nd*	*nd*	16.88	16.23	15.99	18.07:	*nc*	*nc*	*nc*	*nc*	*nc*	*nc*	*nc*	*nc*	*nc*	*nd*	*nd*	*nd*	*nd*	*nd*	*nd*	*nd*	*nd*	*nd*
	–	–	–	–	–	–	–	–	–	(0.02)	(0.02)	(0.03)	(0.23)	–	–	–	–	–	–	–	–	–	–	–	–	–	–	–	–	–	–
GPSV15	*nd*	*nd*	*nd*	*nc*	*nc*	*nc*	>17.21	14.50	11.61	17.45	14.14	11.21	12.24	18.29	15.39	12.59	*nc*	*nc*	*nc*	*nc*	*nc*	*nc*	8.41	6.43	3.72	2.51	4.07	2.87:	2.95:	4.07	2.67
	–	–	–	–	–	–	–	(0.04)	(0.02)	(0.02)	(0.02)	(0.02)	(0.02)	(0.04)	(0.02)	(0.03)	–	–	–	–	–	–	(0.02)	(0.02)	(0.02)	(0.02)	(0.11)	(0.17)	(0.20)	(0.25)	(0.21)
GPSV16	*nd*	*nd*	*nd*	*nc*	*nc*	*nc*	*nd*	*nd*	*nd*	16.66	14.93	13.46	15.67	16.90	15.12	13.83	*nc*	*nc*	11.73	10.75	*nc*	*nc*	12.20	10.80	7.97	5.25	*nd*	*nd*	*nd*	*nd*	*nd*
	–	–	–	–	–	–	–	–	–	(0.02)	(0.02)	(0.02)	(0.03)	(0.07)	(0.04)	(0.04)	–	–	(0.03)	(0.03)	–	–	(0.03)	(0.02)	(0.03)	(0.04)	–	–	–	–	–
GPSV17	*nc*	*nc*	*nc*	*nd*	*nd*	*nd*	*nd*	*nd*	*nd*	18.14	17.88	17.78:	15.43	*nc*	*nc*	*nc*	*nc*	*nc*	*nc*	*nc*	*nc*	*nc*	*nd*	*nd*	*nd*	*nd*	*nd*	*nd*	*nd*	*nd*	*nd*
	–	–	–	–	–	–	–	–	–	(0.05)	(0.08)	(0.16)	(0.02)	–	–	–	–	–	–	–	–	–	–	–	–	–	–	–	–	–	–

a 2008 observations.

b 2005 observations.

nc Not covered in the observations.

nd Not detected in the observations.

> The values represent upper limits.

: Represent uncertain values in the photometry as explained in the text.

Table 4.2: Photometric measurements for DR5 objects.

4.3.2 Robitaille et al. SED fits

Spectral energy distributions are constructed with the help of data from public surveys.

Fits to stars in Table 4.3 were performed with the SED fitting tool of Robitaille et al. (2007). The latter uses 1000000 YSO model SEDs, which are a computed from 20000 sets of physical parameters at 10 viewing angles and 50 aperture sizes from 100 to 10000 AU. The model SEDs are obtained in Robitaille et al. (2006) where the parameters from the models span ranges determined from observations and theory. These parameters can be divided in three categories

- *Central source parameters* which are the stellar mass, radius and temperature.
- *Infalling envelope parameters* the envelope accretion rate, outer radius, inner radius, cavity opening angle and cavity density.
- *Disc parameters* the disc mass, outer radius, inner radius, flaring power and scale height.

In addition a parameter describing the ambient density surrounding the YSO is also included.

Robitaille et al. (2006) first determines the stellar mass, M_*, from a distribution covering the range between 0.1 and 50 $M_\odot$ and the stellar age, t_*, sampling between 10^3 and 10^7 yr. For each M_* and t_*, the stellar radius R_* and temperature T_* are found from interpolating PMS evolutionary tracks. The parameters for the envelope and the disc are sampled randomly between ranges that depend on the evolutionary stage of the YSO. For example the envelope accretion rate is sampled from a $\dot{M}_{env}/M_*$ function that is constant and 2 orders of magnitude wide for $t_* < 10^4$ yr (where the average value is chosen to match the observed value for low- and high-mass YSOs), decreases for ages between 10^5 and 10^6 yr and goes to zero at 10^6 yr. The disc mass is sampled between $M_{disc}/M_* = 0.001$ and 0.1 at early evolutionary stages and between 10^{-8} and 0.1 for later stages. The SED fitting tool compares the observed SED of the source to be analysed to the grid of models described above, using a range of distances d and visual extinctions A_V which are provided by the user. The fitting tool returns the best fit d, A_V and the χ^2 for each SED model in the grid.

The Robitaille et al. models cover a large range in parameter space. The authors study how well the parameters of well-studied YSOs can be constrained by the SED fitting when using different combinations of data points. They show that when using only JHK and IRAC data, a large number of SEDs are able to fit the data, but disc and envelope parameters cannot be properly constrained, showing that these data points alone cannot be used to estimate the evolutionary stage of the YSO. A good constraint on the parameters is only found when using a large range in wavelength from optical to submillimetre data.

The results from the fitting procedure for different objects arising from the GPS and VVV analysis are presented throughout this thesis. However, we do not try to estimate evolutionary stages or values for different parameters of the variable stars in our study since in most cases we do not have information at wavelengths larger than $\sim 24\mu$m. These results are used just as a measure of how well our objects can be fitted to YSO models. Also, we note that in most cases the available near- and mid-infrared data are not contemporaneous observations, so the

fits could be unreliable due to the variability of our objects. In addition we are not certain whether Robitaille et al. models can accurately describe highly variable YSOs, since their discs may have an unusual structure.

In order to perform the fits we did not include every available data point, and in general we only used the information arising from UKIDSS JHK_1, *Spitzer* $I1 - I4$ and *WISE* $22\mu m$. The distances are set to vary between 1-5 kpc and A_v within 0-30 mag. We note that varying the distances in the given range instead of using the known distances for the Serpens objects or GPSV16, had a negligible effect on the measured parameters, i.e. the change in the values were never larger than their estimated errors. The weighted mean values and standard deviation of the parameters (in logarithmic scale) shown in Table 4.3 were determined using the models for which $\chi^2 - \chi^2_{best} < 3N$ (as suggested in Robitaille et al. 2007), where χ^2_{best} is the χ^2 of the best-fitting model and N represents the number of data points used in the fitting process. The last column of Table 4.3 shows the number of models that fulfilled this condition for each of the objects in our sample. The discussion on the results of the fits can be found in the analysis of the individual objects presented below.

4.3.3 Eruptive Variables

Given the faintness of many of our objects, the low resolution VLT/ISAAC spectra were of insufficient quality to clearly detect characteristics of eruptive variables. The subsequent Gemini/NIFS and Magellan/FIRE spectroscopy included only relatively bright sources whose ISAAC spectra suggested a possible eruptive variable classification. The following analysis is then divided between stars where spectral characteristics of eruptive variables could be found and those for which there is only non-spectroscopic evidence for a YSO or eruptive PMS variable classification.

Four stars are defined as likely to be eruptive variables. These correspond to GPSV3, GPSV15, GPSV8 and GPSV16.

GPSV3 and GPSV15

These two objects are the reddest stars in our DR5 sample (see Fig. 4.2), with GPSV3 in fact not being detected in J band in any of the near-infrared surveys nor in our ISAAC imaging. Both stars also show a large (H-K) excess in colour-colour diagrams (Fig. 4.3), beyond what is observed for Classical T Tauri stars and in agreement with what is expected for deeply embedded Class I YSOs. The colours are also similar to those of the deeply embedded FUor-like objects PP13S and AR6B (Aspin & Sandell 2001; Aspin & Reipurth 2003), and the deeply embedded outburst sources OO Ser and GM Cha (Hodapp et al. 1996; Persi et al. 2007). The K band light curves of both objects show similar behaviour, with repetitive increases in magnitude (Fig. 4.10).

Their ISAAC spectra (Fig. 4.11) also show a remarkable resemblance, where we observe a featureless continuum that rises steeply toward longer wavelengths. This is similar to the aforementioned embedded object OO Ser, and not too dissimilar to PP13S and AR6B, which

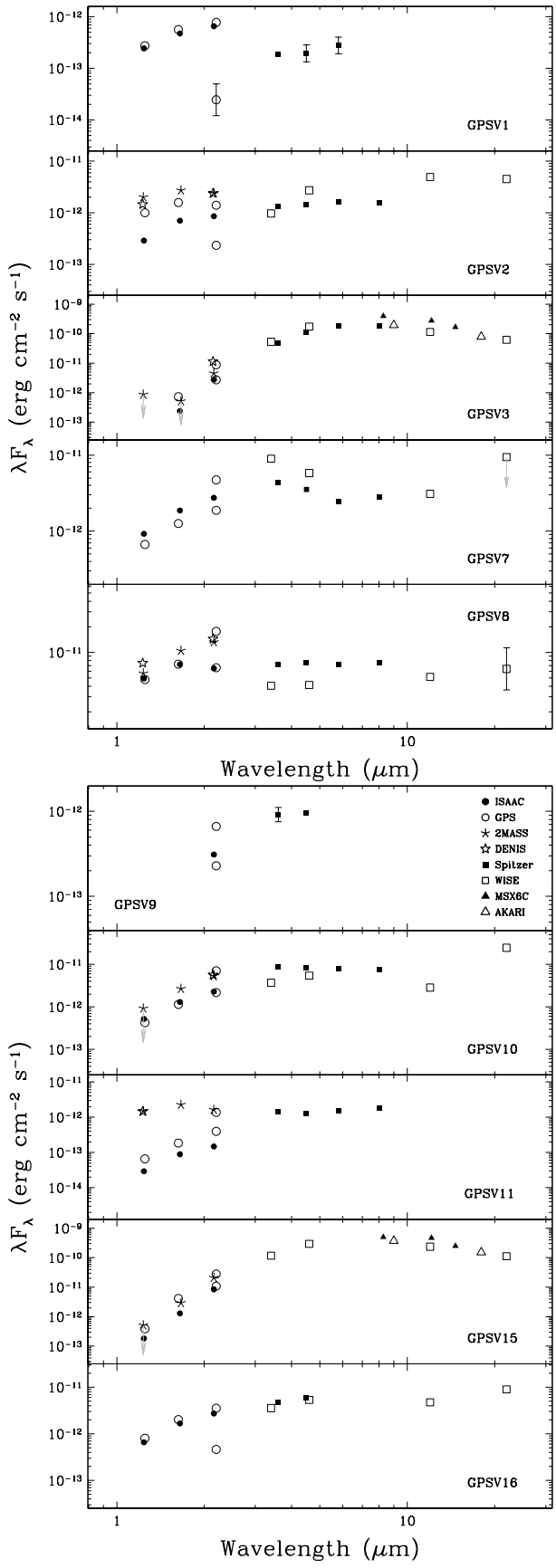

Figure 4.9: Spectral energy distributions of 10 out of 13 DR5 objects within star forming regions. Errors are plotted only for objects that present significant uncertainties on their measurements.

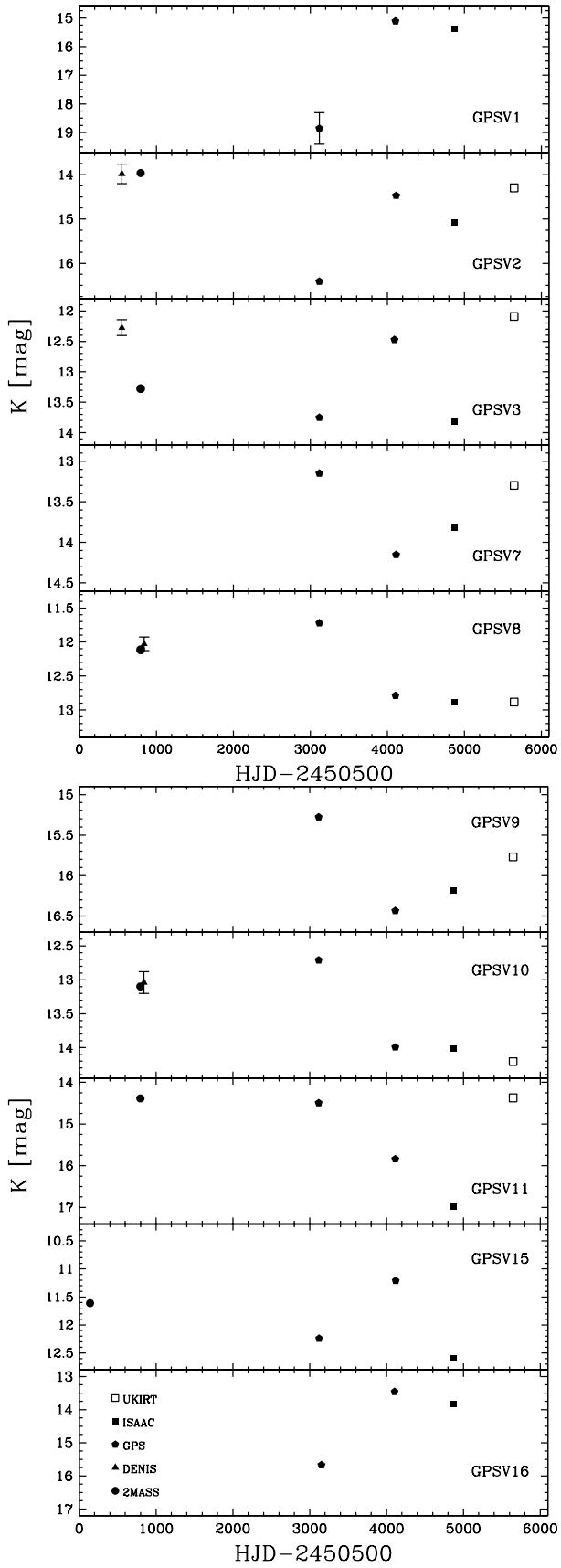

Figure 4.10: K-band light curves for the same DR5 objects in figure 4.9, where errors are plotted only for objects that present significant uncertainties on their measurements.

Table 4.3: Parameters derived from the Robitaille et al. models SED fitting as explained in the text. The standard deviations are shown in brackets and they are often large.

Object	$\log M_*$ ($M_\odot$)	$\log \dot{M}_{disc}$ ($M_\odot$ yr^{-1})	$\log \dot{M}_{env}$ ($M_\odot$ yr^{-1})	$\log L_{tot}$ ($L_\odot$)	χ^2_{best}/N_{data}	N_{fits}
GPSV1	0.06[0.43]	-7.62[1.32]	-3.80[1.05]	1.17[0.75]	0.07	2187
GPSV2	-0.23[0.44]	-7.91[1.50]	-4.95[0.61]	0.74[0.53]	0.20	333
GPSV3	0.79[0.17]	-8.54[1.83]	-0.13[0.82]	3.00[0.56]	1.64	473
GPSV7	0.21[0.43]	-8.99[1.93]	-1.12[1.95]	1.42[0.62]	0.12	1829
GPSV8	0.35[0.26]	-8.54[1.60]	-2.40[2.41]	1.46[0.46]	0.14	518
GPSV10	-0.01[0.52]	-7.02[1.25]	-4.44[0.93]	1.26[0.64]	0.67	237
GPSV11	-0.01[0.45]	-7.81[1.54]	-3.70[1.33]	1.15[0.60]	0.48	1073
GPSV15	0.92[0.14]	-9.56[1.53]	0	3.49[0.47]	0.86	94
GPSV16	0.07[0.53]	-7.82[1.83]	-4.38[1.35]	1.26[0.69]	0.57	349

differ only in that they show a strong v=2-0 CO absorption trough in the 2.3 μm region (see Fig. 5 in Hodapp et al. 1996). The same steep rise is observed in the FIRE spectra of the sources, where GPSV15 is detected in H band but with no sign of the H_2O absorption that is observed in a number of FUor and FUor-like stars.

NIFS higher resolution spectra reveal a more complicated structure in the CO region. The spectra of the objects only show clearly the $v = 2 - 0$ bandhead (stronger in GPSV15) with strong absorption that can be identified with the low J-lines of the P and R branches of the $v = 2 - 0$ transition. The weakness of the bandheads, relative to the lower J transitions, indicates that we are observing gas that is somewhat cooler than is typical of M-type stellar atmospheres, so that only the lower energy levels are populated. Moreover, the spectra in figure 4.11 strongly indicate that the photosphere is obscured from view and that the K band spectra are dominated by circumstellar matter. This is seen especially in the Magellan/FIRE spectra (upper right panel of Fig. 4.11), with a lack of flux at wavelengths shorter than $\sim 1.5\mu m$ (where the stellar component would be expected to contribute to the observed flux of the system) and steeply rising flux at longer wavelengths, in agreement with where a disc following a T $\leq$ 1200 K blackbody distribution is expected to begin contributing to the system.

We removed the slope of the higher resolution spectra by fitting a straight line to the 2.18-2.28 μm region and extrapolating towards the CO region. The results are shown in Fig. 4.12. In GPSV15 we see numerous features rising above the normalised continuum level in between the CO absorption lines. This could be due to emission from the rapidly rotating hot portion of the inner disc, which would show as the wings of rotationally broadened emission lines in between the stronger but narrower absorption lines. Rotation velocities would be of the order of 200 km/s within a few stellar radii of a low mass YSO, which is slightly higher than the NIFS velocity resolution of 60 km/s. Since features in excess of the continuum are not observed in between every pair of adjacent CO absorption lines we cannot be certain of this interpretation. However, the wavelengths where we see no excess above the continuum are mostly located close

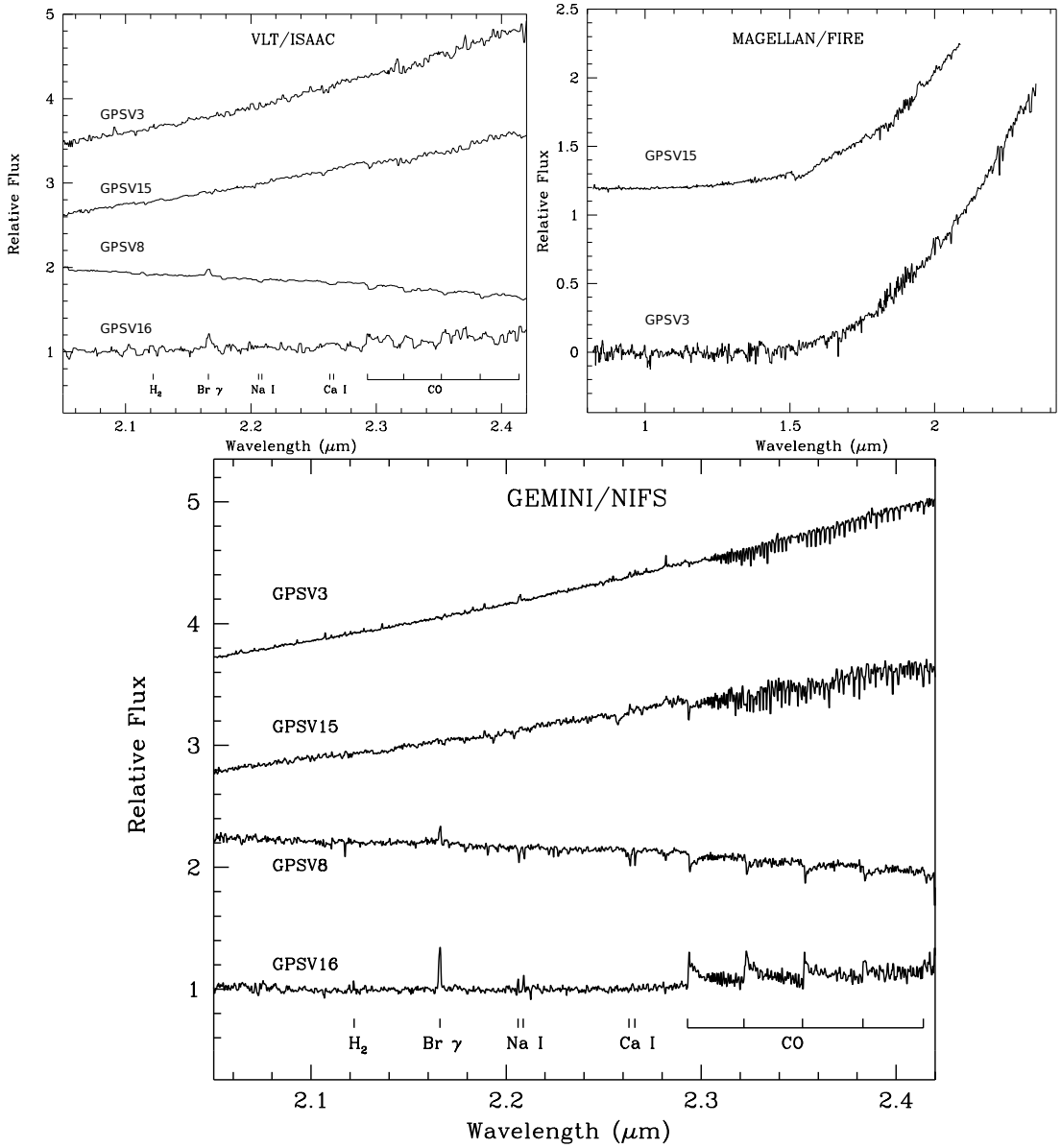

Figure 4.11: 2.2 μm ISAAC (top left) and NIFS (bottom) spectra for the four likely eruptive PMS variables. Spectral features usually found for these type of variable stars are shown in the bottom of each of the plots. It is readily apparent that the R=5000 NIFS spectra reveal far more information than the R=700 ISAAC spectra.(top right) FIRE 0.8-2.5 μm spectra of red sources GPSV3 and GPSV15.

to one of the higher order bandheads (3-1, 4-2 and 5-3) where the close proximity of numerous CO absorption lines disfavours observation of weak rotationally broadened emission features, at this spectral resolution. Observations at higher spectral resolution are therefore desirable in order to resolve the profile of rotationally broadened lines from the disc and verify their existence.

The presence of any such features in GPSV3 is marginal and strongly dependent on the choice of wavelengths used for the removal of the slope of the continuum. However, several emission lines are observed in the high resolution spectrum of GPSV3 (see fig. 4.12, right panel). These lines can be identified with atomic features observed in the photospheric absorption spectra of K-M dwarf stars (see e.g., Wallace & Hinkle 1997). Specifically we detect lines of Mg I, Na I, Ca I, Fe I, Si I, Al I, and perhaps S I and C I, most of which have rarely been reported in emission. A temperature inversion is required to observe lines in emission, which could occur in a hot disc or wind near the star, making these features of circumstellar origin. One of the strongest lines is observed at $\sim$ 2.28 μm (also observed in GPSV15, see fig. 4.12), this is identified as the $4d^3D_{3,2,1} - 6f^3F^{\circ}_{2,3,4}$ transition of Mg I (Kleinmann & Hall 1986). Emission at this wavelength has also been observed in a sample of embedded protostars by Davis et al. (2011) but the authors mark this feature as unknown in their analysis. Evidence for the presence of a hot inner disc in GPSV3 is given by the observed emission of the Na I doublet revealed in the NIFS spectra. This characteristic is observed in EXors when in outburst phase and is explained as arising from a hot inner disc (see e.g., Lorenzetti et al. 2012). However, it is unclear whether we are observing emission arising from a hot inner disc, wind or a combination of both.

In the case of GPSV15, blueshifted absorption of $\sim$ 40 km s^{-1} is observed in the CO bandhead and individual lines. Blueshifted CO absorption has been observed previously in the FU Ori objects V1057 Cyg (Hartmann, Hinkle, & Calvet 2004) and AR6A (Aspin & Reipurth 2003). In the latter, it was suggested that the blueshift might be caused by rotational broadening, as described by Najita et al. (1996a), but this was unclear. In V1057 Cyg, the observed (50 km s^{-1}) blueshifted absorption was interpreted by Hartmann et al. (2004) as arising from an ejected dense and low temperature shell (T$\sim$ 620 K). We note that the 40 km s^{-1} blueshift seen in GPSV15 is too small to significantly affect our discussion concerning the presence of rotationally broadened emission features in between the absorption features.

In summary, the observed CO structure of GPSV15 could be explained by an emission component from an inner disc, combined with absorption by a cooler gas arising in an ejected shell. It is also conceivable that cooler parts of the disc at larger radii are contributing to the absorption (which could also be the case in GPSV3). However, the presence of both emission and absorption components in an individual object is more readily understood in terms of two separate structures.

The SEDs of GPSV3 and GPSV15 are exceptionally red in the 1 to 5 μm region, with J-W2$>$11 mag. This is consistent with a Class I YSO classification but at longer wavelengths their SEDs become roughly flat (from $\sim$5-12 μm) and then decline towards 23 μm, as measured by *Akari* and WISE. The SED flattening and lack of cold dust emission is consistent with an

accretion disc.

We find that for GPSV15, only a relatively small number of models could be used to estimate the values of the parameters in Table 4.3. In addition the χ^2 per data point for the best-fitting model of GPSV3 was found to be larger than the derived values for the remaining objects. Thus, the parameters derived by the fits for GPSV3 and GPSV15, shown in Table 4.3 can be considered as highly unreliable. However the Robitaille et al. fits support our impression from inspection of the SEDs that GPSV3 and GPSV15 are not systems with optically thick envelopes given the lack of emission of cold dust at longer wavelengths.

Even though both sources show clear YSO characteristics, the fact that GPSV15 is not associated with any star forming region raises the doubt that these stars could actually be highly reddened post-AGB stars, or OH/IR stars similar to those mentioned in Section 4.1. Using K band photometry and *Akari 9 μm* observations Ishihara et al. (2011) were able to determine mass loss rates and distances for carbon- and oxygen-rich AGB stars in the Galaxy. The [K]-[9] colours for both GPSV3 and GPSV15 would correspond to AGB stars with very large mass loss rates, as high as $10^{-4.1}$ $M_{\odot}yr^{-1}$ according to Fig. A.2 in Ishihara et al. (2011). However, using these values and their observed fluxes at 9 μm in Eq. A.2 of Ishihara et al. (2011), yields distances larger than 25 kpc from the Sun, which at their Galactic latitude ($b \sim 2-3^{\circ}$) would put them 800 pc above the Galactic plane and well beyond the Galactic disc edge ($R \approx 14$ kpc, see e.g. Minniti et al. 2011), thus ruling out a post-AGB classification for both GPSV3 and GPSV15.

GPSV8 and GPSV16

K band photometry of GPSV8 shows that the star was brighter during 2MASS and GPS K_2 observations in 1999 and 2005 but faded by the epoch of GPS K_1 in 2008 and remained at that state during ISAAC and UKIRT observations in 2010 and 2012 (see Fig. 4.10). The fading is also apparent when comparing *Spitzer* $I1, I2$ ($\sim$ 2006) with *WISE* $W1, W2$ ($\sim$ 2010) photometry, where the difference of both $I1-W1$,$I2-W2$ are larger than the typical difference of $\sim$ 0.2 mag found for field stars with a similar magnitude to GPSV8. The ISAAC spectrum of GPSV8 (Fig. 4.11) shows strong Brγ emission along with CO absorption, with Na I and Ca I also in absorption. The same spectroscopic characteristics can be observed in the recent 2012 NIFS spectroscopic data. They are typical of EXor variables in the quiescent state (Lorenzetti et al. 2012) and consistent with the K band light curve.

GPSV8 is also detected in VPHAS+. Direct comparison of its $r^{'}-i^{'}, r^{'}-H\alpha$ colours places it in the Hα emitters region of Witham et al. (2008). We do note that their actual selection of Hα emitters depended on the magnitude of the source and field where it was located. The aforementioned colours also place it near the unreddened mid M star colours in Figure 6 of Drew et al. (2005). However this classification is not possible given its observed $g^{'}-r^{'}, r^{'}-i^{'}$ colours and the SED of the star does not agree with a mid M star classification. The r$^{'}$-Hα colour implies emission with maximum equivalent width of 40-50 Å, for the case of a heavily veiled YSO or object with a continuum that is free of TiO bands. With near-infrared Brγ emission

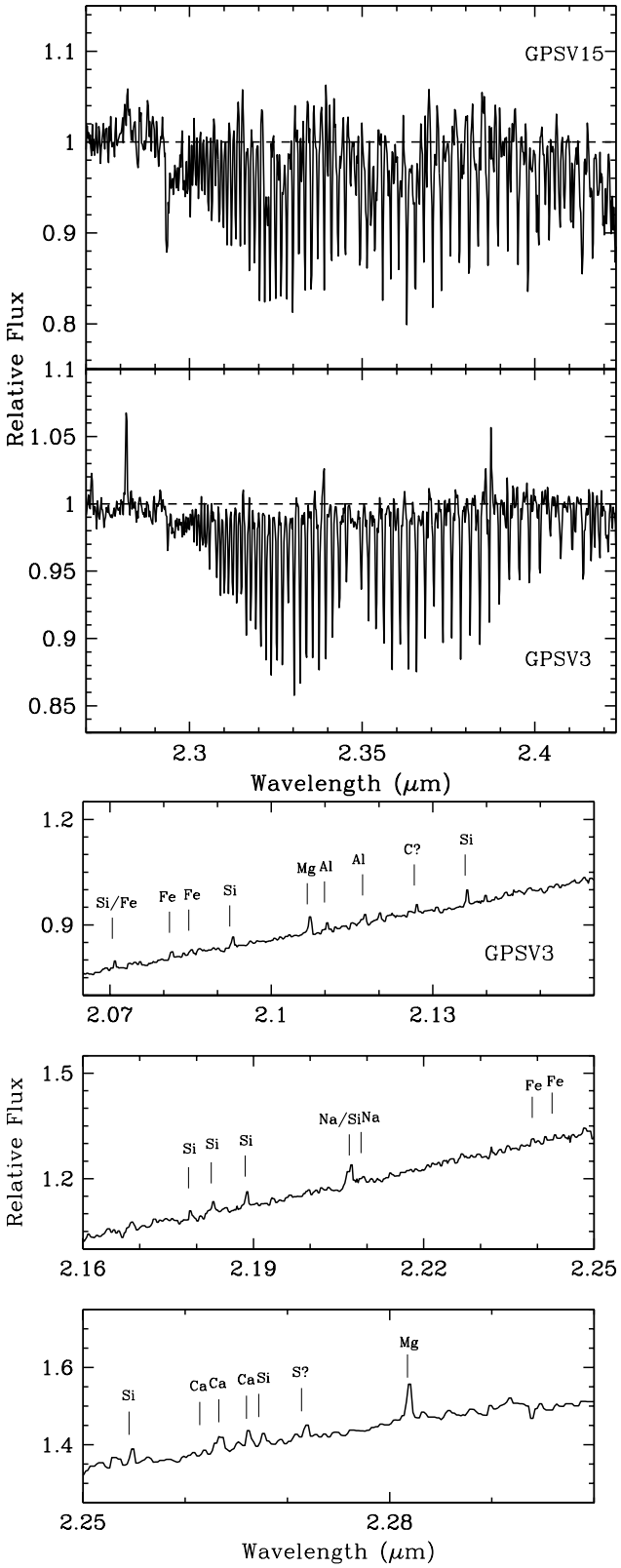

Figure 4.12: Continuum normalized spectra of GPSV3 (middle) and GPSV15 (top) showing the first overtone CO emission/absorption region. The continuum level is marked by a short-dashed line in both spectra. There is a clear emission feature at 2.28 μm that corresponds to a Mg I transition and is discussed in the text. (bottom) Atomic lines identified in the NIFS spectrum of GPSV3.

as well and a low mass Class II YSO fit with the Robitaille et al. models (see Table 4.3) an accreting YSO scenario for GPSV8 is well supported.

The light curve of GPSV16 (see Fig. 4.10) supports an outburst scenario with the star still close to maximum brightness at the moment of our ISAAC observations (2010). Further evidence to support this scenario is given by the fact that the object is not apparent in the 2MASS (1999) images. The ISAAC spectrum shows Brγ emission as well as CO in emission. These emission features are much more clearly seen in the 2012 NIFS spectrum of the source (Fig. 4.11). These are characteristics of an EXor variable in outburst. The fact that the spectrum of GPSV16 has not changed noticeably between the 2010 and 2012 observations suggests that the star was either at a bright state or been fortuitously observed during two separate outbursts.

The SED of GPSV16 shows a strong rise towards 2.2 μm and a flat distribution towards longer wavelengths, similar to what is observed in classical T Tauri stars (CTTS). Supporting a YSO scenario is the fact that the star is located at a projected distance of $\sim$ 170" from the star forming region G71.52-0.39 of the Avedisova (2002) catalog (see Figure 4.5), and although it is not conclusive this could be evidence for a possible association. SED fitting of GPSV16 with the tool of Robitaille et al. (2007) suggests a classification as low mass Class II YSOs (see Table 4.3).

4.3.4 Young stars in Serpens OB2

In addition to GPSV3 and GPSV8, the rest of GPSV1 to GPSV11 are also located in the Serpens OB2 region.

The SEDs of GPSV1, GPSV2, GPSV7, GPSV10 and GPSV11 are consistent with them being YSOs, rising until typically 3.6 μm and then showing flatter SEDs towards longer wavelengths. We note the cases of GPSV7 and GPSV10, which show a dip in their SEDs in the mid-infrared before rising towards 24μm. YSOs with this type of SED have been interpreted as having optically thin or evacuated inner holes and an optically thick edge at a radius of $\sim$10 AU (Hartmann et al. 2005). Alternatively, extinction of the hot inner parts of the disc by an edge-on system orientation can produce a similar effect. We note that the GLIMPSE3D catalogue photometry flags indicate that contamination from a nearby source may have affected the photometry of GPSV7. The same source is probably responsible for the non-detection in 2MASS and DENIS and may well have affected the WISE data.

From the aforementioned sources, only GPSV7 shows interesting spectral features in our low resolution ISAAC spectra, with CO absorption bandheads in the 2.3 μm region (Fig. 4.13) and no sign of Brγ emission. However, its peak-to-trough amplitude in K barely exceeds 1 magnitude, making its eruptive nature questionable.

GPSV1 and GPSV11 correspond to the most interesting cases. The magnitude of GPSV1 rose by 3.75 mag between the two epochs of GPS, then declined by 0.26 mag in our ISAAC photometry. The fact that the star is not visible in the 2MASS image provides some support for a possible recent outburst scenario. Unfortunately even at its brightest state the star is still faint for our ISAAC spectroscopic observations ($K \sim 15.4$ mag) and no characteristic features

for FUor/EXors could be identified from the spectrum of this object. However, the flat slope of the spectrum rules out a normal main sequence classification and, as noted above, the SED rises steeply towards 5.8 μm, consistent with a YSO interpretation. If the variability is due to a YSO outburst, the rate of decline between GPS $K1$ and ISAAC is $\sim$0.01 mag/month and the star would return to its pre-outburst magnitude (assuming the first epoch of UKIDSS GPS photometry as the pre-outburst state) in $\sim$ 30 yrs. This falls in the expected timescale for an FUor outburst (see e.g. Kóspál et al. 2011b).

GPSV11 shows similar magnitudes in both 2MASS (1999) and the first epoch of GPS (2005), followed by a strong decline towards the GPS K_1 (2008) and ISAAC (2010) epochs of $\sim$ 2.5 magnitudes. The recent UKIRT observations (2012) show that the object has returned to a magnitude level similar to that of 2MASS. The magnitude change in this source is probably not related to variable extinction along the line of sight (see below). It is unfortunate however that the spectrum, also dominated by noise, makes it impossible to observe any spectral characteristics that could clarify the nature of the object, however the observed slope in the spectrum of GPSV11 goes against a main sequence star classification which supports the YSO scenario for this star.

GPSV2 and GPSV10 are also highly variable objects with variations of 2.4 and 1.5 mag respectively. However, the variability of the former is more likely related to variable extinction in the line of sight (see below). Similar to GPSV8, GPSV2 is also detected in VPHAS+ and is located on the lower envelope of the Hα emitters distribution from Witham et al. (2008). The case for line emission is also marginal when comparing to Figure 6 in Drew et al. (2005). The $r^{'} - i^{'}$ and $r^{'} - H\alpha$ could be compatible with an unreddened mid-M star. The slope of the observed K band spectrum is incompatible with this scenario. The observed SED also goes against the mid M classification. Then the Hα equivalent width could be 30-40 Å if the underlying SED is free of TiO bands. This supports a YSO classification. The slope of the ISAAC spectrum and the SED of GPSV10 are inconsistent with a normal main sequence star and support the YSO classification.

GPSV9 is a very red (and faint) object. Its relatively low observed amplitude of 1.16 magnitudes makes an eruptive YSO classification questionable, similar to objects GPSV4, GPSV5 and GPSV6. However, the apparent spatial association of these objects with Serpens OB2, makes them likely YSOs. Spectra of the four candidates did not help in the classification of these objects.

4.4 Discussion

4.4.1 Physical Mechanisms

We note that for two of the objects discussed as probable eruptive variables above, GPSV8 and GPSV15, peak-to-trough K-band amplitudes do not exceed $\sim$1.5 mag, bringing some conflict with one of the main characteristics used to define eruptive variables, which is an increase of

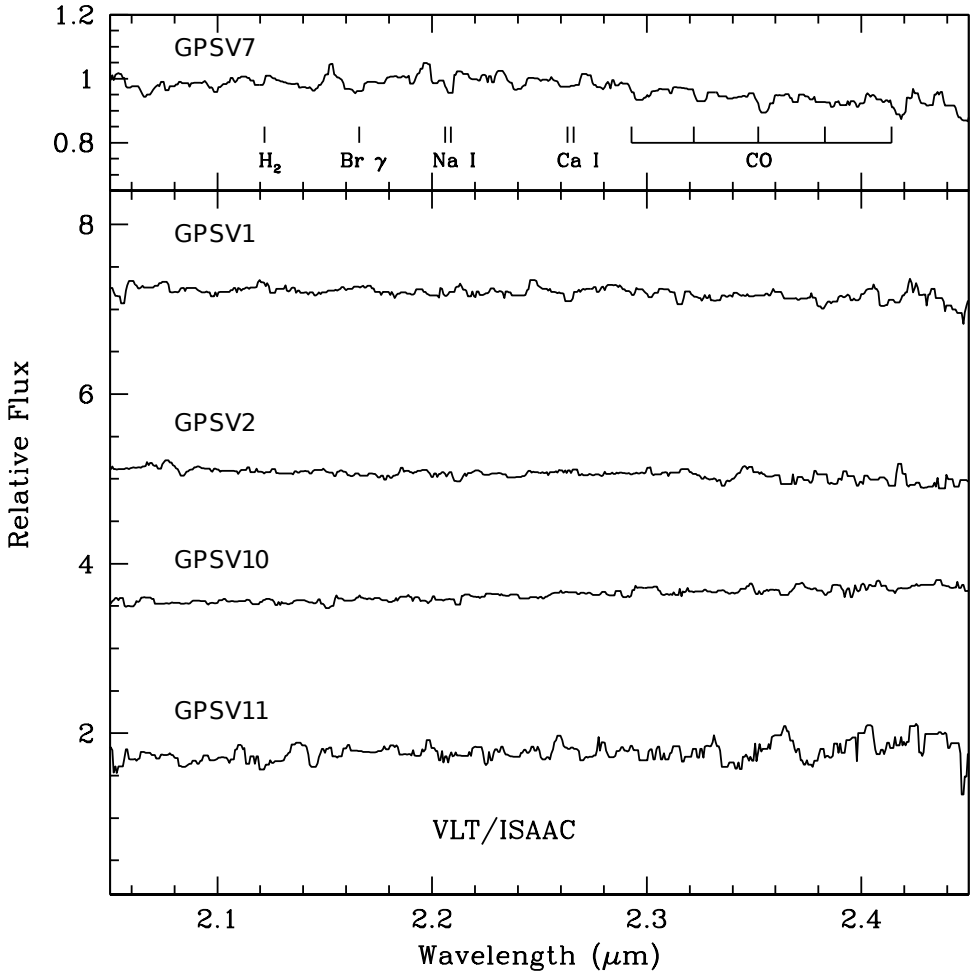

Figure 4.13: Spectra for stars discussed in Section 4.3.4. Spectral features usually found for eruptive variable stars are shown only for GPSV7, the only object where CO absorption bands can be identified. Spectra for the other four objects are dominated by noise.

brightness larger than at least ∼2 mag [2]. Although this is probably due to the incomplete coverage of the light curves, we want to discard other possible physical mechanisms that could be causing large variability.

Several physical mechanisms can explain the near-infrared variability observed in YSOs (see section 2.2). The fact that we use $\Delta K > 1$ mag to select our candidates already discards some of the mechanisms stated before. The changes in colour of the sources discussed above (Fig. 4.14) can provide further information on the nature of the objects; EXor variables for example are expected to have bluer colours as their magnitude increases. However, this is not observed in our sample. We note that due to the limited coverage we are not able to directly compare colours from quiescent and bright states. We can only discard variable extinction as a possible explanation because the stars do not move along the reddening vectors, except in the case of GPSV2.

Carpenter et al. (2001) find 1235 variable stars in their study of the Orion molecular cloud. Visual inspection of their light curves yields 20 variables with K peak-to-trough amplitudes > 1 mag. The variability of most of these stars is of the order of days and is likely to be explained by the physical processes discussed above. However, a handful of stars present large variability (up to 1.7 mag) on longer timescales, driven by a few points in the light curves and resembling what one would expect to observe in eruptive variables. We note that Carpenter et al. (2001) do not claim to have observed any FU Ori type outbursts.

We want to determine the likelihood of detecting any of the 20 high-amplitude Carpenter et al. (2001) variables, by just observing two epochs and as a function of a defined amplitude cut. In order to do so, we selected two random points of the light curve of each star in the high amplitude Carpenter et al. (2001) sample, determine the magnitude difference between the two points and marked a detection if the difference was larger than the defined amplitude cut. The process was iterated a few thousand times. The likelihood of the detection of each star is then defined as the number of detections divided by the number of iterations. The sum of the expected detections over the 20 variables from the Carpenter et al. sample was multiplied by the ratio between the number of OB stars in Serpens OB2 and those within the region of Orion studied by Carpenter et al. (2001).

The described process yields the number of variable stars we would expect to have selected in Serpens OB2 as a function of the amplitude cut (see Fig. 4.15). Even though there are a number of caveats to this analysis, we find that for an amplitude cut of $\Delta K = 1$ mag, we should detect 7 variables, which is remarkably close to our actual number (11). At this amplitude cut, a large part of our sample would be formed by stars whose variability is explained by other processes than abrupt changes in the accretion rate. However, we observe that for $\Delta K > 1.1$ mag, the sample is mostly formed by stars that vary over longer timescales driven by a few points in their light curves (dotted line in Fig. 4.15), and thus more likely associated with accretion-related

[2]This is the limit usually found in the literature. We note that the original classification for these type of objects was done in the optical and amplitudes are usually smaller in the infrared. The K band amplitudes of the (new detections) EXor sample from Lorenzetti et al. (2012) (see their Table 1) show a limit of $\Delta K > 1.2$ mag, with the majority of the sample having $\Delta K > 1.95$ mag.

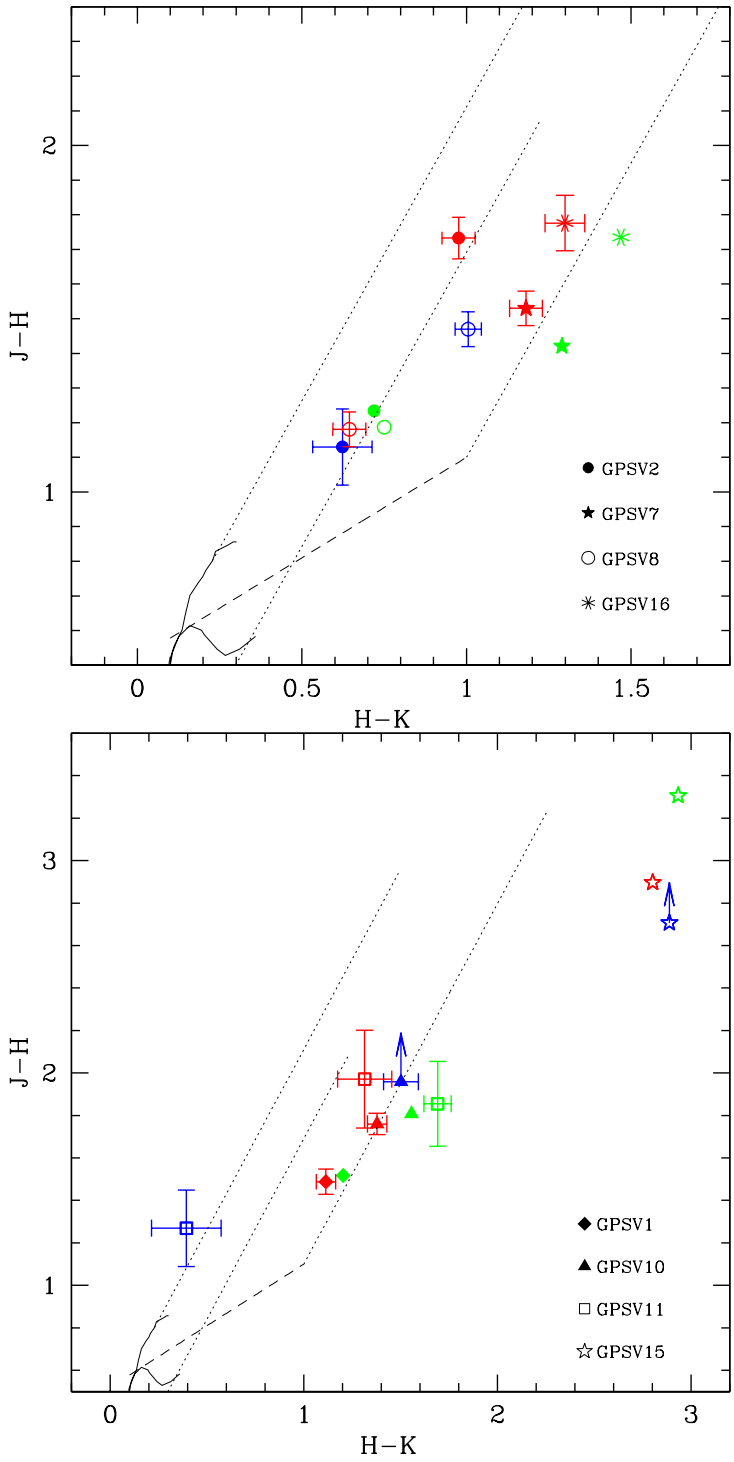

Figure 4.14: $J-H, H-K$ colour-colour plot comparing the 2MASS (blue), GPS (green) and ISAAC (red) colours for some of the objects in our sample. The errors are plotted only for objects that present significant uncertainties on their measurements.

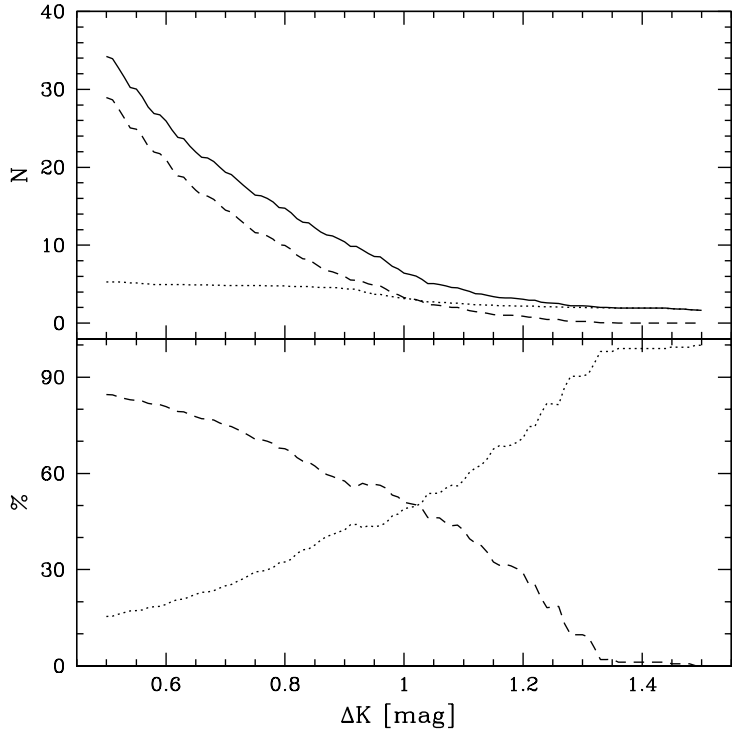

Figure 4.15: *top* Expected number of variable stars to be observed in Serpens OB2 as a function of amplitude (solid line). The results are also divided in stars with short-term variability (dashed line) and long-term variability (dotted line). (bottom) Percentage of detections as a function of ΔK comparing short-term variables (dashed line) with long-term and more likely to be accretion-related variables (dotted line).

variability. Even though our analysis uses sources in Serpens OB2, we can assume that the observed photometric changes in YSOs in our sample which present $\Delta K > 1.1$ mag are more likely related to this type of variability.

4.4.2 Molecular Hydrogen outflows

The visual inspection of the UKIRT $H_2 - K$ difference images reveals the presence of only one pair of bright H_2 molecular outflows in the area of Serpens covered by our study. We identify them as the previously discovered emission features MHO2201 and MHO2202, which are associated with the deeply embedded luminous YSO IRAS 18151-1208 (Varricatt et al. 2010). There is also widespread diffuse H_2 emission in parts of the region, but no other jet-like features that can be associated with a single star. This suggests that the observations were not deep enough to detect jets associated with low mass YSOs. No H_2 outflows could be observed near the eruptive variable candidates GPSV2 to GPSV11. Similarly, there is no sign of an outflow in the NIFS integral field data for the four objects spectroscopically verified as eruptive variables (GPSV3, GPSV8, GPSV15 and GPSV16).

Most FU Orionis objects are known to be associated with Herbig-Haro objects (Reipurth & Aspin 1997) and drive molecular outflows (Evans et al. 1994), whilst EXors generally do not show evidence of shocks as a major mechanism of excitation (Lorenzetti et al. 2009b). FU Orionis itself, although having massive winds, does not drive a molecular outflow (Evans et al. 1994) which could be explained by the lack of organization of magnetic fields required for jet launching and collimation in the binary scenario of Reipurth & Aspin (2004a) or by previous outflows having cleared up the remnant envelope evidencing the lack of swept up material which constitutes the molecular outflows (Evans et al. 1994).

From the objects associated with the deeply embedded subclass of eruptive YSOs, OO Ser is associated with faint H_2 shock fronts (Hodapp et al. 2012), corresponding to MHO 3245 in the catalog of Davis et al. (2010). GM Cha is the driving source of a CO outflow and shows a K band spectrum dominated by H_2 emission with several shocked H_2 emission knots observed along the CO flow (Persi et al. 2007). Finally, V2775 Ori is not associated with any outflows nor H_2 shock emission.

Given the limitation imposed by the sensitivity of the dataset and the fact that outflows are not ubiquitous in eruptive variable YSOs, the lack of observable H_2 emission near our somewhat more distant candidates is not a strong argument against their eruptive variable classification.

4.4.3 Eruptive variable classification

Although four stars in our sample show strong characteristics of eruptive variability, it is difficult to classify them as either of the two known classes of this kind of variables.

GPSV3 and GPSV15 show similar spectra to known deeply-embedded FUor-like objects and that of OO Ser. However, the amplitude and time-scale of the variation, with what appear to be repetitive outbursts, are not in line with the observed behaviour of OO Ser itself and the outbursting protostar [CFT93]216-2 (Caratti o Garatti et al. 2011). In fact, the photometric

behaviour of both candidates is similar to that observed for deeply embedded objects V371 Ser (Hodapp et al. 2012) and source 90 in the study from Varricatt, Davis, & Adamson (2005) of SFR 173.58+2.45. The latter has large infrared colours and it is the driving source of an H_2 molecular outflow. Its variability was first thought to be of the FU Orionis kind but this classification was discarded because of the shorter time scale of the variation. Varricatt et al. (2005) still conclude that its variability probably arises from variable accretion. V371 Ser is classified as a Class I object, also driving a H_2 molecular outflow. Its variability is periodic ($P = 543\ d$) and is thought to be explained by periodic variation of the accretion rate, modulated by the presence of a close companion (Hodapp et al. 2012). A binary companion in an elliptic orbit is a possible explanation for the FUor and EXor phenomena, given that some repetitive EXors have been seen (though not FUors). Hodapp et al. (2012) proposed that V371 Ser represents an extension of eruptive variability to shorter periods.

The spectrum and photometry of GPSV8 from 2010-2012 is consistent with an EXor during quiescent states. However, the star appears to have been at a bright state during 1998-2005 (although this conclusion is based on only two epochs of observations), if so the time-scale is inconsistent with EXor variables. The spectrum of GPSV16 shows strong emission lines (Brγ, CO) during 2010 and 2012 observations, which is usually observed in EXor variables during bright states. However, the photometric data of the object would point towards an FUor type outburst given the longer timescale of the variation.

A number of stars in which the observed eruptive variability is thought to be accretion related have shown characteristics that can be associated with both sub-classes of eruptive variables. e.g. V1647 Ori, V2775 Ori and OO Ser. These objects have been proposed to be intermediate objects between EXors and FUors or being the extension of the phenomenon towards lower luminosities.

This raises the scenario where eruptive variability cannot be simply divided in two distinctive sub-classes but it is instead formed by a continuum of outburst events of different luminosities, amplitudes and time-scales, but triggered by a similar physical mechanism (see e.g. Fedele et al. 2007; Caratti o Garatti et al. 2011; Kóspál et al. 2007; Gibb et al. 2006).

Thus, our results seem consistent with this scenario, where GPSV3 and GPSV15 would be new additions to the deeply-embedded extension of the FUor phenomenon.

Future photometric monitoring of the sources will allow us to better constrain the timescales of the observed variability. Also, spectroscopic analysis of sources in later data releases from GPS (DR7,DR8), with addition of future searches in the multiple K band epochs data from VVV will help us in our effort to characterise and understand the subclasses of eruptive variables.

4.5 Variability outside Star Forming Regions

Five stars from our DR5 sample are marked as variables not associated with SFRs. GPSV15 has already been discussed at length and has been classified as a probable eruptive variable in our analysis. From the remaining four stars, GPSV13 and GPSV17 correspond to blue objects, with GPSV17 already being identified as Nova Sct 2003. The location of GPSV12 in its local

CMD is consistent with a late type dwarf or a distant giant in the Galactic halo, whilst GPSV14 seems to be projected against the dwarf sequence on its CMD in Figure 4.2.

High amplitude variability can be produced by a great number of physical mechanisms. Inspection of Figure 2 of (Corradi et al. 2008) shows that symbiotic stars, classical Be stars and cataclysmic variables, among others, can be found at the location of the objects in near-infrared colour-colour plots. We also note that Algol-type eclipsing variables show large variability at optical wavelengths and while amplitudes at near-infrared wavelengths are lower, it is conceivable that we could detect an extreme case of this type of variable stars.

Not much information is available for objects GPSV12 and GPSV14. The latter was not included in the VLT/ISAAC follow up and only has magnitude information from the UKIDSS GPS data. GPSV12 was faint at the time of our ISAAC observations and the spectrum did not help to draw any conclusion regarding its classification. GPSV12 could plausibly be an AGN (see §2.2) but the higher amplitude of variability in GPSV14 (2.1 mag) makes this interpretation unlikely for that object.

4.5.1 GPSV13, A highly variable classical Be star?

GPSV13 is one of the two blue DR5 sources and it is also one of the brightest variable stars in our sample. Its 1999 2MASS K_s magnitude is very similar to the first K band observation of GPS in 2005. The star was fainter at the second GPS epoch (2008) and continues fading towards our VLT/ISAAC observations (2010). The spectrum of the star at this last epoch shows Brγ in absorption (see figure 4.16).

The object was found to be classified as an Hα emitter in the Witham et al. (2008) catalogue. The IPHAS observation for this object took place in 2004/2005 during the bright state of the object. Figure 4.16 shows the optical spectra of GPSV13 collected in June 2009 at the 1.5 m Fred Laurence Whipple Observatory (FLWO) Tillinghast Telescope using the FAst Spectrograph for the Tillinghast Telescope (FAST, Fabricant et al. 1998), with a spectral resolution of $\Delta\lambda \sim 6$ Å, covering the wavelength range 3500−7500 Å. The equivalent width (EW) of the Hα emission is 9.7 Å, and the spectral typing of the object yields a B5 spectral type based on the EW of the HeI 4471, and just resolved but weak MgII 4481 absorption lines. The reddening is estimated to be $A_V = 3.00 \pm 0.15$. Assuming a B5V classification yields a distance of $\sim$ 2.8 kpc.

The 2004/2005 $r^{'} - i^{'}, r^{'} - H\alpha$ colours of GPSV13 allow us to estimate the EW of the Hα emission as ∼20-22 Å, which is higher than the measured value of 2009 and consistent with the photometric behaviour of the object under the classical Be interpretation described below.

Classical Be stars show variability over long timescales that can be attributed to the dissipation of the disc (Porter & Rivinius 2003). During this process, the star will go from having an emission line spectrum to a normal B type star spectrum (see e.g. McSwain, Huang, Gies, Grundstrom, & Townsend 2008; McSwain, Huang, & Gies 2009). This process could explain the observed behaviour of the spectrum of GPSV13. In addition, dissipation of the disc could explain the large (1.2 mag) decline in brightness in the K band from 2005 to 2010. Inspection of Figure 9 of Carciofi & Bjorkman (2006) shows that the dissipation of a pole-on disc in the

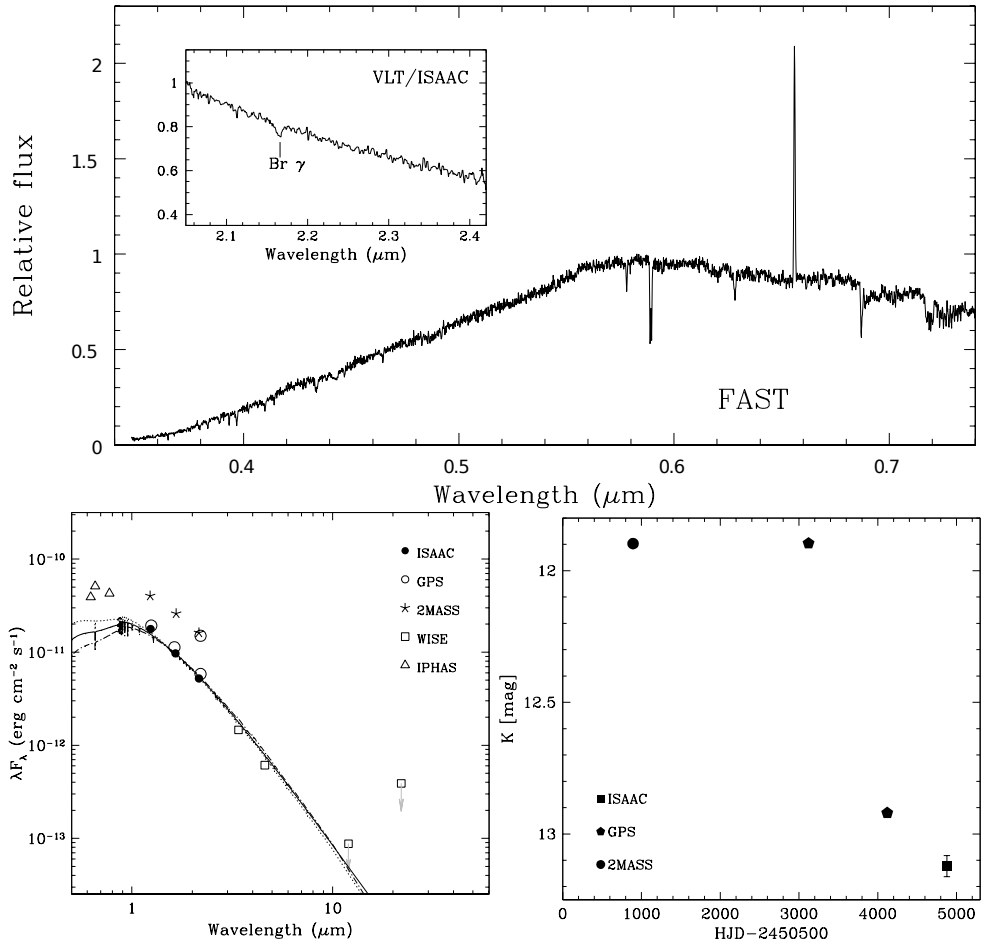

Figure 4.16: The optical FAST spectrum of June 2009, along with the VLT/ISAAC observations of July 2010 (top). K band light curve (bottom right) and spectral energy distribution (bottom left) of the object GPSV13. The latter is compared to a B5V (15400 K) Castelli & Kurucz model atmosphere (solid line) and the same model reddened to $A_V = 2.55$ mag (dotted line) and $A_V = 3.45$ mag (dashed-dotted line). Fluxes of the model where arbitrarily set to match the 2010 H observations of VLT/ISAAC. The models are reddened using the Cardelli, Clayton, & Mathis (1989) extinction law for wavelengths in the range $0.3\mu\text{m} < \lambda < 3.3\mu\text{m}$. Extinction towards longer wavelengths is derived following the Chapman et al. (2009) extinction law for *Spitzer* bands.

models of these authors just reproduce the observed amplitude of the change. This scenario also explains the apparent lack of IR excess in the 2010 WISE W1, W2 magnitudes.

An alternative scenario would be that GPSV13 is a fairly evolved Herbig Ae/Be star with a far IR excess not detectable in WISE data. However the star is not close to any known SFR, there is no observable nebulosity in the WISE colour image of the region and the estimated distance to the object implies that GPSV13 would be $\sim$ 160 pc above the Galactic plane, at least three molecular cloud scale heights for an inner Galaxy object. Figure 2 in Hernández et al. (2005) compares the location of classical Be and Herbig Ae/Be stars in near-infrared colour-colour plots, the authors find that these types of variables seem to occupy different places in these diagrams. The observed colours of GPSV13 would place the object in the classical Be region. Also, its SED resembles those of classical Be stars from the sample of Hernández et al. (2005), see 4.16. Thus the classical Be scenario seems the most likely explanation for GPSV13.

If GPSV13 is in fact a classical Be star, it would correspond to one of the most (if not the most) extreme variable star of this class. To our knowledge classical Be stars have not been observed to vary by more than 1 magnitude (see e.g., Ashok et al. 1984; Dougherty & Taylor 1994).

4.6 Summary

We have presented the results of the first panoramic search for high-amplitude near-infrared variables in the Galactic plane. We summarize our principal results as follows.

- The search for high-amplitude infrared variables in data releases DR5 and DR7 of GPS yields 45 stars which display $\Delta K > 1$ mag. The sample included one known nova and two OH/IR stars. Most notably, two thirds of our candidates are located within known areas of star formation and are likely YSOs. Four other stars also show characteristics of YSOs but do not appear to be close to areas of star formation. Thus we discuss the possibility of high-amplitude IR variables as a tracer of star formation.

- The high YSO fraction found in our study implies an average source density of 0.19 deg^{-2}. We conclude that this number would be likely to rise to $\sim$13 deg^{-2} in the mid-plane, if we had sufficient sensitivity to detect them across the Galaxy, after allowing for the effects of 2-epoch sampling and scale height upon our sample. This would make PMS stars the commonest type of high amplitude variable in the near-infrared.

- Considering the DR5 sample, we assign an eruptive variable classification to four stars based on their observed spectral characteristics and their resemblance to known members of the FUor/EXor class. Two of these are likely new members of the deeply embedded subclass of eruptive variables. Nine stars likely associated with the Serpens OB2 association are confirmed as having YSO characteristics, but an eruptive variable classification

cannot be confirmed. In this context, physical mechanisms that could explain IR variability in YSOs are discussed. Variable extinction along the line of sight is found to be the likely cause of the variation for only one of our variable objects.

- The comparison with the sample of variable YSOs from Carpenter et al. (2001) allows us to estimate that the variability in stars with $\Delta K > 1.1$ mag in two epochs of observation separated by a few years is most likely related to longer timescale variability like that observed in eruptive variables.

- Stars confirmed as eruptive variables show characteristics that could be associated with either of the two known classes of these type of variable stars (EXors or FUors). This is found to be consistent with recent studies that suggest that the episodic accretion phenomena is comprised of a continuum of events with different properties but triggered by a similar physical mechanism.

- Variable stars in the Serpens OB2 region do not show any signs of molecular outflows.

- Four stars in the DR5 sample appear not to be associated with star forming regions. We argue in favour of a classical Be classification for one of such objects. If so, the star would be one of the most variable classical Be stars.

Chapter 5

GPS DR8 and the Spectroscopic Sample

We have extended the search for high-amplitude infrared variables to the data release DR8 of UKIDSS GPS. The search is done as described in section 3.1.1. The inspection of the images yields an additional 26 stars for the GPS sample. Table 5.1 presents the different properties of the selected variable stars. Column 1 gives the source number sorted by ascending right ascension of the objects. Column 2 presents the original designation given to the sources. Column 3 corresponds to the full UKIDSS GPS designation for the source. Coordinates for the objects are given in Columns 4 and 5. The K band magnitude of the source is presented in Column 6, where K_1 represents the K band epoch with contemporaneous J and H photometry[1]. The corresponding $J-K$ and $H-K$ colours are given in columns 7 and 8 respectively. Column 9 gives the K band magnitude difference between the 2 GPS epochs, K_2-K_1. Column 10 presents ΔK_{all}, the absolute value of the peak-to-trough difference when using all of the available data from this work and the literature. Finally, the number of epochs used in the calculation of the latter, N_K, is given in column 11, whilst the data release from which the objects arise is given in column 12.

The majority of the DR8 objects are unknown in the literature. Similar to the results from earlier data releases, most GPS DR8 objects are very red in local $6'\times6'$ $J-K$ vs K CMDs, with the colours of the objects being consistent with many of them being YSOs (figure 5.1). One exception is GPSV50, the reddest object in the sample with $J-K > 7.31$ magnitudes, and which is identified as the infrared source IRAS 19131+1551 in SIMBAD. This object also shows a large $K-[12]$ colour of $\sim$14 magnitudes, which is a common characteristics of dust enshrouded AGB stars (see section 4.1).

In addition, this object is detected at 9 μm in the AKARI survey with $F_{9\mu m} = 15.76$ Jy. An AGB star with this flux would correspond to an object losing mass at $\sim10^{-4}$ $M_{\odot}yr^{-1}$ and with a distance of D$\sim$12 kpc (according to Ishihara et al. 2011), which is plausible for a star in the Galactic disc.

[1]For the sources in this sample K_2 represents the earlier epoch, but this is not true for all GPS sources.

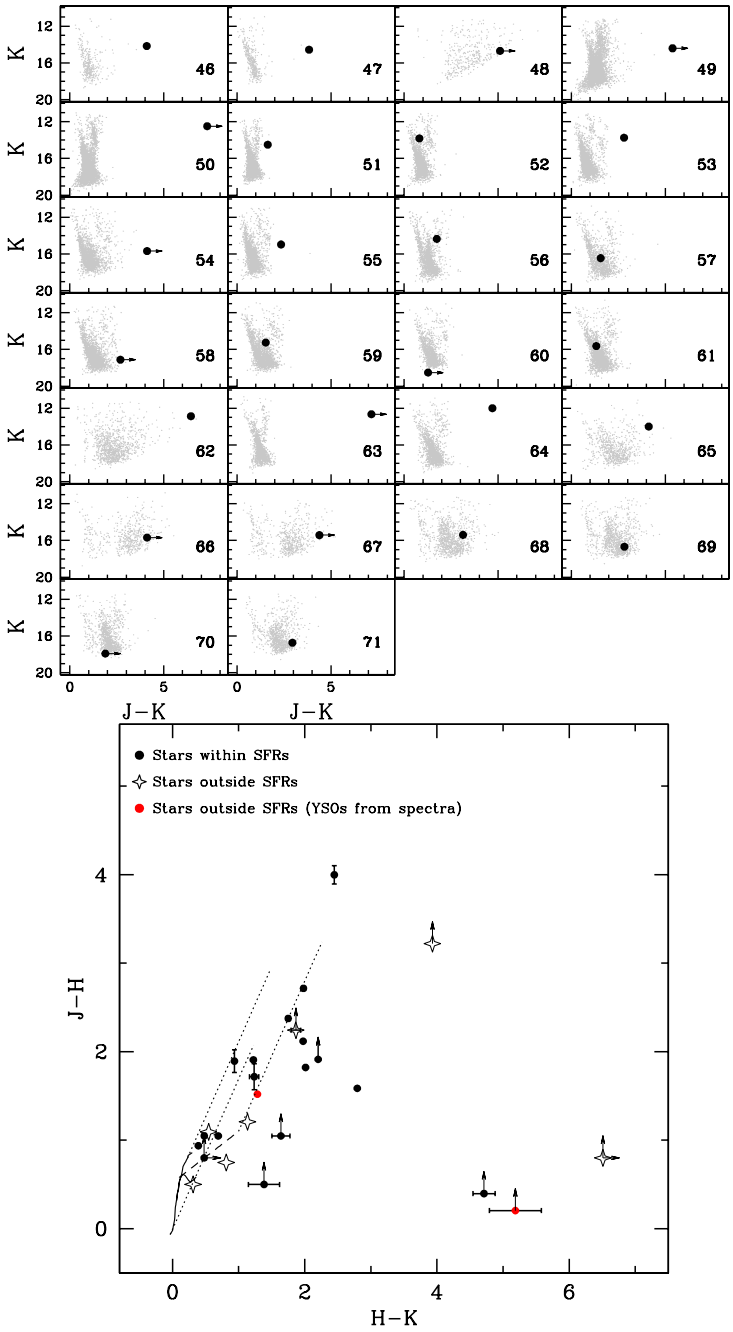

Figure 5.1: (top) Colour-magnitude diagrams of $6^{'} \times 6^{'}$ regions centred on each of the variable candidates arising from DR8. The arrow marks candidates for which J-K colours represent lower limits. Numbers relate to the original designation of the objects given by the authors in column 2 of table 5.1. (bottom) Colour-colour diagram for GPS-selected candidates in DR8. The objects are divided between those associated with SFRs as described in the text (*filled circles*) and objects not found within such areas (open diamonds). The two stars which are not found near areas of star formation, but whose spectra shows characteristics of YSOs are marked in red circles. The classical T Tauri locus of Meyer et al. (1997) is presented (long-dashed line) along with intrinsic colours of dwarf and giants (solid lines) from Bessell & Brett (1988). Reddening vectors of $A_V = 20$ mag are shown as dotted lines. The arrows mark stars for which colours represent lower limits. Errors on both plots are shown only for objects that present significant uncertainties on their measurements.

n°	Object ID	GPS Designation	α (J2000)	δ (J2000)	K_1 (mag)	$J-K_1$ (mag)	$H-K_1$ (mag)	K_2-K_1 (mag)	ΔK_{all} (mag)	N_K	DR
1	GPSV46	UGPS J043333.8+442630.4	04:33:33.81	+44:26:30.43	14.17(0.01)	4.09(0.05)	1.98(0.02)	−1.75	1.90	3	DR8
2	GPSV47	UGPS J070045.7−032023.2	07:00:45.78	−03:20:23.22	14.57(0.01)	3.84(0.04)	2.01(0.02)	−1.90	2.23	3	DR8
3	GPSV48	UGPS J183025.7−021115.2	18:30:25.78	−02:11:15.20	14.69(0.01)	>5.11	4.71(0.17)	−1.00	1.12	4	DR8
4	GPSV49	UGPS J183629.8−024720.6	18:36:29.82	−02:47:20.60	14.41(0.01)	>5.39	5.19(0.39)	1.84	1.84	2	DR8
5	GPSV50	UGPS J191525.0+155632.1	19:15:25.05	+15:56:32.14	12.49(0.01)	>7.31	>6.51	−1.01	1.60	3	DR8
6	GPSV51	UGPS J200641.9+374700.7	20:06:41.96	+37:47:00.72	14.50(0.01)	1.64(0.01)	0.55(0.01)	2.19	2.19	3	DR8
7	GPSV52	UGPS J200920.0+365608.7	20:09:20.01	+36:56:08.78	13.82(0.00)	0.81(0.01)	0.31(0.01)	1.01	1.06	3	DR8
8	GPSV53	UGPS J201228.8+365219.1	20:12:28.84	+36:52:19.18	13.75(0.00)	2.80(0.01)	1.28(0.01)	2.36	2.36	2	DR8
9	GPSV54	UGPS J201331.9+363627.1	20:13:31.99	+36:36:27.17	15.69(0.02)	>4.11	1.87(0.07)	−1.64	1.64	3	DR8
10	GPSV55	UGPS J201336.3+364834.9	20:13:36.33	+36:48:34.93	14.97(0.01)	2.34(0.03)	1.13(0.02)	−1.25	1.25	2	DR8
11	GPSV56	UGPS J202020.2+384208.9	20:20:20.25	+38:42:08.94	14.37(0.01)	1.74(0.01)	0.69(0.01)	1.10	1.80	3	DR8
12	GPSV57	UGPS J202033.4+381608.7	20:20:33.43	+38:16:08.71	16.46(0.04)	1.56(0.05)	0.81(0.05)	−2.30	2.30	3	DR8
13	GPSV58	UGPS J202044.6+385305.6	20:20:44.67	+38:53:05.66	17.11(0.06)	>2.69	1.64(0.14)	−1.44	1.44	2	DR8
14	GPSV59	UGPS J202204.9+390322.9	20:22:04.99	+39:03:22.95	15.25(0.01)	1.53(0.02)	0.48(0.01)	1.74	1.96	3	DR8
15	GPSV60	UGPS J202207.2+393830.8	20:22:07.26	+39:38:30.85	18.52(0.27)	>1.28	>0.48	-3.48	3.48	2	DR8
16	GPSV61	UGPS J202257.9+391958.1	20:22:57.90	+39:19:58.17	15.63(0.02)	1.33(0.02)	0.39(0.02)	−1.40	1.40	3	DR8
17	GPSV62	UGPS J202448.5+391225.7	20:24:48.50	+39:12:25.70	12.86(0.00)	6.45(0.10)	2.45(0.01)	1.45	1.49	3	DR8
18	GPSV63	UGPS J203145.3+363015.4	20:31:45.37	+36:30:15.48	12.65(0.00)	>7.15	3.93(0.02)	2.00	2.00	3	DR8
19	GPSV64	UGPS J203205.2+424847.9	20:32:05.29	+42:48:47.90	11.99(0.00)	4.70(0.01)	1.98(0.00)	1.48	1.48	2	DR8
20	GPSV65	UGPS J203222.5+430910.5	20:32:22.57	+43:09:10.50	13.99(0.00)	4.13(0.03)	1.75(0.01)	2.22	2.22	3	DR8
21	GPSV66	UGPS J203502.7+422346.1	20:35:02.75	+42:23:46.10	15.68(0.02)	>4.12	2.20(0.05)	−1.09	1.09	2	DR8
22	GPSV67	UGPS J203522.1+424035.3	20:35:22.10	+42:40:35.32	15.42(0.01)	>4.38	2.80(0.06)	−1.20	1.20	3	DR8
23	GPSV68	UGPS J203555.9+423048.8	20:35:55.99	+42:30:48.88	15.38(0.02)	3.13(0.05)	1.22(0.02)	1.38	1.38	2	DR8
24	GPSV69	UGPS J203602.5+423059.8	20:36:02.59	+42:30:59.85	16.68(0.05)	2.83(0.13)	0.94(0.06)	−1.36	1.36	2	DR8
25	GPSV70	UGPS J203647.3+423343.9	20:36:47.37	+42:33:43.96	17.92(0.15)	>1.88	1.38(0.24)	−2.13	2.13	2	DR8
26	GPSV71	UGPS J203738.8+423501.0	20:37:38.80	+42:35:01.06	16.74(0.05)	2.95(0.15)	1.24(0.07)	−1.01	1.01	2	DR8

Table 5.1: Parameters of the high-amplitude variables from UKIDSS GPS data release DR8. Columns are described in the text

The objects from DR8 also show a strong concentration towards areas of star formation. In fact, a search in SIMBAD and the Avedisova catalog of SFRs shows that 14 stars are found within the area of the Cygnus-X SFC (see figure 5.2), with three other objects being located near areas of star formation. Five other objects show evidences of being YSOs, but are not found within known SFRs. However, two of these show spectral characteristics of YSOs (GPSV49 and GPSV53, see figure 5.4). This brings support to the idea that we are able to trace areas of star formation through high-amplitude infrared variables. We include these two objects in our sample of variable stars in SFRs, therefore 19/26 objects from DR8 are found to be likely YSOs within areas of star formation. Given that DR8 provides ∼104 deg^2 of additional two epoch coverage, the YSO source density of DR8 is 0.18 deg^{-2}, which is very similar to the estimated number from DR5+DR7. Thus, the surface density estimated in section 4.2 is not altered by the inclusion of DR8 objects.

5.1 The GPS spectroscopic sample

We have Gemini NIFS mid-resolution spectra for 20 objects from the GPS (DR5+DR7+DR8) variable star sample (presented in figures 5.4 and 5.5). All of the sources in the spectroscopic sample are characterized by being red in local CMDs, in addition to showing near-infrared colours with H-K excess emission possibly arising from an accretion disc. The near-infrared

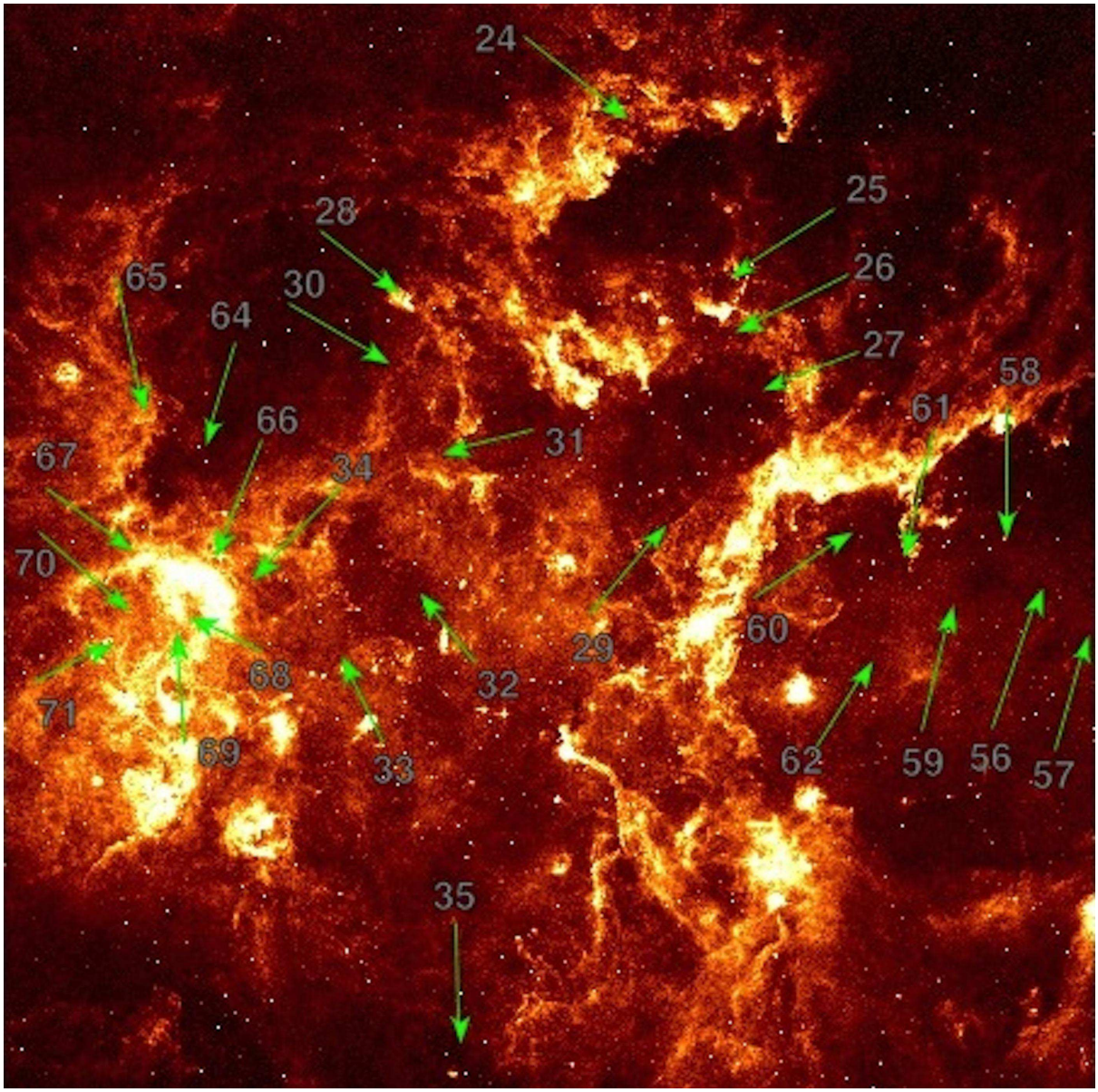

Figure 5.2: $7^\circ \times 7^\circ$ MSX6C 8 μm image of the Cygnus-X star forming complex. Projected location of 26 sources found within this area are marked by arrows with their corresponding GPSV designations.

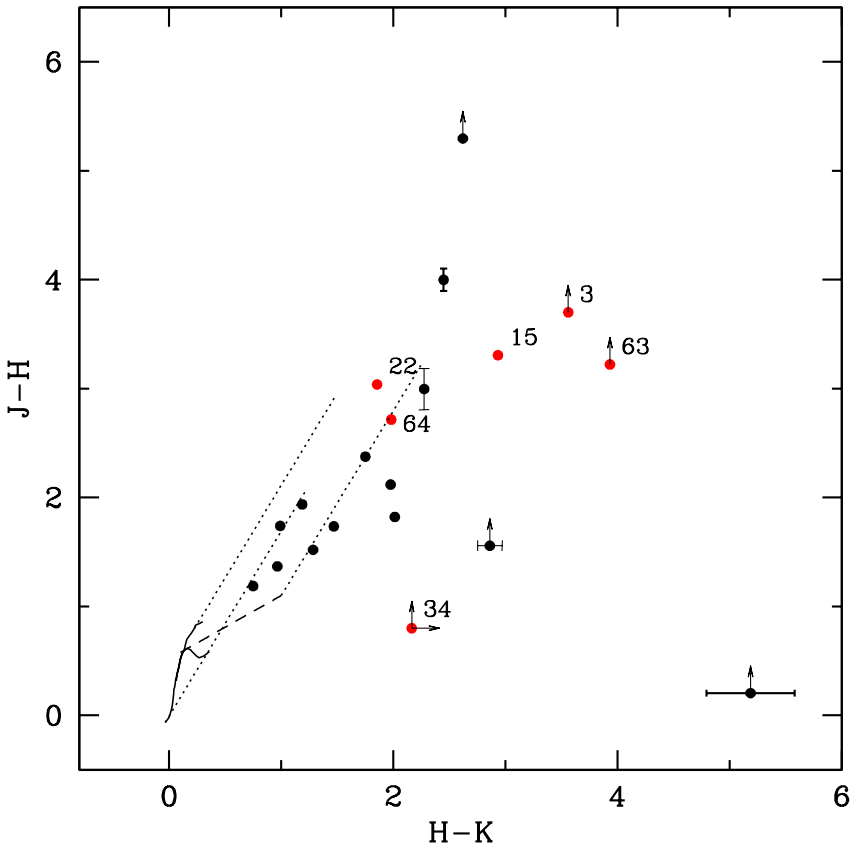

Figure 5.3: Colour-colour diagram of the 20 GPS variables selected for spectroscopic follow up. GPS variables which are discussed as possible FUor objects in this or the previous chapter, are marked in red circles along with their GPSV designations.

colours are shown in figure 5.3.

We search for common spectroscopic signatures of YSOs, such as emission from H I arising in the accretion flow at 2.16 μm, H_2 emission at 2.12 μm, as well as other common signatures from Na I (2.21 μm), Ca I (2.26 μm) and ^{12}CO (2.293 μm). In table 5.2 we present the equivalent widths of the emission/absorption features that were identified in the spectra of the objects. Equivalent widths are measured using SPLOT in IRAF.

Due to the poor signal-to-noise for the object, we are not able to detect any features in the spectrum of GPSV62, although CO bandhead absorption seems to be present. We do not include GPSV62 in the following analysis.

H I emission is found in 9/19 objects, which represents 47% of the sample, whilst H_2 2.12 μm emission is observed in 9/19 objects or 47% of the sample. Six of these show additional lines from H_2 (32%). The observed emission from H_2 likely arises from molecular shocks in every case, given the weakness or lack of higher excited lines (see section 2.1). We also find that 21% of the sample show CO in emission, whilst 57% shows absorption from CO.

Previous spectroscopic studies of YSOs at near-infrared wavelengths report the following frequencies for the studied atomic and molecular features. In the case of Brγ emission, Cooper et al. (2013) finds detection rates of 75% for high-mass YSOs, whilst Carr (1989) and Con-

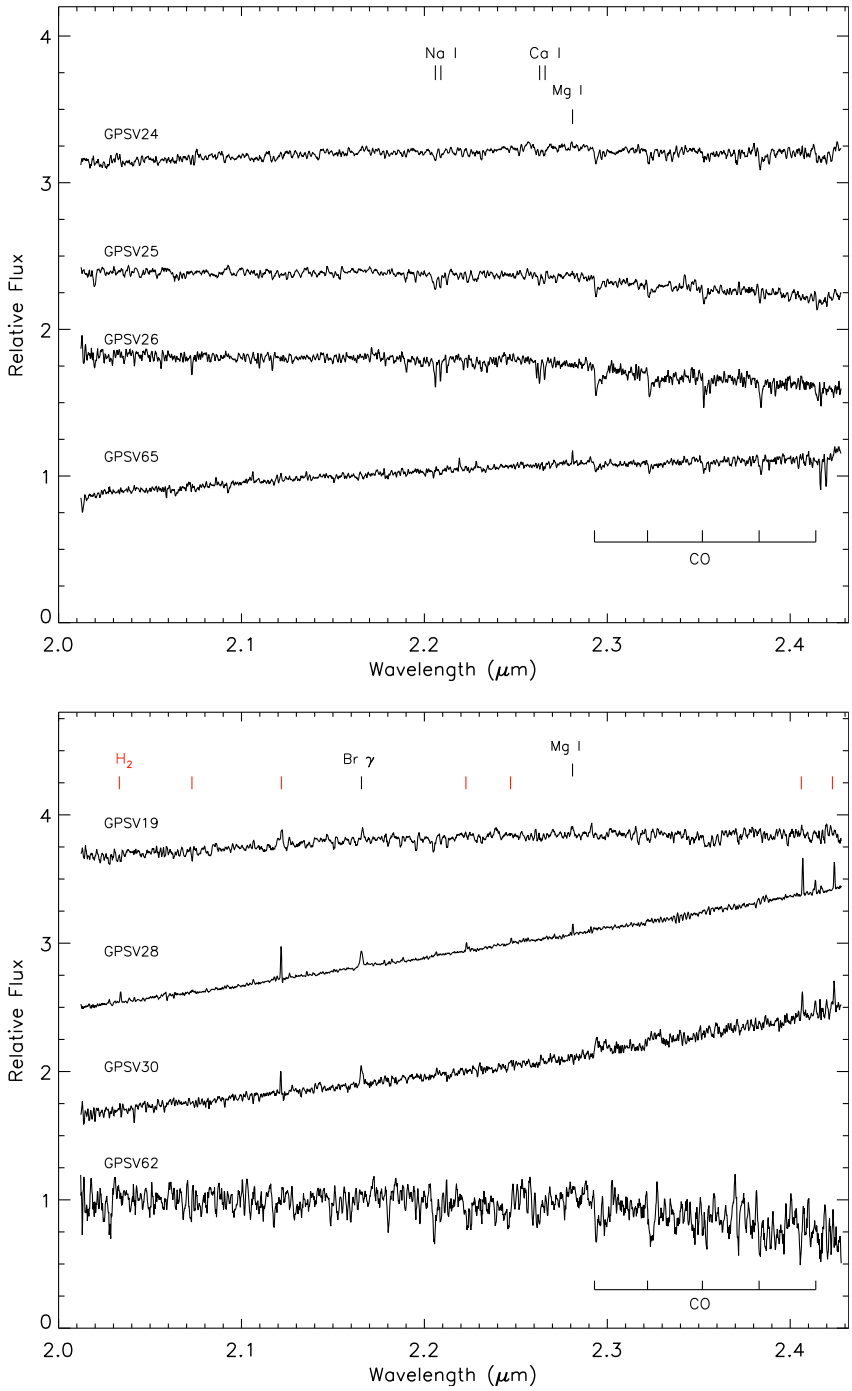

Figure 5.4: Gemini NIFS spectra of GPS variables. Spectroscopic features found in the sample are marked at the top/bottom of each plot.

nelley & Greene (2010) find rates of 71% and 75% respectively for low-mass YSOs. 91% of intermediate-mass and Herbig Ae/Be stars in the study of Ishii et al. (2001) show this feature in emission.

In the case of CO emission, the reported frequencies are 17% for massive YSOs (Cooper et al. 2013), 20% and 22% for low-mass YSOs (Carr 1989; Connelley & Greene 2010), and 22%

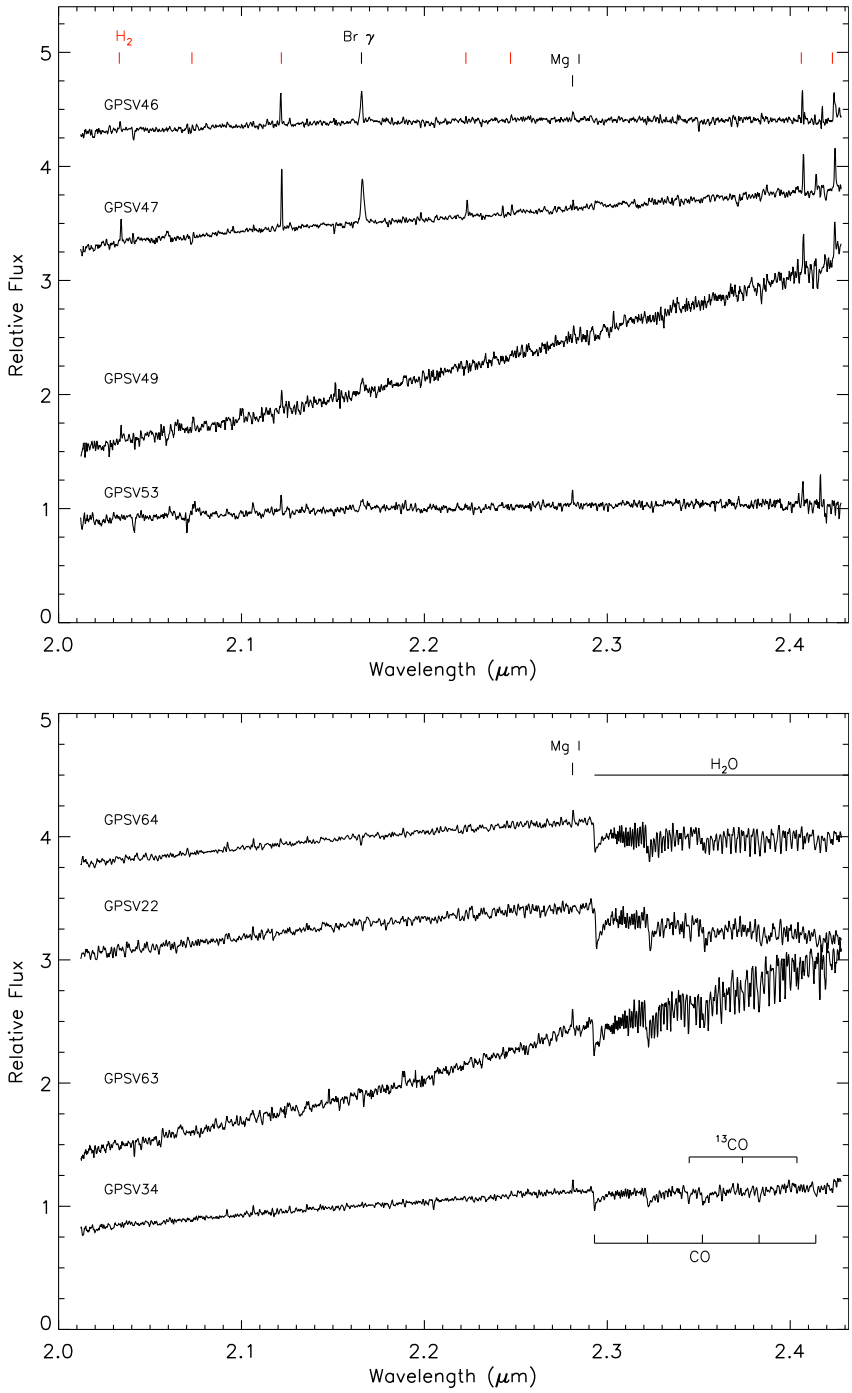

Figure 5.5: Similar to figure 5.4.

for intermediate-mass and Herbig Ae/Be stars (Ishii et al. 2001).

For H_2 emission, Cooper et al. finds rates of 56% (high-mass YSOs), Ishii et al. report 34% for intermediate YSOs, whilst low-mass YSOs are found to show this feature in 25% of the objects of Carr and 42% in the sample of Connelley & Greene.

If all of the objects from the spectroscopic sample are in fact YSOs, the frequencies in which H_2 and CO are found in emission are comparable to those found in previous studies of young

Object	$H_2(2.12\mu m)$	$Br\gamma(2.16\mu m)$	$NaI(2.21\mu m)$	$CaI(2.26\mu m)$	$^{12}CO(2.293\mu m)$	$MgI(2.28\mu m)$
GPSV3	–	–	-0.6±0.1	-0.4±0.1	4.0±1.7	-0.4±0.0
GPSV8	–	-1.4±0.4	2.2±0.3	2.6±0.3	10.5±2.2	0.0±0.0
GPSV15	–	–	0.0± 0.0	–	11.1±2.4	-0.6±0.2
GPSV16	-0.6±0.1	-4.3± 0.4	-1.5±0.2	–	-15.5±6.2	–
GPSV19	-1.6±0.8	-1.0± 0.3	–	–	–	–
GPSV22	–	–	–	–	35.3± 4.9	–
GPSV24	–	–	1.9±0.6	1.8±0.3	10.6±4.3	–
GPSV25	–	–	2.6±0.5	1.8±0.5	16.0±0.6	–
GPSV26	–	–	3.0±0.5	3.6±0.6	18.2±9.2	–
GPSV28	-1.9±0.1	-2.1±0.3	–	–	-1.4±1.8	-0.5±0.1
GPSV30	-1.2±0.2	-2.4±0.8	–	–	-6.6±4.2	–
GPSV34	–	–	–	–	13.1±3.4	–
GPSV46	-2.1±0.3	-3.3±0.6	–	–	–	-0.7±0.2
GPSV47	-3.9±0.3	-7.5±1.1	–	–	-1.1±3.5	-0.4±0.2
GPSV49	-1.7±0.7	-2.2±1.4	–	–	–	–
GPSV53	-1.0±0.3	-1.5±0.6	–	–	–	-0.9±0.2
GPSV62	–	–	–	–	–	–
GPSV63	–	–	–	–	22.0±4.4	-0.7±0.3
GPSV64	-0.4±0.2	–	–	–	37.0±5.3	-0.7±0.3
GPSV65	–	–	1.31±0.40	0.59±0.13	7.7±1.3	-0.5±0.1

Table 5.2: Equivalent widths of common features found in the near-infrared spectra of YSOs and which are detected in our GPS sample.

stellar objects. However, the detection frequency of Brγ is significantly lower than that reported for this kind of object.

Figure 5.6 shows the comparison of the measured equivalent widths of CO with those of Na I+Ca I and Brγ for a sample of class I YSOs from Connelley & Greene (2010). The authors mark three distinct regions in the plot, regions D, E and F. Objects from the cited study that fall in region F are characterized by showing CO and Brγ emission (being located in region A in the bottom plot of figure 5.6), and by having strong veiling from hot circumstellar material. The high veiling is likely associated with objects with high accretion rates. Region D objects are characterized by having low veiling and usually display Brγ emission, but with CO absorption that is arising from a stellar photosphere, in addition to other photospheric absorption features. The equivalent widths of CO and NaI+CaI fall in between the locus of dwarf and giant photospheres. Finally objects in region E show CO absorption in excess of photospheric absorption, with a lack of emission at 2.16 μm. Many objects in the sample of Connelley & Greene falling in this region are FU Orionis stars.

Figure 5.7 shows the comparison of the measured equivalent widths of CO with those of Na I+Ca I and Brγ for our GPS sample, in here we also mark regions D, E, and F mentioned above. From our sample we find

- **Region F** Eight objects fall in this region, including GPSV16, which is discussed in section 4.4.3. All of them show broad Brγ emission with FWHM > 100 km s^{-1} as expected from infall from accretion flows. Four stars show CO in emission, whilst the remaining four do

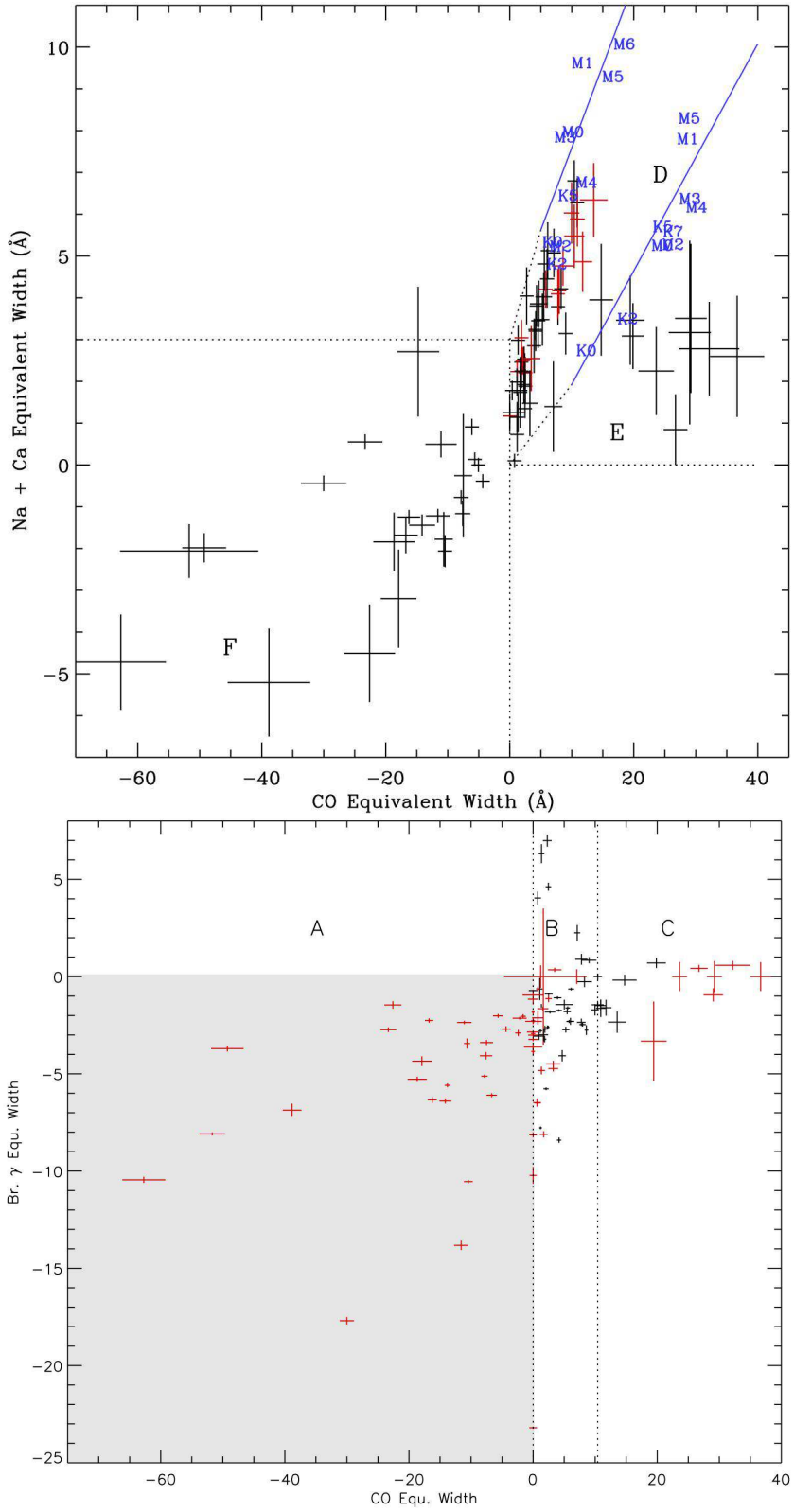

Figure 5.6: Comparison of the equivalent widths of ^{12}CO vs NaI+CaI (top) and ^{12}CO vs Brγ (bottom) for the sample of class I objects from the work of Connelley & Greene (2010) (figures 5 and 8 from that work).

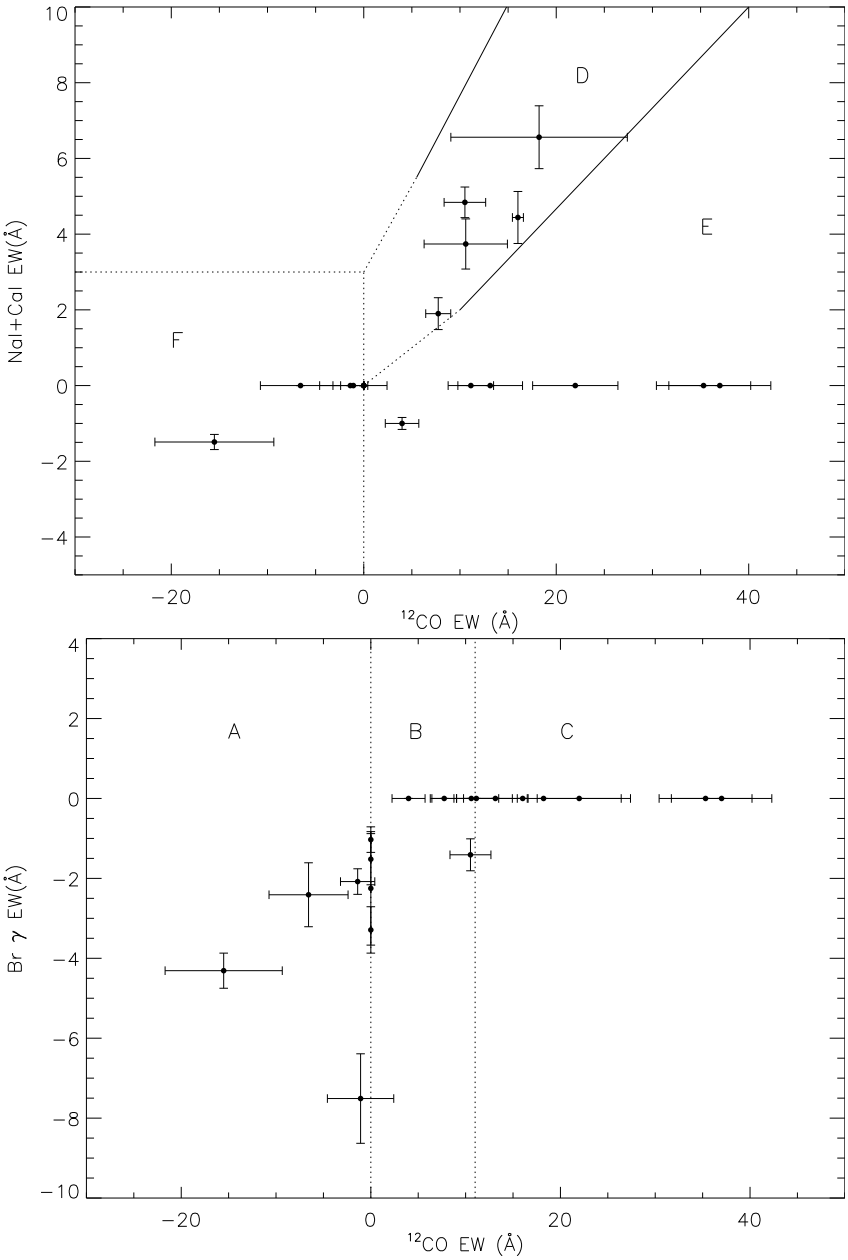

Figure 5.7: Comparison of the equivalent widths of ^{12}CO vs NaI+CaI (top) and ^{12}CO vs Brγ (bottom) for the GPS spectroscopic sample. Regions are based on the work of Connelley & Greene (2010) and are explained in the text.

not show any features at that wavelength. In addition, these objects lack any photospheric features, which favours the idea that these objects are heavily veiled by hot circumstellar material. Every star that falls in this region also shows shock-excited H_2 emission.

- **Region D** Five GPS variable stars are found in this region, including the likely EXor variable from the DR5 sample, GPSV8 (section 4.4.3). The remaining four objects show photospheric absorption from CO, Na I and Ca I, but lack any observable emission from Brγ.

- **Region E** Six objects fall in the area where FUor objects are expected to be found. These include GPSV3 and GPSV15, which have been described in section 4.4.3. The possible classification of remaining four objects as FUor eruptive variables is discussed below.

Inspection of figure 5.6 shows that the majority of stars in the sample of Connelley & Greene (2010) locate in region D described above. The fact that we observe a low detection of objects in this area helps to explain the low Brγ emission detection frequency from our sample.

We have stated before that the high amplitudes observed in our GPS objects are likely being driven by accretion related variability. Thus we expect to detect objects at high accretion states either displaying characteristics of EXors in outbursts, with CO emission and strong veiling of photospheric features (objects in region F), or they will have the strong CO absorption expected in FUors (objects in region E).

5.2 FUor-like objects

From the six objects that fall in region E described above, two are likely new members of the deeply embedded class of eruptive variables (GPSV3 and GPSV15, section 4.4.3). The remaining four objects are discussed in detail below

- **GPSV22** Likely associated with SFR 35.20-1.75 (see section 4.1), this object is 24" from HII region [k97c] 35.2-01.8 (Kuchar & Clark 1997) which has $V_{LSR} = 47$ km/s, implying a near kinematic distance of 3.12 kpc (derived from the Galactic rotation model of Brand & Blitz 1993). Figure 5.8 shows the WISE false colour image around the projected location of GPSV22, the association with the SFR appears to be strong.

  GPSV22 shows $\Delta K_s = 1.7$ magnitudes, being fainter at the earlier GPS epoch ($K = 15.12$). The object is not detected in 2MASS nor DENIS, which would be expected if the object was at a similar magnitude to the earlier GPS epoch. This object probably went into outburst between 2007 and 2009. Mid-IR information for this object is not available, given that it is not covered by any of the Spitzer surveys and not detected in WISE.

  The Gemini NIFS spectrum (figure 5.4) shows strong H_2O and CO absorption, with a lack of any other emission/absorption features. This object shows strong evidences of belonging the the FUor class of eruptive variables.

- **GPSV64** Located in the Cygnus-X SFC region (figure 5.2). The object shows near-infrared colours of a reddened Class II YSO at the edge of the T Tauri locus (figure 5.3). GPSV64 brightened by 1.47 magnitudes between 2006 and 2009 and is not detected in 2MASS. Considering the 7σ limit of 2MASS of K_s=14.8 magnitudes, implies a possible recent outburst with $\Delta K \geq 2.8$ magnitudes.

  GPSV64 shows strong CO bandhead absorption as well as weak H_2 2.12 μm and Mg I emission (figure 5.5). Absorption from H_2O could be present but does not appear as strong as in GPSV22. Nevertheless this object is very likely part of the FUor class of eruptive variables.

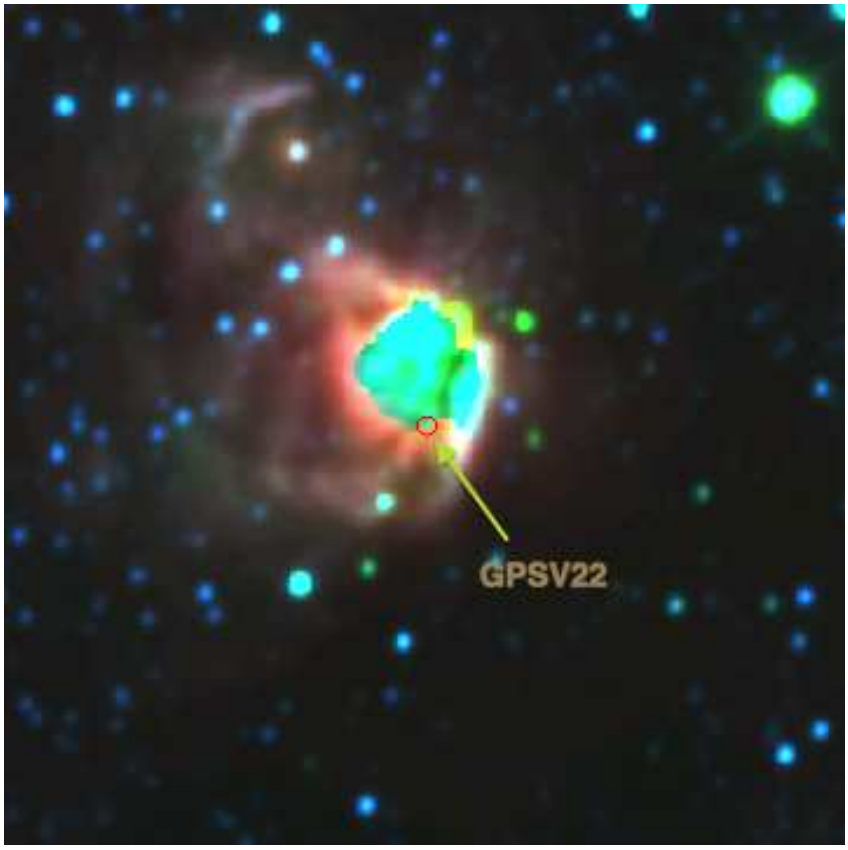

Figure 5.8: False colour WISE image (blue=3.5 μm, green=4.6 μm, red=12 μm) of a $10' \times 10'$ size region centred on GPSV22. The approximate projected location of the object is marked with an arrow.

- **GPSV34** Located in the Cygnus-X SFC region (figure 5.2), the object shows a large ΔK_{GPS} of 2.13 magnitudes. The object is fainter in 2MASS with $K_s = 13.58$ magnitudes, which could point to this object having gone into outburst between 2006 and 2009, albeit this is only considering a light curve of just three points. GPSV34 shows colours that could be consistent with a class I object (figure 5.3).

  The Gemini NIFS spectrum of the object (figure 5.4) shows $\Delta\nu = 2$ bandhead absorption from ^{12}CO in addition to emission from Mg I at 2.28 μm, H_2O absorption is not apparent. Many of these characteristics would point to the object being of a possible FUor classification. However, GPSV34 also shows absorption from $\Delta\nu = 2$ ^{13}CO at 2.344, 2.374 and 2.403 μm. Absorption from this molecule is usually observed in the spectrum of K-M type giant and supergiant stars (see e.g Wallace & Hinkle 1997). The $^{13}C/^{12}C$ ratio increases as a consequence of the first dredge up during the star's ascent through the giant branch. The appearance of this feature (in emission) has also been proposed to help identify evolved Be from Herbig Ae/Be stars by Kraus (2009).

  In section 4.1 we have estimated that normal Miras are unlikely to show in our sample and we note that GPSV34 was included in the objects used in that discussion. Whether this

object could potentially be a dust enshrouded AGB can be addressed in the same manner as was done for GPSV3 and GPSV15 (section 4.4.3). Variable star GPSV34 is detected at 9 μm in the Akari mission, with $F_{9\mu m} = 0.294$ Jy. This implies, $K - [9] \sim 6$ magnitudes, which according to fig. A2 in Ishihara et al. (2011) would correspond to an AGB losing mass at a rate of $\dot{M} \sim 10^{-5.5}$ $M_{\odot}yr^{-1}$. An AGB star losing mass at this rate and with the observed flux at 9 μm would be located at an Heliocentric distance of ∼35 kpc, which would place GPSV34 at d∼ 1.4 kpc above the Galactic plane and well beyond the Galactic disc edge.

Therefore given the presence of absorption by ^{13}CO in the spectrum of GPSV34, the classification of the object as a FUor is highly doubtful. However, the distance argument also seems to rule out an AGB classification.

- **GPSV63** Corresponds to IRAS source IRAS 20298+3619, classified as a star in SIMBAD. There is no evidence of active star formation in the area from SIMBAD or the Avedisova (2002) catalog and figure 5.9 shows that this object seems isolated and not near any areas of star formation. GPSV63 is not detected in UKIDSS in J band, and its near-infrared colours are very similar to those of GPSV3 and GPSV15 (figure 5.3). The object shows a large ΔK_{GPS} of 2 magnitudes, being fainter in the earlier epoch of GPS. The source is detected in 2MASS with $K_s = 13.43$, thus showing a similar variability to GPSV3 and GPSV5 (figure 4.10). The lack of apparent association with a SFR makes it's YSO classification doubtful.

  Using the same arguments of section 4.1, we estimate that this variable star is unlikely to be a normal Mira variable . GPSV63 is also detected in AKARI with $F_{9\mu m} = 0.764$ Jy, which implies $K - [9] = 8.16$ magnitudes. The latter would correspond to an oxygen- or carbon-rich AGB losing mass at $\dot{M} \sim 10^{-4.5}$ $M_{\odot}yr^{-1}$, and located at an Heliocentric distance of 30 kpc, putting GPSV63 ∼ 950 pc above the plane, and beyond the Galactic disc edge.

  Gemini NIFS observations show a red rising spectrum with Mg I emission at 2.28 μm and ^{12}CO bandhead absorption at 2.29 μm, but with a lack of any H_2O features.

  Given the arguments presented above this object could be an isolated YSO belonging to the deeply embedded eruptive variable class, similar to GPSV15.

Due to the doubts in the classification of some objects as FUors, we estimate that the detection frequency of this class of eruptive variables in GPS can vary from 10% to 30%. In the first case, only GPSV22 and GPSV64 would have this classification, given the large similarities of these objects with classical FUors. In any case, the detection frequency of FUors is considerably high. Connelley & Greene (2010) report 9.1% ± 2.9% in their sample of Class I objects. The fact that we are adding 2-6 new objects is very significant, taking into account that only ∼ 21-23 objects are known to be part of this class (Reipurth & Aspin 2010b).

The high fraction of likely FUors in our sample is not surprising if we consider that the high amplitude variability is being driven by large fluctuation in the accretion rate, as we have

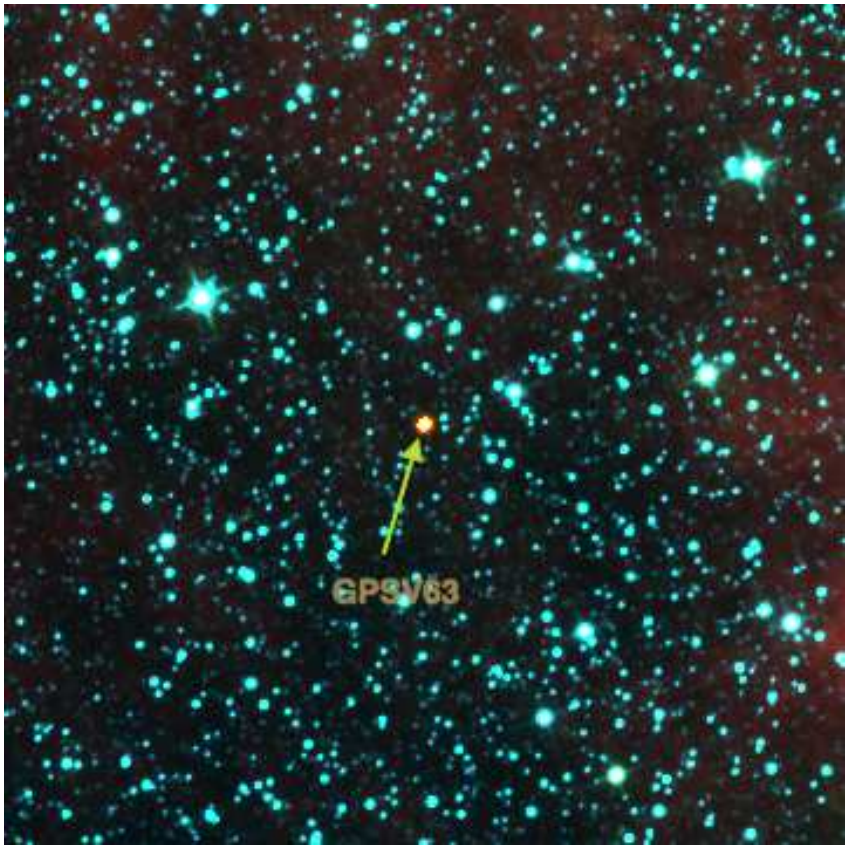

Figure 5.9: WISE false colour image of a region of 30′ centred on variable star GPSV63.

estimated before.

5.3 Eruptive Variables

As we have discussed in a previous section (4.4.3), classifying our variable stars into either of the known classes of eruptive variables is difficult. We have argued that 6 objects in our sample could be new additions to the FUor class. From the remaining 13 objects, 4, which are located in the Cygnus region, only show absorption features that can be attributed to arise from a stellar photosphere, with no signatures of active accretion from Brγ. The variability in these objects might be arising from other physical mechanisms in YSOs rather than from fluctuations in the accretion rate.

The nine variable stars that remain show Brγ emission, with GPSV8 and GPSV16 already classified as likely EXors in section 4.3.3. It is very interesting to see that the seven other GPS objects show H_2 emission at 2.12 μm, which is likely to arise from shock-excited emission. They all fall in region F of figure 5.7 and thus are highly veiled. Three of these also show CO in emission. All of these are characteristics of objects undergoing periods of high accretion, and H_2 could be related to current or past outburst events. Unfortunately, for most objects there is only K band photometry arising from UKIDSS GPS. Given this, is difficult to estimate the timescale of the variability and thus to place this objects into either of the known subclasses of

eruptive variables. Nevertheless these 7 objects with signatures of ongoing accretion are very likely new eruptive variable stars.

Variations in the near-infrared colours would provide additional evidence regarding the mechanisms that drive the variability in these objects. For example changes in the extinction along the line of sight would cause these variations to occur along the redddening vector, as observed in GPSV2 in section 4.4.1. We have discarded this mechanism in DR5 objects GPSV3, GPSV8, GPSV15 and GPSV16.

Unfortunately, the available information is scarce for DR7 and DR8 objects, with nine objects only having near-infrared colours from one the GPS epochs. The remaining seven objects are detected in 2MASS, but in six of them J and/or H photometry is flagged as upper limits, with only GPSV26 having reliable photometry. However, this does not yield additional information as the object has a similar magnitudes in both 2MASS and GPS

Therefore, our UKIDSS GPS study is adding as much as 15 new members to the eruptive variable class, which represents an approximately 30% increase to the current number of known members of this class.

5.4 Summary

- We present the results of the search for high amplitude variables in data release DR8 of the GPS. The search yields 26 additional stars to the overall GPS sample. We find similar results to the searches of DR5 and DR7, in the sense that most variable stars are found to be very red in local CMDs and showing characteristic near-infared colours of YSOs. In addition, we find large concentration of these objects towards areas of star formation.

- The surface density of DR8 YSOs reaches 0.19 deg^{-2}, value which agrees with the one estimated from the DR5 and DR7 searches.

- We present K band high resolution spectroscopic follow-up of 16 objects arising from the DR7 and DR8 searches. The majority of objects show characteristics features of YSOs, such as Brγ, H_2 and CO emission. When including the objects discussed in chapter 4 and for which we have high resolution spectra, i.e. objects GPSV3, GPSV8, GPSV15 and GPSV16, we find that the detection frequencies of emission lines from CO and H_2 are comparable to previous studies of YSOs of all masses. The detection frequency of Brγ on the other hand appears to be lower than usually observed in YSOs.

  This is explained if we are mostly selecting objects that are undergoing high accretion bursts, as expected if high amplitude variability is driven by these bursts. If so, we would expect to observe objects with spectroscopic characteristics of FUors (i.e. lack of Brγ emission) or objects with high veiling, and avoiding "normal" YSOs which show photospheric absorption and Brγ emission in their spectra. The latter constitute the larger part of the sample of class I objects in the sample of Connelley & Greene (2010).

- Four stars show featureless spectra apart from strong CO absorption at 2.29 μm. We

discuss the likelihood of these stars being part of the FUor class. Two of them show strong characteristics of being new additions to the embedded FUor class. This classification remains uncertain for the remaining two objects.

- Seven stars show emission lines spectra with a lack of features arising from a stellar photosphere. The veiling of these features is due to hot circumstellar dust, which could be associated to periods of enhanced accretion onto the star. These seven objects could also be driving molecular outflows. We argue in favour of these objects as being part of the eruptive variable class. However, we lack further photometric information that would allows us to study the timescale of the variability as well as changes in near-infared colours in order to discard variable extinction along the line of sight as the mechanism driving these large changes in magnitude.

- When including the likely eruptive variables from the analysis of DR5 objects, we find that 2-6 objects in our sample could be classified as FUor objects, which represents 10-30% of the GPS sample. This fraction appears to be higher than detected in previous studies.

  In total, we are likely adding as much as 15 new members to the eruptive variable class (EXors and FUors), with the majority of them being embedded sources. This would represent and increase of $\sim$30% of known objects to the class of variable stars, and more significantly we are increasing the number of embedded sources by a factor of ~ 3 .

Chapter 6

VVV

6.1 High Amplitude Infrared Variables from VVV

6.1.1 General characteristics

The selection method of section 3.2.1 yields 816 high amplitude infrared variables. The general properties of the sample can be found in Table 6.1. Column 1 presents the original designation given to the sources. Column 2 corresponds to the full VVV designation for the source. Coordinates for the objects are given in Columns 3 and 4, with columns 5 and 6 presenting the Galactic coordinates of the sources. In columns 7, 8, 9, 10 and 11 we present the nearly contemporaneous Z, Y, J, H, K_s photometry from VVV. Column 12 gives ΔK_s, the absolute value of the peak-to-trough difference from the 2010-2012 light curves from VVV. Column 13 presents α_{class}, the parameter that relates to possible evolutionary class of sources in SFRs. Finally, in column 14 we present whether the object is likely associated with SFRs or not. Most of the variable stars are unknown from searches in SIMBAD and Vizier. Among the known variables there are 2 Novae: Nova Cen 2005 and Nova Cen 2008 (Hughes et al. 2010; Saito et al. 2013), 2 eclipsing binaries, EROS2-GSA J132758-631449 and PT Cen (Derue et al. 2002; Budding et al. 2004), 1 high-mass X-ray binary, BR Cir (see e.g. Tudose et al. 2008), 9 OH/IR stars and ~ 50 stars which are classified as IR sources in SIMBAD. From the remaining, 159 are found in the catalogue of intrinsic red sources from (Robitaille et al. 2008), with the majority being classified as likely YSOs from their mid-IR colours. Figure 6.1 shows the distribution for the 816 VVV variables across the Galactic midplane.

The overall K_s distribution seems to be bimodal, with peaks at $K_s \sim 11.8$ and $K_s \sim 15.8$. This bi-modality appears to be caused by the fact that evolved and other classes of variable stars seem to locate preferentially at the brighter end of the distribution. Figure 6.2 shows that the peak at $K_s \sim 11.8$ is not as evident when only considering stars likely associated with SFRs. However, a two-sided K-S test on the two distributions yields a significance level of 0.46, thus not allowing to reject that these two distributions are drawn from the same population.

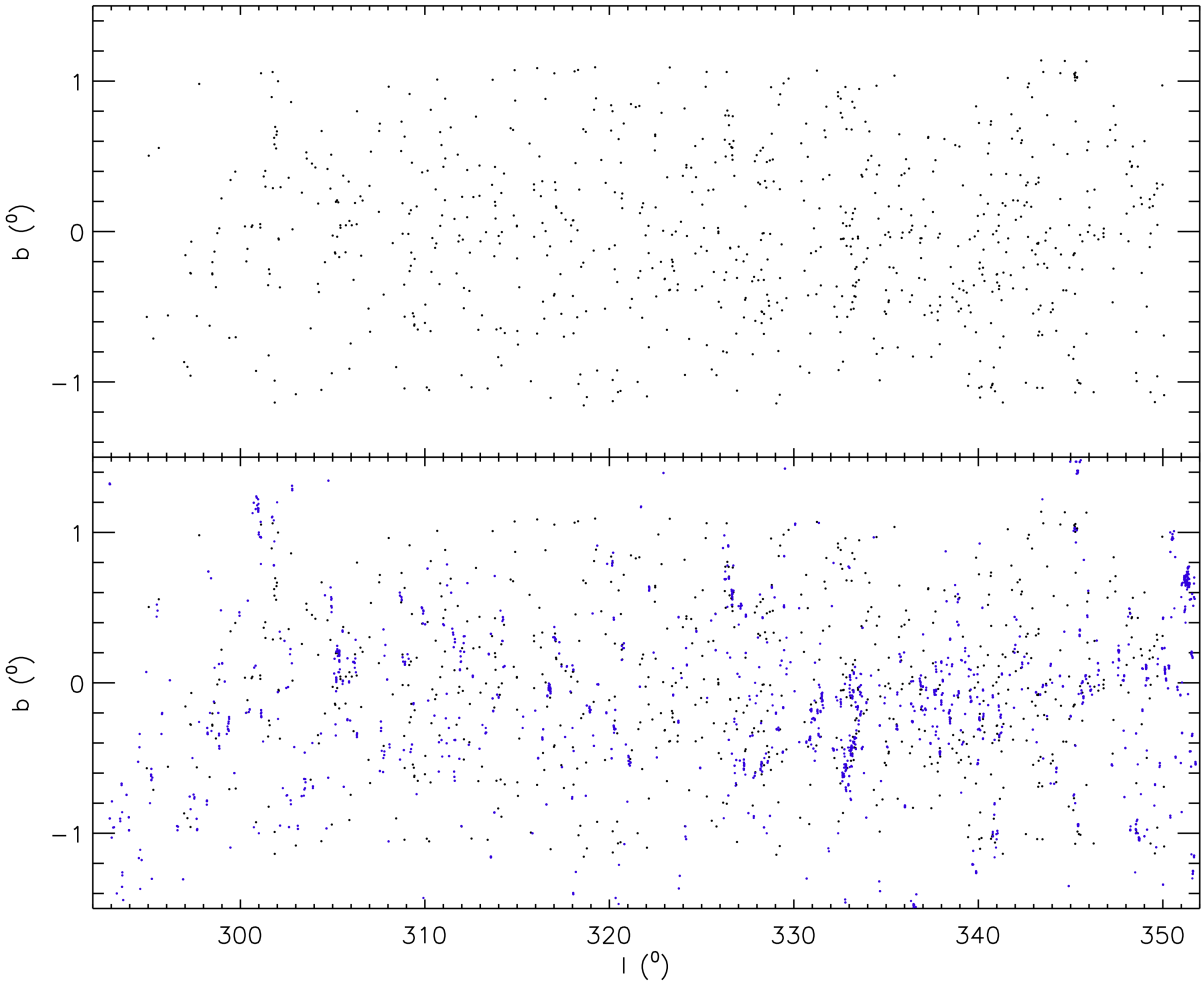

Figure 6.1: Galactic distribution of the 816 high amplitude variable stars (black circles) selected from VVV (top). the bottom graph shows the same distribution, but this time including the areas of star formation from the Avedisova (2002) catalogue (blue circles).

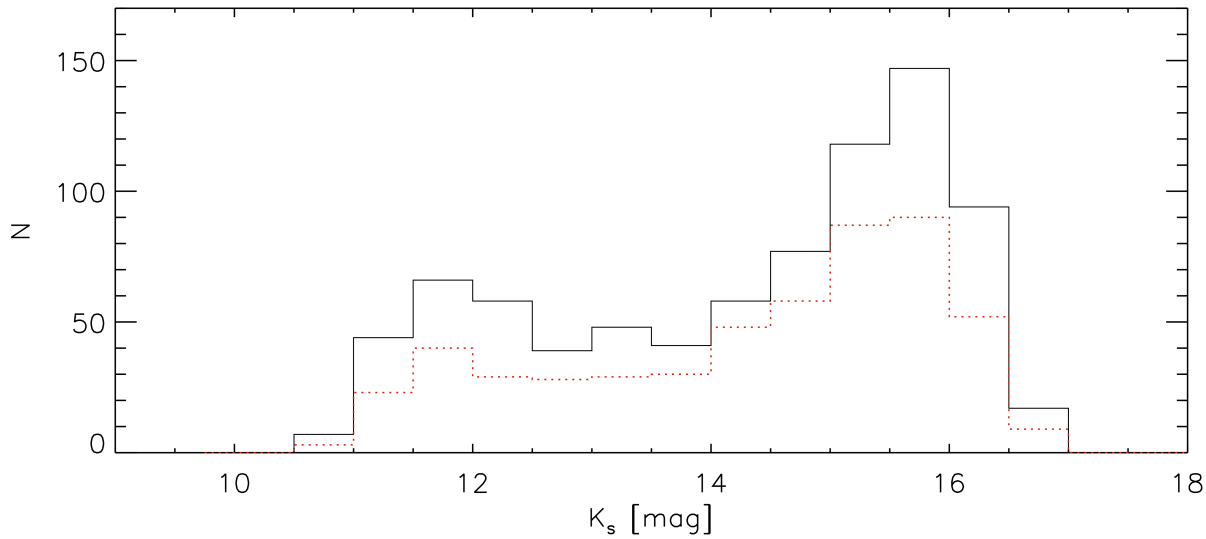

Figure 6.2: K_s distribution of the 816 VVV selected variable stars (solid black line) and for stars likely associated to areas of star formation (dotted red line).

Object ID	VVV Designation	α (J2000)	δ (J2000)	l	b	Z (mag)	Y (mag)	J (mag)	H (mag)	K_s (mag)	ΔK_s^a (mag)	α_{class}	SFR
VVVv1	J114135.16-622055.51	11:41:35.16	-62:20:55.51	294.92603	-0.56770140	–	–	17.99(0.06)	15.95(0.02)	14.44(0.01)	1.16	-0.29	y
VVVv2	J114412.94-623449.09	11:44:12.94	-62:34:49.09	295.28005	-0.71145503	–	–	–	18.78(0.23)	15.71(0.03)	2.01	1.22	y
VVVv3	J115113.03-623729.29	11:51:13.03	-62:37:29.29	296.07199	-0.55784490	13.17(0.01)	12.93(0.01)	12.90(0.01)	12.70(0.01)	12.24(0.01)	1.91	-1.18	n
VVVv4	J115808.69-630708.60	11:58:08.69	-63:07:08.60	296.95057	-0.86785395	–	–	18.23(0.08)	16.62(0.04)	15.32(0.02)	1.02	-0.24	y
VVVv5	J115959.68-622613.20	11:59:59.68	-62:26:13.20	297.02026	-0.15716131	17.69(0.02)	16.62(0.01)	15.87(0.01)	15.25(0.01)	13.53(0.01)	1.30	-0.13	n
VVVv6	J115937.81-631109.77	11:59:37.81	-63:11:09.77	297.12836	-0.89953352	19.02(0.05)	18.08(0.04)	16.80(0.02)	15.95(0.02)	15.50(0.02)	1.02	–	n
VVVv7	J120202.67-623615.60	12:02:02.67	-62:36:15.60	297.28472	-0.27538112	–	–	–	–	17.22(0.12)	1.48	2.39	y
VVVv8	J120059.11-631636.18	12:00:59.11	-63:16:36.18	297.29582	-0.95838309	–	–	–	–	16.86(0.09)	1.39	0.64	y
VVVv9	J120217.23-623647.83	12:02:17.23	-62:36:47.83	297.31381	-0.27887510	–	–	18.29(0.08)	16.33(0.03)	14.64(0.01)	1.84	-0.39	y
VVVv10	J120250.85-622437.62	12:02:50.85	-62:24:37.62	297.33912	-0.067488967	18.57(0.04)	18.23(0.05)	16.97(0.03)	16.35(0.03)	16.07(0.04)	1.19	–	n
VVVv11	J120436.62-625704.60	12:04:36.62	-62:57:04.60	297.63741	-0.56188470	20.20(0.19)	19.01(0.13)	17.87(0.07)	16.79(0.05)	16.08(0.08)	1.10	-1.32	n
VVVv12	J121033.19-630755.71	12:10:33.19	-63:07:55.71	298.33185	-0.62611408	–	–	–	16.30(0.03)	15.04(0.03)	1.42	0.28	y
VVVv13	J121216.83-624838.32	12:12:16.83	-62:48:38.32	298.47603	-0.27813948	–	–	–	–	16.72(0.14)	1.40	1.39	y
VVVv14	J121218.13-624904.48	12:12:18.13	-62:49:04.48	298.47958	-0.28494801	19.48(0.10)	18.88(0.12)	17.84(0.06)	16.74(0.05)	15.56(0.05)	1.01	0.88	y
VVVv15	J121226.09-624416.97	12:12:26.09	-62:44:16.97	298.48252	-0.20370785	19.00(0.07)	17.72(0.04)	16.57(0.02)	15.60(0.02)	15.04(0.03)	1.05	–	y
VVVv16	J121329.76-624107.74	12:13:29.76	-62:41:07.74	298.59498	-0.13364186	18.01(0.03)	17.13(0.02)	16.06(0.01)	14.72(0.01)	13.66(0.01)	1.05	0.92	y
VVVv17	J121352.08-625549.90	12:13:52.08	-62:55:49.90	298.67278	-0.36986131	–	–	–	17.79(0.12)	16.41(0.10)	1.22	0.44	y
VVVv18	J121950.31-632142.24	12:19:50.31	-63:21:42.24	299.39868	-0.70694696	17.82(0.02)	17.29(0.02)	16.20(0.01)	15.52(0.01)	15.32(0.02)	1.03	–	n
VVVv19	J122255.30-632352.56	12:22:55.30	-63:23:52.56	299.74594	-0.70270007	19.56(0.08)	18.67(0.06)	17.55(0.04)	16.40(0.03)	15.61(0.03)	1.23	-0.48	n
VVVv20	J122827.97-625713.97	12:28:27.97	-62:57:13.97	300.32402	-0.19848910	–	–	17.38(0.04)	14.10(0.01)	11.70(0.01)	1.68	0.60	y

[a]

Table 6.1: Parameters of the high-amplitude variables from VVV. For the description of the columns see Section 6.1.1. Here we show the first 20 sources in the list. The complete list is shown in Appendix A

6.1.2 Association with SFRs

Figure 6.1 shows that our objects appear to be highly clustered, with their distribution following that of the SFRs from the Avedisova et al 2002 Catalogue (bottom plot of Fig. 6.1). In order to illustrate how variable stars in VVV are preferentially located in areas of star formation, figure 6.3 shows the K_s image of the area covered in tile d065. Twenty five variable stars are found in this tile, and it is clear that these are not evenly distributed along the area covered in d065, and instead are found clustered around an area of star formation, which is better appreciated in the cutout WISE image.

Using the criteria established in the GPS search (section 4.1), we find 529 of our variable stars are likely associated with SFRs. This represents 65% of our sample, which is remarkably similar to the percentage found in our analysis of GPS. Thus giving further evidence to the fact that YSOs dominate the Galactic population of high-amplitude infrared variables, at least in the range $11 < K < 17$. Our analysis only considered the VVV disc tiles with $|b| < 1°$, this amounts to 76 tiles, covering each 1.636 deg^2 of the sky. Then the total area covered in this part of the survey is given by:

$$area = 76 \times 1.636 - 38 \times 0.135$$
$$area = 119.21 deg^2,$$

where 0.135 deg^2 represents the area that is covered twice by adjacent tiles. The 529 likely YSOs imply a source density of 4.4 deg^{-2}.

When considering the source density of GPS, we estimated that it was originally underestimated due to three main effects. In the case of VVV, given the higher number of epochs

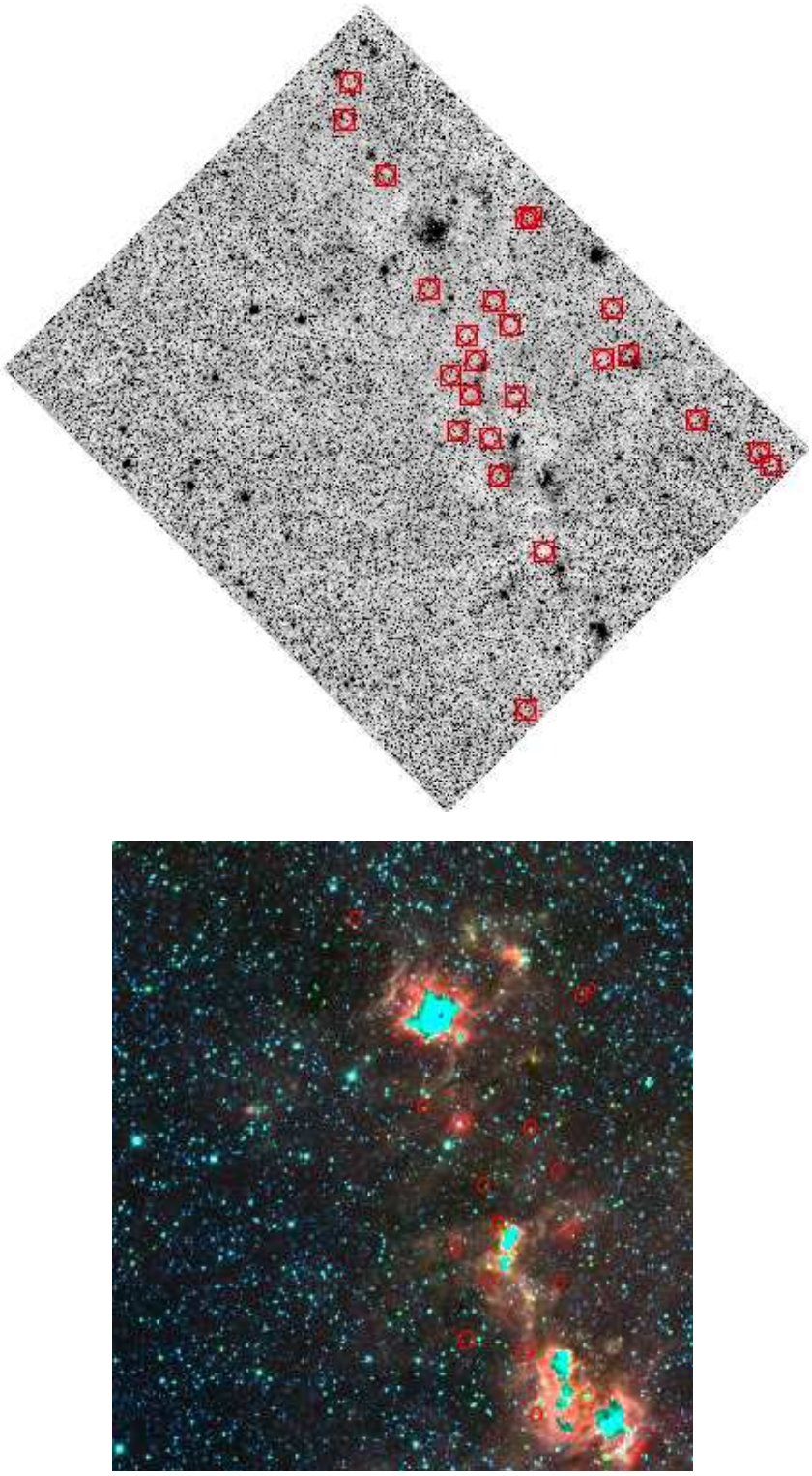

Figure 6.3: The top graph shows the K_s image of tile d065 along with the high amplitude variable stars found in this region. The clustering of the variable stars is already apparent in this image. The bottom graph shows the WISE false colour image of the same region. In here, the fact that variable stars preferentially locate around areas of star formation can be better appreciated.

obtained from this survey, and that this analysis is not biased against areas of star formation, the source density is only likely to be affected by item (2) of the GPS analysis (section 4.2). Figure 6.2 shows the magnitude distribution of the VVV likely YSOs, where we can see a similar behaviour to the GPS results, with the density of sources rising steeply towards faint magnitudes. Contrary to GPS, we do not have a magnitude cut in the VVV analysis, we can see that we detect sources to magnitudes as faint as $K_s \sim 17$. However, the number of sources decreases at $K_s > 16.3$, so we estimate an effective magnitude detection limit of $K_s = 16.5$ magnitudes. This implies that if typical sources from VVV have similar characteristics to GPS objects in Cygnus and Serpens (K=14.8, d=1.4-2 kpc), then we would not detect them at distances d> 3.72 kpc. The complete sample of star forming complexes from Russeil (2003) shows that 77% of them are located beyond these distances. Correcting for this factor we then estimate a true source density of 19.1 deg^{-2}. This number seems to be larger than the one estimated from the GPS analysis, even when taking into account a 10% contamination from possible chance selections.

High luminosity YSOs are less common, but they can be observed at larger distances. GPS would not find such objects at large distances given that it would place them either above or below the Galactic disc in the area covered by this survey. Since VVV is covering the midplane we are able to detect these rare higher luminosity YSOs. This seems to be supported by the larger distances estimated from SED fits of VVV objects. This could in fact explain the larger source density of VVV. However, this large difference could also be explained if the contamination from chance selections is higher than 10%. This could be expected given the larger extinctions in the Galactic midplane and the brighter saturation limit of VVV, allowing for normal Mira variables to show up in our results. Nevertheless, for VVV to match the GPS results we would need an approximately 45% contamination from chance selections.

The estimated source density is still much larger than the one estimated for Mira variables (see section 4.2), thus VVV is confirming the early idea arising from GPS that YSOs dominate the Galactic disc population of high-amplitude infrared variable stars.

In order to study the possible evolutionary stage of the variable stars in SFRs, we use the slope of the SEDs of the stars between $2 < \lambda < 20\mu$m. Following Lada (1987), we define the parameter α as $\alpha = d(\log(\lambda F_\lambda))/d(log(\lambda))$. This parameter is calculated using the photometry arising from VVV and WISE, given that these are contemporaneous measurements. When the objects are not detected in WISE, we use *Spitzer* photometry. However, we note that given the time difference between *Spitzer* and VVV, using the latter might lead to errors in the estimation of α (see Fig. 6.4). In addition a number of sources are not detected at mid-IR wavelengths, in these cases α is left as undefined. Objects are then classified according to their value of α following Greene et al. (1994), also shown in Table 1.1.

The number of objects belonging to different classes are shown in Table 6.2. We find that the large majority of objects in our sample are either class I or flat spectrum sources (47% and 24%). Objects belonging to different classes show some differences in their global properties. Figure 6.5 shows the near-infrared colours of objects in SFRs, as expected the vast majority of objects show colours consistent with them being YSOs. We can also observe that the H-K

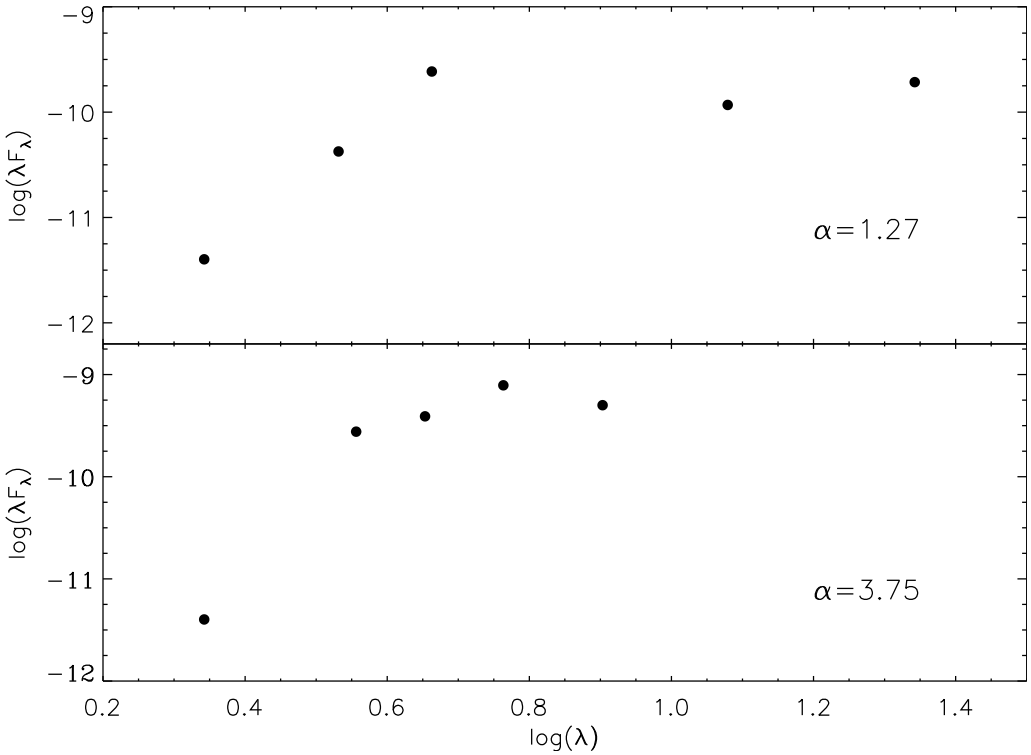

Figure 6.4: Comparison of the estimated α from the SED of VVVv45 when using photometry from WISE (top) and *Spitzer* (bottom).

colour of the objects tends to increase for stars belonging to younger evolutionary stages.

The distribution of $\Delta K_s = |K_{max} - K_{min}|$ (Figure 6.5) shows that objects at younger evolutionary stages tend to have higher ΔK_s. The RMS variability of Figure 6.5 seems to support this. These results agree well with recent studies of YSOs. Rice et al. (2012) find a higher incidence of Class I objects with $\Delta K > 1$ mag ($13 \pm 7\%$) in the Braid Nebula within Cygnus OB7, whilst this incidence is found to be lower in more evolved YSOs (see e.g Carpenter et al. 2001). This could be explained if fluctuations in the accretion rates are higher in Class I objects, which have higher average accretion rates that more evolved Class II or Class III YSOs.

Class	α	N	Percentage
Class I	$\alpha > 0.3$	248	47%
Flat	$-0.3 \leq \alpha \leq 0.3$	126	24%
Class II	$-1.6 < \alpha < -0.3$	89	17%
Class III	$\alpha \leq -1.6$	12	2%
Undefined	n/a	53	10%

Table 6.2: Number of VVV variable stars belonging to the different evolutionary classes of YSOs, as determined from their SEDs.

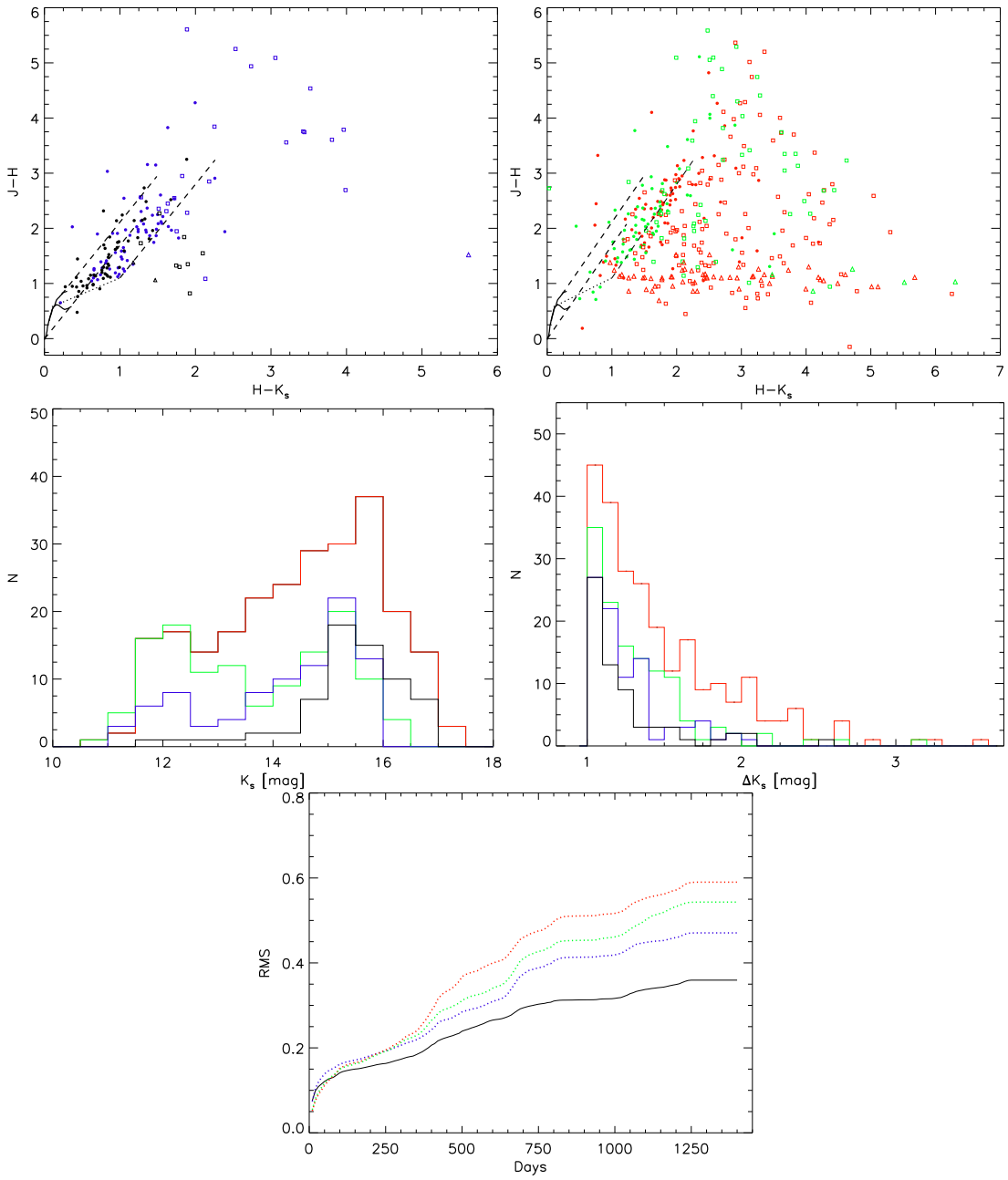

Figure 6.5: (top left) Colour-colour diagram for Class II (blue) and class III YSOs (black) from VVV. In the figure, open triangles mark stars for which $J-H$ represent a lower limit, whislt $J-H$ and $H-K$ colours for stars shown as open squares are lower limits. Objects shown as solid circles have reliable near-infrared colours. The classical T Tauri locus of Meyer et al. (1997) is presented (long-dashed line) along with intrinsic colours of dwarf and giants (solid lines) from Bessell & Brett (1988). Reddening vectors of $A_V = 20$ mag are shown as dotted lines. (top right) Colour-colour diagram for class I (red) and flat-spectrum (green) YSOs. Symbols are the same as for the top left diagram. (middle left) K_s distribution of the different YSO classes. The color coding is the same as used in the top diagrams. (middle right) ΔK_s distribution of the different YSO classes. (bottom) Mean RMS variability for the different YSO classes.

Object	M_* ($M_\odot$)	$\dot{M}_{env}$ (10^{-5} $M_\odot$ yr^{-1})	$\dot{M}_{disc}$ (10^{-6} $M_\odot$ yr^{-1})	log Age (yr)	d (kpc)	log L_{tot} ($L_\odot$)	χ^2_{best}/N	N_{fits}	N_{fits2}
VVVv45 (*Spitzer*)	17.6±9.6	76.1±105.2	17.7±65.8	4.8±0.7	4.5±3.3	4.3±0.6	0.33	9466	9002
VVVv45 (WISE)	8.5±4.1	60.8±140.6	4.1±32.9	5.9±0.9	3.4±2.9	3.3±0.6	0.36	7384	2515

Table 6.3: Comparison of parameters derived from the Robitaille et al. models SED fitting for VVV variable star VVVv45 when using mid-IR information from WISE or *Spitzer*.

Object	M_* ($M_\odot$)	$\dot{M}_{env}$ (10^{-5} $M_\odot$ yr^{-1})	$\dot{M}_{disc}$ (10^{-6} $M_\odot$ yr^{-1})	log Age (yr)	d (kpc)	log L_{tot} ($L_\odot$)	χ^2_{best}/N	N_{fits}	N_{fits2}
VVVv45 (d =1-13 kpc)	8.5±4.1	60.8±140.6	4.1±32.9	5.9±0.9	3.4±2.9	3.3±0.6	0.36	7384	2515
VVVv45 (d =3.4-4.2 kpc)	9.5±2.7	61.6±125.1	3.9±20.7	5.9±0.9	3.7±0.4	3.6±0.4	0.37	1858	560

Table 6.4: Comparison of parameters derived from the Robitaille et al. models SED fitting for VVV variable star VVVv45 when using mid-IR information from WISE but with different ranges for the distance to the object.

6.2 Spectroscopic sample

Even though most of the objects around star forming regions show strong characteristics of YSOs, spectroscopic follow-up is still required to confirm them as young stars. We have spectroscopic observations for 36 VVV objects from the list of the 2010-2012 analysis, with the addition of VVVv815, a star that was selected from its high variability during 2010, but that did not show up in our analysis of the 2010-2012 data (see section 3.2.1).

The observations of 2013 and 2014 were constrained to objects with $K_s < 14.5$ at the closest epoch to the observations. Objects which were observed in 2013 were also selected based on their amplitudes being larger than 2 magnitudes, whilst objects observed in 2014 did not have such a constraint. Figure 6.6 shows the distribution in α and K_s, and the near-infrared colours for the observed sample.

We see that even though the selection was based only on brightness and amplitude of the variability (at least for the 2013 objects), we are covering a wide range in evolutionary stages for the different objects, as determined by α.

6.2.1 SED fits

We use the SED fitting tool from Robitaille et al. (2007) to estimate an approximate value of physical properties of the spectroscopic sample. We already note in section 4.3.2 that this process is unreliable given the high variability of the objects and the lack of contemporaneous near- and mid-infrared photometric measurements. In addition the Robitaille et al. fits might not be able to describe these highly variable sources. In order to reduce the effect of the former, we use, when available, VVV JHK_s and WISE $W1 - W4$ photometry. If WISE measurements were not available, *Spitzer* I1-I4 and MIPS 24 μm photometry is fed to the fitting tool. The use of the latter can provide additional errors to the final results. Some objects are also detected in Hi-Gal PACS and/or SPIRE, when available, these measurements are always used as upper

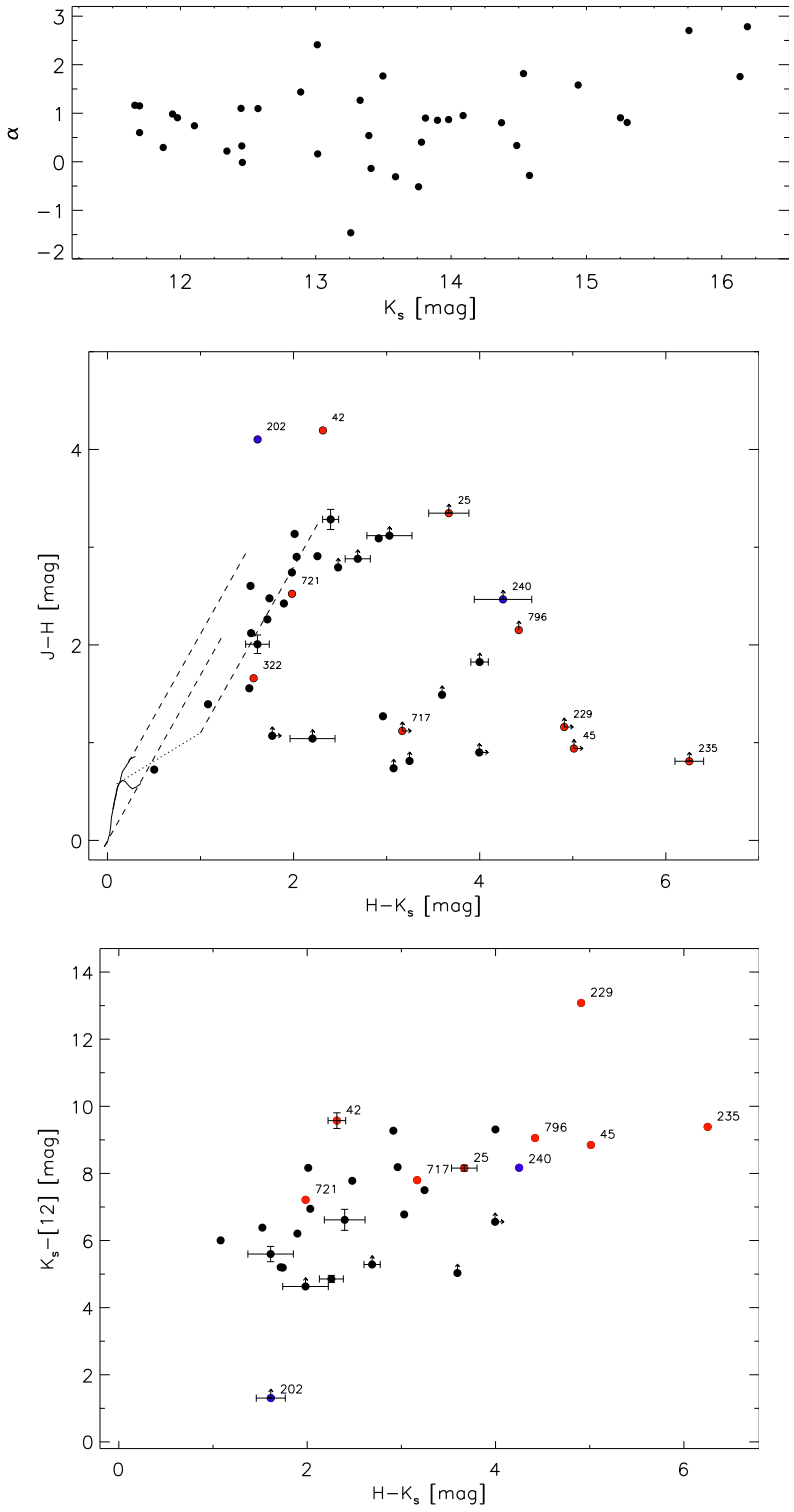

Figure 6.6: (top) K_s vs α for the objects of the VVV spectroscopic sample. (middle) $H-K_s$, $J-H$ colour-colour diagram for the same objects. Red circles show objects that show FUor-like near-infrared spectra, whilst blue circles mark the two objects which are unlikely to be YSOs. The numbers in the plot are from the corresponding VVVv designation of the object. (bottom) $H-K_s$, $K_s-[12]$ for the same objects. Magnitudes at 12 μm are from WISE $W3$ filter. Error bars are only shown for objects with significant errors.

limits for the flux at the corresponding wavelengths.

Table 6.3 shows the results for the VVV variable star VVVv45 when using either WISE or Spitzer photometry. In both cases the distance to the object is left as a free parameter (in the range 1-13 kpc). Here we can see that there are large differences between the two, specially in parameters like mass, age and distance to the object.

We also compare the effect of the range of distance which is given to the fitting tool. All of these objects are found to be likely associated to areas of star formation, and in many cases distance estimates are available. In those cases we use a range of ± 0.5 kpc of such estimates to derive the fits to the SEDs of our objects (except for objects likely associated with the G305 star-forming complex, where a distance of 3.4-4.2 kpc is used, see section 6.4). Table 6.4 shows the results in varying the range in distance to the object VVVv45, which is likely associated with the G305 star-forming complex. In here, we can see that the variation of the weighted mean values occurs within the errors of such values. However, these errors are reduced for every parameter. Therefore, when available, we use the distance to the SFR to which our objects are likely associated with, as the distance to the VVV object.

In our analysis, and as mentioned previously in section 4.3.2, this tool is used as a measure of how well the SED of our objects can be fitted to that of a YSO, and we never take the values of physical parameters as reliable estimates for our variable stars.

Table 6.5 shows the weighted mean values for different parameters of the spectroscopic sample. We note that the infall rate, $\dot{M}_{env}$, is derived only using those models which had a non-zero value for this parameters. The number of models which fulfil this conditions are given by N_{fits2} in the table.

6.2.2 FIRE Spectra

In appendix B we present the final spectra of the observed objects and which are not discussed in detail in this chapter. In table 6.6 we show the equivalent widths obtained from atomic and molecular features which are typically observed in YSOs.

The majority of the objects display typical characteristics of YSOs, i.e. Brγ, H_2 or CO emission/absorption, with some of them having nearly featureless spectra except for strong CO absorption at 2.29μm, which appears to be stronger than expected from a stellar photosphere, these objects will be discussed below. Two variable stars seem to be from a different class, one of them, VVVv202 (figure 6.7), shows strong CO absorption, with Na I and Ca I also in absorption. In addition this object shows absorption features from ^{12}CO$\nu = 3-0, 4-1$ bandheads in its H-band spectrum, as well as strong absorption from ^{13}CO $\nu = 2-0, 3-1$ at 2.3448 and 2.3739 μm, similar to GPSV34 in section 5.2. The ^{13}CO feature is usually observed in the spectrum of K-M giant and supergiant stars (see e.g Wallace & Hinkle 1997). The second object, VVVv240 has a rich emission line spectrum (figure 6.7), with weak Brγ emission as well. However, most of the lines cannot be identified, and we are not able to compare this object to spectra of known YSOs. In the following analysis we do not consider these two stars as they are likely "contaminating" our sample of YSOs.

Object	M_* ($M_\odot$)	$\dot{M}_{env}$ (10^{-5} $M_\odot$ yr^{-1})	$\dot{M}_{disc}$ (10^{-6} $M_\odot$ yr^{-1})	$\log Age$ (yr)	d (kpc)	$\log L_{tot}$ ($L_\odot$)	χ^2_{best}/N	N_{fits}	N_{fits2}
VVVv20	6.15±2.31	1.64±2.91	2.18±12.85	5.34±0.72	5.74±4.16	2.84±0.67	0.21	5402	5320
VVVv25	11.48±2.49	0	0	6.28±0.13	2.06±0.54	3.94±0.27	1.96	137	0
VVVv32	3.11±0.97	3.17±4.01	0.16±1.12	6.62±0.47	2.29±0.58	1.87±0.39	0.12	270	28
VVVv45	9.49±2.66	61.64±125.05	3.98±20.65	5.92±0.89	3.73±0.35	3.62±0.39	0.37	1858	560
VVVv42	11.03±2.19	0	0.31±0.66	6.23±0.14	3.73±0.34	3.89±0.26	4.0	73	0
VVVv63	3.39±1.30	3.57±17.75	0.28±3.53	6.07±0.75	3.35±0.71	1.88±0.48	0.12	10000	5758
VVVv65	3.81±1.04	2.71±7.25	0.078±0.61	6.39±0.49	3.36±0.76	2.15±0.38	0.36	4816	1249
VVVv94	5.21±1.30	5.38± 16.54	0.36±3.76	6.36±0.44	2.43±0.74	2.69±0.37	0.07	7478	1777
VVVv118	3.93±2.18	16.25±23.5	4.71±14.95	4.66±1.02	4.59±2.84	2.21±0.62	1.21	207	206
VVVv202	6.88±1.19	11.08±37.17	1.56±8.14	5.39±0.77	3.97±0.82	3.02±0.34	1.72	2817	2527
VVVv193	5.19±1.62	0.24± 0.27	0.28±1.77	6.38±0.49	4.08±0.81	2.66±0.47	0.84	4098	452
VVVv229	11.21±3.44	0	0.07± 0.09	6.23±0.18	1.45±0.20	3.87±0.38	7.29	39	0
VVVv235	17.39±1.95	0	2.73±9.36	6.06±0.04	4.39±0.32	4.49±0.13	5.75	26	0
VVVv240	12.85±2.82	0	4.45±9.62	6.16±0.09	3.15±0.63	4.11±0.25	0.89	106	0
VVVv270	2.96±1.84	8.43±23.72	1.46±9.16	5.20±0.94	2.10±0.68	1.68±0.54	0.07	10000	7620
VVVv322	2.16±1.61	3.51±7.86	0.46±2.44	5.27±1.11	3.52±0.72	1.44±0.61	0.24	4734	3261
VVVv374	6.65±2.34	36.68±80.02	6.96±23.83	5.40±1.25	2.57±0.77	3.03±0.46	0.40	1636	897
VVVv405	7.25±2.46	0.43±0.71	0.93±4.97	6.33±0.53	1.76±0.71	3.21±0.49	0.03	2632	186
VVVv406	3.50±1.94	7.28±18.56	1.06±3.28	4.89±0.86	1.85±0.70	1.98±0.54	0.02	9492	7952
VVVv452	4.71±1.92	3.20± 13.83	0.43±2.84	5.85±0.75	6.02±4.02	2.45±0.69	0.14	2348	1549
VVVv480	2.66±1.67	12.68±39.11	0.57±7.68	5.77±0.95	3.84±0.34	1.44±0.63	0.03	6879	4241
VVVv473	5.75±1.98	2.48±4.79	4.57± 12.60	5.40±1.10	3.73±0.32	2.87±0.42	0.00	4087	2766
VVVv514	3.00±1.59	3.26± 8.05	0.27± 1.84	5.36±0.53	3.94±0.68	1.57±0.42	0.10	3030	2684
VVVv562	3.94±1.06	3.82± 10.74	0.14±0.97	6.20±0.64	2.78±0.73	2.19±0.38	0.04	7031	3229
VVVv625	5.34±1.67	4.89± 9.74	0.08±0.83	6.47±0.26	2.71±0.76	2.71±0.46	1.38	2979	43
VVVv628	1.75±1.56	4.38±14.12	0.31±3.32	5.29±0.85	1.56±0.67	1.01±0.71	0.11	8375	6010
VVVv630	2.62±1.48	2.75± 6.07	0.24±1.96	5.59±0.81	1.53±0.60	1.48±0.55	0.00	10000	7142
VVVv631	4.48±1.91	8.96± 15.25	0.15± 1.09	6.39±0.54	4.03±0.71	2.39±0.55	0.04	2495	332
VVVv632	3.60±1.15	22.36± 26.98	0.95± 3.65	5.73±1.29	2.40±0.72	2.20±0.33	0.72	287	87
VVVv665	5.72±1.61	0.26± 0.38	0.73± 4.10	6.37±0.51	4.13±0.74	2.86±0.39	0.12	1315	57
VVVv662	5.10±1.41	4.12± 12.64	0.30± 2.11	6.33±0.51	2.94±0.79	2.64±0.42	0.57	6046	1147
VVVv699	5.20±1.23	5.26± 14.89	0.51± 3.11	6.35±0.56	4.09±0.70	2.72±0.33	0.03	2509	449
VVVv717	6.69±3.09	0.32± 0.68	0.44± 2.77	6.42±0.31	4.43±3.58	2.99±0.69	0.22	10000	210
VVVv721	4.49±1.93	13.43± 29.31	2.20± 7.21	5.42±1.23	4.18±0.82	2.43±0.49	0.18	3876	2250
VVVv796	8.03±2.85	0	0.17± 1.71	6.38±0.20	1.12±0.62	3.33±0.54	0.19	1310	0
VVVv800	4.82±1.89	0.50± 0.64	0.87± 4.47	6.28±0.85	1.04±0.56	2.57±0.57	0.10	1718	231
VVVv815	5.51±1.63	7.41± 19.61	1.79± 6.39	5.41±0.96	3.03±0.74	2.71±0.40	0.24	2926	2252

Table 6.5: Parameters derived from the Robitaille et al. models SED fitting as explained in the text

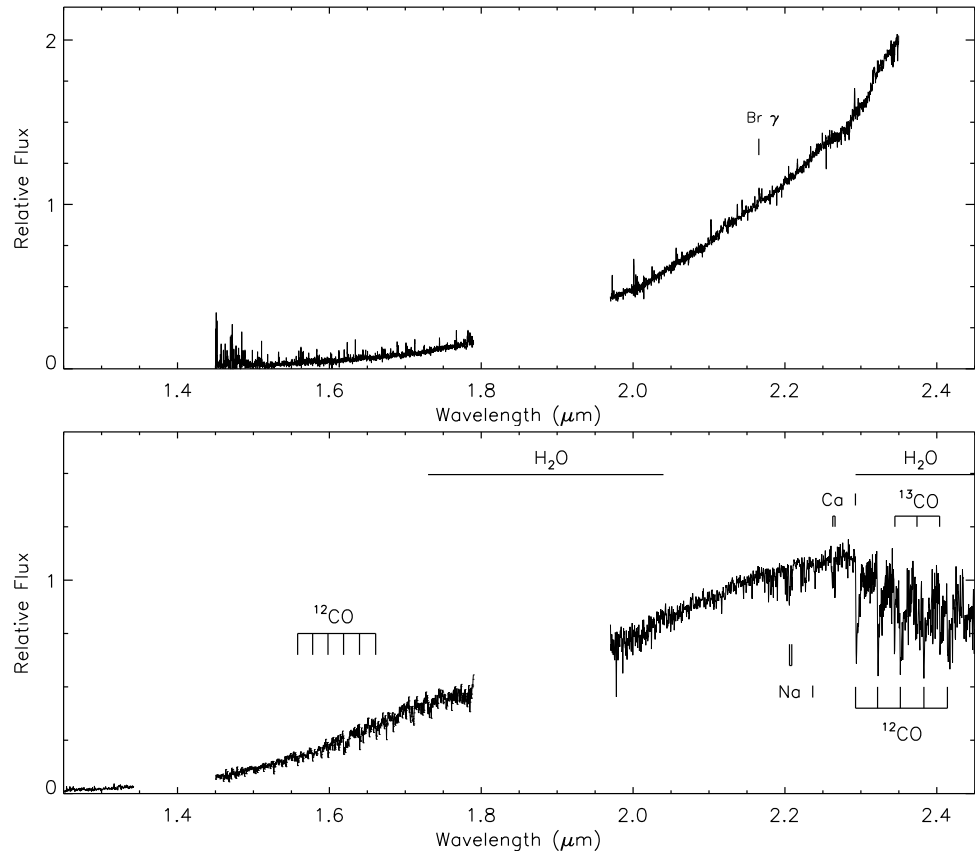

Figure 6.7: FIRE spectra of objects VVVv240 (top) and VVVv202 (bottom).

Between 21-24 objects are found to show have Brγ emission which amounts to $60-69\%$ of the spectroscopic sample. This feature is seen in absorption in only one of our objects. CO emission is observed in $8-11$ objects or $23-31\%$ of the sample, whilst 23 objects (66%) have H_2 2.12 μm emission in their spectra. From the latter 10 objects also show additional lines from H_2. In every case the emission from this molecule is likely arising from shock-excited emission given that higher excited transitions are usually weak or not present in the spectra. Atomic lines of Na I and Ca I are not common in our sample, with 4-5 objects showing absorption at these wavelengths (11-14%) and emission in 6-8 objects (17-23%). When Na I was observed in emission, CO was usually also in emission.

Brγ is not observed neither in absorption nor emission for 10 objects in the sample. One of these correspond to VVVv815, an object for which only strong H_2 emission is present (see figure 6.21 later in this chapter). In fact, the 2.12 μm line has an equivalent width of EW$=-119$ Å which corresponds to the largest equivalent width measured for this line across the whole sample. VVVv406 also does not show any features at the wavelength of Brγ, but is also in general a featureless spectrum with weak H_2 2.12 μm emission. The remaining 8 objects are characterized by having strong CO absorption and/or the presence of cold CO, similar to the case of GPS objects GPSV3 and GPSV15 (section 4.3.3). The presence of other photospheric absorption features is not observed in these 8 objects.

CO absorption is also observed in three objects which show Brγ emission or absorption.

Object	$H_2(2.12\mu m)$	$Br\gamma(2.16\mu m)$	$NaI(2.21\mu m)$	$CaI(2.26\mu m)$	$^{12}CO(2.293\mu m)$	$MgI(2.28\mu m)$
VVVv20	-9.8± 0.4	-3.8± 0.6	-0.7± 0.2	–	-5.3± 2.5	–
VVVv25	–	–	-0.6± 0.3	–	16.0± 7.0	–
VVVv32	–	-5.7± 2.2	–	–	-19.0±10.0	–
VVVv42	-0.3± 0.2	–	-1.0± 0.3	–	8.0± 4.0	–
VVVv45	–	–	–	–	33.0±11.0	–
VVVv63	-4.3± 0.8	-2.1± 0.5	–	–	–	–
VVVv65	–	-1.2± 0.5	–	–	–	–
VVVv94	-0.7± 0.3	-7.0± 1.5	–	–	-5.0± 7.0	–
VVVv118	–	-1.4± 1.0	–	–	–	–
VVVv193	-1.3± 0.6	-2.2± 0.7	–	–	-7.0± 4.0	–
VVVv202	–	–	4.7± 0.4	5.3± 0.5	37.0± 2.0	–
VVVv229	–	–	–	–	25.0± 7.0	–
VVVv235	–	–	–	–	47.0±12.0	–
VVVv240	–	-0.7± 0.3	–	–	–	–
VVVv270	-0.8± 0.3	-2.0± 0.7	–	–	-7.0± 4.0	–
VVVv322(13)	-2.0± 0.8	–	–	–	33.0± 7.0	–
VVVv322(14)	-5.5± 2.1	–	–	–	25.0± 8.0	–
VVVv374	-1.9± 0.2	-2.1± 0.3	-0.8± 0.2	–	-4.5± 1.5	–
VVVv405	-7.5± 1.8	-0.9± 0.4	–	–	–	–
VVVv406	-0.5± 0.2	–	–	–	–	–
VVVv452	-1.2± 0.6	-3.6± 1.1	–	–	-8.0± 4.0	–
VVVv473	-30.1± 3.9	-1.7± 1.2	–	–	-1.3±12.0	–
VVVv480	–	-4.4± 2.2	–	–	–	–
VVVv514	–	-7.8± 2.3	–	–	–	–
VVVv562	-3.2± 0.5	-3.4± 1.1	2.0± 0.3	–	–	–
VVVv625	-0.8± 0.2	-3.6± 1.7	–	–	–	–
VVVv628	-1.7± 0.7	-1.4± 0.5	3.1± 0.6	3.2± 0.9	13.0± 8.0	–
VVVv630	–	0.7± 0.2	1.3± 0.2	1.8± 0.6	14.0± 5.0	–
VVVv631	–	-2.4± 0.4	-1.4± 0.2	–	-1.0± 1.0	–
VVVv632	-1.4± 0.2	-2.1± 0.3	1.2± 0.2	1.1± 0.2	–	–
VVVv662	-0.3± 0.1	-4.1± 1.1	-1.2± 0.4	–	-2.0± 4.0	–
VVVv665	-1.9± 0.7	-2.4± 0.4	-3.4± 0.3	–	-52.0±11.0	–
VVVv699(13)	-14.1± 1.3	-3.5± 0.5	-5.0± 0.4	–	-40.7±11.1	-1.4± 0.5
VVVv699(14)	-15.5± 2.4	-3.1± 1.1	-3.1± 0.5	–	-21.3±10.0	-0.8± 0.3
VVVv717	-0.8± 0.3	-1.1± 0.5	–	–	28.0± 4.0	-0.9± 0.3
VVVv721	–	–	–	–	14.0± 4.0	–
VVVv796	–	–	–	–	27.0± 7.0	–
VVVv800	-2.0± 0.2	-1.2± 0.4	–	–	–	–
VVVv815(13)	-119.0±36.0	–	–	–	–	–
VVVv815(12)	-200.0±27.0	–	–	–	–	–

Table 6.6: Equivalent widths of common features found in the near-infrared spectra of YSOs and which are deceted in our VVV sample.

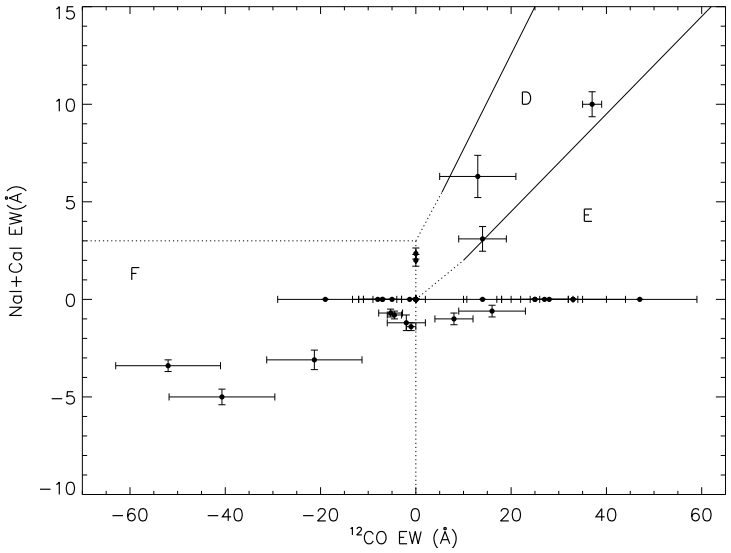

(a) a

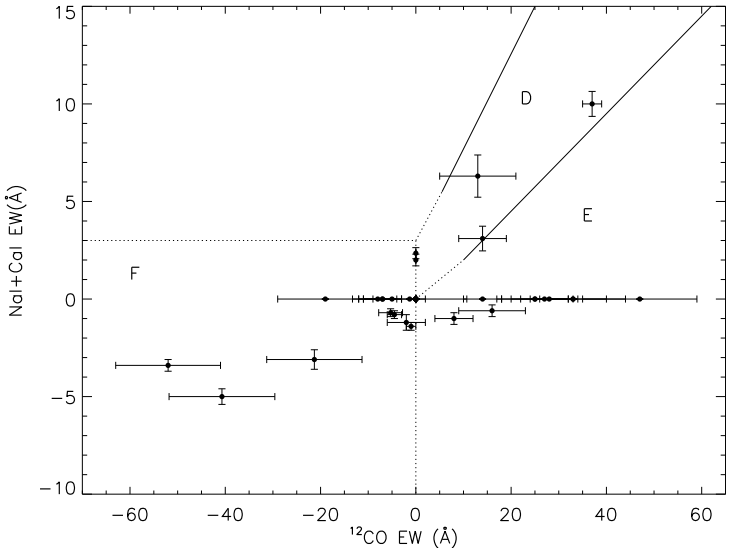

(b) b

Figure 6.8: Comparison of the equivalent widths of ^{12}CO vs NaI+CaI (top) and ^{12}CO vs Brγ (bottom) for the GPS spectroscopic sample. Regions marked on the plots are based on the work of Connelley & Greene (2010).

VVVv717 (see figure6.10 from later in this chapter) shows weak H_2 2.12 μm and possible Mg I 2.28 μm emission. The Brγ emission in this object seems to be on top of an absorption feature. The CO absorption also seems to be a combination of bandhead absorption and cold CO from lower temperature rotational transitions. No other apparent absorption features from a stellar photosphere are observed. The two other objects that show CO absorption are VVVv630 and VVVv628, in both cases the CO absorption seems to arise from a stellar photosphere as other features associated with a photosphere, such as Na I and Ca I are also observed.

The detection frequency for Brγ emission is lower, but not significantly so, than the ones obtained for different classes of YSOs (see section 5.1 and references therein). In the case of

CO emission our numbers seem to be comparable albeit slightly higher than those reported in previous studies. For H_2 emission, the detection rate in our sample appears to be significantly higher.

The detection rates of both H_2 and CO emission in our sample seem to be higher than previous studies. These features are commonly associated with outbursts events. In addition, the lack of detection of photospheric absorption features, implies that these are objects with high veiling from hot circumstellar material. High veiling could be related to high accretion states (Connelley & Greene 2010).

Figure 6.8 shows the relation between the equivalent widths of CO with those of Brγ and Na I+Ca I. Similar to what was observed in the GPS spectroscopic sample, we see that VVV objects avoid region D in figure 6.8a where "normal" class I YSOs with Brγ emission, but with low veiling and the presence of photospheric absorption features preferentially locate in the sample of (Connelley & Greene 2010). The somewhat lower detection of Brγ emission in our sample can be explained by this fact, given that most objects in that study showing this emission feature locate in region D.

Objects in our sample are mostly found in two regions of figure 6.8a: 1) Region F, where objects with high veiling and active states of accretion are expected to be located. This seems to be supported by the fact that objects falling in this region are also located in region A of figure 6.8b , usually showing CO and Brγ emission in addition to shock-excited emission from H_2. 2) Region E, where FUors are usually found. Figure 6.8b also shows the fact that we are avoiding so-called "normal" class I YSOs expected to be located in region B of that figure.

It is very interesting to see the agreement with results from GPS high-amplitude variable YSOs, in that we are mostly selecting objects that display characteristics of undergoing states of high accretion.

In the following section we discuss the possible FUor classification of objects which show deep CO absorption in their spectra.

6.2.3 FUor-like objects

From the spectroscopic sample, 8 objects (including VVVv717) show CO 2.29 μm absorption that appears stronger than expected from a stellar photosphere, with the additional characteristic of not displaying any other features that could be associated with a photosphere. One more star, VVVv42 shows featureless red spectrum dominated by absorption from low-temperature J-branch transitions, very similar to the variable GPSV3 from the UKIDSS sample.

Here we present a summary of the main characteristics of these objects.

- **VVVv322** This object is classified as a FUor object. A more detailed discussion is presented in section 6.3.3

- **VVVv721** Previously identified as a likely YSO in the Robitaille et al. (2008) catalogue of intrinsic red objects, the SED and near-infrared colours of the star are consistent with a class I object. The star is found within 126" of the Dark cloud SDC G338.734+0.584

(Peretto & Fuller 2009) and Molecular clouds [RC2004] G338.7+0.6-72.1 and [RC2004] G338.7+0.6-62.2 (Russeil & Castets 2004), which have a near kinematic distance of 4.2 kpc. Other star formation tracers are found within 300" of the source (HII region, YSOs) and the WISE false colour image reveals evidence of active star formation in the area (figure 6.9).

The light curve shows a slow rise with $\Delta K_s = 1.9$ magnitudes between 2010 and 2014. The classical FUor V1515 Cyg is known for displaying a slow rise in its light curve, and taking approximately 25 years to reach its maximum brightness (Kenyon et al. 1991). This slow rise has been explained as arising from thermal instabilities that spread in an inside-out fashion (see e.g Audard et al. 2014).

VVVv721 is an optically invisible star. The spectrum of the star (figure 6.9) rises longwards of 1.3 μm , and it is nearly featureless, apart from the deep CO feature characteristic of FUors. Absorption from H_2O is also present in the spectrum. This variable star is very likely a new addition to the FUor eruptive variable class.

- **VVVv717** This object has been previously classified as a possible YSO by Robitaille et al. (2008), based on Spitzer and MIPS photometry. The SED and near-infrared colours are those of a Class I object. It is found within 15" of 5 Spitzer dark clouds from Peretto & Fuller (2009), whilst two other likely YSOs from the Robitaille et al. catalogue are found at a distance of 30" from this object. The light curve shows a continuous rise since 2010, showing a drop in brightness in 2012, with $|K_{s,max} - K_{s,min}| = 2.47$ magnitudes. The 2013 data points reveal that this object was probably close to maximum brightness at the time of the spectroscopic follow up. No information is available for photometry in 2014.

  The Robitaille et al. SED fits shows that this object is well fitted by the models. VVVv717 is also an optically invisible star, not being detected in J nor H bands in VVV. Figure 6.10 shows a red rising, nearly featureless spectrum, with no flux at wavelengths shorter than 1.4 μm. The objects shows strong and broad CO absorption and although the object does not show any absorption from H_2O, we note that other deeply embedded FUor objects have been classified as such even when lacking this feature (e.g OO Ser, PP13S, Hodapp et al. 1996; Aspin & Sandell 2001). We conclude that this star is also a likely new member of the FUor class.

- **VVVv45** Figure 6.11 shows that this object locates within several star formation indicators associated with the G305 Star Forming Complex (see e.g. Faimali et al. 2012, and section 6.4). VVVv45 is source 33941 in Table 2 of the study of YSOs towards the G305 star-forming complex of Baume et al. (2009). This object is selected based on its near-infrared colours, but no information can be found whether the authors consider this as a likely YSO and/or a member of the complex.

  The SED of this star is consistent with a Class I object, with $\alpha = 1.26$, and is well fitted to the SED of a YSO according the Robitaille et al. models. This is an optically invisible

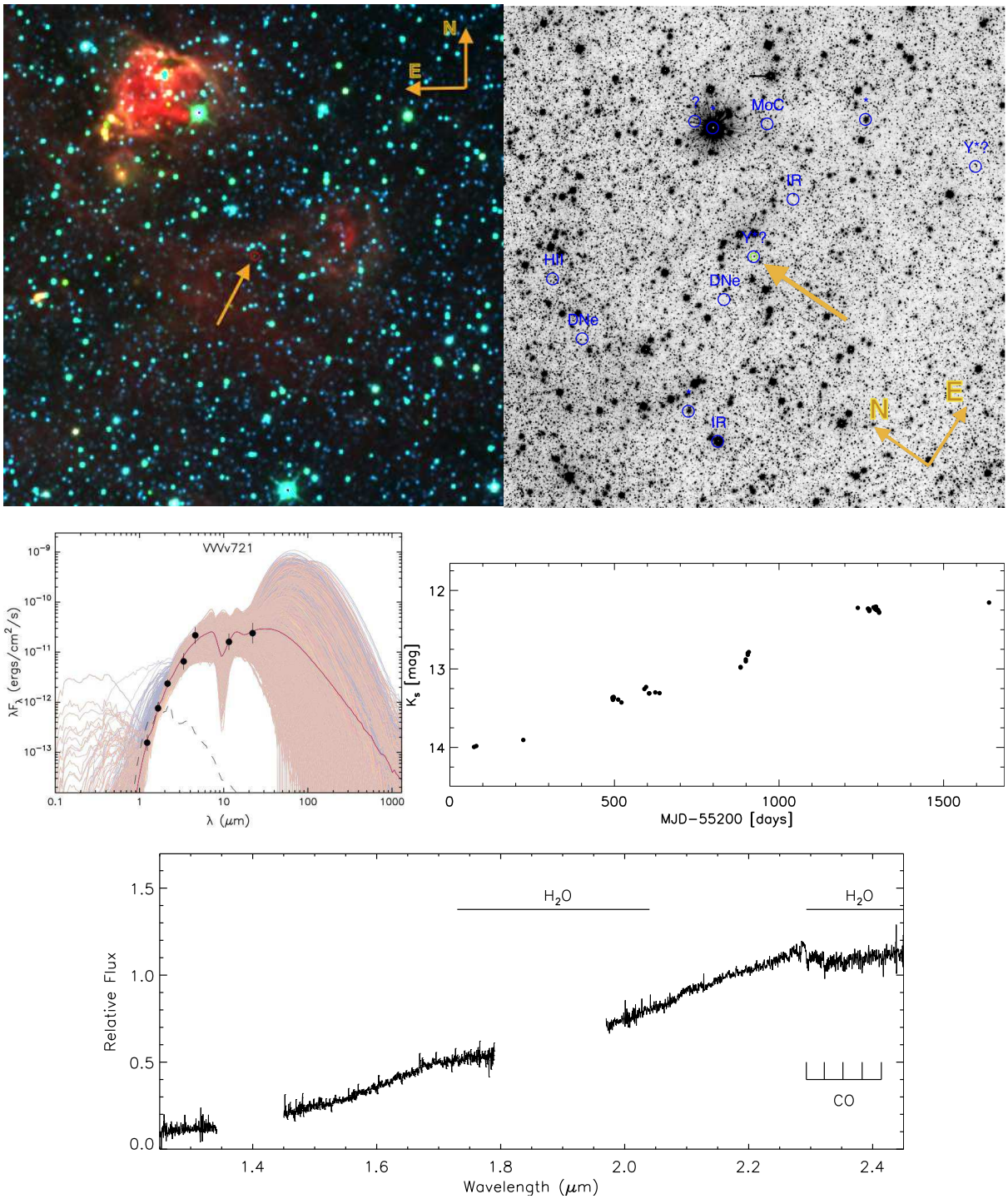

Figure 6.9: (top left) False colour WISE image (blue=3.5 μm, green=4.6 μm, red=12 μm) of a $0.44° \times 0.44°$ area centred on VVVv721. The location of the object is marked by the arrow. (top right) K_s image of a $10' \times 10'$ area centred on VVVv721. The location of the object is marked by the arrow. In addition, blue circles and labels mark objects found in a SIMBAD query with a $5'$ radius. (medium left) SED of VVVv721 along with Robitaille et al. (2007) YSO models that fulfil the criteria of $\chi^2 - \chi^2_{best} < 3N$, with N the number of data points used to generate the fits. This image is generated by the fitting tool. (medium right) K_s light curve of VVVv721. (bottom) FIRE spectrum of VVV721. The spectroscopic features found for this object are marked in the graph.

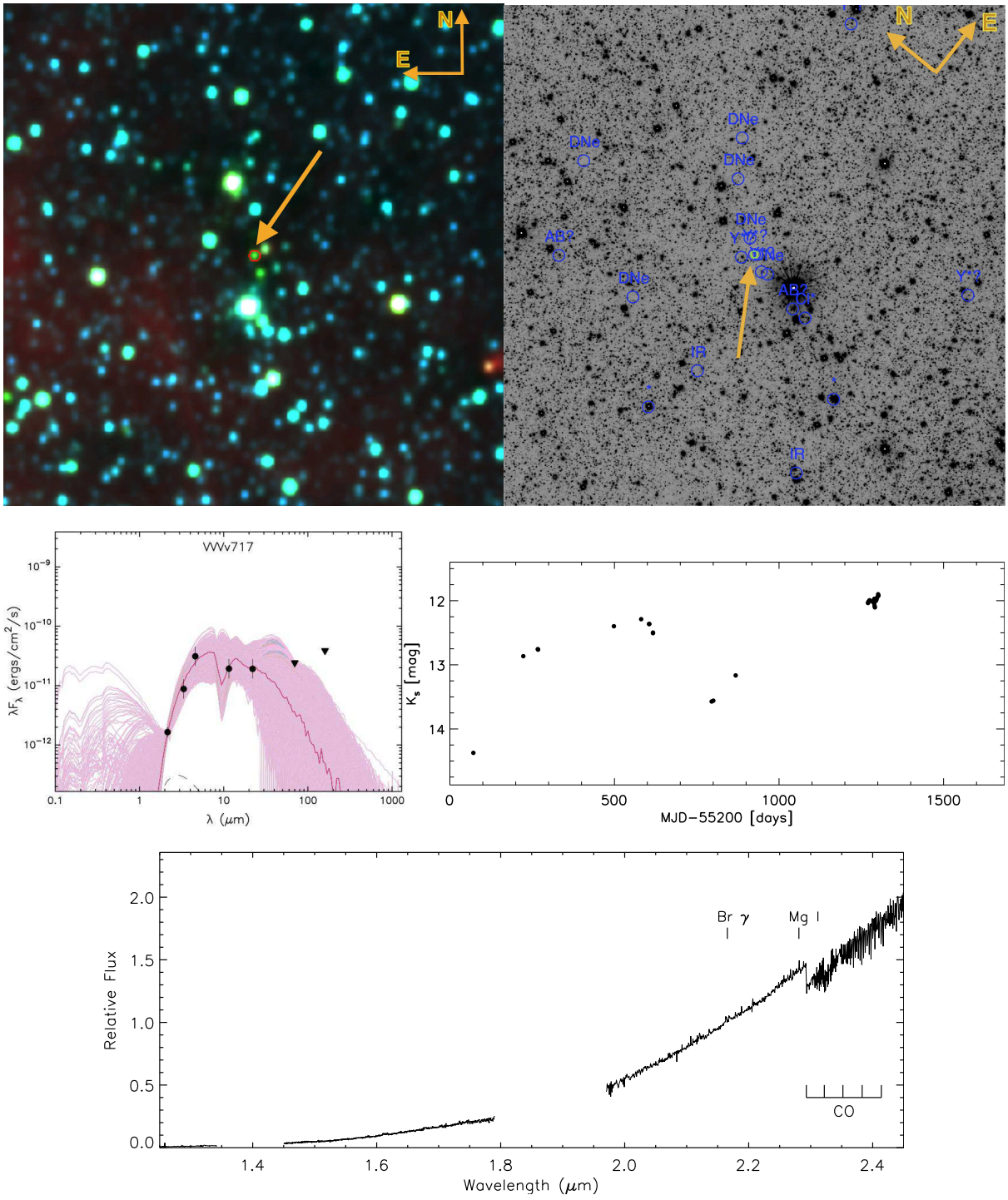

Figure 6.10: Same as figure 6.9. In the top left we present a $10' \times 10'$ WISE false colour image of the area near VVVv717

object which is not detected at J nor H bands in VVV photometry. The spectrum of the object also resembles that of deeply embedded FUor stars, with no flux at wavelengths shorter than 1.9 μm and steeply rising in the K band, with deep CO absorption at 2.29 μm. This object does not show any absorption from H_2O.

The light curve of VVVv45 is different from the previous likely VVV FUors, as it looks to be periodic resembling the light curves of Miras, and with an amplitude of $\Delta K_s = 2.2$ magnitudes. Eruptive variables are not likely to have these kind of periodicity although we note that Hodapp et al. (2012) show that variable star V371 Ser, a class I object driving an H_2 outflow, has a periodic light curve. The authors describe this object as a possible short period extension to the EXor and FUor phenomenon, where the variability arises from periodic fluctuations of the accretion rate, modulated by a binary companion. Variability on shorter timescales, but not necessarily periodic, has also been observed in source 90 of (Varricatt et al. 2005), a possible FUor also driving an H_2 outflow.

Using the distance argument similar to objects in the GPS sample, we can estimate whether a "normal" Mira variable star located within the Galaxy can show up in our survey at the magnitude of VVVv45. The extinction towards G305 is found to be $A_V \sim 10$ by Baume et al. (2009) or $A_K \sim 1.1$ magnitudes. Considering M_K=-7.25 for Mira variables (see section 4.2) yields that this type of AGB star would be located at a distance of 78 kpc. In addition, VVVv45 is detected at 9 μm in the Akari mission with $F_{9\mu m} = 0.52$ Jy. The respective K-[9] colour would correspond to a dust-enshrouded AGB star losing mass at a rate on $10^{-4.55}$ $M_\odot yr^{-1}$ in the work of Ishihara et al. (2011). A star with that observed flux and mass loss rate would be located at a distance of 44.6 kpc according to equation A2 of Ishihara et al.. The estimated distances to a Mira or a dust-enshrouded AGB are much larger than the distance to the Galactic disc edge at the coordinates of VVVv45 ($\sim$ 17 kpc).

The likely association with the G305 star-forming complex and spectrum of the object point to the object being part of the embedded class of eruptive variables. In addition we seem to discard a possible classification as an AGB star. However, the light curve of the object raises some doubts regarding the classification of VVVv45 as a FUor object.

- **VVVv796** This star has been previously been identified as a YSO in the area of HII region RCW 120 (d$\sim$ 1.4 kpc) in the work of Deharveng et al. (2009). These authors identify it as a Class I or Class II object, our estimated value of α identifies this star as a Class I object. The SED of this object is also well fitted by models from Robitaille et al. (2007).

  This is a deeply embedded, optically invisible star, which is only detected at H and K_s in VVV. Accordingly the spectrum of the object lacks any flux at J band. Some flux can be observed at wavelengths greater than 1.5 μm and some H_2O absorption could be present. The spectrum steeply rises beyond 2 μm showing the deep CO absorption characteristics of FUor objects.

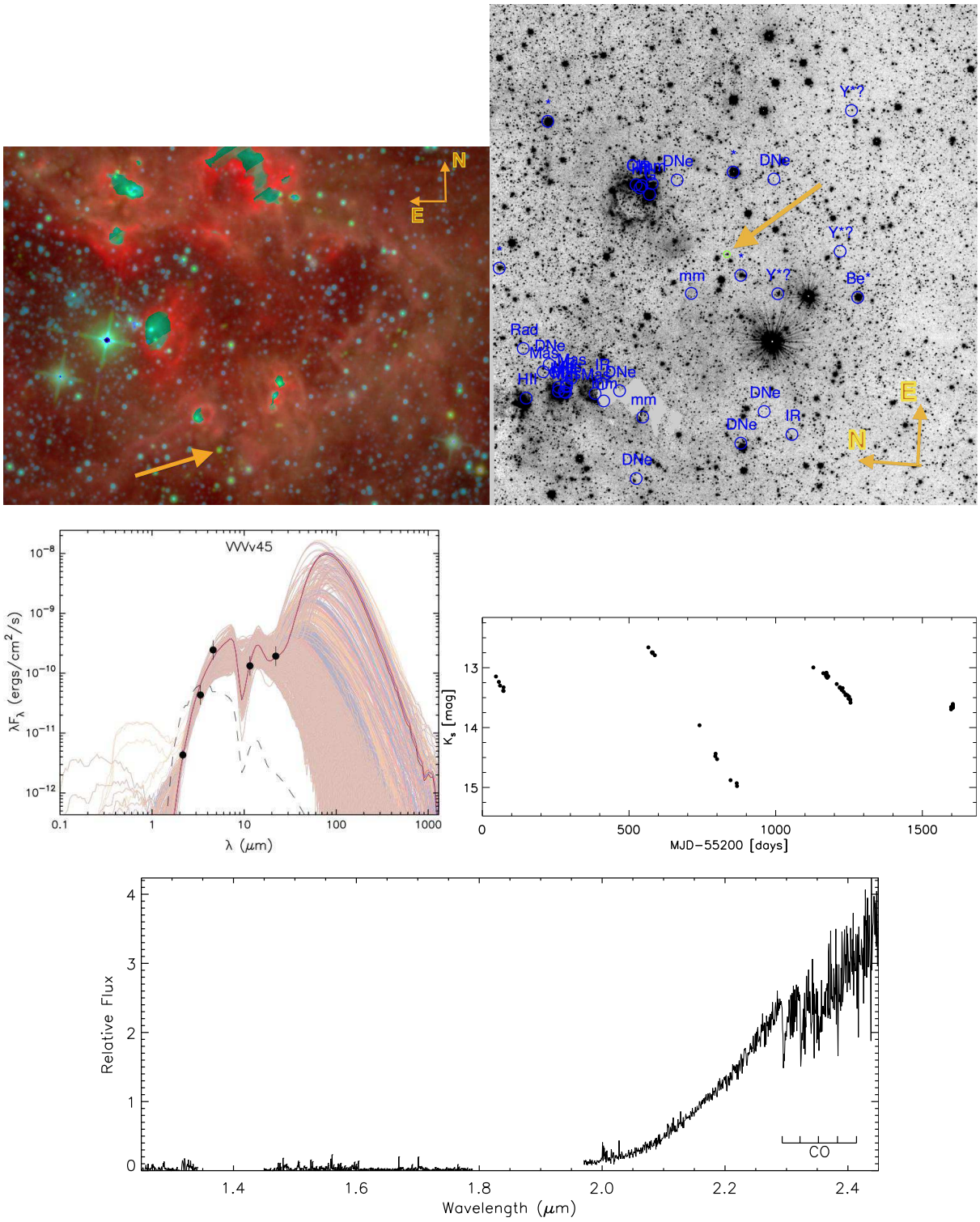

Figure 6.11: Same as figure 6.9. In the top left we present a $0.4° \times 0.4°$ WISE false colour image of the area near VVVv45

The light curve shows $\Delta K_s = 2.6$ magnitudes, and similar to VVVv45 it also seems periodic. This raises some doubts regarding a possible eruptive classification for the object. A Mira variable ($M_K = -7.25$) located at the edge of the Galactic disc at the coordinates of VVVv796 ($d \sim 22.2$ kpc), requires an extinction of $A_k \sim 31$ magnitudes in order to show up in our survey at the magnitude of VVVv796. The object is detected in the Akari survey and has $F_{9\mu m} = 3.05$ Jy. Using similar arguments as in VVVv45, we find that a dust-enshoruded AGB with that flux would be located at a distance of 21.45 kpc, which puts it almost at the edge of the Galactic disc.

Therefore, the classification of this is object as a FUor remains uncertain.

- **VVVv25** This object is optically invisible and shows a very similar SED and spectrum to object GPSV15 (section 4.4.3). WISE and SIMBAD image reveal possible association with SFRs.

  The possible classification as a post-AGB star is discussed based on similar arguments used in section 4.4.3 and for previous likely FUor objects above. The distance the Galactic disc edge at these coordinates correspond to d$\sim$ 16.3 kpc. A Mira variable star with the apparent magnitude of VVVv25 would be located beyond the Galactic disc edge at a distance of 19.4 kpc (considering A_K=2.44 magnitudes from the maps of Schlegel et al. 1998), whilst a Carbon- or Oxygen-rich AGB losing mass at a rate of $\sim 10^{-4.9}$ $M_{\odot}yr^{-1}$ (from its K-[9] colour), would be located at a Heliocentric distance of 29 kpc.

  We can rule out classification as an evolved star, although we note that the estimated distance to a Mira variable star is relatively similar to the distance to the Galactic disc edge. This is a likely new member of the embedded class of FUors.

- **VVVv42** Is found 1.52" from IRAS source IRAS 13063-6233, which is classified as a star in SIMBAD. The object is located within 300" of 5 Spitzer dark clouds and is in the vicinity of the G305 star-forming complex (figure 6.14 and section 6.4). The spectrum of the object is very red and does not show any features that could be associated with a stellar photosphere. The source resembles GPS variable GPSV3 as it is dominated by absorption of low temperature rotational transitions from CO.

  However, some doubts arises given the fact that the object does not seem to be well fitted by YSO models, with a high χ^2 and a low number of models that fulfil the condition $\chi^2 - \chi^2_{best} < 3N$. Using the distance argument for a Mira variable and with the extinction of $A_V \sim 10$ towards G305 (Baume et al. 2009) yields that this type of AGB stars could be located at a distance of 27.7 kpc, larger than the distance to the Galactic disc edge at the coordinates of VVVv42 ($\sim$ 17 kpc). The object is detected in 9 μm in the Akari mission with $F_{9\mu m} = 7.525$ Jy. The respective K-[9] colour would correspond to a dust-enshrouded AGB star losing mass at a rate on $10^{-4.4}$ $M_{\odot}yr^{-1}$ in the work of Ishihara et al. (2011). A star with that observed flux and mass loss rate would be located at a distance of 12.9 kpc according to equation A2 of Ishihara et al., which would place within the Galactic disc.

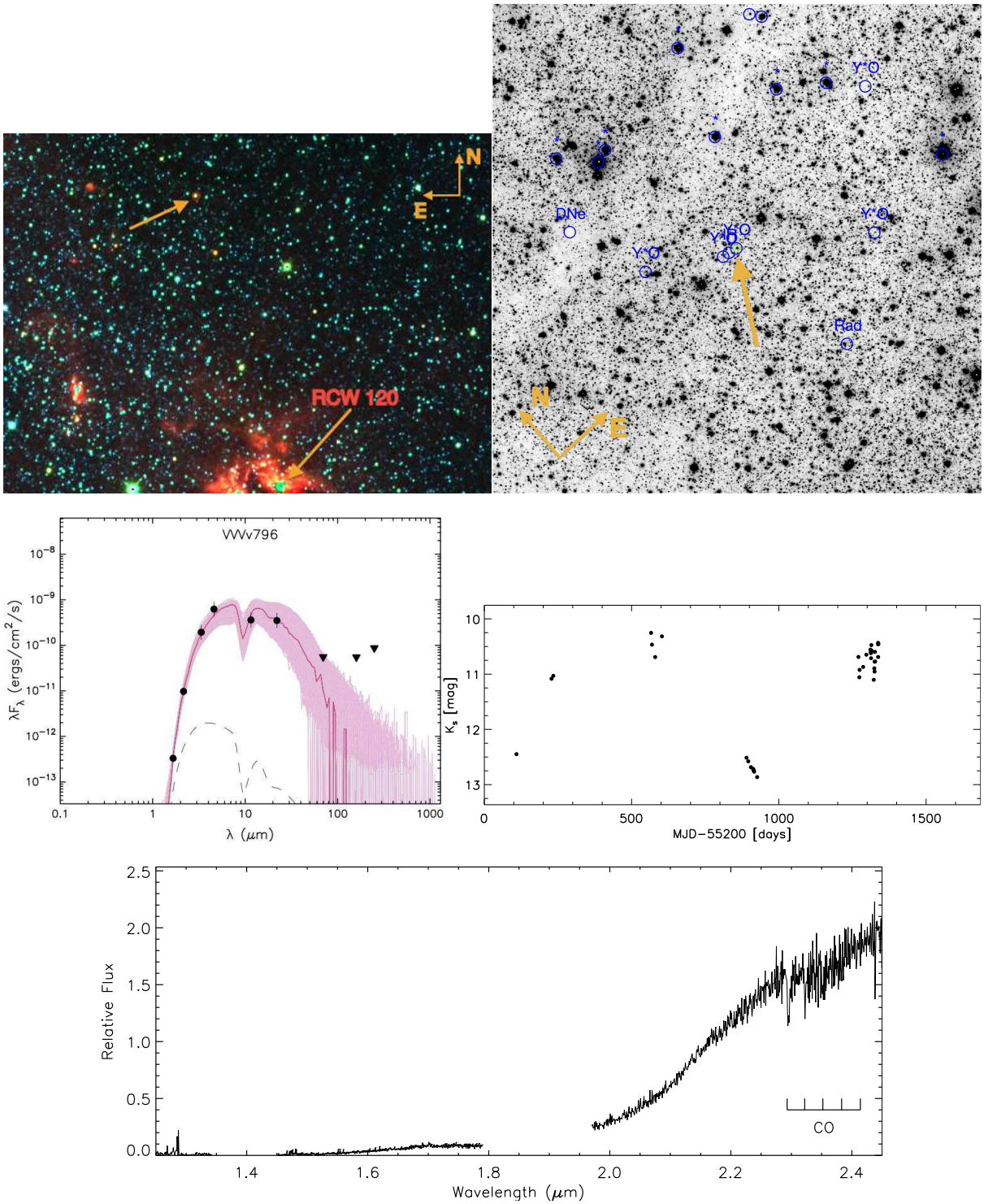

Figure 6.12: Same as figure 6.9. In the top left we present a $0.8° \times 0.6°$ WISE false colour image of the area near VVVv796. The location of HII region RCW 120 is also marked in this image.

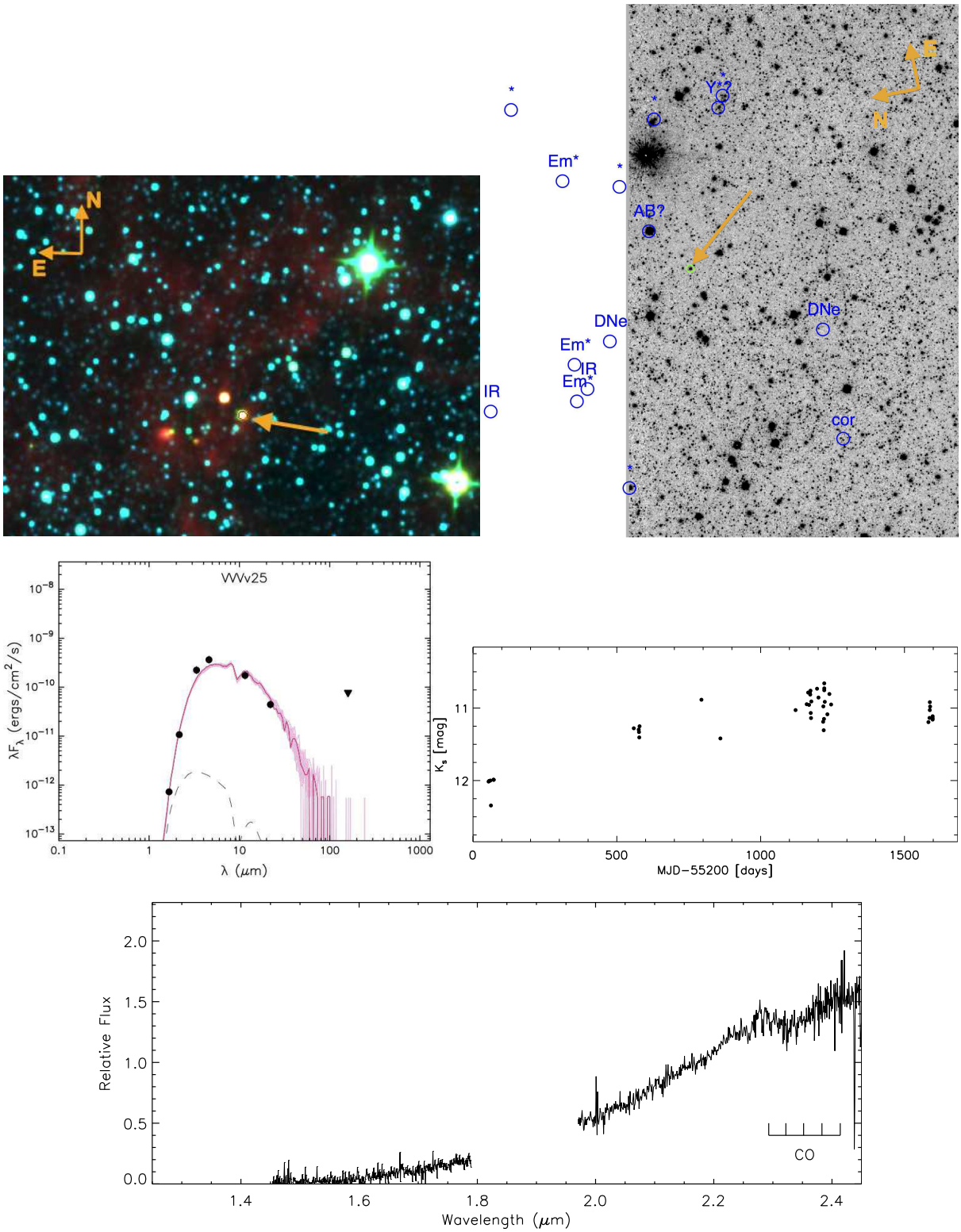

Figure 6.13: Same as figure 6.9. In the top left we present a 20′×15′ WISE false colour image of the area near VVVv25.

Therefore, even though the object shows characteristics of YSOs and association with a SFR, we cannot rule out a different classification for this object.

- **VVVv235** The variable star is likely associated with OH maser OH 330.93-0.14 (Sevenster et al. 1997) which is located 1.4" from the VVV object. This source is also located 164" from several masers, which in fact are part of the maser cluster OH 330.953-0.182, which is associated with massive star formation (Caswell et al. 2010). The light curve is also periodic, similar to previous objects in this sample with deep CO absorption. Given this we have to consider the possibilty that the maser emission is not related to star formation but rather to an evolved star. Galactic OH/IR stars which are characterized by the presence of this type of masers, also show spectra with deep CO absorption, although Na I and Ca I are almost always present. The latter can be suppressed by water absorption (Vanhollebeke et al. 2006). In addition the SED of the object does not appear to fit to the YSO models (Table 6.5). Using the 9 μm flux from the Akari survey, we estimate that a dusty-AGB could be located at d$\sim$16.23 kpc, which is within the Galactic disc edge (located at $\sim$20.8 kpc at this longitude).

  Thus, the classification of this object also remains uncertain.

- **VVVv229** The projected location of this star is within 300" from several indicators of active star formation (Figure 6.16). The star is not detected in both J and H bands in VVV and its spectrum shows the lack of flux at these wavelengths, rapidly rising towards 2 μm and only showing CO absorption at 2.29μm. This is all in agreement with a FUor classification. However, there are several characteristics that point towards a different classification of the star. The light curve is clearly periodic with an amplitude of $\Delta K_s = 3.7$ magnitude, making it the most extreme in the spectroscopic sample and the second most extreme in the whole VVV sample, with the first being VVVv360, an OH/IR star. Its K-[12] colour (using WISE filter $W3$) is 14 magnitudes (see figure 6.6), which is typical of OH/IR stars and embedded Carbon stars (see section 4.1) and larger than any other object in the spectroscopic sample. The star is clearly not well fitted by the YSO models of Robitaille et al., having the largest χ^2 of the spectroscopic sample.

  The observed 9 μm flux is also the largest of the sample, with $F_{9\mu m} = 37.82$ Jy. An OH/IR star with this flux can easily be found within the Galactic disc at a distance of approximately 8.6 kpc and show up in VVV.

  Thus, this object is much more likely an evolved star rather than a YSO.

Considering the arguments presented above, from the 9 objects that fall in region E of figure 6.8a, 4 are likely new members of the FUor class, although presenting a mixture of characteristics, 4 have doubtful classifications as they could be evolved stars contaminating our YSO sample, and finally 1 object is very likely a dust enshrouded AGB star rather than a YSO. This yields a fraction of 11-22% of FUors in our sample. The fact that we are likely adding at least 4 more stars to the FUor class is very significant considering that this represents a

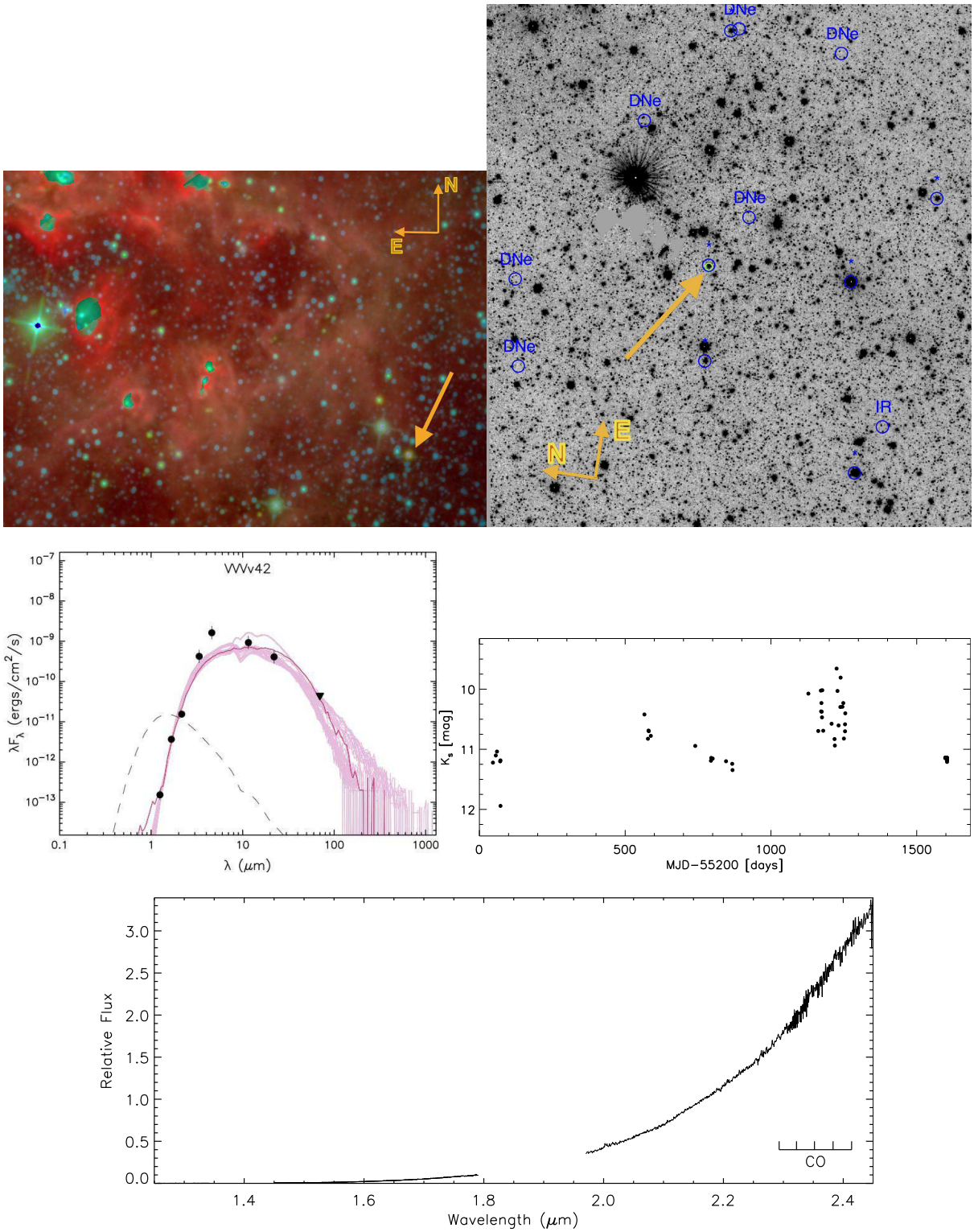

Figure 6.14: Same as figure 6.9. In the top left we present a $0.4° \times 0.4°$ WISE false colour image of the area near VVVv42.

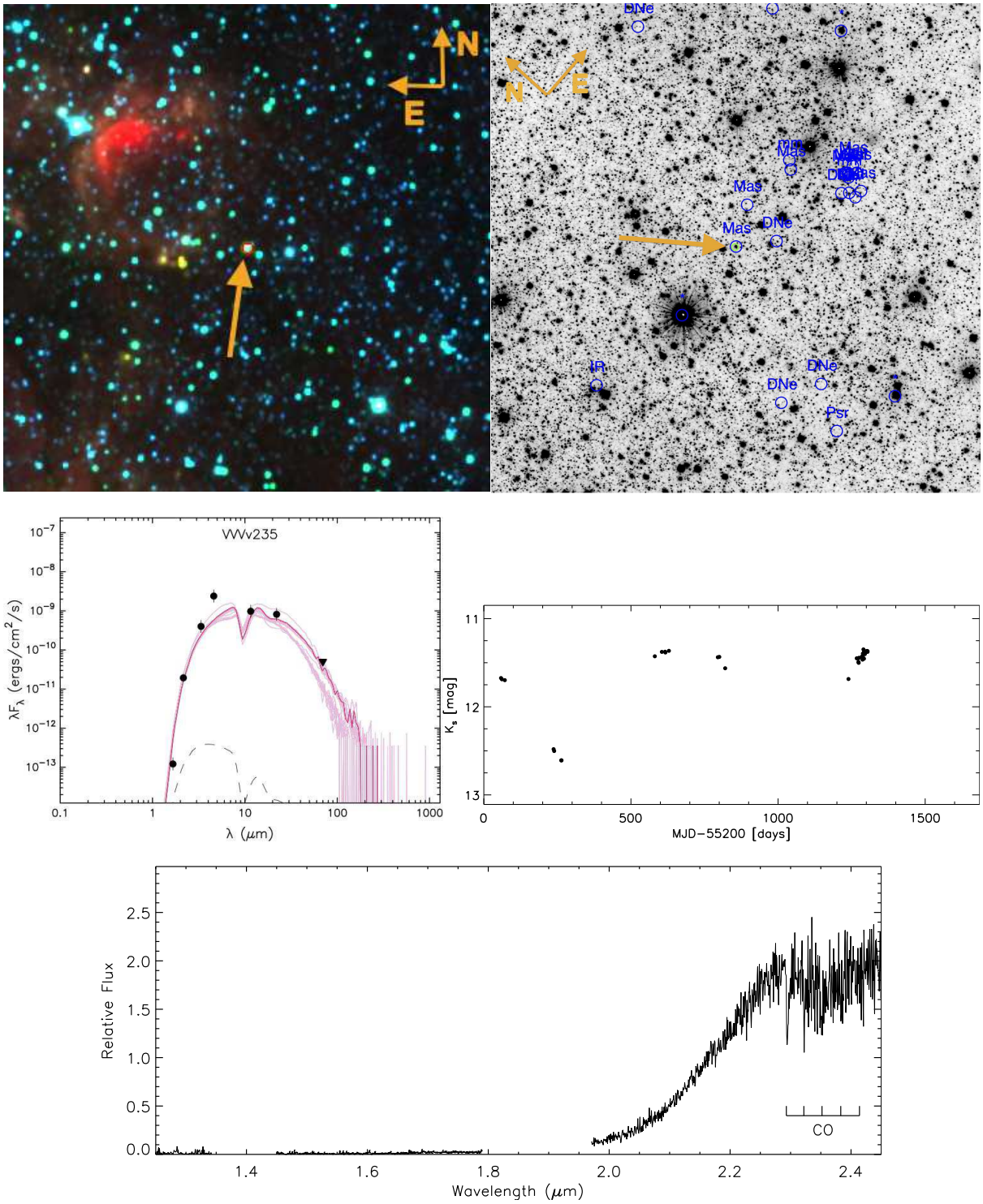

Figure 6.15: Same as figure 6.9. In the top left we present a $20' \times 20'$ WISE false colour image of the area near VVVv235.

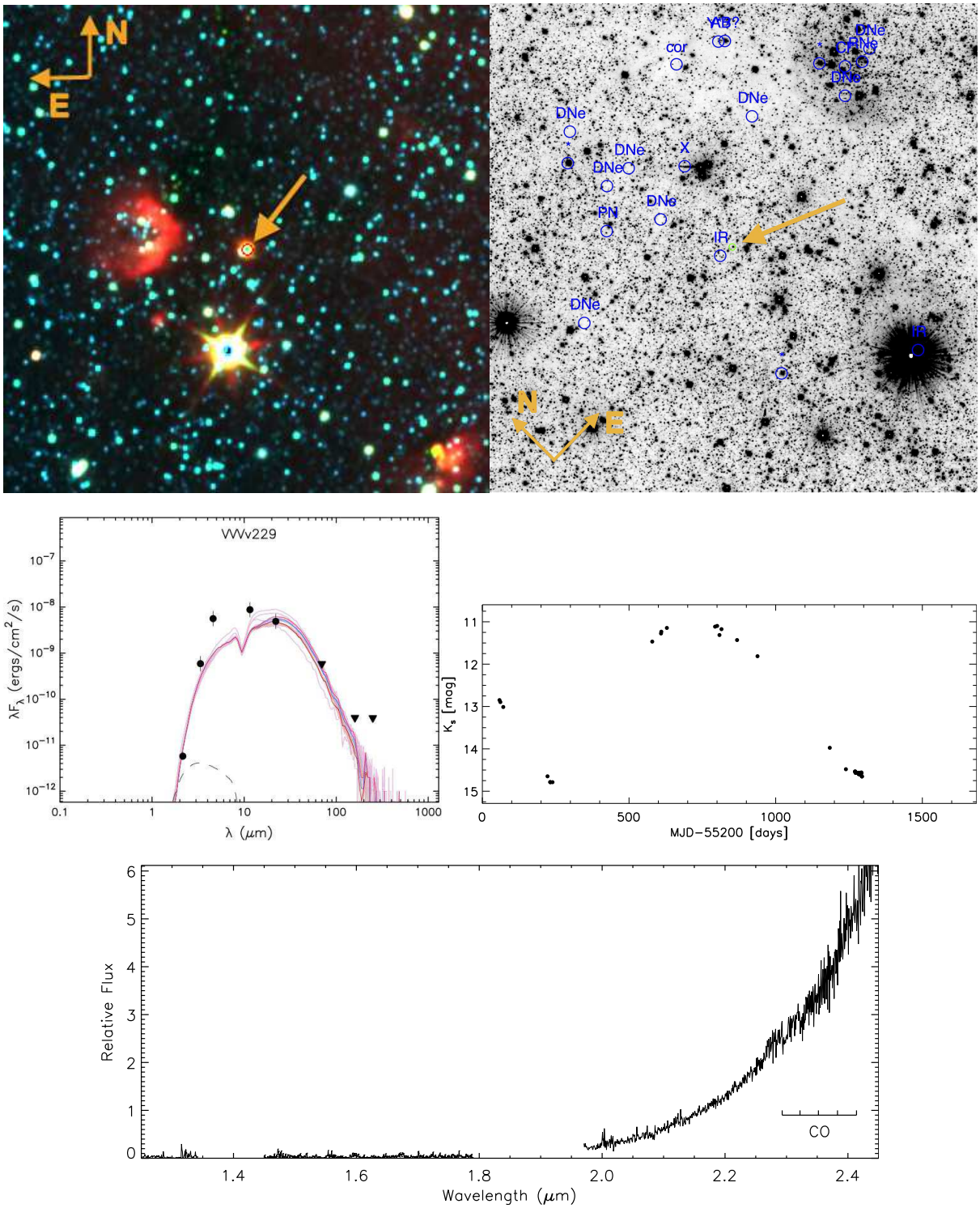

Figure 6.16: Same as figure 6.9. In the top left we present a $20' \times 20'$ WISE false colour image of the area near VVVv229

Object1	ΔK_s^a	Variability	Spectrum
VVVv20	1.71	*long-term*	Brγ, CO, Na I, H_2 emission
VVVv32	2.50	*long-term*	Brγ, CO emission
VVVv63	1.44	*short-term*	Brγ, H_2 emission
VVVv65	1.36	*doubtful*	Brγ emission
VVVv94	1.91	*long-term*	Brγ, CO, H_2 emission
VVVv118	3.92	*long-term*	Brγ emission
VVVv193	1.26	*doubtful*	Brγ, CO, H_2 emission
VVVv270	3.47	*long-term*	Brγ, CO, Na I, H_2 emission
VVVv374	2.33	*long-term*	Brγ, CO, Na I, H_2 emission
VVVv405	2.00	*long-term*	Brγ, H_2 emission
VVVv406	2.06	*long-term*	H_2 emission
VVVv452	2.46	*long-term*	Brγ, CO, H_2 emission
VVVv480	1.70	*long-term*	Brγ, H_2 emission
VVVv473	1.50	*doubtful*	Brγ, CO, H_2 emission
VVVv514	1.73	*long-term*	Brγ emission
VVVv562	2.79	*long-term*	Brγ, H_2 emission. Na I absorption
VVVv625	1.46	*short-term*	Brγ, H_2 emission
VVVv628	1.45	*short-term*	Brγ (?), CO, Na I, Ca I absorption
VVVv630	1.90	*long-term*	Brγ, H_2 emission. CO, Na I, Ca I absorption
VVVv631	2.64	*long-term*	Brγ, CO, Na I emission. H_2O absorption
VVVv632	1.51	*short-term*	Brγ, H_2 emission. Na I, Ca I absorption
VVVv665	1.63	*long-term*	Brγ, CO, Na I, H_2 emission
VVVv662	1.56	*long-term*	Brγ, CO, Na I, H_2 emission
VVVv699	2.28	*long-term*	Brγ, CO, Na I, H_2 emission
VVVv800	1.62	*long-term*	Brγ, H_2 emission
VVVv815	1.71	*long-term*	H_2 emission

Table 6.7: ΔK_s, timescale of the variability and main features observed in the spectra of likely eruptive variables from the spectroscopic sample and which do no not show FUor-like spectra.

$\sim$ 20% increase to this rare type of variable stars and we are doubling the known embedded FUor objects.

6.2.4 Eruptive Variables

In the previous section we have only considered stars which show typical characteristics of FUor objects from their near-infrared spectra. However, the majority of the remaining objects are probably new additions to the eruptive variable class as well, with these objects showing a mixture of characteristics that can be attributed to both FUors and EXors, similar to what has been observed in the more recent detections of eruptive variables (see Introduction).

From the 26 objects in this sample, 23 show Brγ emission, the exceptions corresponding to objects VVVv815, VVVv406, mentioned above, and VVVv630, whose spectrum displays photospheric absorption from CO, Na I and Ca I, with possible Brγ absorption . The majority fall in region F of figure 6.8a, and are thus characterized by the lack of photospheric absorption lines. CO emission and/or H_2 emission is also a usual characteristic of these objects. The

objects with Brγ emission are characterized by having broad emission profiles with FWHM > 100 km s^{-1} as expected from magnetospheric accretion.

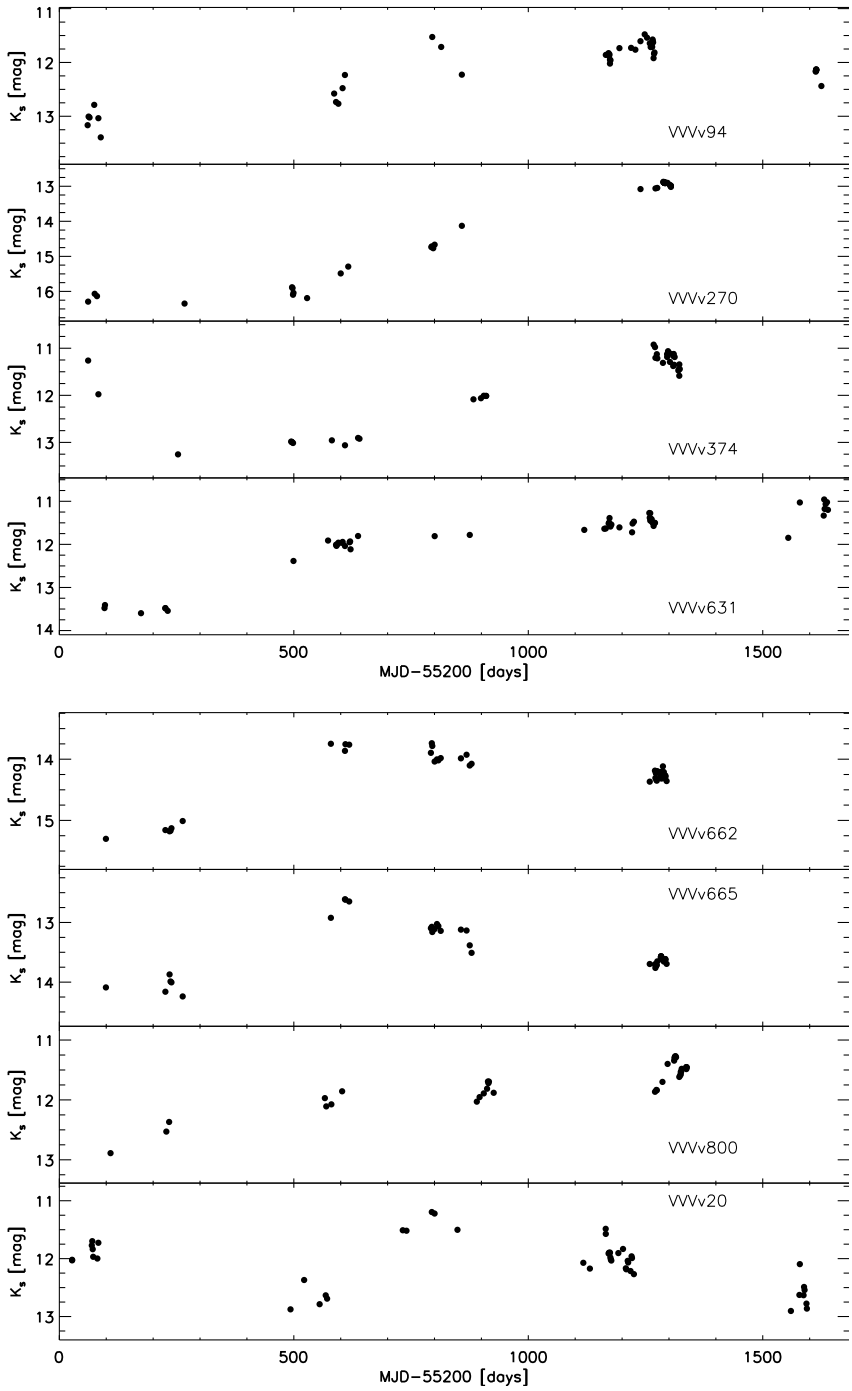

Figure 6.17: K_s light curves of objects in Table 6.7.

Inspection of the light curve of 26 objects (figure 6.17) allows us to confirm that 18 of them have light curves which show large variations occurring on long timescales or show repetitive outbursts with large ΔK$_s$ (such is the case of VVVv118). At least three of these show FUor-like behaviour in terms of the possible duration of the outburst, i.e only one outburst is observed in

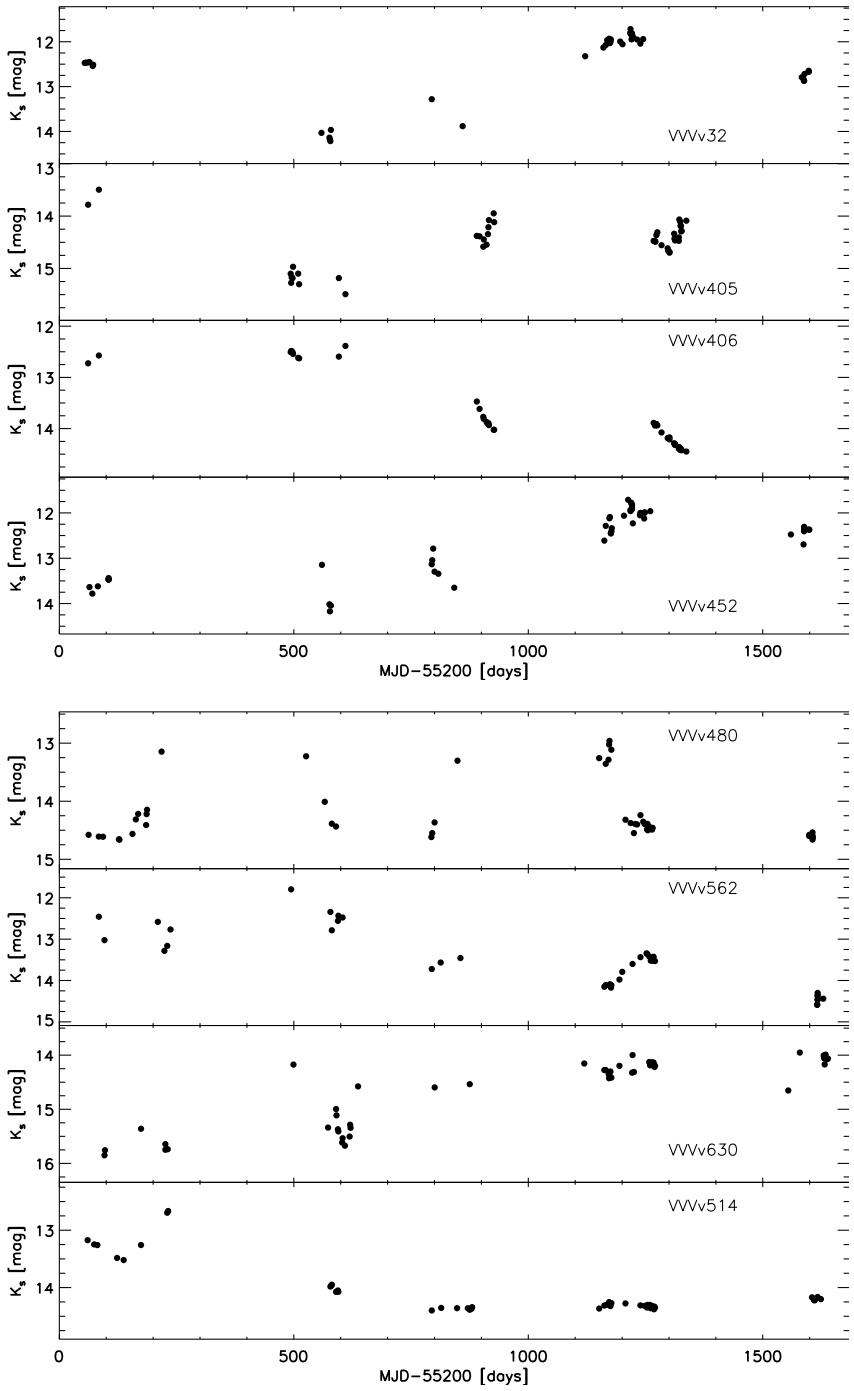

Figure 6.18: Continuation of figure 6.17

the light curve of the stars, and the duration of it seems to extend to periods longer than the one covered by VVV in the period 2010-2014 (when 2014 data is available).

Three objects have a doubtful classification, since their light curve show a relatively low amplitude of the variation and/or apparent short-term variability. The remaining four stars are clearly showing short-term variability. The objects which are classified as doubtful or with short-term variability, have smaller ΔK_s than the sample classified as eruptive. In general $\Delta K_s \leq 1.5$

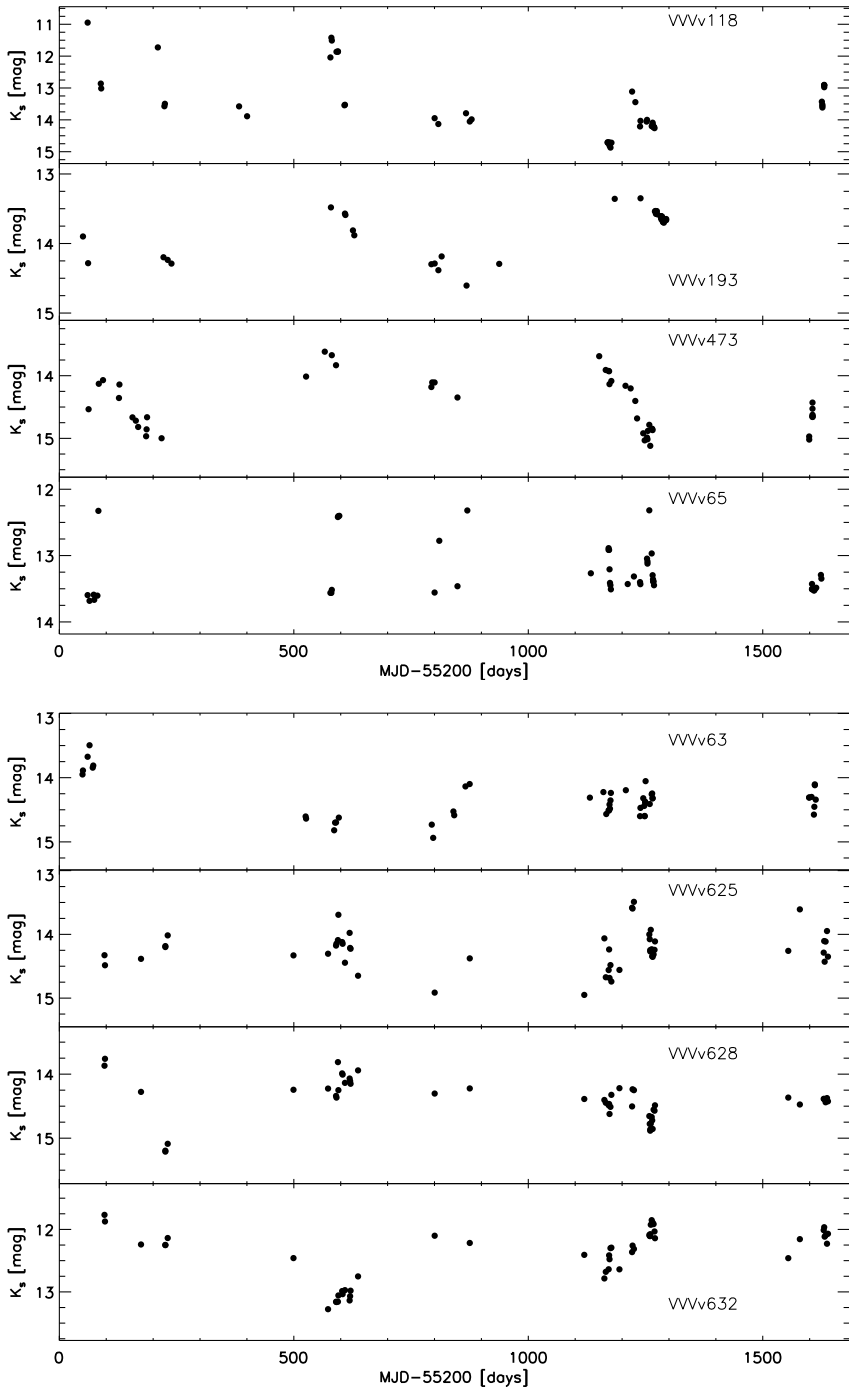

Figure 6.19: Continuation of figure 6.17

magnitudes for doubtful/short-term objects, whilst $\Delta K_s > 1.5$ magnitudes for eruptive objects.

Table 6.7 shows the classification of the objects according to their light curves, as well as their spectroscopic characteristics.

FUor-like?

As mentioned above (section 6.2.4), three objects show large outbursts, which appear to extend beyond the period covered by VVV. These are VVVv631, VVVv270 and VVVv800. The three variable stars are found within areas of star formation, with one of them having been already identified in the literature (VVVv800, see below)

VVVv800 is located in the vicinity of HII region RCW120 (d∼1.4 kpc Deharveng et al. 2009), similar to VVVv796, and has already been classified as a YSO in Martins et al. (2010). The latter have obtained near-infrared spectrum of the object, which shows a lack of absorption features and only has H_2 emission at 2.12, 2.22, 2.03 μm. Our observations of this object shows a similar behaviour, with several transitions from molecular Hydrogen present, as well as Brγ emission. This object also shows strong emission at 1.64 μm from [Fe II]. The variable star seems to be driving a powerful outflow. Unfortunately at the time of writing of this thesis the 2014 VVV data for this region had not been released and it is not possible to estimate whether this object was at a bright state during the 2014 FIRE follow up. We note also that this object is detected in both 2MASS and DENIS with $K_s = 10.82 \pm 0.03$ and $K = 11.02 \pm 0.08$ respectively, suggesting that this object had gone into a bright state prior to our VVV coverage.

VVVv270 is associated with several star formation tracers within 5 arcminutes, such as IR sources, Robitaille et al. (2008) red objects and *Spitzer* dark clouds. The object went into outburst in 2012 and shows $\Delta K_s \sim 3.5$ magnitudes. This star has not been detected in 2MASS nor DENIS, which is to be expected for the magnitude of the star prior to this current outburst ($K_s \sim 16$ magnnitudes). Its spectrum shows strong emission from Brγ, CO, Na I and H_2. As in VVVv800, VVV data from 2014 had not been released in order to estimate the state of the outburst at the moment of the spectroscopy.

VVVv631 also in a rich area of star formation, went into outburst during 2010-2011 and shows $\Delta K_s \sim 2.5$ magnitudes. This star was detected in 2MASS with $K_s = 14.11 \pm 0.12$. The 2014 data shows that the object was at a bright state during our follow-up. The spectrum shows Brγ (2.16 μm) and Pa β (1.28 μm) emission as well as Na I, CO and possible Mg I (1.502 μm) emission. This object also shows blueshifted 1.08 μm He I absorption, probably from a wind. It is very interesting to see that the object displays absorption from H_2O. In addition CO emission is not apparent in the ν=2-0 bandhead and it is only evident starting from ν=3-1. This is more likely related to problems in data reduction rather than an actual feature. The object IRAS 06297+1021(W) in the sample of Connelley & Greene (2010) shows a remarkably similar spectrum, in this case the authors discard it as a FUor object due to its rich emission spectrum. However, the observed photometric behaviour of our object makes it a very strong candidate for being part of the eruptive variable class.

6.3 Spectral variability

Three objects have repeat observations. Two of them, VVVv322 and VVVv699 have high resolution echelle spectra from April 2013 and May 2014, whilst a third object, VVVv815, was

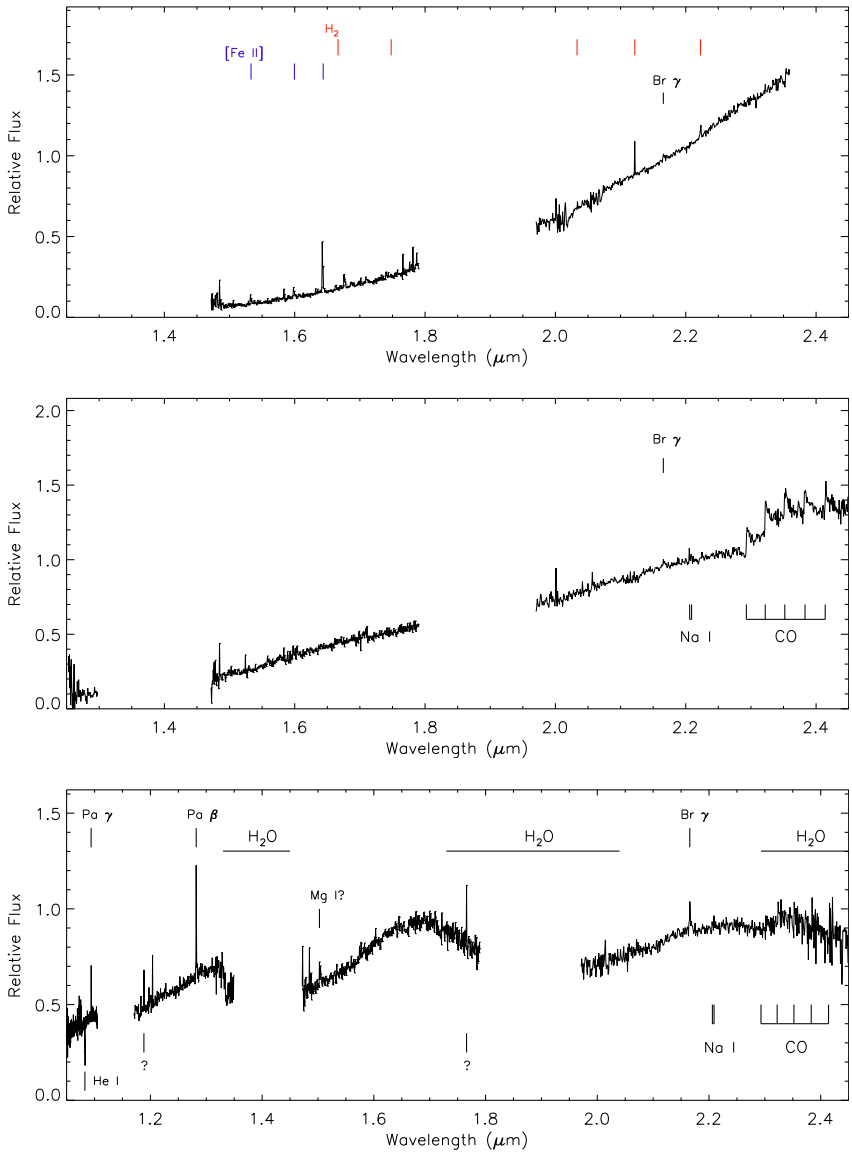

Figure 6.20: Spectra of objects VVVv800 (top), VVVv270 (middle) and VVVv631 (bottom) which show long duration outbursts resembling those of FUors. The main features observed in these objects are marked in each graph.

observed in low resolution mode with FIRE in May 2012 and in high resolution on April 2013. The three objects have strong characteristics of eruptive YSOs.

6.3.1 VVVv815

This object was discovered to show large variability in an early data release of VVV 2010 data and is not selected in the 2010-2012 analysis (see section 3.2.1). It has been found to be an intrinsic red object from mid-IR colours and classified as a likely YSO by Robitaille et al. (2008). The star is likely associated with a SFR (see figure 6.21), and its projected location is 79" from HII region [WHR97] 14222-6026 (V_{LSR}=-44 km s^{-1}, D$\sim$2.5 kpc Walsh et al. 1997). Its SED is consistent with a class I object ($\alpha = 1.58$).

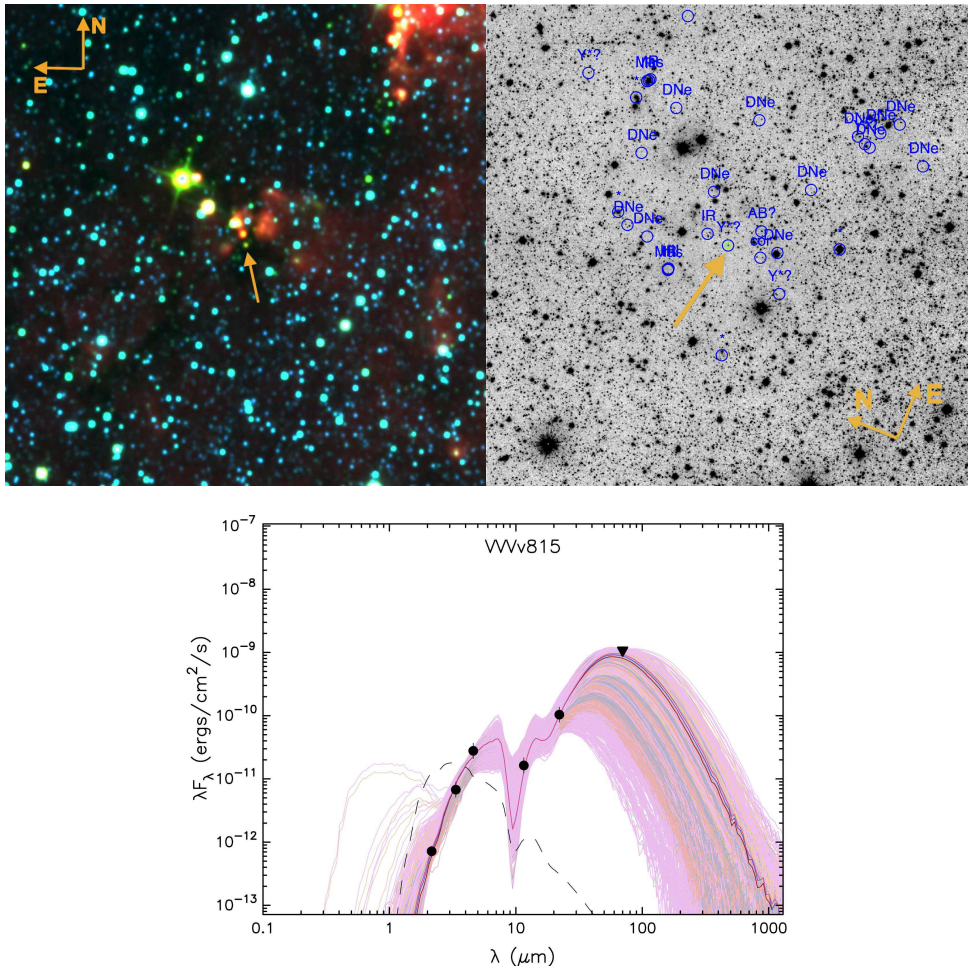

Figure 6.21: (top left) False colour WISE image (blue=3.5 μm, green=4.6 μm, red=12 μm) of a $20' \times 20'$ area centred on VVVv815. The location of the object is marked by the arrow. (top right) K_s image of a $10' \times 10'$ area centred on VVVv815. The location of the object is marked by the arrow. In addition, blue circles and labels mark objects found in a SIMBAD query with a $5'$ radius. (bottom) SED of VVVv815 along with Robitaille et al. (2007) YSO models that fulfil the criteria of $\chi^2 - \chi^2_{best} < 3N$, with N the number of data points used to generate the fits. This image is generated by the fitting tool.

VVVv815 was observed in low-resolution with FIRE in May 2012. The spectrum shows no flux at J or H bands, and is dominated by strong emission of $\nu = 1 - 0$ $\Delta J = -2$ rovibrational transitions from molecular Hydrogen , with the 1-0 S(1) 2.12 μm being the most prominent feature. The lack of higher excited lines in the spectrum of this object points to the emission arising from molecular shocks.

The 2013 medium resolution echelle spectrum from FIRE shows very similar characteristics. The higher quality of this spectrum allows us to derive a ratio $1 - 0$ S(1)/$2 - 1$ S(1) of ~ 6, which agrees with models of emission arising from molecular shocks (see e.g. Smith 1995).

6.3.2 VVVv699

Robitaille et al. (2008) finds the Spitzer IRAC colours of this object to be consistent with those of a YSO, and it is thus classified as such in their study. Our analysis shows the object as a class I YSO, with $\alpha = 2.08$, using the 2010 K band detection from VVV and IRAC, MIPS photomtery from *Spitzer*. The latter are not contemporaneous to VVV, however there doesn't seem to be a large difference between the near- and mid-IR photometry of the system, suggesting that this object was in a quiescent state during *Spitzer* observations. The object is not detected in WISE, however inspection of the images arising from this survey show the possible presence of VVVv699 (figure 6.23).

The light curve (figure 6.24) shows a possible outburst between the 2010 and 2011 campaigns of VVV, with $\Delta K \sim 2.2$ mag. The fact that the object had been on a quiescent state prior to 2010 seems to be supported by mid-IR information (see above). In addition, the object seems to be displaying some shorter-term variability ($\Delta K < 1$ mag) during 2012-2013.

Figure 6.24 shows that VVVv699 is located within 300" of several indicators of active star formation, such as likely YSOs from Robitaille et al. (2008), 6 Spitzer dark clouds, and is within the broken GLIMPSE infrared bubble [CPA2006] S43 (Churchwell et al. 2006). These infrared bubbles are expected to be formed around hot young stars in massive SFRs (Churchwell et al. 2006). Unfortunately no distance information could be found for this object and its possible relation to SFR.

The 2013 follow-up (figure 6.23) reveals a rich emission line spectrum, with strong H_2 lines from several transitions and Brγ emission. CO and Na I are also in emission. CO and NaI emission are usually attributed to a hot inner disc at a distance of a few AU from the central star. The observations from 2014 (6.24) show a decrease in the strength of several lines, most noticeable in the CO and Na I lines, with also an apparent decrease in the intensity of the Brγ emission. The H_2 emission on the other hand seems to increase, an effect that is apparent in all of the observed transitions. We do note that the changes in Brγ and H_2 are within the measurement errors and do not appear to be larger than 10%.

Connelley & Greene (2014) have studied the spectroscopic variability of a sample of Class I YSOs. They have found that tracers of mass accretion, Brγ and CO emission, are variable in all timescales, with CO being most variable (up to a factor of 3) on a timescale of 1-3 yr which correspond to a spatial scale of within 1-2 AU in a Keplerian disc (Connelley & Greene

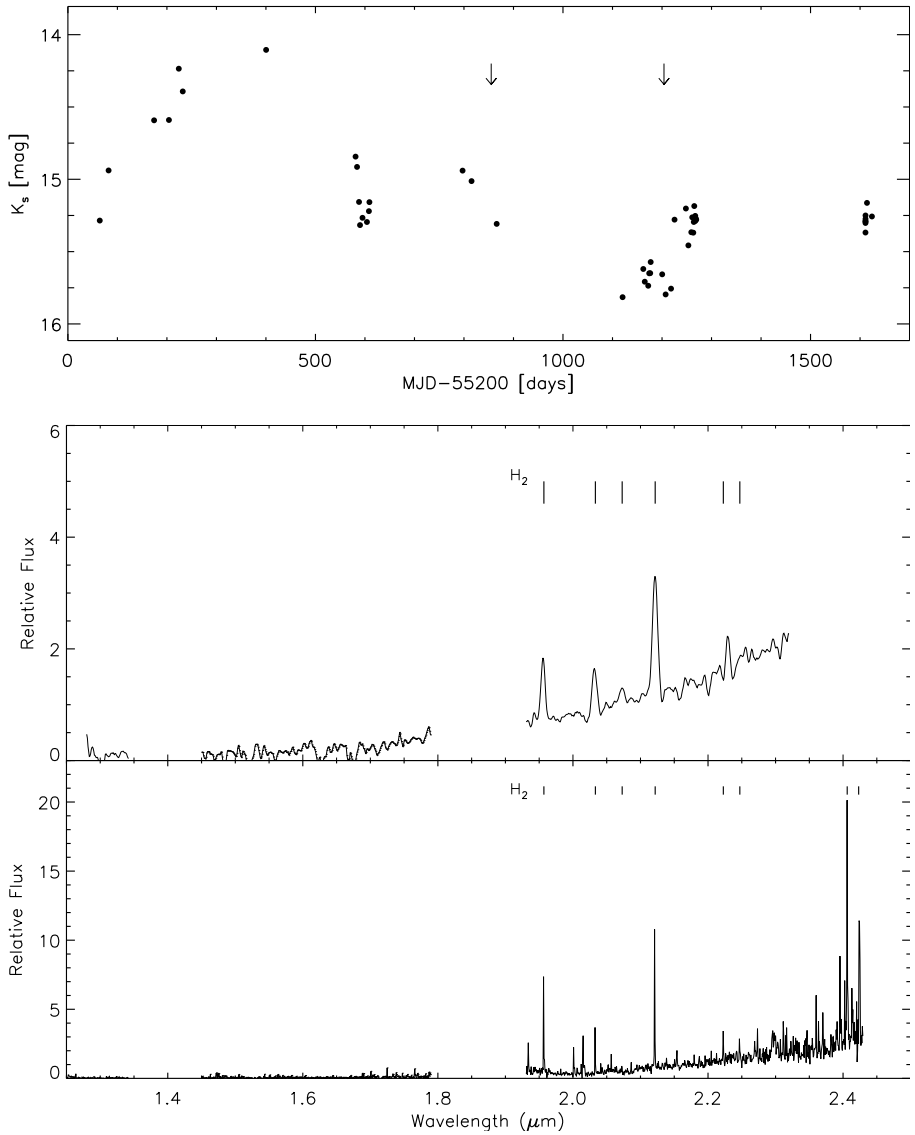

Figure 6.22: (top) K_s light curve of VVVv815, where the arrows mark the dates of the 2012 and 2013 spectroscopic follow-up. (middle) 2012 FIRE low resolution spectrum of VVVv815. (bottom) 2013 FIRE high resolution spectrum of VVVv815. In both spectra the observed rovibrational transitions of H_2 are marked at the top of each graph.

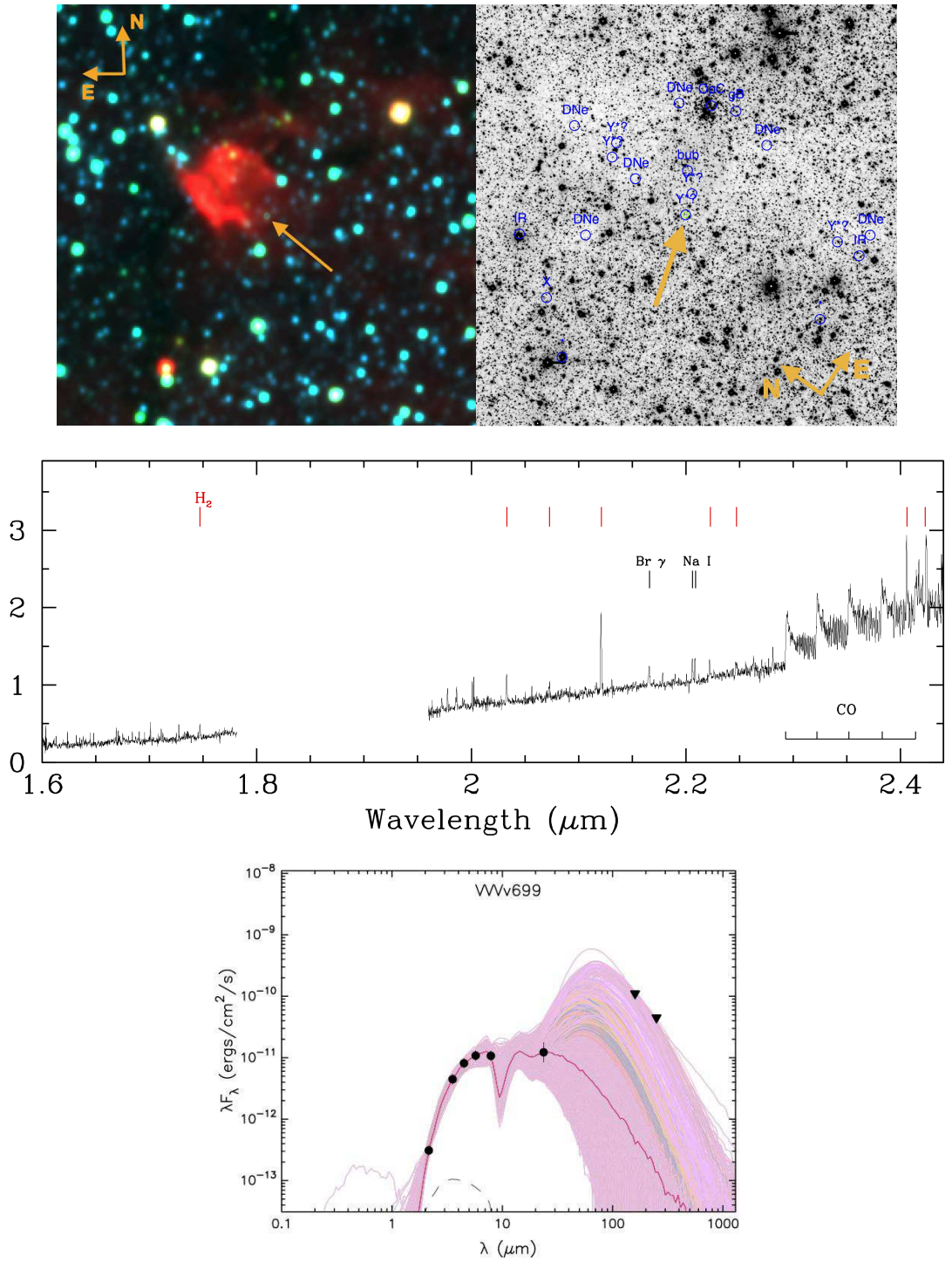

Figure 6.23: (top left) False colour WISE image (blue=3.5 μm, green=4.6 μm, red=12 μm) of a $10' \times 10'$ area centred on VVVv699. The location of the object is marked by the arrow. (top right) K_s image of a $10' \times 10'$ area centred on VVVv699. The location of the object is marked by the arrow. In addition, blue circles and labels mark objects found in a SIMBAD query with a $5'$ radius. (middle) 2013 FIRE spectrum of VVVv699, where spectroscopic features are shown in the graph. (bottom) SED of VVVv699 along with Robitaille et al. (2007) YSO models that fulfil the criteria of $\chi^2 - \chi^2_{best} < 3N$, with N the number of data points used to generate the fits. This image is generated by the fitting tool.

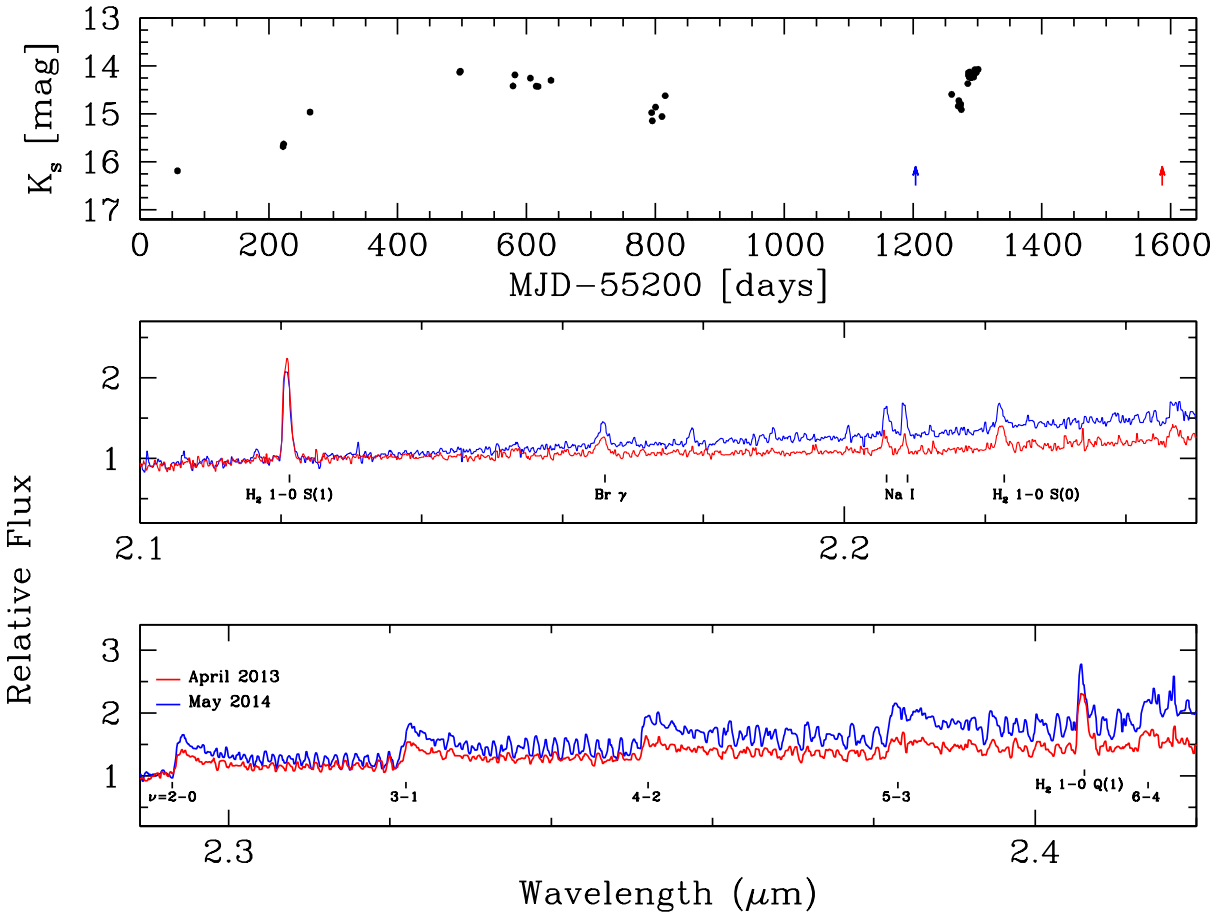

Figure 6.24: (top) K_s light curve of VVVv699. The arrows in the graph mark the dates of the April 2013 (red) and May 2014(blue) FIRE observations. (middle) Graph comparing the 2013 (red) and 2014 (blue) FIRE spectra of VVVv699 in the region 2.1-2.25 μm. Emission lines observed in this object are marked in the graph. (bottom) Similar comparison to the previous graph, but in the region 2.29-2.42 μm.

2014). These authors also find that changes in mass flow onto the central star, as traced by Brγ, are coupled to changes in the disc surface temperature (which give rise to the CO emission), whenever there is a large change in the CO emission and on long timescales. The observed variability in VVVv699 over a period of 1 year, seems to support the latter. We observed a large variation of up to a factor of 2 in CO emission, accompanied by an apparent change in Brγ emission.

We could to try to estimate whether this relates to a change in the accretion rate between the two epochs. Following Muzerolle et al. (1998b) we could estimate the flux of the Brγ emission, $F_{br\gamma}$, using the measured equivalent widths, the extinction A_V to the system and the continuum flux from K band photometry. However, we note that we do not have contemporaneous photometry to the spectroscopic measurements, and as we saw before there seems to be a short-term variability with $\Delta K \sim 0.5$ magnitudes. Thus, trying to assign a K band brightness to the dates of the spectroscopic observations from the light curve of VVVv699 would yield unreliable results.

The visual extinction to the source can be estimated using the H_2 1-0 Q(3)/S(1) ratio, r_{obs}, since these lines originate in the same upper state. We compare the observed ratio to the intrinsic one (0.7, see Beck 2007, and references therein), and derive A_V assuming the Cardelli et al. (1989) extinction law. Then,

$$A_V \left[0.404 \left(\frac{1}{\lambda_{Q(3)}} \right)^{1.61} - 0.404 \left(\frac{1}{\lambda_{S(1)}} \right)^{1.61} \right] = \log \left(\frac{0.7}{r_{obs}} \right), \tag{6.1}$$

where we estimate $A_V = 42$ and $A_V = 23$ magnitudes for 2013 and 2014, respectively. This change in A_V would imply $\Delta K_s \sim 2.2$ magnitudes, which seems highly unlikely from the light curve of this object. We note that Connelley & Greene (2010) argue against this ratio as a reliable measurement of the visual extinction, given the large discrepancies that they found between the values using this method and those found through either photometry or modelling of the continuum. They suspect that the closeness of the Q(3) line to a telluric absorption feature is likely to affect the observed ratio. A_V is also found to be variable in their sample.

Unfortunately due to the uncertainty on the K band brightness, and the lack of a known distance to the source, we cannot estimate an exact value for the accretion rate of VVVv699. Nevertheless, we can estimate a range of values for this parameter from the 2013 observations. We first assume $K = 14.2$ which corresponds to the approximate mean brightness in the 2013 epochs from VVV. From this we obtain the continuum level, F_λ for the Brγ line at 2.1659 μm. In addition, we correct this value for the extinction along the line of sight to the source, assuming $A_V = 32$ (a simple mean of the values obtained using line ratios). The line flux is then estimated from

$$F_{br\gamma} = F_\lambda \times EW \times 10^{0.4 A_\lambda}, \tag{6.2}$$

with A_λ from the Cardelli et al. (1989) law as above. We finally obtain $F_{Br\gamma} = (9.67 \pm 1.38) \times 10^{-15}$ erg s^{-1} cm^{-2}. From Connelley & Greene (2014), we have

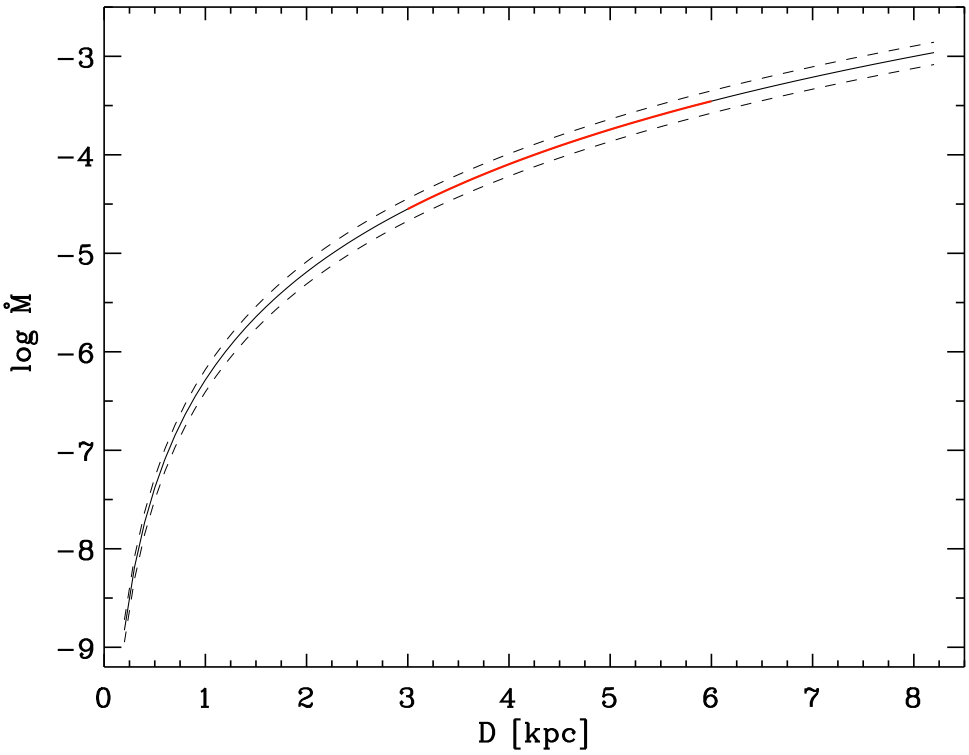

Figure 6.25: $\log \dot{M}$ estimated from the observed flux of the Brγ line in the 2013 observations, and for the distance range of infrared bubbles from Churchwell et al. (2006). The red line marks the estimated $\log \dot{M}$ for $3 < d < 6$ kpc. Errors on $\log \dot{M}$ are shown as dashed lines.

$$\log(F_{Br\gamma}) = -8.85 + 0.55 \log(\dot{M}) \tag{6.3}$$

The log F – $\log \dot{M}$ relation is derived from the Taurus objects studied in Muzerolle et al. (1998b), thus the flux must be corrected for the distance of the Taurus SFR. If we take a range of values for the distance of VVVv699 between 0.2-8.2 kpc, which corresponds to the distribution of near kinematic distances of Galactic bubbles in Churchwell et al. (2006), we obtain a large range in $\log(\dot{M})$, between -9 and -3 $M_\odot yr^{-1}$ (figure 6.25). The peak distribution of the Churchwell et al. sample with known distances is found to be at $d = 4.2$ kpc, with the majority of the sample being located between 3-6 kpc. If we assume the latter range for the distance of [CPA2006] S43, then $\log(\dot{M})$ is found to be within -4.5 and -3.5 $M_\odot yr^{-1}$ for VVVv699. If these values are true, then the accretion rate is ~ 60 times higher than the median rate found in class II objects of Muzerolle et al. (1998b) and higher than the accretion rate observed in typical class I objects (most class I objects in Evans et al. 2009, are found with $\dot{M} < 10^{-6}$ $M_\odot yr^{-1}$). These values in fact would come close to the predicted values for FU Orionis type outbursts.

6.3.3 VVVv322

This object is found to be close to several indicators of star formation as revealed by SIMBAD (see figure 6.26). These include molecular clouds, Spitzer dark clouds, possible YSOs (as deter-

mined by their mid-infrared colours by Robitaille et al. 2008) and most interestingly to several X-ray sources that could be associated with the young massive cluster Westerlund 1, which is located at $d = 3.55 \pm 0.17$ kpc and with an age of $4 - 5$ Myr (Clark et al. 2005). The projected location of VVV variable star VVVv322 is 651" from the centre of the massive cluster. The object is classified as being associated with SFRs, although its association with Westerlund 1 is not clear.

The near-infrared colours of the star show H-K excess that can be attributed to warm circumstellar material. The SED of the star is constructed using Spitzer photometry and shows the star having mid-IR excess that cannot be explained through reddening alone. The α parameter for this star is of $\alpha = 0.92$ which would classify it as a class I YSO. However, the Spitzer and VVV measurements are not contemporaneous, thus making this parameter unreliable. The star is not detected in WISE.

The light curve of VVVv322 (figure 6.27) shows the object was in a quiescent state at K_s ~15.5 mag before going into outburst between the end of the 2011 coverage and the beginning of the 2012 campaign. The brightness of the object is already declining by 2013. Due to the lack of complete coverage we cannot be certain of the amplitude of the outburst but it is likely to be $\Delta K_s > 2.5$ mag.

The observed light curve during 2013 implies a decline rate of ~ 0.0043 mag day^{-1}. If the brightness of the object continues at this rate, it would reach its quiescent state around September/October 2014. This implies that the duration of the outburst would not be longer than approximately 3 years.

The spectrum for this object was obtained in April 2013, and although the area is not covered in VVV at this epoch, inspection of the light curve allow us to assume that this observation was taken close to maximum brightness. The spectrum shows the presence of strong H_2O absorption bands at $1.3 - 1.4, 1.7 - 2, 2.3 - 2.5\mu$m and CO absorption at $2.29\mu m$. In addition there is weak emission feature at 2.12μm corresponding to molecular H_2 1-0 S(1). The spectrum lacks any other absorption features that could be associated with a stellar photosphere (see figure 6.27).

The May 2014 spectrum was taken at a time where the object has apparently faded by about 1.3 magnitudes. By this time the H_2O and CO features seem to have weakened (see figure 6.27). However, the H_2 line at 2.12 μm has become stronger. The spectrum, as in 2013, does not show any apparent photospheric features

The evidence presented above supports the scenario of VVVv322 being an eruptive YSO. However, the classification of this object within the known classes of eruptive variables seems to be uncertain. The 2013 spectrum resembles that of FU Orionis stars during periods of high accretion, (see e.g. V2775 Ori and V900 Mon, Caratti o Garatti et al. 2011; Reipurth et al. 2012) and it would agree with the fact that the star was observed at a point close to maximum brightness. However, the duration of the outburst would seem to be much shorter than expected for FU Orionis stars, but longer than for EXors. In this sense this object resembles more recently discovered objects which display mixed characteristics of eruptive variable classes (see e.g V1647 Ori, V2775 Ori, Fedele et al. 2007; Caratti o Garatti et al. 2011)

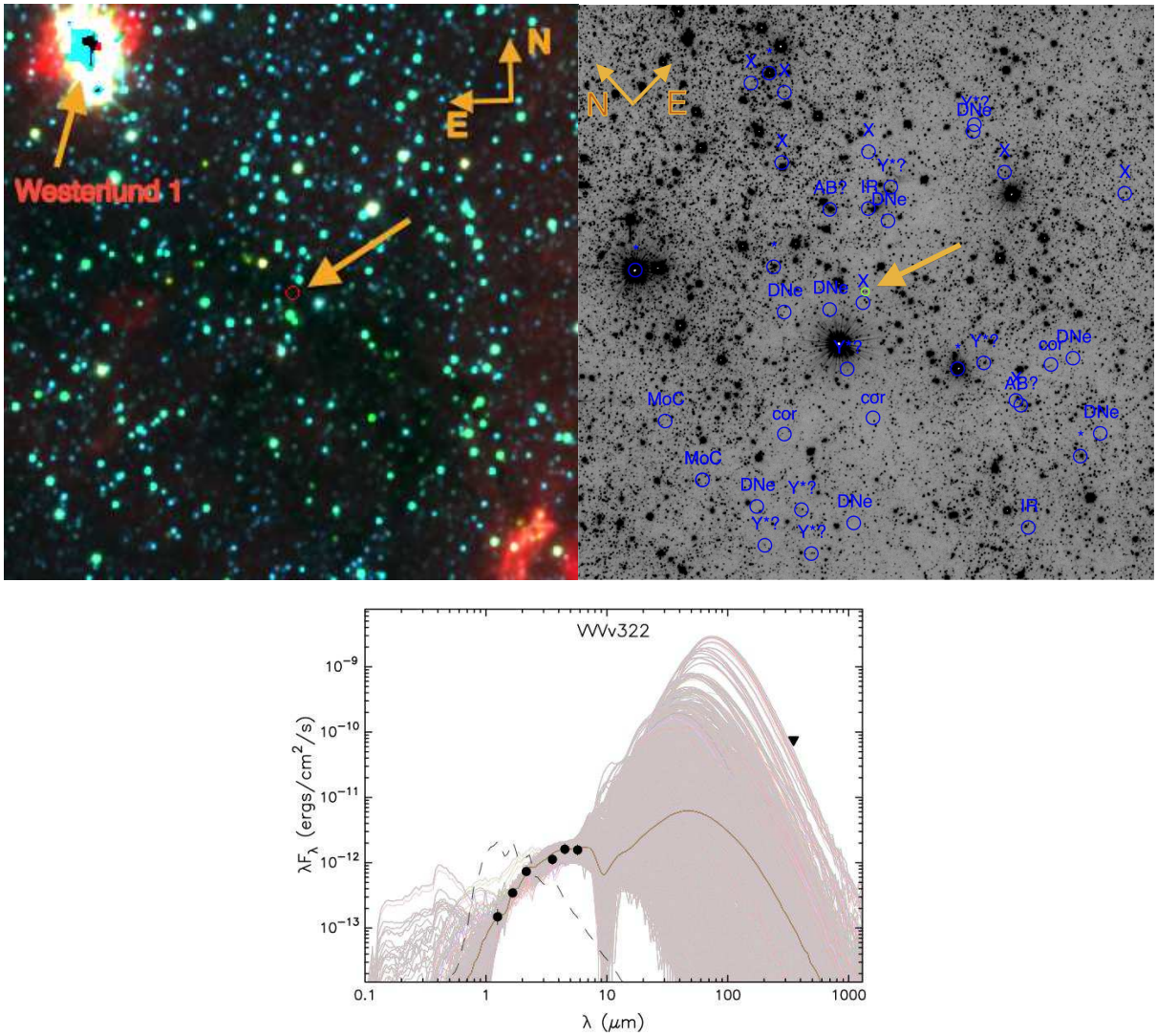

Figure 6.26: (top left) False colour WISE image (blue=3.5 μm, green=4.6 μm, red=12 μm) of a $20' \times 20'$ area centred on VVVv322. The location of the object is marked by the arrow. The SFR Westerlund 1 is also shown in the image. (top right) K_s image of a $10' \times 10'$ area centred on VVVv322. The location of the object is marked by the arrow. In addition, blue circles and labels mark objects found in a SIMBAD query with a $5'$ radius. (bottom) SED of VVVv322 along with Robitaille et al. (2007) YSO models that fulfil the criteria of $\chi^2 - \chi^2_{best} < 3N$, with N the number of data points used to generate the fits. This image is generated by the fitting tool.

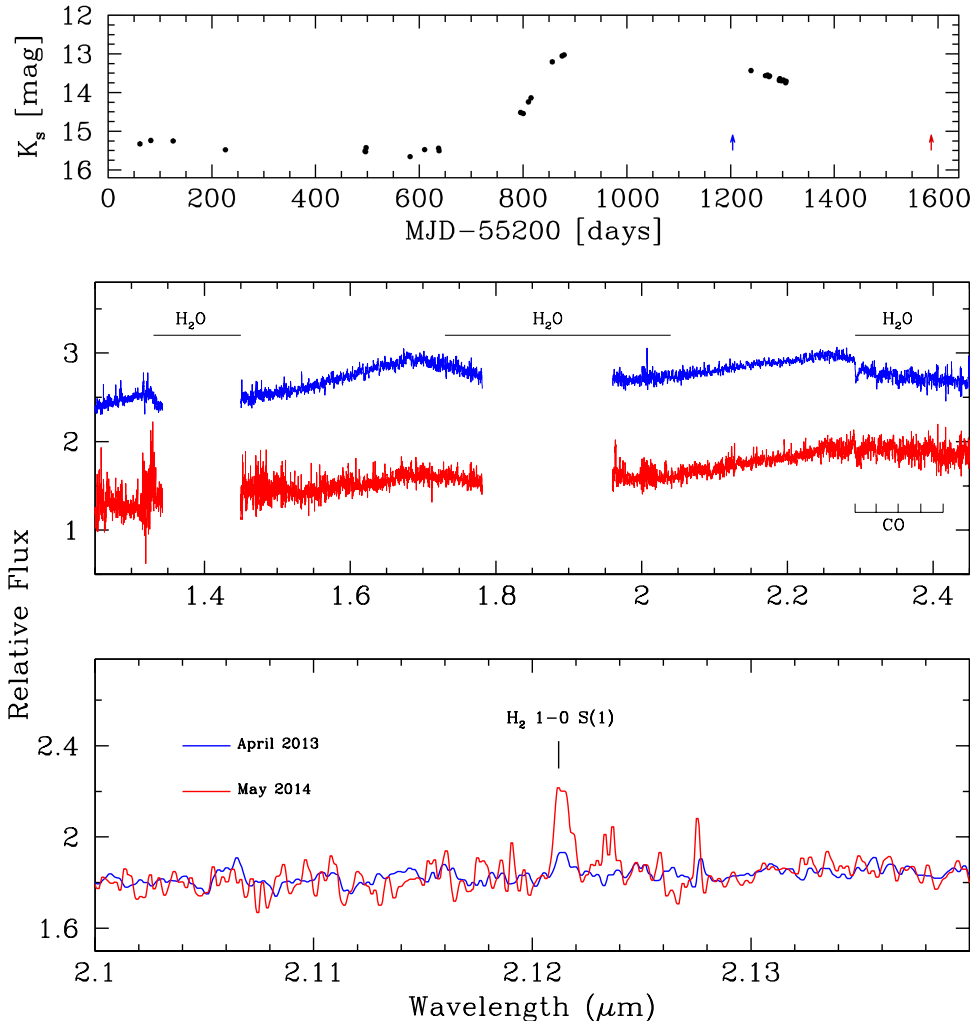

Figure 6.27: (top) K_s light curve of VVVv322. The arrows in the graph mark the dates of the April 2013 (red) and May 2014(blue) FIRE observations. (middle) Graph comparing the 2013 (red) and 2014 (blue) FIRE spectra of VVVv322, where we mark the observed absorption features of H_2O and CO. (bottom) 2013 and 2014 observations in the region 2.10-2.13 μm comparing the 2.12 μm 1-0 S(1) H_2 emission line.

Object	M_* ($M_\odot$)	$\dot{M}_{env}$ (10^{-5} $M_\odot$ yr^{-1})	$\dot{M}_{disc}$ (10^{-6} $M_\odot$ yr^{-1})	log Age (yr)	d (kpc)	log L_{tot} ($L_\odot$)	χ^2_{best}/N_{data}	N_{fits}	N_{fits2}
VVVv42	11.03±2.19	0	0.31±0.66	6.23±0.14	3.73±0.34	3.89±0.26	4.0	73	0
VVVv816	18.40±1.44	0	0.008±0.004	6.15±0.03	3.78±0.18	4.56±0.10	22.56	3	0
VVVv43	2.01±1.59	6.41±29.98	0.16±1.18	5.44±0.77	3.75±0.32	1.11±0.60	0.01	10000	8023
VVVv44	3.17±1.66	5.17±9.91	0.99±5.32	5.59±1.15	3.77±0.30	1.85±0.59	0.00	10000	6982
VVVv45	9.49±2.66	61.64±125.05	3.98±20.65	5.92±0.89	3.73±0.35	3.62±0.39	0.37	1858	560
VVVv49	9.14±1.59	0	0.09±0.15	6.27±0.19	3.59±0.24	3.63±0.21	3.57	42	0
VVVv51	4.11±1.05	0.08± 0.26	0.06±0.49	6.52±0.30	3.79±0.35	2.30±0.37	0.31	3119	273
VVVv473	5.75±1.98	2.48±4.79	4.57± 12.60	5.40±1.10	3.73±0.32	2.87±0.42	0.00	4087	2766
VVVv476	5.23±1.42	10.19±17.44	0.79± 2.65	5.61±0.96	3.73±0.34	2.54±0.33	0.04	3753	1766
VVVv480	2.66±1.67	12.68± 39.11	0.57± 7.68	5.77±0.95	3.84±0.34	1.44±0.63	0.03	6879	4241
VVVv481	2.09±2.06	13.63±42.41	1.78± 12.37	4.78±0.81	3.79±0.33	1.35±0.65	0.40	1591	1458
VVVv482	1.45±1.13	2.12±3.58	0.21± 1.02	5.18±1.03	3.79±0.33	1.05±0.55	0.02	6906	4676

Table 6.8: Parameters derived from the Robitaille et al. SED fitting for objects in the area of G305.

We note that the weakening of the H_2O and CO features by 2014 agrees with the fact that the luminosity of the star had faded by this epoch. As seen in section 2.1.1 the lack of Brγ emission in FU Orionis objects has been attributed to the fact that for high accretion rates ($\dot{M} > 10^{-5}$ $M_\odot yr^{-1}$) there is a breakdown in the magnetospheric accretion model. It would be very interesting to see that with VVVv322 returning to a quiescent state, the star would show absorption features arising from a stellar photosphere rather than the disc and Brγ returning to emission in the spectrum of the object.

The H_2 2.12 μm emission feature has become stronger between 2013 and 2014 (see figure 6.27), with the equivalent width increasing by a factor of 2. The emission does not appear to be spatially extended in any of the two epochs. The presence of this feature could be associated with shocks from molecular outflows linked to this particular outburst event. However, this is not certain, but continuous monitoring of the object could help clarify this picture. A direct link between outburst and outflows has been observed in V2494 Cyg (Magakian et al. 2013)

6.4 Incidence of High Amplitude Variability.

One of the main questions regarding episodic accretion is whether all of the stars suffer episodic outbursts of accretion. Although we cannot provide a definite answer to this question, we can try to obtain a rough estimate on the incidence of episodic accretion in areas of star formation.

For this purpose we study the variable stars which are found in the area of the G305 star-forming complex, which corresponds to one of the most massive and luminous star forming regions in the Galaxy (Faimali 2013, and references therein). G305 locates in the Galactic plane at $l = 305°$, $b = 0°$ and with an estimated distance of 3.4-4.2 kpc (Faimali 2013).

Faimali (2013) searches for YSOs in the area of G305 using 2MASS, VVV + GLIMPSE data along with Hi-Gal information. They find 601 YSOs in this area. Their study is found to be complete for YSOs with M> 2.6$M_\odot$, where physical parameters are obtained from SED fitting using models from Robitaille et al. (2006).

Most of the area of the G305 star forming complex is covered by VVV tiles d046 and d084 and 13 variable stars are found in these tiles (see figure 6.28). We used the YSO fitting tool of Robitaille et al. (2007) to derive physical parameters of the variable stars in G305. The results are presented in Table 6.8.

From the 13 stars, 6 are not considered in the subsequent analysis. One object, VVVv48, does not have any information at mid-infrared wavelengths, therefore we are not able to obtain physical parameters from SED fitting. Objects VVVv43, VVVv481 and VVVv482 have M< 2.6M$_\odot$, the completeness limit of the Faimali (2013) study. Finally objects VVVv49 and VVVv816 are most likely evolved stars.

From the remaining seven objects, four have α of Class I objects, whilst two have SEDs of flat spectrum sources. The remaining object, VVVv44, is not detected in either WISE nor any of the *Spitzer* surveys. Mid- to far-infrared fluxes for this object arise from a Hi-Gal detection located at ~ 3.5" from the VVV coordinates. It shows the object with a rising SED towards longer wavelenghts. We thus consider it as a likely class I object.

We note that the classification of objects in Faimali (2013) follows that of Robitaille et al. (2006) where objects are defined as Stage 0/I objects if $\dot{M}_{env}/M_* > 10^{-6}\mathrm{yr}^{-1}$, Stage II if $\dot{M}_{env}/M_* < 10^{-6}\mathrm{yr}^{-1}$ and $M_{disc}/M_* > 10^{-6}$, and Stage III objects if $\dot{M}_{env}/M_* < 10^{-6}\mathrm{yr}^{-1}$ and $M_{disc}/M_* < 10^{-6}$. Inspection of the results of Table 6.8 shows that 5 objects fall in the Stage 0/I class, whilst 2 are in Stage II. For the rest of the analysis we assume that a fraction of 5/7 of VVV variable stars in G305 are class(stage) I objects.

Four out of the seven objects in G305 are part of the VVV spectroscopic sample, corresponding to VVVv42, VVVv45, VVVv473 and VVVv480. From the discussion from earlier in this chapter we find that a fraction 2/4 objects are likely to be part of the eruptive variable class.

We also have to consider the fraction of objects we are not detecting in our search for high amplitude variable stars due to selection effects, i.e having a stellar classification in every epoch from VVV and/or the fact that objects having a number of epochs below the completeness limit of VVV[1] are less likely to show up in every epoch. In order to account for these effects we selected class I objects from the sample of Faimali (2013) with M> 2.6M$_\odot$ that fall in the area covered by tiles d046 and d084. We find 23 objects. From these only 8 have a stellar classification throughout all of the epochs of the corresponding master catalogues. Therefore, we consider that a correction factor of 23/8 or 2.875 needs to be applied to the number of variable stars in G305. Also, we need to take into account the fact that 2 out of 7 VVV objects would not fall in the classification of Faimali (2013) given his requirement of objects in their sample having $K_s < 13.5$ magnitudes.

Finally the fraction of Class I objects in high accretion states is

$$\frac{0.5 \times (5/7) \times (2/7) \times 2.875 \times N_{VVV}}{N_{classI,Faimali}},$$

[1]This limit is found to be at $K_s \sim 15.4$ magnitudes by a fellow PhD student, Leigh Smith, who is working on a proper motion catalogue using VVV data.

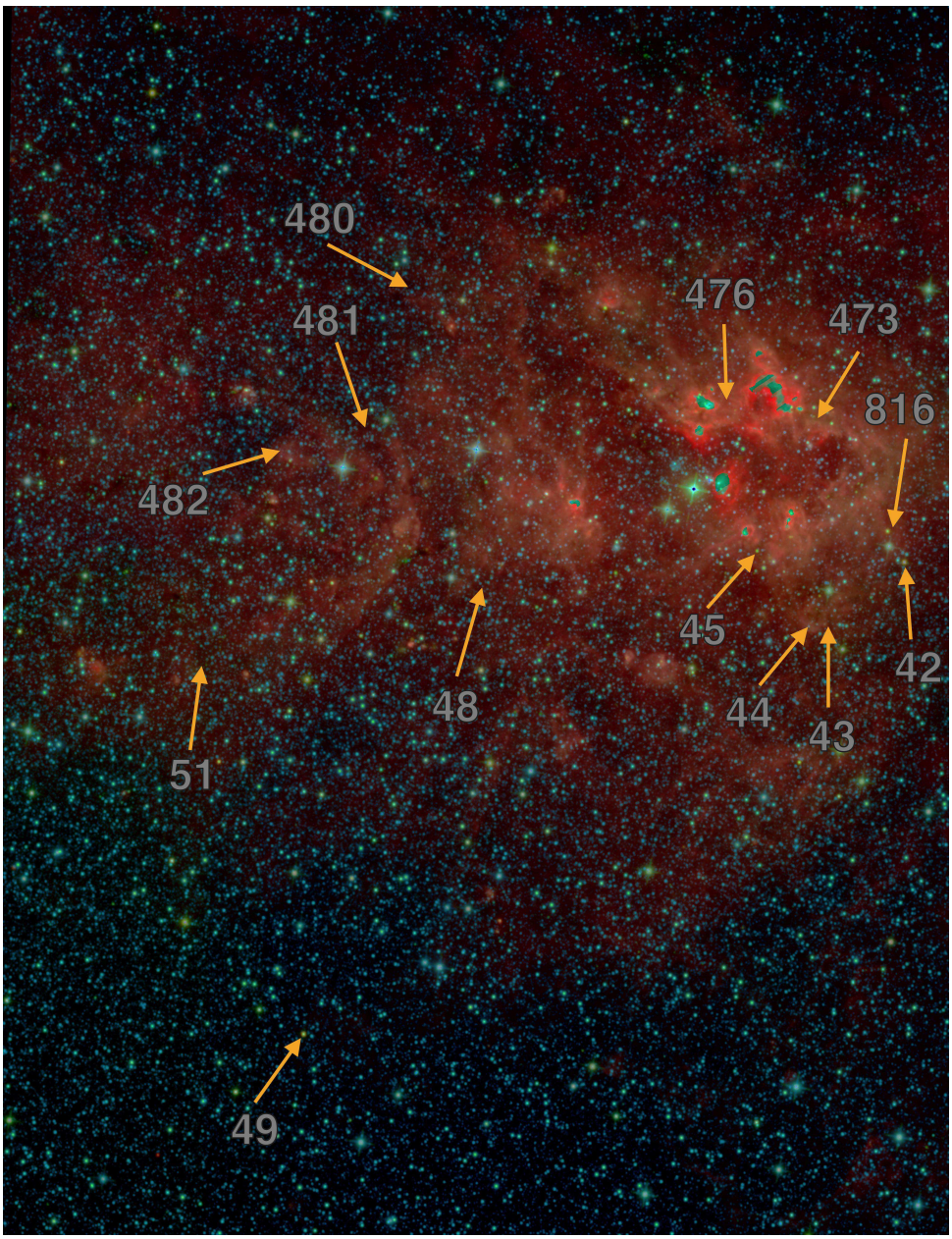

Figure 6.28: False colour WISE image (blue=3.5 μm, green=4.6 μm, red=12 μm) of a $1.6^\circ \times 3^\circ$ area of the G305 star forming complex covered by VVV tiles d046 and d084. The projected location of 13 variables stars found in this area are marked by the arrows, along with their VVVv designation.

which corresponds to ∼9%. This is somewhat higher than the percentage estimated by Evans et al. (2009) and Enoch et al. (2009) of 5-7%, and the percentage of the lifetime of the stars which is predicted to be spent at high accretion states of 5% by Hartmann & Kenyon (1996).

6.5 Summary

- We find 816 high amplitude infrared variable stars in the area of the Galactic mid-plane covered by the VVV survey. In agreement with the previous results from searches in the GPS, we observe a large concentration of objects towards areas of star formation. The variable stars found in these areas are characterized by having near-infrared colours and SEDs of YSOs. If all of them are in fact young stars, we find a YSO surface density of 4.4 deg^{-2}, which could reach 19.1 deg^{-2} if we take into account the fact that we are likely missing YSOs at distances larger than 3.8 kpc.

- The estimated surface density of VVV is higher than the one from GPS. Contamination from chance selections is bound to be higher in VVV. However, we would require a large percentage of $\sim$ 45% of contamination in order to match the VVV and GPS surface densities. The more likely explanation is that VVV is detecting a larger number of higher luminosity YSOs located at larger distances in the Galaxy.

- We study the possible evolutionary stage of the YSOs associated with SFRs, as determined from their SEDs at near- to mid-infrared wavelengths. We find a large fraction of class I and flat spectrum sources ($\sim$ 71% of the sample). These objects tend to have larger amplitudes than older class II and class III stars. This is expected if fluctuation in the accretion rates are higher at younger evolutionary stages.

- We present the results of the spectroscopic follow-up of 37 VVV high amplitude variable stars. Two stars show characteristics that makes them unlikely YSOs. From the remaining 35 objects we find a comparable-to-high detection frequencies of H_2 and CO emission as compared to previous studies of YSOs. Similarly to GPS results, we find a somewhat lower frequency of Brγ emission which could be explained as in section 5.4.

- Nine objects shows the characteristic strong CO absorption and lack of photospheric features of FU Orionis stars. We discuss their properties at length where we find that 4 objects are very likely new additions to the FUor class, 4 remain with uncertain classification and 1 object is very likely a dust-enshrouded AGB star rather than a YSO.

  Twenty six other objects are discussed in terms of their possible classifications as eruptive variables. From these, 18 objects have light curves which are characterized by large variations ($\Delta K_s > 1.5$ magnitudes) and over long timescales, which resemble those of either EXors or FUors. The same objects show emission line spectra with Brγ, CO and/or H_2 almost always present. The H_2 emission agrees with shock-excited emission from molecular outflows. We conclude that these are likely new additions to the eruptive variable class.

Three objects show outburst durations that extend over the period covered by VVV, which would be expected if these are FUor-like outbursts. However, their near-infrared spectra does not show the usual CO and H_2O absorption characteristic of the FUor class. Instead, they are dominated by emission from CO, H_2 and Brγ, which is more expected in EXors. This agrees with recent discoveries of eruptive class show a mixture of characteristics between FUors and EXors.

The VVV spectroscopic sample then shows that 11-20% of our objects are FUors, which is higher than estimates in previous surveys and agrees with the results from GPS. Once again we are adding a large number of objects towards the eruptive variable classes, especially to the embedded subclass.

- For three objects we have repeat observations that allows us to study the spectroscopic variability of eruptive variables. In two of them the observed changes relate to fluctuations in the accretion rate. Object VVVv322 is of special interest. The light curve of the object shows a large outburst and its near-infrared spectrum closely resembles those of classical FUors. However, the duration of the outburst appears to be of $\sim$ 3 years, much shorter than expected for classical FU Orionis stars. The spectrum of the object also shows variation as absorption features from CO and H_2O become weaker as the star goes back into quiescence.

- We make a first attempt to study the incidence of episodic accretion in SFRs. We use the variable stars in our sample that are likely associated with the star-forming complex G305. We find that 9% of class I YSOs in G305 are undergoing states of high accretion onto the central star.

Chapter 7

Summary and Future Work.

We have presented the results of the panoramic search for high-amplitude near-infrared variables in the Galactic plane using the infrared surveys UKIDSS Galactic Plane Survey and the Vista Variables in the Via Lactea. We summarize our principal results as follows.

The search for high-amplitude infrared variables in data releases DR5, DR7 and DR8 of GPS yields 71 stars which display $\Delta K > 1$ mag. The search for stars showing this level of K_s variability in the 2010-2012 data from VVV tiles of the Galactic disc with $|b| < 1^\circ$ yields 816 stars. In both GPS and VVV searches we find different classes of variable stars, such as known novae, eclipsing binaries, high-mass X-ray binaries and OH/IR stars. The most striking results from both samples is that two thirds of the candidates are located within areas of star formation and show characteristics that make them likely young stellar objects.

The high fraction of YSOs found in our studies implies a YSO surface density of 0.19 deg^{-2} in the area covered by GPS. We conclude that this number could reach $\sim$13 deg^{-2} in the mid-plane after allowing for the effects of 2-epoch sampling and scale height upon our sample. We find from VVV that this number could be as high as $\sim$19 deg^{-2}. The differences between GPS and VVV could be explained by a larger contamination from chance selection in the latter. However, this could be better explained by the fact that VVV is detecting a higher number of high luminosity YSOs located at greater distances in the Galactic disc. In any case we estimate that PMS stars the commonest type of high amplitude variables in the near-infrared.

We have found from the YSO sample of Carpenter et al. (2001) that the variability in stars with $\Delta K > 1.1$ mag in two epochs of observation separated by a few years (such as the one obtained from GPS) is most likely related to longer timescale variability like that observed in eruptive variables. From the higher number of epochs of VVV we observe that the high amplitude variability of YSOs in SFRs occurs over timescales of hundreds of days or longer. We also observe that the amplitude of the variability increases for objects at younger evolutionary stages. This is expected if fluctuations in the accretion rates are larger at these younger stages.

Spectroscopic follow up of a subset of GPS and VVV objects allows us to confirm many of them as belonging to the eruptive variable class. In fact, as many as 37 objects are likely new members, which almost doubles the current known objects classified as young eruptive variables. The new additions from our work are mostly found to be optically invisible. This

will increase the number of embedded objects from this class by a much larger factor.

Stars confirmed as eruptive variables show characteristics that could be associated with either of the two known classes of these type of variable stars (EXors or FUors). This is found to be consistent with recent studies that suggest that the episodic accretion phenomena is comprised of a continuum of events with different properties but triggered by a similar physical mechanism.

We make a first attempt to study the incidence of episodic accretion in SFRs. We use the variable stars in our sample that are likely associated with the star-forming complex G305. We find that 9% of class I YSOs in G305 are undergoing states of high accretion onto the central star.

7.1 Future Work.

There are several areas that can be studied in the future using the data generated in this thesis. The future plans include

- Publish the global properties of the catalogue of 816 high-amplitude infrared variables from the 2010-2012 analysis, along with the analysis of the spectroscopic sub-sample.
- Publish the analysis of the spectroscopic sample from GPS.
- Perform a census of YSOs in the nearer VVV regions by searching for low-amplitude variability in these objects. In addition a more accurate measure of the completeness of the 2010-2012 search is needed in order to quantify the incidence of eruptive variability on timescales of a few years. The issue of the completeness is already being studied by fellow PhD student Wayne Stimson.
- Generate models that can explain the observed infrared emission in objects which are part of our spectroscopic sample and that show CO emission and/or H_2 emission. The CO bandhead emission will be modelled as arising from a hot inner disc at a distance of a few stellar radii from the central star, following the work of Najita et al. 1996. This will allow us to estimate the temperatures of the hot emitting gas and of the cold absorbing material. In addition we would be able to estimate the mass of the central protostar as well as the accretion rate of the disk if the disk rotation velocity is high enough. I will also study whether the presence of H2 lines arise from an UV or shock excited spectrum.
- We plan to model the SEDs of high amplitude variables. In addition, we will study the SED variability of these objects aided by the NEOWISE 3.3 and 4.6 μm multi-epoch survey Mainzer et al. (2011).
- Nanda Kumar (Universtiy of Porto) has been studying the observed variability of a number of objects from the VVV sample that have characteristics of high-mass protostars. I have been strongly involved in this project and we plan to publish soon.

- Expand the search to include more recent epochs from 2013 and 2014, and also to disc tiles with $|b| > 1^{\circ}$. The procedures needed for this step are the same that were used for the original analysis of the 2010-2012 data, however this will be more time consuming given the larger number of epochs and disc tiles to be analysed. In addition to confirm the true variability of the candidates, images and light curves have to be inspected visually.

Bibliography

Alves de Oliveira, C., & Casali, M. 2008, A&A, 485, 155

Andre, P., Ward-Thompson, D., & Barsony, M. 1993, ApJ, 406, 122

Antoniucci, S., Nisini, B., Giannini, T., & Lorenzetti, D. 2008, A&A, 479, 503

Armitage, P. J., Livio, M., & Pringle, J. E. 2001, MNRAS, 324, 705

Ashok, N. M., Bhatt, H. C., Kulkarni, P. V., & Joshi, S. C. 1984, MNRAS, 211, 471

Aspin, C., Greene, T. P., & Reipurth, B. 2009a, AJ, 137, 2968

Aspin, C., & Reipurth, B. 2003, AJ, 126, 2936

Aspin, C., & Sandell, G. 2001, MNRAS, 328, 751

Aspin, C., et al. 2009b, ApJ, 692, L67

Audard, M., et al. 2014, ArXiv:1401.3368

Avedisova, V. S. 2002, Astronomy Reports, 46, 193

Bally, J., Morse, J., & Reipurth, B. 1996, in Science with the Hubble Space Telescope - II, ed. P. Benvenuti, F. D. Macchetto, & E. J. Schreier, 491

Bans, A., & Königl, A. 2012, ApJ, 758, 100

Baraffe, I., Chabrier, G., & Gallardo, J. 2009, ApJ, 702, L27

Baraffe, I., Vorobyov, E., & Chabrier, G. 2012, ApJ, 756, 118

Baume, G., Carraro, G., & Momany, Y. 2009, MNRAS, 398, 221

Beck, T. L. 2007, AJ, 133, 1673

Beck, T. L., Bary, J. S., & McGregor, P. J. 2010, ApJ, 722, 1360

Beck, T. L., McGregor, P. J., Takami, M., & Pyo, T.-S. 2008, ApJ, 676, 472

Bedijn, P. J. 1987, A&A, 186, 136

Bell, K. R., & Lin, D. N. C. 1994, ApJ, 427, 987

Bell, K. R., Lin, D. N. C., Hartmann, L. W., & Kenyon, S. J. 1995, ApJ, 444, 376

Benjamin, R. A., et al. 2003, PASP, 115, 953

Bessell, M. S., & Brett, J. M. 1988, PASP, 100, 1134

Bonnell, I., & Bastien, P. 1992, ApJL, 401, L31

Bouvier, J., Cabrit, S., Fernandez, M., Martin, E. L., & Matthews, J. M. 1993, A&A, 272, 176

Bouvier, J., Covino, E., Kovo, O., Martin, E. L., Matthews, J. M., Terranegra, L., & Beck, S. C. 1995, A&A, 299, 89

Bouvier, J., Grankin, K., Ellerbroek, L. E., Bouy, H., & Barrado, D. 2013, A&A, 557, A77

Bouvier, J., et al. 1999, A&A, 349, 619

Brand, J., & Blitz, L. 1993, A&A, 275, 67

Briceño, C., Calvet, N., Hernández, J., Vivas, A. K., Hartmann, L., Downes, J. J., & Berlind, P. 2005, AJ, 129, 907

Budding, E., Erdem, A., Çiçek, C., Bulut, I., Soydugan, F., Soydugan, E., Bakiş, V., & Demircan, O. 2004, A&A, 417, 263

Burgasser, A. J., Reid, I. N., Siegler, N., Close, L., Allen, P., Lowrance, P., & Gizis, J. 2007, Protostars and Planets V, 427

Calvet, N., Patino, A., Magris, G. C., & D'Alessio, P. 1991, ApJ, 380, 617

Caratti o Garatti, A., Eislöffel, J., Froebrich, D., Nisini, B., Giannini, T., & Calzoletti, L. 2009, A&A, 502, 579

Caratti o Garatti, A., et al. 2011, A&A, 526, L1

—. 2012, A&A, 538, A64

Carciofi, A. C., & Bjorkman, J. E. 2006, ApJ, 639, 1081

Cardelli, J. A., Clayton, G. C., & Mathis, J. S. 1989, ApJ, 345, 245

Carey, S. J., et al. 2009, PASP, 121, 76

Carpenter, J. M., Hillenbrand, L. A., & Skrutskie, M. F. 2001, AJ, 121, 3160

Carr, J. S. 1989, ApJ, 345, 522

Casali, M., et al. 2007, A&A, 467, 777

Casali, M. M., & Matthews, H. E. 1992, MNRAS, 258, 399

Castelli, F., & Kurucz, R. L. 2004, ArXiv:astro-ph/0405087

Caswell, J. L., Kramer, B. H., Sukom, A., & Reynolds, J. E. 2010, MNRAS, 402, 2649

Chapman, N. L., Mundy, L. G., Lai, S.-P., & Evans, II, N. J. 2009, ApJ, 690, 496

Churchwell, E., et al. 2006, ApJ, 649, 759

Cioni, M.-R. L., Marquette, J.-B., Loup, C., Azzopardi, M., Habing, H. J., Lasserre, T., & Lesquoy, E. 2001, A&A, 377, 945

Cioni, M.-R. L., et al. 2011, A&A, 527, A116

—. 2013, A&A, 549, A29

Clark, J. S., Negueruela, I., Crowther, P. A., & Goodwin, S. P. 2005, A&A, 434, 949

Connelley, M. S., & Greene, T. P. 2010, AJ, 140, 1214

—. 2014, AJ, 147, 125

Cooper, H. D. B., et al. 2013, MNRAS, 430, 1125

Corradi, R. L. M., et al. 2008, A&A, 480, 409

—. 2010, A&A, 509, A41

Crutcher, R. M., & Chu, Y. H. 1982, in Astrophysics and Space Science Library, Vol. 93, Regions of Recent Star Formation, ed. R. S. Roger & P. E. Dewdney, 53–60

Cutri, R. M., & et al. 2012, VizieR Online Data Catalog, 2311, 0

Davis, C. J., Gell, R., Khanzadyan, T., Smith, M. D., & Jenness, T. 2010, A&A, 511, A24

Davis, C. J., Nisini, B., Takami, M., Pyo, T.-S., Smith, M. D., Whelan, E., Ray, T. P., & Chrysostomou, A. 2006, ApJ, 639, 969

Davis, C. J., Ray, T. P., Desroches, L., & Aspin, C. 2001, MNRAS, 326, 524

Davis, C. J., et al. 2011, A&A, 528, A3

Deharveng, L., Zavagno, A., Schuller, F., Caplan, J., Pomarès, M., & De Breuck, C. 2009, A&A, 496, 177

Derue, F., et al. 2002, A&A, 389, 149

Dörr, M., Chini, R., Haas, M., Lemke, R., & Nürnberger, D. 2013, A&A, 553, A48

Dougherty, S. M., & Taylor, A. R. 1994, MNRAS, 269, 1123

Drew, J. E., et al. 2005, MNRAS, 362, 753

Dunham, M. M., & Vorobyov, E. I. 2012, ApJ, 747, 52

Dunham, M. M., et al. 2014, ArXiv:1401.1809

Dutra, C. M., & Bica, E. 2002, A&A, 383, 631

Dye, S., et al. 2006, MNRAS, 372, 1227

Elia, D., et al. 2010, A&A, 518, L97

Elias, F., Cabrera-Caño, J., & Alfaro, E. J. 2006, AJ, 131, 2700

Elias, J. H. 1978, ApJ, 223, 859

Enoch, M. L., Evans, II, N. J., Sargent, A. I., & Glenn, J. 2009, ApJ, 692, 973

Evans, II, N. J., Balkum, S., Levreault, R. M., Hartmann, L., & Kenyon, S. 1994, ApJ, 424, 793

Evans, II, N. J., et al. 2003, PASP, 115, 965

—. 2009, ApJS, 181, 321

Fabricant, D., Cheimets, P., Caldwell, N., & Geary, J. 1998, PASP, 110, 79

Faimali, A. 2013, PhD thesis, Universtiy of Hertfordhsire

Faimali, A., et al. 2012, MNRAS, 426, 402

Fedele, D., van den Ancker, M. E., Petr-Gotzens, M. G., & Rafanelli, P. 2007, A&A, 472, 207

Ferreira, J., Dougados, C., & Cabrit, S. 2006, A&A, 453, 785

Fischer, W. J., et al. 2012, ApJ, 756, 99

Folha, D. F. M., & Emerson, J. P. 2001, A&A, 365, 90

Forbes, D. 2000, AJ, 120, 2594

Gammie, C. F. 1996, ApJ, 457, 355

Gibb, E. L., Rettig, T. W., Brittain, S. D., Wasikowski, D., Simon, T., Vacca, W. D., Cushing, M. C., & Kulesa, C. 2006, ApJ, 641, 383

Gonzalez, O. A., Rejkuba, M., Zoccali, M., Valenti, E., & Minniti, D. 2011, A&A, 534, A3

Greene, T. P., Aspin, C., & Reipurth, B. 2008, AJ, 135, 1421

Greene, T. P., Wilking, B. A., Andre, P., Young, E. T., & Lada, C. J. 1994, ApJ, 434, 614

Gutermuth, R. A., Megeath, S. T., Myers, P. C., Allen, L. E., Pipher, J. L., & Fazio, G. G. 2009, ApJS, 184, 18

Hambly, N. C., et al. 2008, MNRAS, 384, 637

Hartmann, L. 2000, in Astronomical Society of the Pacific Conference Series, Vol. 219, Disks, Planetesimals, and Planets, ed. G. Garzón, C. Eiroa, D. de Winter, & T. J. Mahoney, 95

Hartmann, L. 2001, AJ, 121, 1030

Hartmann, L., Hewett, R., & Calvet, N. 1994, ApJ, 426, 669

Hartmann, L., Hinkle, K., & Calvet, N. 2004, ApJ, 609, 906

Hartmann, L., & Kenyon, S. J. 1996, ARA&A, 34, 207

Hartmann, L., Megeath, S. T., Allen, L., Luhman, K., Calvet, N., D'Alessio, P., Franco-Hernandez, R., & Fazio, G. 2005, ApJ, 629, 881

Hashimoto, O. 1994, A&AS, 107, 445

Herbig, G. H. 1960, ApJS, 4, 337

—. 1966, Vistas in Astronomy, 8, 109

—. 1977, ApJ, 217, 693

Herbig, G. H. 1989, in European Southern Observatory Conference and Workshop Proceedings, Vol. 33, European Southern Observatory Conference and Workshop Proceedings, ed. B. Reipurth, 233–246

Herbig, G. H., Petrov, P. P., & Duemmler, R. 2003, ApJ, 595, 384

Herbst, W., Herbst, D. K., Grossman, E. J., & Weinstein, D. 1994, AJ, 108, 1906

Herbst, W., & Shevchenko, V. S. 1999, AJ, 118, 1043

Hernández, J., Calvet, N., Hartmann, L., Briceño, C., Sicilia-Aguilar, A., & Berlind, P. 2005, AJ, 129, 856

Hillenbrand, L. A. 2009, in IAU Symposium, Vol. 258, IAU Symposium, ed. E. E. Mamajek, D. R. Soderblom, & R. F. G. Wyse, 81–94

Hodapp, K. W., Chini, R., Watermann, R., & Lemke, R. 2012, ApJ, 744, 56

Hodapp, K.-W., Hora, J. L., Rayner, J. T., Pickles, A. J., & Ladd, E. F. 1996, ApJ, 468, 861

Hora, J., et al. 2007, in Spitzer Proposal ID #40184, 40184

Hughes, J. P., Slane, P., Posselt, B., Charles, P., Rajoelimanana, A., Sefako, R., Halpern, J., & Steeghs, D. 2010, The Astronomer's Telegram, 2771, 1

Hunter, D. A., Thronson, Jr., H. A., & Wilton, C. 1990, AJ, 100, 1915

Ioannidis, G., & Froebrich, D. 2012, MNRAS, 425, 1380

Irwin, M. J., et al. 2004, in Society of Photo-Optical Instrumentation Engineers (SPIE) Conference Series, Vol. 5493, Optimizing Scientific Return for Astronomy through Information Technologies, ed. P. J. Quinn & A. Bridger, 411–422

Ishihara, D., Kaneda, H., Onaka, T., Ita, Y., Matsuura, M., & Matsunaga, N. 2011, A&A, 534, A79

Ishii, M., Nagata, T., Sato, S., Yao, Y., Jiang, Z., & Nakaya, H. 2001, AJ, 121, 3191

Jiménez-Esteban, F. M., García-Lario, P., Engels, D., & Perea Calderón, J. V. 2006, A&A, 446, 773

Joy, A. H. 1945, ApJ, 102, 168

Kenyon, S. J., Hartmann, L. W., & Kolotilov, E. A. 1991, PASP, 103, 1069

Kenyon, S. J., Hartmann, L. W., Strom, K. M., & Strom, S. E. 1990, AJ, 99, 869

Kleinmann, S. G., & Hall, D. N. B. 1986, ApJS, 62, 501

Knapp, G. R. 1987, PASP, 99, 1134

Kóspál, Á., Ábrahám, P., Prusti, T., Acosta-Pulido, J., Hony, S., Moór, A., & Siebenmorgen, R. 2007, A&A, 470, 211

Kóspál, Á., et al. 2011a, ApJ, 736, 72

—. 2011b, A&A, 527, A133

Kouzuma, S., & Yamaoka, H. 2012, ApJ, 747, 14

Kraus, M. 2009, A&A, 494, 253

Kuchar, T. A., & Clark, F. O. 1997, ApJ, 488, 224

Lada, C. J. 1987, in IAU Symposium, Vol. 115, Star Forming Regions, ed. M. Peimbert & J. Jugaku, 1–17

Lada, C. J. 2005, Progress of Theoretical Physics Supplement, 158, 1

Lamm, M. H., Bailer-Jones, C. A. L., Mundt, R., Herbst, W., & Scholz, A. 2004, A&A, 417, 557

Larson, R. B. 1980, MNRAS, 190, 321

Lawrence, A., et al. 2007, MNRAS, 379, 1599

Lebzelter, T., & Wood, P. R. 2005, A&A, 441, 1117

Lewis, B. M. 2000, ApJ, 533, 959

Lodato, G., & Clarke, C. J. 2004, MNRAS, 353, 841

Lodato, G., & Rice, W. K. M. 2004, MNRAS, 351, 630

Lorenzetti, D., Larionov, V. M., Giannini, T., Arkharov, A. A., Antoniucci, S., Nisini, B., & Di Paola, A. 2009a, ApJ, 693, 1056

—. 2009b, ApJ, 693, 1056

Lorenzetti, D., et al. 2012, ApJ, 749, 188

Lucas, P. W., et al. 2008, MNRAS, 391, 136

Lynds, B. T. 1962, ApJS, 7, 1

Machida, M. N., Inutsuka, S.-i., & Matsumoto, T. 2011, ApJ, 729, 42

Maddox, N., Hewett, P. C., Warren, S. J., & Croom, S. M. 2008, MNRAS, 386, 1605

Magakian, T. Y. 2003, A&A, 399, 141

Magakian, T. Y., et al. 2013, MNRAS, 432, 2685

Mainzer, A., et al. 2011, ApJ, 731, 53

Martin, S. C. 1997, ApJL, 478, L33

Martins, F., Pomarès, M., Deharveng, L., Zavagno, A., & Bouret, J. C. 2010, A&A, 510, A32

McLaughlin, D. B. 1945, AJ, 51, 136

McSwain, M. V., Huang, W., & Gies, D. R. 2009, ApJ, 700, 1216

McSwain, M. V., Huang, W., Gies, D. R., Grundstrom, E. D., & Townsend, R. H. D. 2008, ApJ, 672, 590

Meyer, M. R., Calvet, N., & Hillenbrand, L. A. 1997, AJ, 114, 288

Miller, A. A., et al. 2011, ApJ, 730, 80

Minniti, D., Saito, R. K., Alonso-García, J., Lucas, P. W., & Hempel, M. 2011, ApJL, 733, L43

Minniti, D., et al. 2010, NewA, 15, 433

Molinari, S., et al. 2010, PASP, 122, 314

Mundt, R., Stocke, J., Strom, S. E., Strom, K. M., & Anderson, E. R. 1985, ApJ, 297, L41

Murakami, H., et al. 2007, PASJ, 59, 369

Muzerolle, J., Calvet, N., & Hartmann, L. 1998a, ApJ, 492, 743

—. 2001, ApJ, 550, 944

Muzerolle, J., D'Alessio, P., Calvet, N., & Hartmann, L. 2004, ApJ, 617, 406

Muzerolle, J., Hartmann, L., & Calvet, N. 1998b, AJ, 116, 2965

Najita, J., Carr, J. S., Glassgold, A. E., Shu, F. H., & Tokunaga, A. T. 1996a, ApJ, 462, 919

Najita, J., Carr, J. S., & Tokunaga, A. T. 1996b, ApJ, 456, 292

Nakano, S., Sato, H., Nishimura, H., Nakamura, T., Wakuda, S., Yamaoka, H., & Pearce, A. 2003, IAUC, 8190, 1

Natta, A., & Whitney, B. A. 2000, A&A, 364, 633

Neugebauer, G., et al. 1984, ApJ, 278, L1

Olivier, E. A., Whitelock, P., & Marang, F. 2001, MNRAS, 326, 490

Ortiz, R., & Maciel, W. J. 1996, A&A, 313, 180

Parihar, P., Messina, S., Distefano, E., Shantikumar, N. S., & Medhi, B. J. 2009, MNRAS, 400, 603

Peretto, N., & Fuller, G. A. 2009, A&A, 505, 405

Persi, P., Tapia, M., Gòmez, M., Whitney, B. A., Marenzi, A. R., & Roth, M. 2007, AJ, 133, 1690

Petrov, P. P., & Herbig, G. H. 1992, ApJ, 392, 209

Porter, J. M., & Rivinius, T. 2003, PASP, 115, 1153

Price, S. D., Egan, M. P., Carey, S. J., Mizuno, D. R., & Kuchar, T. A. 2001, AJ, 121, 2819

Quireza, C., Rood, R. T., Bania, T. M., Balser, D. S., & Maciel, W. J. 2006, ApJ, 653, 1226

Reed, B. C. 2000, AJ, 120, 314

Reipurth, B. 2000, AJ, 120, 3177

Reipurth, B., & Aspin, C. 1997, AJ, 114, 2700

—. 2004a, ApJL, 606, L119

—. 2004b, ApJL, 608, L65

Reipurth, B., & Aspin, C. 2010a, in Evolution of Cosmic Objects through their Physical Activity, ed. H. A. Harutyunian, A. M. Mickaelian, & Y. Terzian, 19–38

Reipurth, B., & Aspin, C. 2010b, in Evolution of Cosmic Objects through their Physical Activity, ed. H. A. Harutyunian, A. M. Mickaelian, & Y. Terzian, 19–38

Reipurth, B., Aspin, C., & Herbig, G. H. 2012, ApJL, 748, L5

Reipurth, B., & Bally, J. 2001, ARA&A, 39, 403

Reipurth, B., Pedrosa, A., & Lago, M. T. V. T. 1996, A&AS, 120, 229

Rice, T. S., Wolk, S. J., & Aspin, C. 2012, ApJ, 755, 65

Robitaille, T. P., Whitney, B. A., Indebetouw, R., & Wood, K. 2007, ApJS, 169, 328

Robitaille, T. P., Whitney, B. A., Indebetouw, R., Wood, K., & Denzmore, P. 2006, ApJS, 167, 256

Robitaille, T. P., et al. 2008, AJ, 136, 2413

Romanova, M. M., Ustyugova, G. V., Koldoba, A. V., & Lovelace, R. V. E. 2013, MNRAS, 430, 699

Russeil, D. 2003, A&A, 397, 133

Russeil, D., & Castets, A. 2004, A&A, 417, 107

Saito, R. K., et al. 2012, A&A, 537, A107

—. 2013, A&A, 554, A123

Samus, N. N., Kazarovets, E. V., Kireeva, N. N., Pastukhova, E. N., & Durlevich, O. V. 2010, Odessa Astronomical Publications, 23, 102

Schlegel, D. J., Finkbeiner, D. P., & Davis, M. 1998, ApJ, 500, 525

Scholz, A. 2012, MNRAS, 420, 1495

Scholz, A., Froebrich, D., & Wood, K. 2013, MNRAS, 430, 2910

Scholz, A., Xu, X., Jayawardhana, R., Wood, K., Eislöffel, J., & Quinn, C. 2009, MNRAS, 398, 873

Scoville, N., Kleinmann, S. G., Hall, D. N. B., & Ridgway, S. T. 1983, ApJ, 275, 201

Scoville, N. Z., Hall, D. N. B., Ridgway, S. T., & Kleinmann, S. G. 1979, ApJL, 232, L121

Scoville, N. Z., Yun, M. S., Sanders, D. B., Clemens, D. P., & Waller, W. H. 1987, ApJS, 63, 821

Sevenster, M. N., Chapman, J. M., Habing, H. J., Killeen, N. E. B., & Lindqvist, M. 1997, A&AS, 124, 509

Shakura, N. I., & Sunyaev, R. A. 1973, A&A, 24, 337

Shu, F. H., Adams, F. C., & Lizano, S. 1987, ARA&A, 25, 23

Sipos, N., Ábrahám, P., Acosta-Pulido, J., Juhász, A., Kóspál, Á., Kun, M., Moór, A., & Setiawan, J. 2009, A&A, 507, 881

Skrutskie, M. F., et al. 2006, AJ, 131, 1163

Smith, M. D. 1995, A&A, 296, 789

Soszynski, I., et al. 2005, AcA, 55, 331

Stamatellos, D., & Whitworth, A. P. 2009, MNRAS, 392, 413

Stamatellos, D., Whitworth, A. P., & Hubber, D. A. 2011, ApJ, 730, 32

Toomre, A. 1964, ApJ, 139, 1217

Tudose, V., Fender, R. P., Tzioumis, A. K., Spencer, R. E., & van der Klis, M. 2008, MNRAS, 390, 447

Turner, N. J., Fromang, S., Gammie, C., Klahr, H., Lesur, G., Wardle, M., & Bai, X.-N. 2014, ArXiv:1401.7306

Udalski, A., Szymanski, M., Kaluzny, J., Kubiak, M., & Mateo, M. 1992, AcA, 42, 253

Vacca, W. D., Cushing, M. C., & Rayner, J. T. 2003, PASP, 115, 389

van Loon, J. T., Zijlstra, A. A., Whitelock, P. A., Waters, L. B. F. M., Loup, C., & Trams, N. R. 1997, A&A, 325, 585

Vanhollebeke, E., Blommaert, J. A. D. L., Schultheis, M., Aringer, B., & Lançon, A. 2006, A&A, 455, 645

Varricatt, W. P., Davis, C. J., & Adamson, A. J. 2005, MNRAS, 359, 2

Varricatt, W. P., Davis, C. J., Ramsay, S., & Todd, S. P. 2010, MNRAS, 404, 661

Vijh, U. P., et al. 2009, AJ, 137, 3139

Volk, K., Kwok, S., & Langill, P. P. 1992, ApJ, 391, 285

Vorobyov, E. I., & Basu, S. 2005, ApJL, 633, L137

—. 2006, ApJ, 650, 956

—. 2010, ApJ, 719, 1896

Wallace, L., & Hinkle, K. 1997, ApJS, 111, 445

Walsh, A. J., Hyland, A. R., Robinson, G., & Burton, M. G. 1997, MNRAS, 291, 261

Warren, S. J., et al. 2007, ArXiv:astro-ph/0703037

Weights, D. J., Lucas, P. W., Roche, P. F., Pinfield, D. J., & Riddick, F. 2009, MNRAS, 392, 817

Whitelock, P., Feast, M., & Catchpole, R. 1991, MNRAS, 248, 276

Whitelock, P. A., Feast, M. W., & van Leeuwen, F. 2008, MNRAS, 386, 313

Wilking, B. A. 1989, PASP, 101, 229

Witham, A. R., Knigge, C., Drew, J. E., Greimel, R., Steeghs, D., Gänsicke, B. T., Groot, P. J., & Mampaso, A. 2008, MNRAS, 384, 1277

Wolfire, M. G., & Konigl, A. 1991, ApJ, 383, 205

Wright, E. L., et al. 2010, AJ, 140, 1868

Zhang, B., Zheng, X. W., Reid, M. J., Menten, K. M., Xu, Y., Moscadelli, L., & Brunthaler, A. 2009, ApJ, 693, 419

Zhu, Z., Hartmann, L., & Gammie, C. 2009, ApJ, 694, 1045

Appendix A

VVV High Amplitude Variables

Table A.1: Properties of high amplitude variable stars from VVV.

Object ID	VVV Designation	α (J2000)	δ (J2000)	l	b	Z (mag)	Y (mag)	J (mag)	H (mag)	K_s (mag)	ΔK_s^a (mag)	α_{class}	SFR
VVVv1	VVV J114135.16-622055.51	11:41:35.16	-62:20:55.51	294.92603	-0.56770140	–	–	17.99(0.06)	15.95(0.02)	14.44(0.01)	1.16	-0.29	y
VVVv2	VVV J114412.94-623449.09	11:44:12.94	-62:34:49.09	295.28005	-0.71145503	–	–	–	18.78(0.23)	15.71(0.03)	2.01	1.22	y
VVVv3	VVV J115113.03-623729.29	11:51:13.03	-62:37:29.29	296.07199	-0.55784490	13.17(0.01)	12.93(0.01)	12.90(0.01)	12.70(0.01)	12.24(0.01)	1.91	-1.18	n
VVVv4	VVV J115808.69-630708.60	11:58:08.69	-63:07:08.60	296.95057	-0.86785395	–	–	18.23(0.08)	16.62(0.04)	15.32(0.02)	1.02	-0.24	y
VVVv5	VVV J115959.68-622613.20	11:59:59.68	-62:26:13.20	297.02026	-0.15716131	17.69(0.02)	16.62(0.01)	15.87(0.01)	15.25(0.01)	13.53(0.01)	1.30	-0.13	n
VVVv6	VVV J115937.81-631109.77	11:59:37.81	-63:11:09.77	297.12836	-0.89953352	19.02(0.05)	18.08(0.04)	16.80(0.02)	15.95(0.02)	15.50(0.02)	1.02	–	n
VVVv7	VVV J120202.67-623615.60	12:02:02.67	-62:36:15.60	297.28472	-0.27538112	–	–	–	–	17.22(0.12)	1.48	2.39	y
VVVv8	VVV J120059.11-631636.18	12:00:59.11	-63:16:36.18	297.29582	-0.95838309	–	–	–	–	16.86(0.09)	1.39	0.64	y
VVVv9	VVV J120217.23-623647.83	12:02:17.23	-62:36:47.83	297.31381	-0.27887510	–	–	18.29(0.08)	16.33(0.03)	14.64(0.01)	1.84	-0.39	y
VVVv10	VVV J120250.85-622437.62	12:02:50.85	-62:24:37.62	297.33912	-0.067488967	18.57(0.04)	18.23(0.05)	16.97(0.03)	16.35(0.03)	16.07(0.04)	1.19	–	n
VVVv11	VVV J120436.62-625704.60	12:04:36.62	-62:57:04.60	297.63741	-0.56188470	20.20(0.19)	19.01(0.13)	17.87(0.07)	16.79(0.05)	16.08(0.08)	1.10	-1.32	n
VVVv12	VVV J121033.19-630755.71	12:10:33.19	-63:07:55.71	298.33185	-0.62611408	–	–	–	16.30(0.03)	15.04(0.03)	1.42	0.28	y
VVVv13	VVV J121216.83-624838.32	12:12:16.83	-62:48:38.32	298.47603	-0.27813948	–	–	–	–	16.72(0.14)	1.40	1.39	y
VVVv14	VVV J121218.13-624904.48	12:12:18.13	-62:49:04.48	298.47958	-0.28494801	19.48(0.10)	18.88(0.12)	17.84(0.06)	16.74(0.05)	15.56(0.05)	1.01	0.88	y
VVVv15	VVV J121226.09-624416.97	12:12:26.09	-62:44:16.97	298.48252	-0.20370785	19.00(0.07)	17.72(0.04)	16.57(0.02)	15.60(0.02)	15.04(0.03)	1.05	–	y
VVVv16	VVV J121329.76-624107.74	12:13:29.76	-62:41:07.74	298.59498	-0.13364186	18.01(0.03)	17.13(0.02)	16.06(0.01)	14.72(0.01)	13.66(0.01)	1.05	0.92	y
VVVv17	VVV J121352.08-625549.90	12:13:52.08	-62:55:49.90	298.67278	-0.36986131	–	–	–	17.79(0.12)	16.41(0.10)	1.22	0.44	y
VVVv18	VVV J121950.31-632142.24	12:19:50.31	-63:21:42.24	299.39868	-0.70694696	17.82(0.02)	17.29(0.02)	16.20(0.01)	15.52(0.01)	15.32(0.02)	1.03	–	n
VVVv19	VVV J122255.30-632352.56	12:22:55.30	-63:23:52.56	299.74594	-0.70270007	19.56(0.08)	18.67(0.06)	17.55(0.04)	16.40(0.03)	15.61(0.03)	1.23	-0.48	n
VVVv20	VVV J122827.97-625713.97	12:28:27.97	-62:57:13.97	300.32402	-0.19848910	–	–	17.38(0.04)	14.10(0.01)	11.70(0.01)	1.68	0.60	y
VVVv21	VVV J122902.24-625234.10	12:29:02.24	-62:52:34.10	300.38193	-0.11533229	–	–	–	17.12(0.05)	15.80(0.03)	1.79	0.86	y
VVVv22	VVV J123105.60-624457.34	12:31:05.60	-62:44:57.34	300.60547	0.030572382	–	–	18.81(0.14)	16.94(0.05)	15.55(0.03)	1.34	-0.34	y
VVVv23	VVV J123128.53-624433.10	12:31:28.53	-62:44:33.10	300.64855	0.040704993	19.44(0.07)	18.37(0.05)	17.14(0.03)	15.57(0.02)	14.40(0.01)	1.51	-0.20	y
VVVv24	VVV J123235.68-634319.61	12:32:35.68	-63:43:19.61	300.84794	-0.92661506	17.17(0.01)	16.13(0.01)	14.05(0.01)	12.95(0.01)	12.23(0.01)	1.20	-0.59	n
VVVv25	VVV J123514.37-624715.63	12:35:14.37	-62:47:15.63	301.08129	0.025874751	–	–	–	16.01(0.02)	12.34(0.01)	1.46	0.22	y
VVVv26	VVV J123845.66-631136.03	12:38:45.66	-63:11:36.03	301.50320	-0.35674318	–	–	19.67(0.29)	16.70(0.04)	14.71(0.01)	1.66	1.07	y
VVVv27	VVV J123848.33-633939.15	12:38:48.33	-63:39:39.15	301.53114	-0.82346677	–	–	–	–	12.04(0.01)	2.25	5.33	n
VVVv28	VVV J123911.54-630524.76	12:39:11.54	-63:05:24.76	301.54688	-0.25137729	–	–	–	18.91(0.32)	16.78(0.09)	1.39	0.54	y
VVVv29	VVV J123931.48-630720.38	12:39:31.48	-63:07:20.38	301.58593	-0.28169556	–	–	–	–	16.94(0.10)	1.56	1.32	y
VVVv30	VVV J124140.56-635033.57	12:41:40.56	-63:50:33.57	301.85616	-0.99128045	17.92(0.02)	17.22(0.02)	16.40(0.02)	15.66(0.02)	15.23(0.02)	1.21	-2.14	n
VVVv31	VVV J124140.15-635918.05	12:41:40.15	-63:59:18.05	301.86093	-1.1368922	13.91(0.01)	13.27(0.01)	12.46(0.01)	12.08(0.01)	11.69(0.01)	1.02	-2.49	n
VVVv32	VVV J124357.15-625445.09	12:43:57.15	-62:54:45.09	302.07991	-0.053137952	19.58(0.07)	18.08(0.04)	16.07(0.01)	14.07(0.01)	12.45(0.01)	1.76	0.33	y
VVVv33	VVV J124425.05-631355.76	12:44:25.05	-63:13:55.76	302.14153	-0.37116019	–	–	–	18.10(0.16)	16.43(0.07)	1.15	0.64	n
VVVv34	VVV J125029.87-625124.93	12:50:29.87	-62:51:24.93	302.82470	0.014648658	19.22(0.05)	18.32(0.05)	17.86(0.06)	16.70(0.04)	15.71(0.03)	1.21	-0.34	y
VVVv35	VVV J125206.52-635711.52	12:52:06.52	-63:57:11.52	303.00557	-1.0815235	17.62(0.01)	16.85(0.01)	17.13(0.03)	16.21(0.03)	15.97(0.04)	1.14	-0.58	n
VVVv36	VVV J125917.72-633008.44	12:59:17.72	-63:30:08.44	303.80825	-0.64394398	14.38(0.01)	13.84(0.01)	13.27(0.01)	12.56(0.01)	11.81(0.01)	1.03	-0.11	y
VVVv37	VVV J130243.05-631130.00	13:02:43.05	-63:11:30.00	304.20331	-0.34774357	18.80(0.03)	17.75(0.03)	16.74(0.02)	15.89(0.02)	15.38(0.03)	1.34	–	n
VVVv38	VVV J130311.38-631439.09	13:03:11.38	-63:14:39.09	304.25411	-0.40259280	–	–	–	17.79(0.13)	16.32(0.07)	1.23	1.20	y
VVVv39	VVV J130440.98-635313.45	13:04:40.98	-63:53:13.45	304.38893	-1.0527733	18.67(0.03)	17.89(0.03)	17.57(0.05)	16.38(0.04)	15.49(0.03)	1.03	-0.09	n
VVVv40	VVV J130600.43-630144.40	13:06:00.43	-63:01:44.40	304.58298	-0.20394282	20.71(0.20)	19.49(0.14)	16.52(0.02)	15.42(0.02)	14.69(0.01)	1.18	-1.46	n
VVVv41	VVV J130944.05-634431.38	13:09:44.05	-63:44:31.38	304.95408	-0.94213806	18.09(0.02)	17.50(0.03)	15.83(0.01)	15.22(0.01)	14.90(0.02)	1.20	–	n
VVVv42	VVV J130934.64-624932.52	13:09:34.64	-62:49:32.52	305.00126	-0.026832595	–	–	18.45(0.10)	14.26(0.01)	11.94(0.01)	1.52	0.98	n
VVVv43	VVV J131044.06-625541.32	13:10:44.06	-62:55:41.32	305.12535	-0.13858313	–	–	–	17.62(0.11)	16.14(0.06)	1.23	0.53	y
VVVv44	VVV J131054.29-625604.36	13:10:54.29	-62:56:04.36	305.14420	-0.14642207	–	–	19.34(0.23)	16.83(0.05)	15.15(0.02)	1.27	–	y
VVVv45	VVV J131143.07-624854.77	13:11:43.07	-62:48:54.77	305.24579	-0.034589051	–	–	–	–	13.33(0.01)	2.32	1.27	y
VVVv46	VVV J131246.62-625628.58	13:12:46.62	-62:56:28.58	305.35595	-0.16997743	–	–	–	17.32(0.09)	15.80(0.04)	1.30	0.12	y
VVVv47	VVV J131313.97-624429.31	13:13:13.97	-62:44:29.31	305.42449	0.024768023	–	–	19.12(0.19)	17.27(0.08)	15.93(0.05)	1.06	0.04	y
VVVv48	VVV J131545.37-625244.45	13:15:45.37	-62:52:44.45	305.69929	-0.13798327	–	–	19.53(0.28)	17.39(0.09)	16.09(0.05)	1.05	–	y

Continued on next page

Table A.1 – *Continued from previous page*

Object ID	VVV Designation	α (J2000)	δ (J2000)	l	b	Z (mag)	Y (mag)	J (mag)	H (mag)	K_s (mag)	ΔK_s^a (mag)	α_{class}	SFR
VVVv49	VVV J131816.29-633743.65	13:18:16.29	-63:37:43.65	305.90658	-0.91210748	19.98(0.13)	–	18.35(0.09)	–	12.48(0.01)	1.25	1.33	n
VVVv50	VVV J131843.99-632716.96	13:18:43.99	-63:27:16.96	305.97598	-0.74437900	17.60(0.02)	17.30(0.02)	16.24(0.01)	15.81(0.02)	15.60(0.03)	1.14	–	n
VVVv51	VVV J131942.87-630101.88	13:19:42.87	-63:01:01.88	306.13293	-0.32129420	–	–	–	16.86(0.05)	14.49(0.01)	1.73	0.29	y
VVVv52	VVV J132308.94-624835.13	13:23:08.94	-62:48:35.13	306.54533	-0.16067607	14.49(0.01)	13.64(0.01)	12.75(0.01)	12.66(0.01)	12.16(0.01)	1.07	-2.34	n
VVVv53	VVV J132702.40-630622.47	13:27:02.40	-63:06:22.47	306.94521	-0.51222226	–	–	–	16.61(0.06)	14.53(0.02)	2.41	0.66	y
VVVv54	VVV J132758.65-631448.97	13:27:58.65	-63:14:48.97	307.03032	-0.66629476	12.89(0.01)	12.51(0.01)	–	12.49(0.01)	12.12(0.01)	1.02	-1.93	n
VVVv55	VVV J133403.43-625325.69	13:34:03.43	-62:53:25.69	307.76515	-0.41932813	20.11(0.21)	18.92(0.15)	16.87(0.03)	15.93(0.03)	15.39(0.03)	1.06	–	n
VVVv56	VVV J133746.01-622807.54	13:37:46.01	-62:28:07.54	308.25687	-0.076940272	19.21(0.08)	17.48(0.03)	15.52(0.01)	13.41(0.01)	12.45(0.01)	1.20	0.18	y
VVVv57	VVV J134041.89-631440.96	13:40:41.89	-63:14:40.96	308.44250	-0.90119565	–	–	18.10(0.06)	16.69(0.04)	15.85(0.04)	1.05	–	n
VVVv58	VVV J134213.00-621825.35	13:42:13.00	-62:18:25.35	308.79362	-0.014572925	17.48(0.02)	16.46(0.01)	15.04(0.01)	13.79(0.01)	12.61(0.01)	1.16	-0.16	n
VVVv59	VVV J134330.94-623719.95	13:43:30.94	-62:37:19.95	308.87836	-0.35322710	–	–	17.64(0.04)	14.68(0.01)	12.62(0.01)	1.03	-0.09	n
VVVv60	VVV J134452.75-631740.41	13:44:52.75	-63:17:40.41	308.89356	-1.0430378	–	18.78(0.09)	16.98(0.02)	15.82(0.02)	15.15(0.02)	1.11	–	n
VVVv61	VVV J134406.00-624932.88	13:44:06.00	-62:49:32.88	308.90289	-0.56613861	–	–	–	18.27(0.17)	15.54(0.03)	1.04	1.11	n
VVVv62	VVV J134550.28-622827.70	13:45:50.28	-62:28:27.70	309.17062	-0.26335743	–	–	–	–	14.01(0.01)	1.58	1.13	y
VVVv63	VVV J134620.48-622530.81	13:46:20.48	-62:25:30.81	309.23785	-0.22755314	–	–	18.53(0.09)	15.79(0.02)	13.81(0.01)	1.44	0.90	y
VVVv64	VVV J134623.81-622003.09	13:46:23.81	-62:20:03.09	309.26338	-0.13993603	–	–	–	14.96(0.01)	11.44(0.01)	1.18	-0.31	y
VVVv65	VVV J134751.09-624237.46	13:47:51.09	-62:42:37.46	309.34673	-0.54335348	–	–	18.75(0.10)	15.85(0.02)	13.59(0.01)	1.36	-0.31	y
VVVv66	VVV J134820.90-624309.74	13:48:20.90	-62:43:09.74	309.40035	-0.56450602	–	–	18.12(0.06)	16.64(0.03)	15.41(0.03)	1.08	0.02	y
VVVv67	VVV J134838.70-624627.31	13:48:38.70	-62:46:27.31	309.42145	-0.62549998	–	–	19.33(0.17)	16.98(0.05)	15.61(0.03)	1.08	0.40	y
VVVv68	VVV J134843.51-624549.42	13:48:43.51	-62:45:49.42	309.43271	-0.61724943	–	–	19.90(0.28)	16.42(0.03)	14.56(0.01)	1.03	0.14	y
VVVv69	VVV J134759.94-622011.92	13:47:59.94	-62:20:11.92	309.44451	-0.18220644	–	–	19.69(0.24)	17.55(0.08)	16.34(0.06)	1.26	0.49	n
VVVv70	VVV J135020.05-624524.09	13:50:20.05	-62:45:24.09	309.61377	-0.65148596	–	20.14(0.21)	18.05(0.05)	16.35(0.03)	15.31(0.02)	1.11	-1.74	n
VVVv71	VVV J135332.54-623724.91	13:53:32.54	-62:37:24.91	310.00262	-0.60748016	–	–	19.15(0.14)	16.79(0.04)	15.23(0.02)	1.15	-0.80	n
VVVv72	VVV J135328.30-623001.48	13:53:28.30	-62:30:01.48	310.02404	-0.48590749	21.20(0.33)	19.39(0.11)	17.77(0.04)	16.53(0.03)	15.83(0.04)	1.02	–	n
VVVv73	VVV J135517.97-630055.44	13:55:17.97	-63:00:55.44	310.10271	-1.0361549	16.43(0.01)	15.27(0.01)	15.21(0.01)	14.29(0.01)	13.64(0.01)	1.00	-1.44	n
VVVv74	VVV J135625.78-630003.44	13:56:25.78	-63:00:03.44	310.23056	-1.0538256	17.69(0.02)	17.21(0.02)	16.50(0.01)	15.91(0.02)	15.57(0.03)	1.04	–	n
VVVv75	VVV J135613.31-623609.30	13:56:13.31	-62:36:09.30	310.30662	-0.66205942	–	–	18.81(0.10)	17.09(0.05)	15.86(0.04)	1.14	0.06	n
VVVv76	VVV J135547.01-621233.21	13:55:47.01	-62:12:33.21	310.35477	-0.26837365	–	–	19.88(0.28)	15.35(0.01)	11.94(0.01)	1.02	0.56	n
VVVv77	VVV J135706.18-620016.61	13:57:06.18	-62:00:16.61	310.55520	-0.10864949	–	19.74(0.16)	18.83(0.11)	17.63(0.08)	16.87(0.10)	1.06	–	y
VVVv78	VVV J135733.86-615736.39	13:57:33.86	-61:57:36.39	310.61885	-0.079257084	20.79(0.23)	19.14(0.09)	17.59(0.04)	16.04(0.02)	15.13(0.02)	1.01	-2.04	n
VVVv79	VVV J135935.30-621036.12	13:59:35.30	-62:10:36.12	310.79224	-0.34948644	–	–	–	18.68(0.25)	16.75(0.15)	1.08	–	y
VVVv80	VVV J135903.61-614733.53	13:59:03.61	-61:47:33.53	310.83213	0.037490748	–	–	18.87(0.12)	16.74(0.04)	15.45(0.05)	1.14	-0.99	y
VVVv81	VVV J140700.55-615115.98	14:07:00.55	-61:51:15.98	311.71777	-0.27859549	–	–	–	17.32(0.07)	13.20(0.01)	1.66	0.67	y
VVVv82	VVV J140719.19-613717.46	14:07:19.19	-61:37:17.46	311.82022	-0.066209954	–	–	–	15.71(0.02)	11.75(0.01)	1.14	-0.32	y
VVVv83	VVV J141056.71-622513.45	14:10:56.71	-62:25:13.45	311.98995	-0.95513638	–	17.99(0.03)	16.39(0.01)	14.44(0.01)	12.75(0.01)	1.02	0.22	y
VVVv84	VVV J140911.55-613224.31	14:09:11.55	-61:32:24.31	312.05712	-0.053578278	20.05(0.13)	19.33(0.11)	17.10(0.03)	14.02(0.01)	11.97(0.01)	2.69	0.03	y
VVVv85	VVV J141046.67-615734.01	14:10:46.67	-61:57:34.01	312.11070	-0.50984837	19.81(0.10)	18.86(0.07)	17.68(0.04)	16.20(0.03)	15.39(0.04)	1.29	-1.23	n
VVVv86	VVV J141028.74-614946.06	14:10:28.74	-61:49:46.06	312.11632	-0.37529855	–	–	18.34(0.08)	13.78(0.01)	10.78(0.01)	1.82	0.57	n
VVVv87	VVV J141254.98-614527.53	14:12:54.98	-61:45:27.53	312.41250	-0.39485632	–	–	–	18.52(0.22)	15.40(0.04)	1.52	0.23	y
VVVv88	VVV J141227.76-613027.81	14:12:27.76	-61:30:27.81	312.43848	-0.14051542	–	–	18.42(0.08)	16.68(0.04)	15.71(0.06)	1.47	–	y
VVVv89	VVV J141534.31-621945.07	14:15:34.31	-62:19:45.07	312.52810	-1.0352796	–	–	–	15.71(0.02)	12.28(0.01)	2.22	1.08	n
VVVv90	VVV J141730.13-615054.83	14:17:30.13	-61:50:54.83	312.89716	-0.65337490	–	–	–	17.68(0.10)	16.08(0.08)	2.05	1.15	y
VVVv91	VVV J141649.12-611516.58	14:16:49.12	-61:15:16.58	313.01334	-0.065229497	–	–	–	17.82(0.11)	15.71(0.06)	1.52	1.29	y
VVVv92	VVV J141848.92-614133.03	14:18:48.92	-61:41:33.03	313.09512	-0.55705078	19.94(0.09)	18.67(0.05)	17.28(0.03)	16.11(0.02)	15.60(0.05)	1.11	–	n
VVVv93	VVV J142239.35-620248.52	14:22:39.35	-62:02:48.52	313.40139	-1.0435294	21.05(0.25)	20.11(0.21)	18.77(0.11)	17.10(0.06)	15.98(0.07)	1.49	–	n
VVVv94	VVV J142257.76-610547.03	14:22:57.76	-61:05:47.03	313.76407	-0.16426726	–	–	–	16.42(0.03)	13.39(0.01)	1.87	0.54	y
VVVv95	VVV J142517.08-613042.02	14:25:17.08	-61:30:42.02	313.87973	-0.65085613	–	20.11(0.25)	18.07(0.06)	16.66(0.04)	15.98(0.04)	1.09	–	n
VVVv96	VVV J142634.45-613900.61	14:26:34.45	-61:39:00.61	313.97367	-0.83496274	–	19.91(0.21)	18.48(0.08)	16.78(0.04)	15.92(0.04)	1.05	-0.93	n
VVVv97	VVV J142422.62-605320.62	14:24:22.62	-60:53:20.62	313.99705	-0.029704132	–	–	19.21(0.16)	17.04(0.05)	15.71(0.03)	1.07	–	y

Continued on next page

Table A.1 – *Continued from previous page*

Object ID	VVV Designation	α (J2000)	δ (J2000)	l	b	Z (mag)	Y (mag)	J (mag)	H (mag)	K_s (mag)	ΔK_s^a (mag)	α_{class}	SFR
VVVv98	VVV J142500.68-605448.20	14:25:00.68	-60:54:48.20	314.06065	-0.079633857	–	–	–	18.08(0.14)	14.61(0.01)	1.32	0.60	y
VVVv99	VVV J142701.20-612525.27	14:27:01.20	-61:25:25.27	314.10472	-0.64275203	13.48(0.01)	13.04(0.01)	12.74(0.01)	12.78(0.01)	12.39(0.01)	1.01	-2.34	n
VVVv100	VVV J142807.13-613816.91	14:28:07.13	-61:38:16.91	314.14907	-0.88998650	18.30(0.03)	17.51(0.02)	16.63(0.02)	15.71(0.02)	15.33(0.02)	1.13	–	n
VVVv101	VVV J142538.25-604811.19	14:25:38.25	-60:48:11.19	314.17103	-0.0035383980	–	–	–	17.60(0.09)	15.61(0.03)	1.04	0.43	y
VVVv102	VVV J142852.17-612217.27	14:28:52.17	-61:22:17.27	314.32991	-0.67463613	–	–	19.05(0.14)	15.27(0.01)	12.37(0.01)	1.75	0.79	n
VVVv103	VVV J143227.49-603942.58	14:32:27.49	-60:39:42.58	314.99820	-0.17867802	–	–	19.78(0.28)	16.83(0.04)	14.75(0.01)	1.49	0.94	y
VVVv104	VVV J143404.67-610609.65	14:34:04.67	-61:06:09.65	315.01158	-0.66136721	18.20(0.02)	17.57(0.03)	16.64(0.02)	15.64(0.01)	14.77(0.01)	1.06	-0.53	n
VVVv105	VVV J143437.21-611023.13	14:34:37.21	-61:10:23.13	315.04474	-0.75159689	18.29(0.03)	17.92(0.03)	16.94(0.02)	16.29(0.03)	15.99(0.04)	1.10	–	n
VVVv106	VVV J143357.09-604737.87	14:33:57.09	-60:47:37.87	315.11639	-0.37046494	–	–	–	14.88(0.01)	11.91(0.01)	1.48	0.74	n
VVVv107	VVV J144044.97-610704.39	14:40:44.97	-61:07:04.39	315.74517	-0.99527111	–	–	16.35(0.02)	12.93(0.01)	11.32(0.01)	1.54	0.06	n
VVVv108	VVV J143853.29-601007.32	14:38:53.29	-60:10:07.32	315.92142	-0.035107365	–	–	17.74(0.05)	15.05(0.01)	13.44(0.01)	1.12	-1.52	n
VVVv109	VVV J144212.43-604125.50	14:42:12.43	-60:41:25.50	316.08250	-0.67846509	–	19.33(0.11)	16.66(0.02)	14.21(0.01)	12.36(0.01)	1.35	0.12	y
VVVv110	VVV J144351.27-602150.93	14:43:51.27	-60:21:50.93	316.40259	-0.46621051	–	–	19.44(0.26)	16.64(0.05)	14.40(0.01)	1.13	1.29	y
VVVv111	VVV J144444.70-602616.44	14:44:44.70	-60:26:16.44	316.47132	-0.57938884	–	–	–	–	13.22(0.01)	1.64	1.23	y
VVVv112	VVV J144427.29-595924.99	14:44:27.29	-59:59:24.99	316.62747	-0.15833964	–	–	18.79(0.13)	14.92(0.01)	12.02(0.01)	1.07	-0.10	y
VVVv113	VVV J144523.82-595209.70	14:45:23.82	-59:52:09.70	316.78555	-0.098682368	–	–	–	18.58(0.27)	15.72(0.04)	1.49	1.85	y
VVVv114	VVV J144906.82-604557.11	14:49:06.82	-60:45:57.11	316.81448	-1.1059247	–	–	–	–	15.78(0.04)	3.02	2.91	n
VVVv115	VVV J144802.41-600427.26	14:48:02.41	-60:04:27.26	316.99634	-0.42561223	20.02(0.11)	18.86(0.07)	17.71(0.05)	16.40(0.04)	15.47(0.03)	1.17	-0.58	n
VVVv116	VVV J144812.64-600310.10	14:48:12.64	-60:03:10.10	317.02482	-0.41553387	19.66(0.08)	18.49(0.05)	17.41(0.04)	16.50(0.04)	15.96(0.05)	1.09	–	n
VVVv117	VVV J145003.98-594734.18	14:50:03.98	-59:47:34.18	317.34758	-0.28338020	–	20.39(0.27)	18.14(0.07)	16.55(0.04)	15.49(0.03)	1.15	–	y
VVVv118	VVV J145120.97-600027.40	14:51:20.97	-60:00:27.40	317.39680	-0.54718287	16.61(0.01)	15.98(0.01)	16.09(0.01)	14.54(0.01)	13.01(0.01)	3.18	0.16	y
VVVv119	VVV J145253.28-600452.73	14:52:53.28	-60:04:52.73	317.53562	-0.69901203	–	–	18.30(0.08)	15.49(0.02)	13.71(0.01)	1.22	0.02	y
VVVv120	VVV J145300.70-591443.50	14:53:00.70	-59:14:43.50	317.92578	0.040414726	17.94(0.02)	17.71(0.02)	17.37(0.04)	16.55(0.04)	15.94(0.05)	1.20	–	n
VVVv121	VVV J145521.85-593709.11	14:55:21.85	-59:37:09.11	318.02247	-0.42843540	18.58(0.03)	16.84(0.01)	15.06(0.01)	13.65(0.01)	12.76(0.01)	1.09	-0.94	n
VVVv122	VVV J145630.67-594925.77	14:56:30.67	-59:49:25.77	318.05670	-0.67663412	–	–	19.39(0.19)	17.03(0.05)	15.42(0.03)	1.08	0.55	y
VVVv123	VVV J145731.64-593810.86	14:57:31.64	-59:38:10.86	318.25710	-0.56990617	–	–	–	14.17(0.01)	11.27(0.01)	2.21	0.78	y
VVVv124	VVV J145531.30-590703.08	14:55:31.30	-59:07:03.08	318.27027	0.0082299030	20.32(0.16)	19.24(0.11)	17.59(0.04)	15.89(0.02)	14.12(0.01)	1.17	0.47	y
VVVv125	VVV J145940.19-595943.02	14:59:40.19	-59:59:43.02	318.32666	-1.0132060	–	–	18.32(0.07)	16.83(0.04)	16.04(0.05)	1.20	–	n
VVVv126	VVV J150007.69-595334.83	15:00:07.69	-59:53:34.83	318.42562	-0.95026032	–	19.24(0.11)	16.50(0.01)	14.04(0.01)	12.18(0.01)	1.60	0.57	n
VVVv127	VVV J145747.25-591424.34	14:57:47.25	-59:14:24.34	318.47092	-0.23465810	–	–	–	–	16.93(0.11)	1.13	2.03	y
VVVv128	VVV J145829.67-590940.29	14:58:29.67	-59:09:40.29	318.58781	-0.20719883	–	–	19.62(0.24)	17.15(0.06)	14.47(0.01)	1.90	0.95	y
VVVv129	VVV J150213.13-595904.80	15:02:13.13	-59:59:04.80	318.61195	-1.1557905	16.90(0.01)	16.49(0.01)	15.92(0.01)	15.25(0.01)	15.00(0.02)	1.39	–	n
VVVv130	VVV J150043.33-592229.68	15:00:43.33	-59:22:29.68	318.73777	-0.52997224	–	20.34(0.31)	17.07(0.02)	14.40(0.01)	12.65(0.01)	1.02	0.42	y
VVVv131	VVV J150310.44-595120.55	15:03:10.44	-59:51:20.55	318.77903	-1.1005633	19.84(0.10)	18.72(0.07)	18.30(0.07)	17.40(0.07)	16.78(0.09)	1.31	–	n
VVVv132	VVV J150201.88-584927.58	15:02:01.88	-58:49:27.58	319.14859	-0.12670835	–	–	19.08(0.15)	17.31(0.07)	16.38(0.06)	1.02	–	n
VVVv133	VVV J150620.36-592544.52	15:06:20.36	-59:25:44.52	319.33663	-0.92401220	19.89(0.11)	19.01(0.10)	17.88(0.05)	16.61(0.04)	15.78(0.04)	1.08	–	n
VVVv134	VVV J150738.24-585138.25	15:07:38.24	-58:51:38.25	319.76324	-0.51313412	–	–	18.57(0.11)	16.04(0.03)	14.32(0.01)	1.14	-0.83	y
VVVv135	VVV J150738.65-582404.65	15:07:38.65	-58:24:04.65	319.99291	-0.11534117	–	–	–	17.57(0.11)	15.18(0.02)	1.06	1.52	y
VVVv136	VVV J151216.89-590331.54	15:12:16.89	-59:03:31.54	320.17950	-0.98686000	19.05(0.05)	18.04(0.04)	17.15(0.03)	16.36(0.04)	15.97(0.05)	1.05	–	n
VVVv137	VVV J151252.81-591036.72	15:12:52.81	-59:10:36.72	320.18465	-1.1276528	17.29(0.01)	16.34(0.01)	15.04(0.01)	13.95(0.01)	13.06(0.01)	1.12	-0.99	n
VVVv138	VVV J151007.47-582209.73	15:10:07.47	-58:22:09.73	320.29002	-0.25102100	17.81(0.02)	16.83(0.01)	15.92(0.01)	15.03(0.01)	14.60(0.01)	1.02	-2.43	n
VVVv139	VVV J150932.71-581345.47	15:09:32.71	-58:13:45.47	320.29513	-0.091687463	–	–	–	18.17(0.19)	16.06(0.05)	2.18	-0.03	y
VVVv140	VVV J151338.45-585243.48	15:13:38.45	-58:52:43.48	320.42244	-0.92287920	–	–	–	16.06(0.03)	13.32(0.01)	1.91	0.63	y
VVVv141	VVV J151120.96-582222.07	15:11:20.96	-58:22:22.07	320.42657	-0.33558965	18.01(0.02)	17.19(0.02)	17.28(0.03)	15.54(0.02)	14.09(0.01)	1.01	-0.48	y
VVVv142	VVV J151430.54-585847.00	15:14:30.54	-58:58:47.00	320.46581	-1.0673254	–	–	–	17.99(0.16)	16.23(0.06)	1.12	0.52	n
VVVv143	VVV J151523.39-585404.60	15:15:23.39	-58:54:04.60	320.60367	-1.0596642	20.83(0.25)	19.81(0.19)	18.15(0.08)	15.62(0.02)	12.63(0.01)	1.83	0.86	n
VVVv144	VVV J151636.38-580912.14	15:16:36.38	-58:09:12.14	321.13146	-0.50643319	–	18.88(0.09)	17.80(0.07)	16.62(0.06)	16.00(0.07)	1.09	–	n
VVVv145	VVV J151656.42-580326.30	15:16:56.42	-58:03:26.30	321.21961	-0.44807936	–	–	–	16.94(0.08)	14.59(0.02)	1.04	1.23	y
VVVv146	VVV J152110.72-582125.91	15:21:10.72	-58:21:25.91	321.53117	-0.99989731	18.06(0.02)	17.44(0.03)	16.93(0.03)	16.39(0.05)	15.87(0.06)	1.03	–	n

Continued on next page

Table A.1 – *Continued from previous page*

Object ID	VVV Designation	α (J2000)	δ (J2000)	l	b	Z (mag)	Y (mag)	J (mag)	H (mag)	K_s (mag)	ΔK_s^a (mag)	α_{class}	SFR
VVVv147	VVV J151837.80-574504.85	15:18:37.80	-57:45:04.85	321.57219	-0.30778764	–	–	–	18.65(0.40)	15.90(0.06)	1.29	1.39	n
VVVv148	VVV J151906.61-573927.84	15:19:06.61	-57:39:27.84	321.67639	-0.26286291	–	–	–	–	16.23(0.08)	1.37	1.07	n
VVVv149	VVV J152100.25-575153.34	15:21:00.25	-57:51:53.34	321.77808	-0.57326503	–	–	–	–	15.53(0.04)	2.03	1.69	y
VVVv150	VVV J151958.89-571807.48	15:19:58.89	-57:18:07.48	321.96587	-0.025361160	–	–	18.52(0.13)	16.44(0.05)	15.13(0.03)	1.14	-0.58	y
VVVv151	VVV J152447.81-580940.66	15:24:47.81	-58:09:40.66	322.03681	-1.0959855	–	–	–	–	16.19(0.07)	1.07	1.77	y
VVVv152	VVV J152040.85-571000.26	15:20:40.85	-57:10:00.26	322.11848	0.037741224	15.65(0.01)	14.44(0.01)	13.46(0.01)	12.50(0.01)	11.82(0.01)	1.42	-1.28	n
VVVv153	VVV J152128.41-571847.88	15:21:28.41	-57:18:47.88	322.12944	-0.14352346	–	–	–	–	16.70(0.13)	1.02	0.30	y
VVVv154	VVV J152405.24-574954.21	15:24:05.24	-57:49:54.21	322.13999	-0.76916561	18.33(0.03)	17.19(0.02)	16.27(0.02)	16.07(0.04)	14.94(0.03)	1.08	-1.39	n
VVVv155	VVV J152308.09-571712.94	15:23:08.09	-57:17:12.94	322.33200	-0.24356776	–	–	–	17.10(0.10)	14.99(0.03)	1.73	0.73	n
VVVv156	VVV J152511.24-571946.17	15:25:11.24	-57:19:46.17	322.54002	-0.43158088	18.96(0.05)	17.81(0.03)	16.69(0.02)	15.61(0.02)	14.99(0.02)	1.30	–	n
VVVv157	VVV J152548.43-565949.91	15:25:48.43	-56:59:49.91	322.79413	-0.20155833	–	19.32(0.12)	17.70(0.05)	16.32(0.04)	15.37(0.03)	1.05	0.08	n
VVVv158	VVV J152542.31-564529.64	15:25:42.31	-56:45:29.64	322.91517	0.0049552600	–	19.12(0.10)	16.70(0.02)	15.28(0.01)	14.52(0.01)	1.15	-1.62	n
VVVv159	VVV J152729.60-565854.70	15:27:29.60	-56:58:54.70	322.99331	-0.31691312	–	–	18.82(0.14)	17.09(0.08)	16.04(0.06)	1.02	–	n
VVVv160	VVV J152734.81-565811.76	15:27:34.81	-56:58:11.76	323.00980	-0.31366671	16.66(0.01)	15.19(0.01)	13.74(0.01)	12.91(0.01)	12.32(0.01)	1.05	-2.15	n
VVVv161	VVV J152939.43-571119.22	15:29:39.43	-57:11:19.22	323.11960	-0.65340532	–	–	–	18.35(0.24)	16.64(0.10)	1.33	0.90	y
VVVv162	VVV J152917.51-565411.95	15:29:17.51	-56:54:11.95	323.24023	-0.39007426	–	–	–	–	14.01(0.01)	1.69	0.31	y
VVVv163	VVV J152934.08-565225.52	15:29:34.08	-56:52:25.52	323.28806	-0.38705316	–	–	18.71(0.13)	16.17(0.03)	14.74(0.02)	1.28	0.34	y
VVVv164	VVV J152921.67-563902.13	15:29:21.67	-56:39:02.13	323.39104	-0.18705517	19.50(0.09)	18.25(0.05)	17.19(0.03)	16.02(0.03)	15.55(0.04)	1.06	–	n
VVVv165	VVV J152941.48-564020.33	15:29:41.48	-56:40:20.33	323.41614	-0.23065525	–	–	17.99(0.07)	15.56(0.02)	13.78(0.01)	1.08	1.53	y
VVVv166	VVV J152940.33-563823.01	15:29:40.33	-56:38:23.01	323.43245	-0.20231949	–	–	18.87(0.15)	17.00(0.07)	16.10(0.06)	1.01	–	n
VVVv167	VVV J153021.60-563844.55	15:30:21.60	-56:38:44.55	323.50687	-0.26092559	20.18(0.16)	18.26(0.05)	15.70(0.01)	13.34(0.01)	11.84(0.01)	1.33	0.46	y
VVVv168	VVV J153200.86-563842.58	15:32:00.86	-56:38:42.58	323.69382	-0.39040201	–	–	–	16.45(0.04)	14.27(0.01)	1.96	-0.57	y
VVVv169	VVV J153157.36-563609.37	15:31:57.36	-56:36:09.37	323.71166	-0.35094168	–	–	–	15.32(0.02)	12.44(0.01)	1.15	0.33	y
VVVv170	VVV J153647.49-565210.20	15:36:47.49	-56:52:10.20	324.09644	-0.95329522	–	–	–	17.67(0.17)	15.17(0.03)	1.20	1.22	y
VVVv171	VVV J153706.12-563233.54	15:37:06.12	-56:32:33.54	324.32323	-0.71407947	–	19.42(0.15)	17.33(0.05)	16.24(0.04)	15.61(0.05)	1.28	-1.88	n
VVVv172	VVV J153640.80-555258.91	15:36:40.80	-55:52:58.91	324.66374	-0.14610140	20.61(0.23)	18.66(0.07)	18.03(0.09)	16.60(0.06)	15.86(0.06)	1.04	-1.13	n
VVVv173	VVV J153746.87-560415.21	15:37:46.87	-56:04:15.21	324.67753	-0.38864250	–	–	18.23(0.10)	17.26(0.11)	16.10(0.07)	1.05	–	n
VVVv174	VVV J153815.79-553951.62	15:38:15.79	-55:39:51.62	324.97249	-0.10079843	–	–	19.19(0.26)	17.11(0.10)	16.03(0.07)	1.22	–	n
VVVv175	VVV J153939.81-555046.92	15:39:39.81	-55:50:46.92	325.02281	-0.36427177	–	–	19.40(0.31)	17.16(0.10)	15.73(0.05)	1.16	-0.40	y
VVVv176	VVV J153837.25-552821.44	15:38:37.25	-55:28:21.44	325.12683	0.023659844	–	–	–	–	14.56(0.02)	1.22	2.97	y
VVVv177	VVV J154007.59-553015.85	15:40:07.59	-55:30:15.85	325.27927	-0.12884295	–	19.58(0.17)	18.22(0.11)	17.22(0.11)	16.75(0.13)	1.37	–	n
VVVv178	VVV J154249.38-560011.63	15:42:49.38	-56:00:11.63	325.28237	-0.75551952	19.84(0.11)	18.92(0.10)	17.76(0.07)	16.91(0.08)	16.43(0.10)	1.12	–	n
VVVv179	VVV J154502.34-555807.95	15:45:02.34	-55:58:07.95	325.54925	-0.91681352	–	–	18.45(0.11)	16.58(0.05)	15.45(0.04)	1.56	-0.51	y
VVVv180	VVV J154252.38-552311.07	15:42:52.38	-55:23:11.07	325.66138	-0.26880695	–	–	–	–	12.18(0.01)	1.74	0.60	n
VVVv181	VVV J154639.17-555028.27	15:46:39.17	-55:50:28.27	325.80621	-0.95485088	20.42(0.17)	19.40(0.14)	17.81(0.06)	15.02(0.01)	12.72(0.01)	2.15	0.72	y
VVVv182	VVV J154309.19-550153.01	15:43:09.19	-55:01:53.01	325.90823	-0.010552867	–	–	19.08(0.19)	16.98(0.08)	15.16(0.03)	1.04	0.47	y
VVVv183	VVV J154307.07-550119.87	15:43:07.07	-55:01:19.87	325.90979	-0.00016657300	–	–	–	16.80(0.07)	14.51(0.02)	1.35	0.76	y
VVVv184	VVV J154513.00-552251.04	15:45:13.00	-55:22:51.04	325.92885	-0.46699902	–	19.84(0.23)	17.35(0.04)	15.58(0.02)	14.54(0.02)	1.07	-1.94	n
VVVv185	VVV J154605.44-551957.68	15:46:05.44	-55:19:57.68	326.05649	-0.50512799	–	–	19.42(0.26)	17.33(0.11)	15.46(0.04)	1.03	0.80	y
VVVv186	VVV J154758.12-552938.44	15:47:58.12	-55:29:38.44	326.16666	-0.79655063	14.57(0.01)	13.99(0.01)	13.43(0.01)	12.91(0.01)	12.55(0.01)	1.26	-2.27	n
VVVv187	VVV J154617.80-550439.61	15:46:17.80	-55:04:39.61	326.23646	-0.32206890	–	–	–	–	12.88(0.01)	1.57	9.01	n
VVVv188	VVV J154635.47-545846.03	15:46:35.47	-54:58:46.03	326.33016	-0.27062331	–	–	–	14.19(0.01)	11.68(0.01)	1.30	0.11	y
VVVv189	VVV J154905.50-552236.60	15:49:05.50	-55:22:36.60	326.36429	-0.80370475	19.67(0.08)	18.92(0.10)	18.80(0.15)	17.60(0.14)	16.65(0.11)	1.49	–	n
VVVv190	VVV J154703.56-544310.15	15:47:03.56	-54:43:10.15	326.54350	-0.10749672	–	–	18.83(0.15)	15.60(0.02)	13.49(0.01)	1.31	1.25	y
VVVv191	VVV J154707.98-544302.68	15:47:07.98	-54:43:02.68	326.55314	-0.11241798	–	–	–	–	15.63(0.04)	1.08	2.57	y
VVVv192	VVV J155121.51-545723.34	15:51:21.51	-54:57:23.34	326.87990	-0.67856418	–	–	–	18.10(0.17)	14.45(0.01)	1.18	0.64	y
VVVv193	VVV J154914.34-543423.66	15:49:14.34	-54:34:23.66	326.88153	-0.18832110	–	–	–	16.59(0.04)	13.90(0.01)	1.12	0.86	y
VVVv194	VVV J154957.50-543838.27	15:49:57.50	-54:38:38.27	326.91875	-0.30859755	–	–	–	–	15.54(0.04)	1.16	0.98	y
VVVv195	VVV J155314.61-551333.40	15:53:14.61	-55:13:33.40	326.91871	-1.0578058	19.67(0.11)	18.83(0.09)	18.55(0.10)	16.97(0.06)	15.91(0.05)	1.70	-0.33	y

Continued on next page

Table A.1 – *Continued from previous page*

Object ID	VVV Designation	α (J2000)	δ (J2000)	l	b	Z (mag)	Y (mag)	J (mag)	H (mag)	K_s (mag)	ΔK_s^a (mag)	α_{class}	SFR
VVVv196	VVV J154932.40-542534.67	15:49:32.40	-54:25:34.67	327.00734	-0.10071860	–	–	–	18.14(0.18)	16.10(0.06)	1.14	2.07	y
VVVv197	VVV J155122.71-542010.52	15:51:22.71	-54:20:10.52	327.27238	-0.19828853	–	–	–	16.78(0.05)	12.50(0.01)	1.37	0.56	y
VVVv198	VVV J155307.15-543639.89	15:53:07.15	-54:36:39.89	327.29485	-0.57105578	20.53(0.23)	19.49(0.16)	19.11(0.16)	17.72(0.12)	14.75(0.02)	1.61	2.06	y
VVVv199	VVV J155256.17-542852.83	15:52:56.17	-54:28:52.83	327.35655	-0.45388078	–	–	19.24(0.18)	16.80(0.05)	15.28(0.03)	1.08	0.72	y
VVVv200	VVV J155302.80-542708.40	15:53:02.80	-54:27:08.40	327.38735	-0.44160884	–	–	–	–	12.68(0.01)	1.34	1.00	y
VVVv201	VVV J155211.02-541051.16	15:52:11.02	-54:10:51.16	327.46158	-0.15175610	–	–	–	–	14.62(0.02)	2.54	1.97	n
VVVv202	VVV J155426.41-540829.40	15:54:26.41	-54:08:29.40	327.74188	-0.33087074	–	–	17.38(0.03)	13.28(0.01)	11.66(0.01)	1.31	1.16	y
VVVv203	VVV J155643.05-542945.28	15:56:43.05	-54:29:45.28	327.76983	-0.81574271	–	18.26(0.05)	16.65(0.02)	15.19(0.01)	14.39(0.01)	1.09	-1.19	n
VVVv204	VVV J155450.66-540315.87	15:54:50.66	-54:03:15.87	327.84307	-0.30161347	–	–	–	–	14.17(0.01)	2.61	2.39	y
VVVv205	VVV J155628.83-541406.86	15:56:28.83	-54:14:06.86	327.91112	-0.59397360	19.69(0.11)	18.78(0.09)	16.31(0.01)	14.97(0.01)	13.79(0.01)	1.25	-0.98	y
VVVv206	VVV J155608.75-535525.81	15:56:08.75	-53:55:25.81	328.07362	-0.32383333	–	–	–	16.24(0.03)	11.62(0.01)	1.15	-0.25	y
VVVv207	VVV J155544.14-533732.94	15:55:44.14	-53:37:32.94	328.21834	-0.056356997	–	–	–	16.12(0.03)	12.28(0.01)	1.69	0.18	y
VVVv208	VVV J155641.55-534553.75	15:56:41.55	-53:45:53.75	328.23755	-0.25395471	–	19.61(0.18)	–	16.79(0.05)	12.52(0.01)	1.53	0.20	y
VVVv209	VVV J155758.41-535807.08	15:57:58.41	-53:58:07.08	328.25034	-0.53141930	–	–	19.17(0.17)	16.68(0.05)	15.34(0.03)	1.22	–	y
VVVv210	VVV J155819.39-540133.97	15:58:19.39	-54:01:33.97	328.25230	-0.60849002	–	–	–	15.47(0.02)	11.67(0.01)	1.09	-0.37	y
VVVv211	VVV J155807.52-535714.66	15:58:07.52	-53:57:14.66	328.27680	-0.53477923	–	–	–	–	15.51(0.04)	1.13	3.43	y
VVVv212	VVV J155558.91-533219.30	15:55:58.91	-53:32:19.30	328.30224	-0.012937775	–	19.38(0.15)	16.56(0.02)	14.07(0.01)	12.36(0.01)	3.11	0.58	y
VVVv213	VVV J155617.48-532950.20	15:56:17.48	-53:29:50.20	328.36411	-0.010735849	–	–	17.79(0.07)	14.54(0.01)	12.65(0.01)	1.98	-2.82	y
VVVv214	VVV J155741.02-534347.63	15:57:41.02	-53:43:47.63	328.37212	-0.32167335	–	–	–	16.26(0.05)	14.06(0.01)	1.01	0.45	y
VVVv215	VVV J155916.48-540006.12	15:59:16.48	-54:00:06.12	328.37445	-0.68066691	–	–	19.15(0.23)	14.52(0.01)	11.65(0.01)	1.99	-0.32	n
VVVv216	VVV J155844.58-535337.80	15:58:44.58	-53:53:37.80	328.38508	-0.54784787	–	–	18.88(0.18)	16.95(0.09)	15.60(0.05)	1.73	-0.61	y
VVVv217	VVV J155902.40-534116.97	15:59:02.40	-53:41:16.97	328.55209	-0.41986014	17.70(0.02)	16.69(0.01)	15.30(0.01)	14.04(0.01)	12.99(0.01)	1.75	-0.52	y
VVVv218	VVV J155807.87-532943.96	15:58:07.87	-53:29:43.96	328.57433	-0.18587857	–	19.25(0.14)	17.54(0.06)	15.48(0.02)	12.12(0.01)	1.38	0.72	n
VVVv219	VVV J155938.19-533959.95	15:59:38.19	-53:39:59.95	328.63309	-0.46108532	–	–	–	16.95(0.08)	14.50(0.02)	1.49	-0.28	y
VVVv220	VVV J155954.74-534027.71	15:59:54.74	-53:40:27.71	328.65906	-0.49357133	–	–	–	17.79(0.18)	15.46(0.04)	1.30	0.07	y
VVVv221	VVV J160046.60-534036.32	16:00:46.60	-53:40:36.32	328.75440	-0.57900405	–	–	–	15.93(0.03)	12.29(0.01)	1.31	1.29	n
VVVv222	VVV J160448.76-535412.84	16:04:48.76	-53:54:12.84	329.05271	-1.1427110	–	–	18.39(0.11)	14.95(0.01)	12.21(0.01)	1.65	0.14	n
VVVv223	VVV J160202.72-532218.87	16:02:02.72	-53:22:18.87	329.09671	-0.47265151	–	–	17.53(0.05)	13.46(0.01)	11.69(0.01)	1.01	-0.92	n
VVVv224	VVV J160347.48-533418.99	16:03:47.48	-53:34:18.99	329.15985	-0.79441331	–	–	–	16.64(0.06)	13.31(0.01)	2.46	0.77	n
VVVv225	VVV J160528.47-534420.45	16:05:28.47	-53:44:20.45	329.23518	-1.0849927	17.16(0.01)	16.09(0.01)	14.89(0.01)	13.99(0.01)	13.31(0.01)	1.09	-1.79	n
VVVv226	VVV J160206.29-530850.39	16:02:06.29	-53:08:50.39	329.25116	-0.30937117	–	–	–	16.82(0.08)	14.18(0.01)	1.82	0.73	y
VVVv227	VVV J160133.14-525521.83	16:01:33.14	-52:55:21.83	329.33616	-0.085496493	18.05(0.02)	17.13(0.02)	17.38(0.05)	16.44(0.06)	15.68(0.05)	1.05	-0.45	n
VVVv228	VVV J160335.44-531414.20	16:03:35.44	-53:14:14.20	329.35903	-0.52380854	–	–	–	16.82(0.08)	13.76(0.01)	1.20	0.62	y
VVVv229	VVV J160424.48-530114.01	16:04:24.48	-53:01:14.01	329.59450	-0.44282427	–	–	–	–	13.01(0.01)	3.69	2.41	n
VVVv230	VVV J161006.42-525119.46	16:10:06.42	-52:51:19.46	330.34185	-0.89678562	–	–	17.43(0.05)	15.94(0.03)	14.93(0.03)	1.22	-0.43	n
VVVv231	VVV J160825.89-521333.77	16:08:25.89	-52:13:33.77	330.57989	-0.26091255	–	–	–	15.52(0.02)	12.81(0.01)	1.41	-0.21	y
VVVv232	VVV J161004.42-521301.46	16:10:04.42	-52:13:01.46	330.77123	-0.42439353	–	–	–	16.75(0.07)	14.81(0.02)	2.07	1.21	y
VVVv233	VVV J161240.47-523302.72	16:12:40.47	-52:33:02.72	330.83416	-0.93907257	–	–	19.04(0.23)	17.09(0.10)	15.76(0.06)	1.18	-0.20	n
VVVv234	VVV J161146.65-521915.53	16:11:46.65	-52:19:15.53	330.89153	-0.67792890	18.15(0.03)	17.73(0.04)	17.15(0.04)	15.68(0.03)	11.95(0.01)	1.29	0.73	n
VVVv235	VVV J160935.53-515414.08	16:09:35.53	-51:54:14.08	330.92907	-0.14398113	–	–	–	17.95(0.22)	11.70(0.01)	1.24	1.15	y
VVVv236	VVV J160937.74-514027.52	16:09:37.74	-51:40:27.52	331.08873	0.021115542	19.43(0.08)	17.88(0.04)	16.45(0.02)	15.36(0.02)	14.58(0.02)	1.04	-1.80	y
VVVv237	VVV J161048.22-514245.01	16:10:48.22	-51:42:45.01	331.19651	-0.13049419	–	19.46(0.21)	18.44(0.15)	16.25(0.05)	13.83(0.01)	1.24	1.10	y
VVVv238	VVV J161210.99-515417.23	16:12:10.99	-51:54:17.23	331.22135	-0.41653972	–	–	19.20(0.31)	16.71(0.07)	14.95(0.03)	1.30	0.32	y
VVVv239	VVV J161153.85-513059.51	16:11:53.85	-51:30:59.51	331.45432	-0.10280464	–	–	–	–	15.71(0.06)	1.27	1.42	y
VVVv240	VVV J161303.44-514151.91	16:13:03.44	-51:41:51.91	331.46161	-0.35818975	–	–	–	16.35(0.05)	12.10(0.01)	1.17	0.74	y
VVVv241	VVV J161706.22-511730.81	16:17:06.22	-51:17:30.81	332.19736	-0.49979014	18.35(0.04)	16.72(0.02)	15.33(0.01)	14.19(0.01)	13.51(0.01)	1.24	-2.11	y
VVVv242	VVV J161703.71-510640.99	16:17:03.71	-51:06:40.99	332.31823	-0.36555934	–	–	–	15.26(0.02)	12.06(0.01)	1.70	-0.54	y
VVVv243	VVV J161802.02-511439.85	16:18:02.02	-51:14:39.85	332.33479	-0.56710101	–	–	–	–	15.64(0.05)	1.14	2.33	y
VVVv244	VVV J162001.99-512602.11	16:20:01.99	-51:26:02.11	332.42494	-0.92108095	–	–	17.62(0.07)	14.99(0.01)	13.05(0.01)	1.59	0.79	y

Continued on next page

Table A.1 – *Continued from previous page*

Object ID	VVV Designation	α (J2000)	δ (J2000)	l	b	Z (mag)	Y (mag)	J (mag)	H (mag)	K_s (mag)	ΔK_s^a (mag)	α_{class}	SFR
VVVv245	VVV J161920.93-511107.06	16:19:20.93	-51:11:07.06	332.52333	-0.66895075	–	–	–	17.48(0.14)	15.61(0.05)	1.01	-0.53	n
VVVv246	VVV J161841.84-505702.76	16:18:41.84	-50:57:02.76	332.61452	-0.42986004	–	–	–	17.76(0.18)	16.27(0.10)	1.23	–	n
VVVv247	VVV J161713.24-503845.65	16:17:13.24	-50:38:45.65	332.66002	-0.048740215	17.47(0.01)	16.71(0.01)	15.93(0.01)	14.87(0.01)	12.46(0.01)	1.64	0.84	y
VVVv248	VVV J162051.74-511336.09	16:20:51.74	-51:13:36.09	332.66283	-0.86503642	–	–	19.68(0.30)	17.17(0.08)	15.27(0.03)	1.27	0.85	y
VVVv249	VVV J161724.00-503658.01	16:17:24.00	-50:36:58.01	332.70127	-0.047088410	–	20.04(0.22)	18.10(0.07)	15.86(0.02)	14.83(0.02)	1.27	–	y
VVVv250	VVV J161819.35-503227.95	16:18:19.35	-50:32:27.95	332.85853	-0.095485371	–	–	–	15.79(0.02)	12.30(0.01)	1.43	0.47	y
VVVv251	VVV J162034.52-505106.31	16:20:34.52	-50:51:06.31	332.89495	-0.56713469	–	–	–	17.29(0.09)	15.03(0.02)	1.51	-0.05	y
VVVv252	VVV J161920.52-502317.47	16:19:20.52	-50:23:17.47	333.08142	-0.099801669	–	–	–	–	17.13(0.17)	2.39	4.30	y
VVVv253	VVV J162115.82-504027.98	16:21:15.82	-50:40:27.98	333.09714	-0.51807941	–	–	19.72(0.30)	17.97(0.16)	13.77(0.01)	1.74	2.16	y
VVVv254	VVV J161943.16-502401.84	16:19:43.16	-50:24:01.84	333.11563	-0.15077631	–	–	18.62(0.11)	16.36(0.04)	14.71(0.02)	1.05	0.25	y
VVVv255	VVV J162122.89-503514.65	16:21:22.89	-50:35:14.65	333.17183	-0.46962211	–	–	–	18.05(0.18)	15.61(0.04)	1.21	1.20	y
VVVv256	VVV J161935.14-501640.86	16:19:35.14	-50:16:40.86	333.18641	-0.048550015	–	–	–	18.57(0.29)	15.16(0.03)	1.12	0.37	y
VVVv257	VVV J162101.87-502912.99	16:21:01.87	-50:29:12.99	333.20324	-0.35913859	–	–	–	17.76(0.13)	15.42(0.04)	1.66	1.72	y
VVVv258	VVV J162153.24-503407.34	16:21:53.24	-50:34:07.34	333.24186	-0.51312317	–	–	–	17.70(0.13)	15.43(0.04)	1.62	1.59	y
VVVv259	VVV J162141.05-502857.12	16:21:41.05	-50:28:57.12	333.27994	-0.42934841	–	–	–	–	16.91(0.14)	1.81	2.12	y
VVVv260	VVV J162105.71-501916.41	16:21:05.71	-50:19:16.41	333.32734	-0.24883880	14.41(0.01)	13.52(0.01)	13.20(0.01)	13.02(0.01)	12.47(0.01)	1.22	1.01	y
VVVv261	VVV J162136.83-502407.96	16:21:36.83	-50:24:07.96	333.32877	-0.36459238	–	–	–	17.38(0.09)	14.27(0.01)	1.03	2.19	y
VVVv262	VVV J162159.58-502620.59	16:21:59.58	-50:26:20.59	333.34544	-0.43335162	19.02(0.05)	18.23(0.04)	17.30(0.03)	16.32(0.04)	15.67(0.05)	1.03	–	y
VVVv263	VVV J162144.17-502041.41	16:21:44.17	-50:20:41.41	333.38312	-0.33778751	–	–	–	16.81(0.06)	13.24(0.01)	1.06	1.21	y
VVVv264	VVV J162120.67-501547.33	16:21:20.67	-50:15:47.33	333.39653	-0.23577408	–	–	–	–	15.07(0.03)	2.18	1.31	y
VVVv265	VVV J162047.39-500359.42	16:20:47.39	-50:03:59.42	333.47223	-0.033719289	–	–	17.09(0.03)	14.72(0.01)	13.05(0.01)	1.13	-0.02	y
VVVv266	VVV J162052.46-500415.80	16:20:52.46	-50:04:15.80	333.47864	-0.046498906	–	20.13(0.25)	18.13(0.07)	16.15(0.03)	15.08(0.03)	1.04	-0.88	y
VVVv267	VVV J162217.53-501402.98	16:22:17.53	-50:14:02.98	333.52419	-0.32239608	–	–	–	–	14.77(0.02)	1.94	2.41	y
VVVv268	VVV J162255.11-495757.37	16:22:55.11	-49:57:57.37	333.78515	-0.20437521	–	–	–	17.99(0.17)	15.38(0.04)	1.29	-0.11	y
VVVv269	VVV J162330.97-495006.51	16:23:30.97	-49:50:06.51	333.94581	-0.18067598	–	–	–	16.89(0.06)	12.92(0.01)	1.61	-0.10	y
VVVv270	VVV J162327.14-494443.96	16:23:27.14	-49:44:43.96	334.00225	-0.11032589	–	–	–	18.34(0.23)	16.14(0.07)	2.22	1.76	y
VVVv271	VVV J162733.92-495537.61	16:27:33.92	-49:55:37.61	334.33558	-0.71174047	–	–	18.25(0.08)	16.58(0.05)	15.47(0.04)	1.06	–	n
VVVv272	VVV J162841.05-495311.78	16:28:41.05	-49:53:11.78	334.48953	-0.81369506	18.97(0.05)	18.14(0.04)	16.85(0.02)	15.78(0.02)	15.08(0.03)	1.22	-1.36	y
VVVv273	VVV J163010.37-495319.51	16:30:10.37	-49:53:19.51	334.65324	-0.98892539	17.95(0.02)	17.07(0.02)	15.63(0.01)	14.35(0.01)	13.37(0.01)	1.00	-0.65	y
VVVv274	VVV J162618.97-491433.07	16:26:18.97	-49:14:33.07	334.68700	-0.090312355	–	–	–	17.05(0.08)	13.38(0.01)	1.07	0.99	y
VVVv275	VVV J162951.29-493754.93	16:29:51.29	-49:37:54.93	334.80437	-0.77500564	20.31(0.16)	18.71(0.07)	17.26(0.03)	16.14(0.03)	15.47(0.04)	1.00	–	n
VVVv276	VVV J162917.42-492231.45	16:29:17.42	-49:22:31.45	334.92721	-0.53187194	–	–	–	17.97(0.17)	13.81(0.01)	1.22	0.88	n
VVVv277	VVV J162708.30-490019.80	16:27:08.30	-49:00:19.80	334.95085	-0.022074093	–	–	–	–	15.95(0.06)	1.49	1.78	y
VVVv278	VVV J162856.75-491343.89	16:28:56.75	-49:13:43.89	334.99454	-0.39010356	–	19.73(0.17)	17.67(0.05)	16.02(0.03)	15.06(0.03)	1.00	-2.08	y
VVVv279	VVV J162939.57-492006.48	16:29:39.57	-49:20:06.48	334.99782	-0.54768464	–	–	–	17.97(0.17)	15.40(0.04)	1.92	1.00	y
VVVv280	VVV J162952.41-491102.80	16:29:52.41	-49:11:02.80	335.13140	-0.46904123	–	–	19.11(0.18)	16.24(0.04)	14.42(0.02)	2.30	0.93	y
VVVv281	VVV J162749.92-485144.00	16:27:49.92	-48:51:44.00	335.13307	-0.0046919650	–	–	17.08(0.03)	15.61(0.02)	14.52(0.02)	1.14	-0.23	y
VVVv282	VVV J162953.95-490948.69	16:29:53.95	-49:09:48.69	335.14921	-0.45790797	–	–	19.92(0.38)	17.14(0.08)	15.67(0.05)	1.39	-0.16	y
VVVv283	VVV J162904.28-485908.99	16:29:04.28	-48:59:08.99	335.18456	-0.23721644	–	–	–	–	13.37(0.01)	1.28	-0.09	y
VVVv284	VVV J162820.68-484917.24	16:28:20.68	-48:49:17.24	335.22089	-0.037321979	–	–	–	15.07(0.01)	12.09(0.01)	1.45	0.76	y
VVVv285	VVV J162959.38-484955.29	16:29:59.38	-48:49:55.29	335.40001	-0.24061851	–	20.24(0.27)	18.15(0.08)	15.26(0.01)	12.75(0.01)	1.19	0.41	y
VVVv286	VVV J163051.43-484356.65	16:30:51.43	-48:43:56.65	335.57057	-0.27604937	18.21(0.04)	17.23(0.03)	17.29(0.04)	15.60(0.03)	14.15(0.02)	1.07	0.64	y
VVVv287	VVV J163317.78-490138.74	16:33:17.78	-49:01:38.74	335.62893	-0.77045996	–	–	17.51(0.05)	16.07(0.04)	15.04(0.03)	1.19	-1.22	y
VVVv288	VVV J163058.02-482220.40	16:30:58.02	-48:22:20.40	335.84512	-0.042370239	–	19.02(0.14)	17.18(0.04)	16.00(0.04)	15.20(0.04)	1.14	–	y
VVVv289	VVV J163232.83-483609.97	16:32:32.83	-48:36:09.97	335.85597	-0.39098511	–	–	17.82(0.07)	15.51(0.02)	14.23(0.02)	1.15	-0.87	y
VVVv290	VVV J163231.47-480227.03	16:32:31.47	-48:02:27.03	336.26444	-0.0050757550	–	–	–	15.39(0.02)	12.56(0.01)	1.03	1.10	y
VVVv291	VVV J163441.08-482000.21	16:34:41.08	-48:20:00.21	336.29434	-0.46801598	–	18.49(0.08)	16.28(0.02)	13.56(0.01)	12.04(0.01)	1.18	-0.99	n
VVVv292	VVV J163252.77-475717.93	16:32:52.77	-47:57:17.93	336.36776	0.0099675930	–	–	16.62(0.02)	14.66(0.01)	13.23(0.01)	1.64	-1.68	y
VVVv293	VVV J163455.76-481324.47	16:34:55.76	-48:13:24.47	336.40284	-0.42363713	18.78(0.06)	18.31(0.07)	17.54(0.06)	16.80(0.08)	16.33(0.11)	1.54	–	n

Continued on next page

Table A.1 – *Continued from previous page*

Object ID	VVV Designation	α (J2000)	δ (J2000)	l	b	Z (mag)	Y (mag)	J (mag)	H (mag)	K_s (mag)	ΔK_s^a (mag)	α_{class}	SFR
VVVv294	VVV J163257.43-475355.83	16:32:57.43	-47:53:55.83	336.41772	0.038676047	–	–	–	17.13(0.11)	15.22(0.04)	1.16	0.49	y
VVVv295	VVV J163657.31-482731.22	16:36:57.31	-48:27:31.22	336.45585	-0.83087722	–	–	16.45(0.02)	13.15(0.01)	11.67(0.01)	1.56	0.48	n
VVVv296	VVV J163559.12-475138.62	16:35:59.12	-47:51:38.62	336.78964	-0.30905988	–	–	17.80(0.08)	16.18(0.04)	15.25(0.04)	1.09	–	y
VVVv297	VVV J163510.88-473943.17	16:35:10.88	-47:39:43.17	336.84518	-0.075251015	17.74(0.03)	17.20(0.03)	16.97(0.03)	16.49(0.06)	16.06(0.09)	1.12	–	y
VVVv298	VVV J163506.52-473750.51	16:35:06.52	-47:37:50.51	336.85998	-0.045081815	19.92(0.18)	18.40(0.08)	17.07(0.04)	16.17(0.04)	15.43(0.05)	1.03	–	y
VVVv299	VVV J163549.32-474139.27	16:35:49.32	-47:41:39.27	336.89416	-0.17660370	–	19.65(0.25)	17.36(0.05)	16.07(0.04)	15.29(0.05)	1.06	–	y
VVVv300	VVV J163520.86-473509.87	16:35:20.86	-47:35:09.87	336.92010	-0.044645009	–	–	–	16.79(0.08)	12.72(0.01)	1.35	0.27	y
VVVv301	VVV J163815.13-474825.10	16:38:15.13	-47:48:25.10	337.08476	-0.55507088	–	–	16.50(0.02)	13.82(0.01)	11.90(0.01)	1.56	0.77	y
VVVv302	VVV J163716.53-473816.00	16:37:16.53	-47:38:16.00	337.10049	-0.31978619	–	–	18.75(0.18)	16.58(0.07)	15.37(0.05)	1.61	1.07	y
VVVv303	VVV J163909.57-473235.02	16:39:09.57	-47:32:35.02	337.38326	-0.49276708	–	–	–	15.59(0.03)	12.47(0.01)	1.40	-0.07	y
VVVv304	VVV J164056.68-474302.70	16:40:56.68	-47:43:02.70	337.45259	-0.83342448	–	18.90(0.10)	17.32(0.05)	14.86(0.01)	13.06(0.01)	1.09	0.37	y
VVVv305	VVV J163942.31-473033.43	16:39:42.31	-47:30:33.43	337.46978	-0.53904527	–	–	–	15.97(0.04)	13.57(0.01)	1.36	0.87	y
VVVv306	VVV J164057.54-471531.45	16:40:57.54	-47:15:31.45	337.79806	-0.53166457	–	–	–	17.51(0.17)	15.52(0.06)	1.03	0.42	y
VVVv307	VVV J164113.16-471747.09	16:41:13.16	-47:17:47.09	337.79902	-0.58970005	–	–	–	16.28(0.05)	16.26(0.11)	1.13	0.06	y
VVVv308	VVV J164220.97-471911.31	16:42:20.97	-47:19:11.31	337.90787	-0.74909084	–	–	16.95(0.03)	14.45(0.01)	12.36(0.01)	1.38	0.76	n
VVVv309	VVV J164058.19-470631.93	16:40:58.19	-47:06:31.93	337.91164	-0.43386987	–	–	–	17.32(0.14)	13.53(0.01)	1.89	1.63	y
VVVv310	VVV J164118.44-470744.80	16:41:18.44	-47:07:44.80	337.93443	-0.49031564	–	–	–	–	15.55(0.06)	1.34	1.49	y
VVVv311	VVV J164222.77-463204.23	16:42:22.77	-46:32:04.23	338.50224	-0.23580574	–	–	18.84(0.18)	16.87(0.08)	15.53(0.05)	1.03	-0.51	y
VVVv312	VVV J164336.63-463555.56	16:43:36.63	-46:35:55.56	338.59283	-0.43753677	–	–	–	16.26(0.05)	11.86(0.01)	1.99	0.50	y
VVVv313	VVV J164322.08-463031.47	16:43:22.08	-46:30:31.47	338.63345	-0.34702073	–	–	–	–	16.44(0.11)	1.16	2.55	y
VVVv314	VVV J164436.13-462642.81	16:44:36.13	-46:26:42.81	338.82057	-0.46604135	19.29(0.08)	19.03(0.11)	16.14(0.02)	14.11(0.01)	12.39(0.01)	1.29	0.03	y
VVVv315	VVV J164319.07-460818.16	16:43:19.07	-46:08:18.16	338.90723	-0.097443893	–	–	16.91(0.03)	14.88(0.01)	13.66(0.01)	1.35	-1.57	y
VVVv316	VVV J164517.96-462415.96	16:45:17.96	-46:24:15.96	338.92986	-0.53047297	–	–	19.38(0.29)	16.64(0.07)	14.73(0.02)	2.25	0.62	y
VVVv317	VVV J164447.36-461634.12	16:44:47.36	-46:16:34.12	338.96971	-0.38009088	–	–	–	15.91(0.03)	13.27(0.01)	1.77	0.81	y
VVVv318	VVV J164542.89-461737.70	16:45:42.89	-46:17:37.70	339.06053	-0.51288223	–	–	–	14.66(0.01)	12.10(0.01)	1.12	-0.16	y
VVVv319	VVV J164517.04-460555.44	16:45:17.04	-46:05:55.44	339.16005	-0.32928830	–	–	17.35(0.05)	14.75(0.01)	12.58(0.01)	1.58	0.01	y
VVVv320	VVV J164541.05-460645.91	16:45:41.05	-46:06:45.91	339.19456	-0.39104787	20.04(0.16)	19.33(0.14)	18.33(0.11)	16.88(0.08)	15.84(0.06)	1.02	0.31	y
VVVv321	VVV J164703.25-461214.67	16:47:03.25	-46:12:14.67	339.27907	-0.63079588	18.01(0.03)	17.58(0.03)	17.67(0.06)	16.09(0.04)	14.56(0.02)	1.30	0.61	y
VVVv322	VVV J164624.57-455921.04	16:46:24.57	-45:59:21.04	339.37029	-0.40641436	–	–	18.48(0.13)	16.82(0.08)	15.25(0.04)	2.63	0.91	y
VVVv323	VVV J164925.09-461955.83	16:49:25.09	-46:19:55.83	339.44450	-1.0257324	–	–	–	16.19(0.04)	14.22(0.01)	1.28	0.94	y
VVVv324	VVV J164711.61-455737.06	16:47:11.61	-45:57:37.06	339.48056	-0.49144099	–	–	17.83(0.07)	15.98(0.03)	14.51(0.02)	1.47	0.70	y
VVVv325	VVV J164916.71-461417.94	16:49:16.71	-46:14:17.94	339.50098	-0.94696818	15.95(0.01)	15.38(0.01)	13.46(0.01)	12.62(0.01)	11.91(0.01)	1.02	0.28	y
VVVv326	VVV J164528.77-453801.97	16:45:28.77	-45:38:01.97	339.53491	-0.052289054	–	–	–	17.89(0.20)	13.35(0.01)	2.01	1.04	y
VVVv327	VVV J164746.43-455444.92	16:47:46.43	-45:54:44.92	339.58225	-0.53749618	–	–	17.29(0.04)	15.42(0.02)	13.94(0.01)	1.02	-0.94	y
VVVv328	VVV J164737.86-453948.08	16:47:37.86	-45:39:48.08	339.75637	-0.35759386	–	–	18.32(0.11)	15.59(0.03)	14.27(0.02)	1.08	-2.04	y
VVVv329	VVV J164623.58-452459.68	16:46:23.58	-45:24:59.68	339.80405	-0.032609821	–	–	–	13.38(0.01)	10.66(0.01)	2.04	0.41	n
VVVv330	VVV J164925.34-454635.09	16:49:25.34	-45:46:35.09	339.87121	-0.66959415	–	–	–	16.35(0.05)	12.57(0.01)	1.96	1.33	n
VVVv331	VVV J164654.11-451521.92	16:46:54.11	-45:15:21.92	339.98421	0.0033821620	–	–	19.84(0.30)	16.52(0.06)	15.74(0.07)	1.60	0.59	y
VVVv332	VVV J165142.03-455238.00	16:51:42.03	-45:52:38.00	340.04734	-1.0392745	–	–	–	16.85(0.08)	15.35(0.05)	1.16	0.61	y
VVVv333	VVV J164815.42-452141.77	16:48:15.42	-45:21:41.77	340.05765	-0.24662861	–	–	–	–	15.99(0.09)	1.05	6.22	y
VVVv334	VVV J164809.91-451905.07	16:48:09.91	-45:19:05.07	340.08052	-0.20623518	–	–	–	15.21(0.02)	12.16(0.01)	1.31	0.42	y
VVVv335	VVV J165209.73-455249.55	16:52:09.73	-45:52:49.55	340.09595	-1.1033241	17.20(0.01)	16.11(0.01)	14.61(0.01)	12.55(0.01)	11.82(0.01)	2.10	0.52	y
VVVv336	VVV J165106.53-454324.24	16:51:06.53	-45:43:24.24	340.10021	-0.86179164	–	–	–	–	15.47(0.06)	2.15	0.77	y
VVVv337	VVV J165207.12-454634.45	16:52:07.12	-45:46:34.45	340.17162	-1.0312752	–	–	18.55(0.09)	14.78(0.01)	13.43(0.01)	1.43	-0.23	y
VVVv338	VVV J164900.46-451559.95	16:49:00.46	-45:15:59.95	340.21527	-0.28649758	–	19.42(0.20)	17.99(0.06)	12.88(0.01)	10.53(0.01)	1.14	-0.27	y
VVVv339	VVV J164856.73-451230.02	16:48:56.73	-45:12:30.02	340.25289	-0.24062303	–	–	–	16.88(0.08)	15.07(0.04)	1.06	0.28	y
VVVv340	VVV J164831.39-450636.17	16:48:31.39	-45:06:36.17	340.28023	-0.12039194	18.31(0.03)	17.56(0.04)	17.33(0.03)	15.72(0.03)	12.86(0.01)	1.21	0.02	y
VVVv341	VVV J164936.97-451216.30	16:49:36.97	-45:12:16.30	340.33168	-0.32872716	–	–	–	15.76(0.03)	12.31(0.01)	1.21	-0.85	y
VVVv342	VVV J165400.57-452249.43	16:54:00.57	-45:22:49.43	340.68757	-1.0367356	20.10(0.17)	18.46(0.09)	17.58(0.04)	15.68(0.03)	14.98(0.04)	1.23	-0.87	y

Continued on next page

Table A.1 – *Continued from previous page*

Object ID	VVV Designation	α (J2000)	δ (J2000)	l	b	Z (mag)	Y (mag)	J (mag)	H (mag)	K_s (mag)	ΔK_s^a (mag)	α_{class}	SFR
VVVv343	VVV J165207.50-450636.51	16:52:07.50	-45:06:36.51	340.68672	-0.60889147	17.01(0.01)	15.91(0.01)	15.60(0.01)	14.42(0.01)	14.43(0.02)	1.10	-2.44	n
VVVv344	VVV J165408.46-451939.80	16:54:08.46	-45:19:39.80	340.74304	-1.0214433	20.70(0.30)	18.73(0.11)	17.96(0.06)	15.93(0.03)	15.48(0.06)	1.15	-0.22	y
VVVv345	VVV J165128.98-445511.43	16:51:28.98	-44:55:11.43	340.76133	-0.40026165	–	–	–	17.12(0.10)	12.97(0.01)	3.12	1.65	n
VVVv346	VVV J165412.34-451756.95	16:54:12.34	-45:17:56.95	340.77239	-1.0122568	–	19.58(0.24)	18.05(0.06)	15.73(0.03)	14.95(0.04)	1.22	–	y
VVVv347	VVV J164957.30-443856.10	16:49:57.30	-44:38:56.10	340.79657	-0.018595354	–	–	–	–	12.36(0.01)	1.02	-1.04	y
VVVv348	VVV J165357.35-451050.19	16:53:57.35	-45:10:50.19	340.83662	-0.90333968	–	–	–	14.76(0.01)	11.60(0.01)	1.43	0.41	y
VVVv349	VVV J165453.41-451345.52	16:54:53.41	-45:13:45.52	340.90250	-1.0618364	19.43(0.09)	17.57(0.04)	16.20(0.01)	–	13.38(0.01)	1.02	-0.16	y
VVVv350	VVV J165030.84-442939.22	16:50:30.84	-44:29:39.22	340.97914	0.0039031360	–	19.03(0.14)	15.96(0.01)	12.93(0.01)	12.10(0.01)	1.01	-1.12	y
VVVv351	VVV J165149.25-444006.46	16:51:49.25	-44:40:06.46	340.99336	-0.28645836	–	–	–	14.25(0.01)	11.72(0.01)	1.02	-0.32	y
VVVv352	VVV J165153.69-443850.98	16:51:53.69	-44:38:50.98	341.01790	-0.28327294	–	–	–	16.94(0.08)	15.66(0.07)	1.33	-0.38	y
VVVv353	VVV J165209.03-444046.25	16:52:09.03	-44:40:46.25	341.02208	-0.33871290	–	–	–	14.41(0.01)	11.35(0.01)	1.12	-0.47	y
VVVv354	VVV J165049.33-442228.30	16:50:49.33	-44:22:28.30	341.10638	0.038051470	18.16(0.03)	17.42(0.03)	16.97(0.02)	15.62(0.03)	14.77(0.03)	2.02	–	y
VVVv355	VVV J165113.82-442732.78	16:51:13.82	-44:27:32.78	341.08776	-0.072021694	–	–	–	13.91(0.01)	11.44(0.01)	1.10	0.12	y
VVVv356	VVV J165240.98-443802.07	16:52:40.98	-44:38:02.07	341.11746	-0.38294811	–	–	–	16.13(0.04)	12.00(0.01)	2.34	1.00	y
VVVv357	VVV J165238.49-443632.52	16:52:38.49	-44:36:32.52	341.13199	-0.36144466	–	18.44(0.08)	17.19(0.03)	15.16(0.02)	14.79(0.03)	1.13	-0.47	y
VVVv358	VVV J165433.46-445023.87	16:54:33.46	-44:50:23.87	341.16816	-0.77117153	–	–	–	14.04(0.01)	11.84(0.01)	1.05	-0.25	n
VVVv359	VVV J165329.81-443421.75	16:53:29.81	-44:34:21.75	341.25655	-0.45630935	–	19.22(0.17)	17.54(0.04)	15.09(0.02)	14.33(0.02)	1.21	1.07	y
VVVv360	VVV J165643.64-445641.92	16:56:43.64	-44:56:41.92	341.32737	-1.1363227	–	–	–	–	16.81(0.20)	3.71	2.68	n
VVVv361	VVV J165454.74-443841.67	16:54:54.74	-44:38:41.67	341.35939	-0.69735343	–	–	–	15.48(0.02)	12.65(0.01)	1.06	0.24	n
VVVv362	VVV J165304.23-442234.26	16:53:04.23	-44:22:34.26	341.36060	-0.27304865	–	–	–	17.46(0.13)	15.33(0.05)	1.41	1.35	y
VVVv363	VVV J165300.74-441028.62	16:53:00.74	-44:10:28.62	341.50999	-0.13732998	–	–	18.32(0.09)	15.47(0.02)	12.17(0.01)	1.67	0.37	n
VVVv364	VVV J165432.55-440446.80	16:54:32.55	-44:04:46.80	341.75703	-0.29021808	–	–	18.40(0.10)	14.12(0.01)	12.12(0.01)	1.28	-0.50	y
VVVv365	VVV J165521.41-440217.92	16:55:21.41	-44:02:17.92	341.88120	-0.37796256	17.33(0.01)	16.61(0.01)	15.83(0.01)	15.08(0.01)	14.65(0.02)	1.08	–	n
VVVv366	VVV J165644.69-433017.90	16:56:44.69	-43:30:17.90	342.45393	-0.23927021	–	–	18.10(0.07)	15.84(0.03)	14.59(0.02)	1.17	0.03	y
VVVv367	VVV J170029.61-435300.34	17:00:29.61	-43:53:00.34	342.57740	-1.0055029	–	–	–	17.32(0.11)	13.69(0.01)	1.02	1.50	y
VVVv368	VVV J165755.54-432803.82	16:57:55.54	-43:28:03.82	342.61656	-0.38353278	–	–	–	17.72(0.16)	16.09(0.08)	1.15	–	n
VVVv369	VVV J165641.41-431129.86	16:56:41.41	-43:11:29.86	342.69237	-0.035726376	–	18.66(0.08)	17.41(0.04)	16.33(0.04)	15.79(0.06)	1.03	–	n
VVVv370	VVV J165748.65-430442.53	16:57:48.65	-43:04:42.53	342.90831	-0.12501581	–	–	–	14.57(0.01)	12.01(0.01)	1.14	0.25	y
VVVv371	VVV J165950.04-431721.62	16:59:50.04	-43:17:21.62	342.97146	-0.54511876	–	19.26(0.11)	17.75(0.04)	15.79(0.02)	14.60(0.01)	1.12	-0.19	y
VVVv372	VVV J165834.31-425647.04	16:58:34.31	-42:56:47.04	343.09823	-0.15193584	–	–	–	14.73(0.01)	11.99(0.01)	1.14	-0.52	y
VVVv373	VVV J170242.77-432514.46	17:02:42.77	-43:25:14.46	343.18920	-1.0387808	–	–	–	14.23(0.01)	11.66(0.01)	1.26	0.29	n
VVVv374	VVV J165833.99-424955.25	16:58:33.99	-42:49:55.25	343.18734	-0.080208728	–	–	17.12(0.02)	13.99(0.01)	11.98(0.01)	1.99	0.91	y
VVVv375	VVV J165916.71-425325.43	16:59:16.71	-42:53:25.43	343.22235	-0.21877425	–	–	17.47(0.03)	13.64(0.01)	12.01(0.01)	1.05	-0.61	y
VVVv376	VVV J165844.44-424736.58	16:58:44.44	-42:47:36.58	343.23737	-0.081374877	–	–	17.28(0.03)	14.67(0.01)	12.83(0.01)	1.36	0.34	y
VVVv377	VVV J170123.56-430945.16	17:01:23.56	-43:09:45.16	343.24620	-0.69077939	–	–	20.17(0.34)	16.56(0.03)	14.40(0.01)	1.85	0.13	y
VVVv378	VVV J165846.18-424637.73	16:58:46.18	-42:46:37.73	343.25349	-0.075407111	–	–	–	15.94(0.02)	12.32(0.01)	1.50	0.82	y
VVVv379	VVV J170043.40-430219.08	17:00:43.40	-43:02:19.08	343.26885	-0.51825518	–	–	–	–	17.09(0.14)	1.79	1.05	y
VVVv380	VVV J170128.15-430612.43	17:01:28.15	-43:06:12.43	343.30142	-0.66552796	14.12(0.01)	14.11(0.01)	12.84(0.01)	12.79(0.01)	12.46(0.01)	1.04	-2.83	n
VVVv381	VVV J170056.90-425637.41	17:00:56.90	-42:56:37.41	343.36899	-0.49230700	–	–	–	16.67(0.04)	13.71(0.01)	1.14	0.87	y
VVVv382	VVV J170206.05-425926.64	17:02:06.05	-42:59:26.64	343.46124	-0.68763059	19.48(0.08)	19.13(0.10)	18.62(0.09)	17.83(0.11)	14.32(0.01)	2.96	1.64	n
VVVv383	VVV J170340.88-431135.78	17:03:40.88	-43:11:35.78	343.47692	-1.0398060	–	19.97(0.21)	16.54(0.01)	12.98(0.01)	11.24(0.01)	1.73	0.67	n
VVVv384	VVV J170024.90-423701.24	17:00:24.90	-42:37:01.24	343.56623	-0.21407368	–	–	19.28(0.16)	14.46(0.01)	11.96(0.01)	1.25	0.48	y
VVVv385	VVV J165952.37-422429.44	16:59:52.37	-42:24:29.44	343.66897	-0.0066053640	17.24(0.01)	16.78(0.01)	16.25(0.01)	15.70(0.02)	15.50(0.03)	1.29	–	n
VVVv386	VVV J170105.37-423008.44	17:01:05.37	-42:30:08.44	343.73305	-0.24140458	–	–	19.55(0.19)	17.41(0.07)	16.45(0.08)	1.06	–	y
VVVv387	VVV J170300.08-423144.81	17:03:00.08	-42:31:44.81	343.92764	-0.53629706	20.31(0.18)	19.18(0.10)	17.55(0.03)	16.39(0.03)	15.74(0.04)	1.02	–	y
VVVv388	VVV J170302.23-422515.48	17:03:02.23	-42:25:15.48	344.01736	-0.47554505	–	–	–	–	16.10(0.06)	1.46	0.84	y
VVVv389	VVV J170317.18-422549.88	17:03:17.18	-42:25:49.88	344.03782	-0.51779740	–	–	–	16.69(0.04)	13.51(0.01)	1.16	0.71	y
VVVv390	VVV J170203.10-420332.27	17:02:03.10	-42:03:32.27	344.19236	-0.10990473	–	–	19.49(0.19)	17.46(0.08)	15.82(0.05)	1.06	-0.58	y
VVVv391	VVV J170430.33-422215.38	17:04:30.33	-42:22:15.38	344.22202	-0.66024713	–	–	–	–	15.88(0.05)	1.22	0.39	y

Continued on next page

Table A.1 – *Continued from previous page*

Object ID	VVV Designation	α (J2000)	δ (J2000)	l	b	Z (mag)	Y (mag)	J (mag)	H (mag)	K_s (mag)	ΔK_s^a (mag)	α_{class}	SFR
VVVv392	VVV J170310.35-415131.99	17:03:10.35	-41:51:31.99	344.47807	-0.15255587	–	–	–	16.19(0.04)	12.31(0.01)	1.39	-0.20	y
VVVv393	VVV J170436.13-415410.75	17:04:36.13	-41:54:10.75	344.60491	-0.39060544	–	–	18.08(0.07)	16.71(0.06)	15.74(0.05)	1.05	0.10	n
VVVv394	VVV J170507.70-414631.38	17:05:07.70	-41:46:31.38	344.76581	-0.39125105	–	–	–	15.65(0.02)	13.89(0.01)	1.02	0.24	n
VVVv395	VVV J170724.60-415541.50	17:07:24.60	-41:55:41.50	344.89996	-0.82238594	–	–	18.92(0.15)	17.27(0.11)	16.35(0.09)	2.66	–	n
VVVv396	VVV J170347.02-412326.48	17:03:47.02	-41:23:26.48	344.91895	0.042059666	–	–	–	14.23(0.01)	12.23(0.01)	1.05	-0.15	y
VVVv397	VVV J170501.10-413310.92	17:05:01.10	-41:33:10.92	344.93032	-0.24026520	–	–	–	–	13.98(0.01)	1.17	0.33	y
VVVv398	VVV J170818.57-414440.23	17:08:18.57	-41:44:40.23	345.14743	-0.84650572	–	–	18.91(0.15)	16.52(0.05)	15.12(0.03)	1.11	-0.11	y
VVVv399	VVV J170523.37-411925.23	17:05:23.37	-41:19:25.23	345.15502	-0.15684685	–	–	18.42(0.10)	16.98(0.08)	15.64(0.05)	1.24	0.10	y
VVVv400	VVV J170805.25-414002.24	17:08:05.25	-41:40:02.24	345.18452	-0.76711262	–	–	19.27(0.21)	17.03(0.08)	15.53(0.04)	1.01	-0.43	y
VVVv401	VVV J170528.32-411709.21	17:05:28.32	-41:17:09.21	345.19448	-0.14634119	–	–	–	17.39(0.12)	12.09(0.01)	1.20	0.35	y
VVVv402	VVV J170533.12-411547.18	17:05:33.12	-41:15:47.18	345.22171	-0.14452445	–	–	–	–	15.07(0.03)	1.19	1.34	y
VVVv403	VVV J170645.11-412444.47	17:06:45.11	-41:24:44.47	345.23847	-0.41419832	–	–	18.76(0.13)	16.84(0.07)	15.39(0.04)	1.12	-0.49	n
VVVv404	VVV J170936.20-414740.73	17:09:36.20	-41:47:40.73	345.25111	-1.0700320	–	–	–	16.23(0.04)	13.00(0.01)	1.49	1.15	y
VVVv405	VVV J170938.62-413851.81	17:09:38.62	-41:38:51.81	345.37370	-0.98867736	–	–	–	17.50(0.13)	13.50(0.01)	2.00	1.77	y
VVVv406	VVV J170957.47-413548.87	17:09:57.47	-41:35:48.87	345.44947	-1.0056544	–	18.89(0.12)	17.51(0.04)	14.61(0.01)	12.57(0.01)	1.64	1.10	y
VVVv407	VVV J171014.46-413159.13	17:10:14.46	-41:31:59.13	345.53228	-1.0103636	–	–	18.73(0.13)	17.24(0.11)	16.32(0.10)	1.07	0.60	y
VVVv408	VVV J170719.60-405954.28	17:07:19.60	-40:59:54.28	345.63430	-0.25183392	–	19.75(0.25)	18.82(0.14)	16.90(0.08)	15.27(0.04)	1.23	0.13	y
VVVv409	VVV J170633.12-405257.01	17:06:33.12	-40:52:57.01	345.63897	-0.065257290	19.08(0.07)	18.26(0.06)	17.05(0.03)	15.95(0.03)	15.30(0.04)	1.25	-1.19	y
VVVv410	VVV J170951.32-410424.87	17:09:51.32	-41:04:24.87	345.85893	-0.67912138	–	–	–	17.42(0.20)	13.37(0.01)	1.84	1.17	n
VVVv411	VVV J170714.78-403616.02	17:07:14.78	-40:36:16.02	345.94021	-0.0031228510	–	–	–	17.43(0.20)	15.95(0.09)	1.08	1.27	y
VVVv412	VVV J170719.21-403041.54	17:07:19.21	-40:30:41.54	346.02292	0.041462683	–	–	–	14.86(0.02)	12.15(0.01)	1.26	0.20	y
VVVv413	VVV J171244.60-405917.67	17:12:44.60	-40:59:17.67	346.24984	-1.0679064	–	–	–	15.76(0.04)	11.66(0.01)	1.57	0.99	n
VVVv414	VVV J170826.92-402011.77	17:08:26.92	-40:20:11.77	346.29166	-0.025705629	–	–	–	15.64(0.04)	12.14(0.01)	1.36	0.58	n
VVVv415	VVV J170913.65-401051.69	17:09:13.65	-40:10:51.69	346.50518	-0.052048596	19.34(0.09)	18.22(0.07)	16.90(0.04)	15.06(0.02)	11.55(0.01)	1.76	0.72	n
VVVv416	VVV J170954.59-395612.24	17:09:54.59	-39:56:12.24	346.77920	-0.011535080	19.12(0.07)	18.20(0.07)	17.17(0.06)	14.73(0.02)	11.69(0.01)	1.79	0.27	n
VVVv417	VVV J171002.75-395634.95	17:10:02.75	-39:56:34.95	346.78961	-0.036240317	–	–	–	16.04(0.06)	14.38(0.02)	1.28	-0.23	n
VVVv418	VVV J170950.73-395404.21	17:09:50.73	-39:54:04.21	346.80045	0.019534873	–	–	–	14.71(0.02)	11.64(0.01)	1.07	-0.34	n
VVVv419	VVV J171322.75-394816.82	17:13:22.75	-39:48:16.82	347.27891	-0.47067455	16.34(0.01)	15.86(0.01)	15.25(0.01)	14.68(0.02)	14.42(0.03)	1.07	-2.08	n
VVVv420	VVV J171234.47-393812.04	17:12:34.47	-39:38:12.04	347.32392	-0.24675972	–	19.20(0.21)	17.73(0.12)	16.48(0.10)	15.65(0.09)	1.04	–	n
VVVv421	VVV J171416.64-385217.39	17:14:16.64	-38:52:17.39	348.13698	-0.064824443	–	17.63(0.05)	14.03(0.01)	12.47(0.01)	11.49(0.01)	1.19	0.36	n
VVVv422	VVV J171910.90-390227.06	17:19:10.90	-39:02:27.06	348.55130	-0.94006412	–	–	–	–	15.42(0.07)	1.84	2.05	y
VVVv423	VVV J171803.97-385228.88	17:18:03.97	-38:52:28.88	348.56253	-0.66712391	–	–	–	17.23(0.19)	15.09(0.05)	1.34	-0.79	y
VVVv424	VVV J171929.84-390253.81	17:19:29.84	-39:02:53.81	348.58037	-0.99454361	–	–	17.53(0.11)	15.63(0.05)	14.66(0.03)	1.00	-0.54	y
VVVv425	VVV J171717.53-382435.22	17:17:17.53	-38:24:35.22	348.85491	-0.27532453	–	–	–	14.52(0.01)	11.58(0.01)	1.36	0.18	y
VVVv426	VVV J171901.66-381856.10	17:19:01.66	-38:18:56.10	349.12795	-0.49911265	–	18.90(0.10)	16.98(0.04)	15.58(0.04)	14.68(0.03)	1.09	0.28	y
VVVv427	VVV J171751.37-375720.53	17:17:51.37	-37:57:20.53	349.28963	-0.10357362	–	–	16.82(0.03)	13.67(0.01)	12.20(0.01)	1.01	-0.50	y
VVVv428	VVV J172200.73-382816.84	17:22:00.73	-38:28:16.84	349.33401	-1.0681146	–	18.71(0.08)	17.30(0.05)	15.42(0.03)	14.63(0.03)	1.14	-1.65	n
VVVv429	VVV J171737.48-375148.58	17:17:37.48	-37:51:48.58	349.33859	-0.013090265	–	–	–	14.71(0.02)	11.99(0.01)	1.66	0.33	y
VVVv430	VVV J172258.00-381855.60	17:22:58.00	-38:18:55.60	349.56849	-1.1338853	–	–	–	15.33(0.03)	12.29(0.01)	1.55	0.45	y
VVVv431	VVV J172237.25-380642.48	17:22:37.25	-38:06:42.48	349.69794	-0.96260621	19.01(0.05)	17.96(0.04)	17.59(0.07)	15.50(0.03)	13.95(0.02)	1.30	-1.24	y
VVVv432	VVV J171827.35-373153.62	17:18:27.35	-37:31:53.62	349.70459	0.043934653	–	–	17.99(0.10)	15.12(0.02)	11.85(0.01)	2.31	0.88	y
VVVv433	VVV J172230.65-373952.40	17:22:30.65	-37:39:52.40	350.05420	-0.69130736	–	–	–	15.49(0.03)	12.48(0.01)	1.47	0.05	y
VVVv434	VVV J172412.71-375231.53	17:24:12.71	-37:52:31.53	350.07010	-1.0878196	19.70(0.09)	18.91(0.10)	16.96(0.04)	15.64(0.04)	14.78(0.03)	1.20	–	y
VVVv435	VVV J114449.44-612030.53	11:44:49.44	-61:20:30.53	295.03186	0.50401669	–	–	19.31(0.23)	17.01(0.06)	15.27(0.02)	1.59	0.13	y
VVVv436	VVV J114920.18-612533.85	11:49:20.18	-61:25:33.85	295.57625	0.55563046	20.07(0.13)	18.87(0.08)	17.62(0.05)	15.29(0.01)	13.54(0.01)	2.15	0.10	y
VVVv437	VVV J120800.72-612716.02	12:08:00.72	-61:27:16.02	297.76730	0.98109758	18.82(0.06)	18.10(0.05)	17.07(0.02)	16.27(0.02)	15.82(0.03)	1.01	–	n
VVVv438	VVV J121458.74-623509.84	12:14:58.74	-62:35:09.84	298.74931	-0.010753240	–	–	–	17.52(0.07)	15.26(0.02)	1.05	0.16	y
VVVv439	VVV J121555.97-623408.87	12:15:55.97	-62:34:08.87	298.85571	0.021302909	–	–	–	17.74(0.08)	15.97(0.03)	1.02	0.26	y
VVVv440	VVV J121710.81-622317.02	12:17:10.81	-62:23:17.02	298.97406	0.22015931	18.52(0.04)	17.68(0.03)	16.76(0.02)	16.00(0.02)	15.56(0.02)	1.14	–	y

Continued on next page

Table A.1 – *Continued from previous page*

Object ID	VVV Designation	α (J2000)	δ (J2000)	l	b	Z (mag)	Y (mag)	J (mag)	H (mag)	K_s (mag)	ΔK_s^a (mag)	α_{class}	SFR
VVVv441	VVV J122130.75-621939.83	12:21:30.75	-62:19:39.83	299.46516	0.34243604	19.72(0.11)	17.82(0.04)	16.08(0.01)	14.63(0.01)	13.73(0.01)	1.08	-1.75	n
VVVv442	VVV J122346.20-621804.25	12:23:46.20	-62:18:04.25	299.72280	0.39806718	20.09(0.15)	18.57(0.07)	16.88(0.02)	15.30(0.01)	14.42(0.01)	1.36	-0.46	n
VVVv443	VVV J122758.25-624255.21	12:27:58.25	-62:42:55.21	300.24623	0.033996536	18.78(0.05)	18.01(0.05)	17.28(0.03)	16.12(0.02)	15.33(0.02)	1.00	-1.79	n
VVVv444	VVV J123511.19-624550.01	12:35:11.19	-62:45:50.01	301.07374	0.049228926	19.92(0.14)	18.70(0.07)	17.32(0.03)	15.93(0.02)	15.18(0.02)	1.13	-0.81	y
VVVv445	VVV J123605.64-614556.40	12:36:05.64	-61:45:56.40	301.11794	1.0520469	–	–	19.01(0.13)	16.42(0.03)	14.20(0.01)	1.13	-0.24	y
VVVv446	VVV J123659.77-622732.15	12:36:59.77	-62:27:32.15	301.26334	0.36604062	18.77(0.05)	18.21(0.05)	17.44(0.03)	16.45(0.03)	16.42(0.05)	1.03	–	n
VVVv447	VVV J123745.17-622536.29	12:37:45.17	-62:25:36.29	301.34896	0.40295289	19.14(0.06)	18.24(0.05)	17.00(0.02)	16.22(0.02)	15.75(0.03)	1.09	–	n
VVVv448	VVV J123746.96-623154.07	12:37:46.96	-62:31:54.07	301.35798	0.29834531	18.95(0.06)	17.96(0.04)	16.98(0.02)	16.02(0.02)	14.05(0.01)	1.48	2.24	n
VVVv449	VVV J124055.13-615710.28	12:40:55.13	-61:57:10.28	301.69559	0.89365993	20.57(0.25)	18.94(0.09)	17.01(0.02)	14.70(0.01)	12.84(0.01)	1.10	0.03	y
VVVv450	VVV J124124.20-614717.91	12:41:24.20	-61:47:17.91	301.74609	1.0603533	–	–	18.65(0.09)	17.04(0.05)	15.77(0.03)	1.11	0.24	y
VVVv451	VVV J124115.97-623337.44	12:41:15.97	-62:33:37.44	301.76038	0.28822820	–	–	–	18.97(0.27)	14.89(0.01)	1.55	1.26	y
VVVv452	VVV J124158.06-621342.90	12:41:58.06	-62:13:42.90	301.82894	0.62290300	–	–	18.10(0.06)	15.68(0.01)	13.78(0.01)	1.38	0.40	y
VVVv453	VVV J124205.43-621621.45	12:42:05.43	-62:16:21.45	301.84484	0.57941375	–	–	18.48(0.08)	16.85(0.04)	15.81(0.03)	1.06	-0.26	y
VVVv454	VVV J124228.93-620929.37	12:42:28.93	-62:09:29.37	301.88639	0.69543037	–	–	–	17.72(0.08)	14.95(0.01)	1.15	1.34	y
VVVv455	VVV J124251.78-621810.74	12:42:51.78	-62:18:10.74	301.93566	0.55219716	–	–	–	15.21(0.01)	11.92(0.01)	1.03	0.22	y
VVVv456	VVV J124303.86-621246.44	12:43:03.86	-62:12:46.44	301.95610	0.64300186	–	–	18.96(0.12)	17.16(0.05)	15.77(0.03)	1.32	-0.05	y
VVVv457	VVV J124316.34-621127.15	12:43:16.34	-62:11:27.15	301.97963	0.66579601	–	18.19(0.05)	14.86(0.01)	12.31(0.01)	11.26(0.01)	1.93	-0.54	y
VVVv458	VVV J124352.55-615134.62	12:43:52.55	-61:51:34.62	302.04027	0.99906036	14.96(0.01)	14.27(0.01)	13.67(0.01)	12.47(0.01)	11.80(0.01)	1.17	-0.02	y
VVVv459	VVV J124349.50-625419.27	12:43:49.50	-62:54:19.27	302.06520	-0.046394093	20.62(0.21)	19.11(0.09)	18.21(0.07)	17.26(0.06)	16.75(0.09)	1.14	–	y
VVVv460	VVV J124452.97-623402.84	12:44:52.97	-62:34:02.84	302.17700	0.29470493	–	19.22(0.10)	17.82(0.05)	16.30(0.02)	15.10(0.02)	1.37	0.03	n
VVVv461	VVV J124841.99-623046.38	12:48:41.99	-62:30:46.38	302.61596	0.35720713	19.97(0.12)	18.81(0.07)	17.54(0.04)	16.38(0.03)	15.79(0.04)	1.34	-1.28	n
VVVv462	VVV J124951.84-620038.13	12:49:51.84	-62:00:38.13	302.74722	0.86061410	20.92(0.27)	19.78(0.17)	18.73(0.11)	17.33(0.07)	16.75(0.09)	2.88	0.02	n
VVVv463	VVV J125455.60-623638.34	12:54:55.60	-62:36:38.34	303.33315	0.25840247	–	20.05(0.22)	18.14(0.06)	16.66(0.03)	15.40(0.03)	1.05	-0.12	n
VVVv464	VVV J125658.47-622019.66	12:56:58.47	-62:20:19.66	303.57447	0.52606759	18.17(0.03)	17.22(0.02)	16.24(0.01)	15.32(0.01)	14.79(0.01)	1.18	-2.23	n
VVVv465	VVV J125710.56-622245.50	12:57:10.56	-62:22:45.50	303.59696	0.48505559	18.47(0.03)	17.85(0.03)	17.05(0.02)	16.22(0.02)	15.80(0.03)	1.02	–	n
VVVv466	VVV J125936.70-622418.69	12:59:36.70	-62:24:18.69	303.87834	0.45155821	–	–	–	–	14.58(0.01)	2.41	-0.13	y
VVVv467	VVV J130113.23-622527.93	13:01:13.23	-62:25:27.93	304.06381	0.42584410	–	–	17.05(0.02)	14.65(0.01)	12.90(0.01)	1.12	-0.12	y
VVVv468	VVV J130237.59-623928.81	13:02:37.59	-62:39:28.81	304.21624	0.18586275	–	–	–	16.46(0.03)	14.29(0.01)	1.07	-0.02	y
VVVv469	VVV J130402.14-621003.89	13:04:02.14	-62:10:03.89	304.40186	0.66806275	–	18.54(0.07)	17.63(0.04)	16.31(0.02)	13.15(0.01)	2.16	1.30	n
VVVv470	VVV J130653.37-622408.51	13:06:53.37	-62:24:08.51	304.72042	0.41573753	13.93(0.01)	13.51(0.01)	13.08(0.01)	12.85(0.01)	12.51(0.01)	1.01	-2.33	n
VVVv471	VVV J130819.74-623121.15	13:08:19.74	-62:31:21.15	304.87894	0.28535747	–	–	–	17.99(0.11)	15.62(0.03)	1.04	0.78	y
VVVv472	VVV J130834.09-621741.78	13:08:34.09	-62:17:41.78	304.92159	0.51063674	–	–	18.47(0.09)	16.56(0.04)	15.66(0.03)	1.02	-0.56	y
VVVv473	VVV J131057.49-623522.34	13:10:57.49	-62:35:22.34	305.17637	0.19713571	–	–	–	–	14.53(0.01)	1.38	1.82	y
VVVv474	VVV J131102.14-623513.07	13:11:02.14	-62:35:13.07	305.18548	0.19902536	–	–	–	18.11(0.15)	16.36(0.06)	1.07	–	y
VVVv475	VVV J131129.71-623426.91	13:11:29.71	-62:34:26.91	305.23920	0.20774003	–	–	–	18.08(0.14)	16.18(0.06)	1.82	–	y
VVVv476	VVV J131204.60-623457.16	13:12:04.60	-62:34:57.16	305.30528	0.19408149	–	–	–	–	15.57(0.03)	1.17	2.10	y
VVVv477	VVV J131309.69-624330.96	13:13:09.69	-62:43:30.96	305.41772	0.041607821	–	–	–	17.88(0.12)	16.52(0.07)	1.02	0.79	y
VVVv478	VVV J131415.24-622300.25	13:14:15.24	-62:23:00.25	305.57265	0.37132549	14.13(0.01)	13.80(0.01)	12.20(0.01)	12.66(0.01)	12.05(0.01)	1.04	-2.60	n
VVVv479	VVV J131546.03-624155.02	13:15:46.03	-62:41:55.02	305.71754	0.041494275	–	19.76(0.20)	18.65(0.11)	17.41(0.08)	16.65(0.08)	1.07	–	y
VVVv480	VVV J131650.32-622341.61	13:16:50.32	-62:23:41.61	305.86975	0.33190202	16.94(0.01)	16.46(0.01)	15.81(0.01)	15.08(0.01)	14.58(0.01)	1.52	-0.28	y
VVVv481	VVV J131723.85-623904.20	13:17:23.85	-62:39:04.20	305.90837	0.070485202	18.85(0.05)	18.40(0.06)	18.08(0.06)	16.93(0.05)	16.11(0.05)	1.03	0.39	y
VVVv482	VVV J131832.04-624000.36	13:18:32.04	-62:40:00.36	306.03658	0.041554503	–	–	19.19(0.18)	17.45(0.08)	15.95(0.04)	1.09	0.68	y
VVVv483	VVV J131954.87-623001.95	13:19:54.87	-62:30:01.95	306.21246	0.18970934	18.42(0.03)	17.63(0.03)	16.21(0.01)	15.06(0.01)	14.40(0.01)	1.28	-0.39	y
VVVv484	VVV J132049.78-623750.56	13:20:49.78	-62:37:50.56	306.30262	0.048547667	15.78(0.01)	15.14(0.01)	14.37(0.01)	13.66(0.01)	12.84(0.01)	1.05	1.56	n
VVVv485	VVV J132015.07-615257.98	13:20:15.07	-61:52:57.98	306.32004	0.79930679	–	19.16(0.12)	17.33(0.03)	15.92(0.02)	15.08(0.02)	1.00	-1.83	n
VVVv486	VVV J132223.72-622522.25	13:22:23.72	-62:25:22.25	306.50625	0.23388757	20.13(0.16)	18.57(0.07)	16.66(0.02)	14.44(0.01)	12.68(0.01)	1.15	0.43	y
VVVv487	VVV J132325.88-622610.52	13:23:25.88	-62:26:10.52	306.62359	0.20597409	–	–	–	–	17.27(0.15)	1.18	1.45	n
VVVv488	VVV J132631.34-621727.54	13:26:31.34	-62:17:27.54	306.99787	0.30349384	–	–	–	18.31(0.20)	16.07(0.05)	1.05	0.73	n
VVVv489	VVV J132654.40-620318.49	13:26:54.40	-62:03:18.49	307.07449	0.53101420	–	–	18.50(0.10)	15.84(0.02)	14.06(0.01)	1.29	0.67	y

Continued on next page

Table A.1 – *Continued from previous page*

Object ID	VVV Designation	α (J2000)	δ (J2000)	l	b	Z (mag)	Y (mag)	J (mag)	H (mag)	K_s (mag)	ΔK_s^a (mag)	α_{class}	SFR
VVVv490	VVV J133104.45-622318.47	13:31:04.45	-62:23:18.47	307.50652	0.13073785	16.26(0.01)	15.82(0.01)	15.65(0.01)	14.84(0.01)	13.72(0.01)	1.09	1.55	n
VVVv491	VVV J133031.03-615116.55	13:30:31.03	-61:51:16.55	307.52336	0.66829764	17.70(0.02)	17.00(0.02)	16.44(0.02)	15.76(0.02)	15.39(0.03)	1.04	-2.17	n
VVVv492	VVV J133044.67-614803.84	13:30:44.67	-61:48:03.84	307.55799	0.71714423	20.30(0.19)	19.21(0.13)	17.91(0.06)	16.44(0.04)	15.61(0.03)	1.09	-1.90	n
VVVv493	VVV J133425.10-612855.50	13:34:25.10	-61:28:55.50	308.03945	0.96273059	19.27(0.06)	18.20(0.04)	17.10(0.03)	16.10(0.02)	15.57(0.03)	1.10	-1.62	n
VVVv494	VVV J134038.29-614700.31	13:40:38.29	-61:47:00.31	308.71294	0.53487041	–	–	–	19.59(0.58)	14.92(0.02)	1.21	2.98	y
VVVv495	VVV J134030.34-613514.32	13:40:30.34	-61:35:14.32	308.73464	0.73040787	–	–	–	18.52(0.21)	15.99(0.04)	1.15	2.09	y
VVVv496	VVV J134148.93-620635.35	13:41:48.93	-62:06:35.35	308.78618	0.18797801	–	–	–	17.15(0.06)	15.28(0.02)	1.44	0.20	y
VVVv497	VVV J134202.43-613911.50	13:42:02.43	-61:39:11.50	308.90099	0.63073018	19.05(0.05)	18.34(0.05)	17.63(0.04)	16.50(0.03)	15.66(0.03)	1.11	–	y
VVVv498	VVV J134449.97-621446.41	13:44:49.97	-62:14:46.41	309.10389	-0.016005816	–	–	–	14.42(0.01)	11.30(0.01)	1.78	0.61	y
VVVv499	VVV J134500.58-620616.25	13:45:00.58	-62:06:16.25	309.15326	0.11842305	–	–	–	18.45(0.20)	16.19(0.05)	1.39	0.58	y
VVVv500	VVV J134346.56-611919.69	13:43:46.56	-61:19:19.69	309.16963	0.91416546	–	–	–	17.66(0.10)	15.07(0.02)	1.02	0.62	n
VVVv501	VVV J134540.86-620350.24	13:45:40.86	-62:03:50.24	309.23854	0.14180158	–	–	–	18.05(0.14)	16.40(0.06)	1.32	-0.15	y
VVVv502	VVV J134536.57-614435.04	13:45:36.57	-61:44:35.04	309.29723	0.45738952	19.24(0.06)	18.31(0.05)	17.26(0.03)	16.44(0.03)	16.01(0.04)	1.07	–	n
VVVv503	VVV J134816.19-615819.55	13:48:16.19	-61:58:19.55	309.55482	0.16668749	–	–	18.97(0.11)	17.21(0.05)	16.23(0.05)	1.34	–	y
VVVv504	VVV J135017.97-614106.77	13:50:17.97	-61:41:06.77	309.85215	0.39314772	–	–	20.07(0.30)	16.31(0.02)	14.05(0.01)	1.12	0.56	y
VVVv505	VVV J135241.63-613622.63	13:52:41.63	-61:36:22.63	310.14697	0.40440258	–	20.10(0.20)	17.74(0.04)	16.32(0.02)	15.22(0.02)	1.51	-1.34	y
VVVv506	VVV J135317.06-611021.46	13:53:17.06	-61:10:21.46	310.31808	0.80909648	20.08(0.11)	18.79(0.06)	17.71(0.04)	16.28(0.02)	15.12(0.02)	1.04	-0.66	n
VVVv507	VVV J135543.10-615844.13	13:55:43.10	-61:58:44.13	310.40415	-0.043302335	20.04(0.10)	17.59(0.02)	15.39(0.01)	13.20(0.01)	11.70(0.01)	1.86	0.09	n
VVVv508	VVV J135631.54-613714.61	13:56:31.54	-61:37:14.61	310.58535	0.28007875	–	–	19.53(0.18)	17.90(0.10)	16.47(0.06)	1.00	1.05	n
VVVv509	VVV J135541.73-605333.65	13:55:41.73	-60:53:33.65	310.66909	1.0101454	12.69(0.01)	12.60(0.01)	13.90(0.01)	13.10(0.01)	12.91(0.01)	1.02	-1.48	n
VVVv510	VVV J135741.61-611127.48	13:57:41.61	-61:11:27.48	310.82869	0.66086606	–	19.24(0.09)	17.87(0.06)	16.39(0.03)	15.37(0.03)	1.33	-0.82	y
VVVv511	VVV J135826.40-611522.53	13:58:26.40	-61:15:22.53	310.89890	0.57481604	17.48(0.01)	17.17(0.02)	16.33(0.02)	15.86(0.02)	15.61(0.03)	1.08	–	n
VVVv512	VVV J135943.90-614155.63	13:59:43.90	-61:41:55.63	310.93326	0.10745893	–	–	–	15.27(0.01)	11.79(0.01)	1.93	0.71	n
VVVv513	VVV J135935.48-612208.31	13:59:35.48	-61:22:08.31	311.00322	0.43019644	19.07(0.04)	18.23(0.04)	17.00(0.03)	15.84(0.02)	15.10(0.02)	1.17	-0.85	y
VVVv514	VVV J140045.37-613339.95	14:00:45.37	-61:33:39.95	311.08692	0.20825953	–	–	17.40(0.04)	14.80(0.01)	13.26(0.01)	1.73	-1.46	y
VVVv515	VVV J135923.70-605422.36	13:59:23.70	-60:54:22.36	311.10087	0.88316246	–	–	–	17.84(0.11)	15.74(0.04)	1.18	0.86	y
VVVv516	VVV J140017.60-611719.20	14:00:17.60	-61:17:19.20	311.10552	0.48563222	–	–	–	14.16(0.01)	10.80(0.01)	1.86	0.81	y
VVVv517	VVV J140211.33-610039.77	14:02:11.33	-61:00:39.77	311.40000	0.69214690	19.49(0.06)	18.71(0.06)	17.76(0.05)	16.54(0.03)	15.48(0.03)	1.12	-0.48	y
VVVv518	VVV J140513.13-613222.17	14:05:13.13	-61:32:22.17	311.60408	0.083753365	–	–	–	17.29(0.06)	12.92(0.01)	1.33	0.94	y
VVVv519	VVV J140537.97-610446.32	14:05:37.97	-61:04:46.32	311.78161	0.51096641	19.63(0.07)	17.31(0.02)	15.21(0.01)	13.58(0.01)	12.63(0.01)	1.34	-1.08	n
VVVv520	VVV J140737.39-613408.44	14:07:37.39	-61:34:08.44	311.86998	-0.026420231	–	–	–	14.07(0.01)	11.15(0.01)	1.31	0.16	y
VVVv521	VVV J140811.24-611646.87	14:08:11.24	-61:16:46.87	312.01884	0.23068054	19.63(0.07)	18.79(0.06)	17.58(0.05)	16.48(0.03)	16.05(0.05)	1.05	–	y
VVVv522	VVV J141041.45-611941.89	14:10:41.45	-61:19:41.89	312.29134	0.094980690	–	–	18.59(0.09)	16.22(0.03)	14.75(0.01)	1.00	-0.30	y
VVVv523	VVV J140956.15-610140.83	14:09:56.15	-61:01:40.83	312.29472	0.40874069	–	–	–	17.71(0.10)	15.86(0.04)	1.16	–	y
VVVv524	VVV J141300.81-610550.91	14:13:00.81	-61:05:50.91	312.62817	0.22920274	–	–	18.05(0.06)	15.21(0.01)	13.22(0.01)	1.57	0.27	y
VVVv525	VVV J141245.69-603242.92	14:12:45.69	-60:32:42.92	312.77000	0.76378206	19.22(0.06)	18.30(0.04)	17.33(0.03)	16.28(0.03)	15.90(0.04)	1.18	–	n
VVVv526	VVV J141535.32-605907.91	14:15:35.32	-60:59:07.91	312.95929	0.23731838	–	–	–	18.17(0.15)	15.79(0.04)	1.17	0.73	y
VVVv527	VVV J141503.90-604740.38	14:15:03.90	-60:47:40.38	312.95974	0.43863932	–	–	–	14.67(0.01)	12.12(0.01)	1.54	0.66	n
VVVv528	VVV J141900.72-610554.36	14:19:00.72	-61:05:54.36	313.31429	-0.0043768590	–	–	–	16.42(0.03)	12.22(0.01)	2.41	0.90	n
VVVv529	VVV J142040.61-604133.22	14:20:40.61	-60:41:33.22	313.64094	0.31027283	–	–	–	–	11.77(0.01)	1.70	1.76	n
VVVv530	VVV J141902.00-600125.01	14:19:02.00	-60:01:25.01	313.67352	1.0086418	–	–	19.10(0.15)	14.17(0.01)	10.89(0.01)	1.63	0.79	n
VVVv531	VVV J142212.30-604442.26	14:22:12.30	-60:44:42.26	313.79874	0.19725995	–	19.65(0.16)	18.33(0.08)	16.25(0.03)	14.74(0.01)	1.09	-0.35	y
VVVv532	VVV J142134.09-603135.20	14:21:34.09	-60:31:35.20	313.80021	0.42939964	20.73(0.22)	19.60(0.15)	18.40(0.08)	16.96(0.05)	16.52(0.07)	1.05	–	y
VVVv533	VVV J142226.67-604542.45	14:22:26.67	-60:45:42.45	313.82047	0.17150298	–	–	–	–	12.96(0.01)	1.19	0.06	y
VVVv534	VVV J142245.57-605018.07	14:22:45.57	-60:50:18.07	313.83014	0.086391321	–	–	–	17.70(0.11)	14.79(0.02)	1.23	1.39	y
VVVv535	VVV J142440.39-603412.20	14:24:40.39	-60:34:12.20	314.14310	0.25620353	–	–	–	17.55(0.09)	15.28(0.02)	1.08	-0.18	y
VVVv536	VVV J142524.24-602352.49	14:25:24.24	-60:23:52.49	314.28816	0.38541097	–	–	18.04(0.06)	16.28(0.03)	15.27(0.02)	1.02	0.02	y
VVVv537	VVV J142713.67-595918.35	14:27:13.67	-59:59:18.35	314.64640	0.68660539	–	19.78(0.18)	17.87(0.05)	16.61(0.04)	15.87(0.04)	1.08	–	n
VVVv538	VVV J142815.52-595700.73	14:28:15.52	-59:57:00.73	314.78046	0.67539516	19.79(0.10)	19.18(0.10)	17.30(0.03)	16.08(0.02)	15.31(0.02)	1.00	-1.19	n

Continued on next page

Table A.1 – *Continued from previous page*

Object ID	VVV Designation	α (J2000)	δ (J2000)	l	b	Z (mag)	Y (mag)	J (mag)	H (mag)	K_s (mag)	ΔK_s^a (mag)	α_{class}	SFR
VVVv539	VVV J143013.42-602755.92	14:30:13.42	-60:27:55.92	314.81753	0.10639642	–	–	–	–	16.20(0.05)	1.80	1.29	y
VVVv540	VVV J142743.97-593258.83	14:27:43.97	-59:32:58.83	314.86459	1.0725511	19.25(0.06)	18.92(0.08)	18.17(0.07)	16.88(0.05)	15.88(0.04)	1.23	–	y
VVVv541	VVV J142831.88-594338.38	14:28:31.88	-59:43:38.38	314.89380	0.87034293	19.43(0.07)	18.60(0.06)	17.06(0.02)	15.36(0.01)	13.87(0.01)	1.40	0.15	y
VVVv542	VVV J143142.37-602810.18	14:31:42.37	-60:28:10.18	314.98545	0.034313195	–	–	19.07(0.15)	17.35(0.08)	16.18(0.05)	1.01	0.12	y
VVVv543	VVV J143142.52-602751.76	14:31:42.52	-60:27:51.76	314.98767	0.038932218	19.91(0.10)	18.75(0.07)	17.58(0.04)	16.31(0.03)	15.66(0.03)	1.11	-1.14	y
VVVv544	VVV J143506.67-594150.43	14:35:06.67	-59:41:50.43	315.67339	0.58493363	–	18.92(0.09)	17.47(0.03)	16.14(0.02)	15.44(0.03)	1.04	-1.58	n
VVVv545	VVV J143742.20-595110.66	14:37:42.20	-59:51:10.66	315.91205	0.31349590	–	–	–	15.26(0.01)	11.74(0.01)	1.78	1.02	n
VVVv546	VVV J143752.06-595303.52	14:37:52.06	-59:53:03.52	315.91849	0.27652056	19.05(0.08)	17.57(0.03)	15.93(0.01)	14.25(0.01)	13.01(0.01)	1.53	-1.09	n
VVVv547	VVV J143633.66-590426.59	14:36:33.66	-59:04:26.59	316.08736	1.0861654	18.72(0.06)	17.78(0.03)	16.77(0.02)	15.90(0.02)	15.47(0.03)	1.11	-1.52	n
VVVv548	VVV J143915.54-593353.29	14:39:15.54	-59:33:53.29	316.20727	0.49888597	–	19.08(0.11)	17.39(0.03)	16.30(0.03)	15.64(0.03)	1.16	-1.46	n
VVVv549	VVV J144040.89-594625.51	14:40:40.89	-59:46:25.51	316.28658	0.23503723	–	–	–	–	16.22(0.05)	2.04	2.39	n
VVVv550	VVV J144054.93-593906.08	14:40:54.93	-59:39:06.08	316.36340	0.33437637	18.69(0.06)	17.39(0.02)	16.06(0.01)	14.94(0.01)	14.32(0.01)	1.08	-2.45	n
VVVv551	VVV J144153.75-595401.48	14:41:53.75	-59:54:01.48	316.37370	0.056927459	–	–	–	16.70(0.04)	14.34(0.01)	1.68	0.67	y
VVVv552	VVV J144023.74-590454.89	14:40:23.74	-59:04:54.89	316.53560	0.88152975	–	–	–	16.54(0.04)	12.46(0.01)	1.48	1.24	n
VVVv553	VVV J144318.26-595246.19	14:43:18.26	-59:52:46.19	316.54309	0.0026597510	–	–	–	17.65(0.10)	15.54(0.03)	1.28	0.43	y
VVVv554	VVV J144315.42-584340.86	14:43:15.42	-58:43:40.86	317.01816	1.0516020	–	–	–	–	16.80(0.11)	1.49	–	y
VVVv555	VVV J144553.20-592208.58	14:45:53.20	-59:22:08.58	317.05440	0.32777461	18.24(0.03)	16.79(0.01)	15.52(0.01)	14.13(0.01)	13.26(0.01)	1.45	0.95	y
VVVv556	VVV J144617.31-592406.72	14:46:17.31	-59:24:06.72	317.08665	0.27625992	–	–	–	17.41(0.10)	15.84(0.04)	1.06	1.36	y
VVVv557	VVV J144648.87-592926.55	14:46:48.87	-59:29:26.55	317.10897	0.16734940	–	–	–	17.09(0.07)	15.25(0.03)	1.15	0.49	y
VVVv558	VVV J144656.53-592936.63	14:46:56.53	-59:29:36.63	317.12240	0.15786190	–	–	–	18.70(0.32)	16.86(0.11)	1.14	0.30	y
VVVv559	VVV J144903.47-592411.99	14:49:03.47	-59:24:11.99	317.40378	0.12261156	–	–	–	–	14.97(0.02)	1.73	1.57	y
VVVv560	VVV J145047.08-592039.71	14:50:47.08	-59:20:39.71	317.62724	0.078816855	–	–	–	17.34(0.09)	14.95(0.02)	1.20	0.45	y
VVVv561	VVV J145322.68-592024.94	14:53:22.68	-59:20:24.94	317.92475	-0.065326779	–	–	–	15.33(0.02)	11.73(0.01)	1.54	0.56	y
VVVv562	VVV J145333.59-591021.73	14:53:33.59	-59:10:21.73	318.02120	0.073651110	–	–	16.68(0.02)	14.20(0.01)	12.46(0.01)	1.93	-0.01	y
VVVv563	VVV J145344.28-590933.73	14:53:44.28	-59:09:33.73	318.04759	0.075212168	–	–	–	17.51(0.11)	15.40(0.03)	1.09	-0.04	y
VVVv564	VVV J145047.04-581441.58	14:50:47.04	-58:14:41.58	318.11405	1.0646673	17.77(0.02)	17.28(0.02)	16.49(0.02)	15.50(0.02)	15.01(0.02)	1.04	–	n
VVVv565	VVV J145313.19-584603.42	14:53:13.19	-58:46:03.42	318.16502	0.45487058	–	–	18.91(0.14)	16.62(0.05)	15.34(0.03)	1.69	0.42	n
VVVv566	VVV J145202.35-580908.23	14:52:02.35	-58:09:08.23	318.30337	1.0740118	–	–	–	17.82(0.15)	14.81(0.02)	1.02	1.81	y
VVVv567	VVV J145513.69-584957.65	14:55:13.69	-58:49:57.65	318.36715	0.27874630	–	–	–	18.76(0.35)	15.81(0.05)	1.01	0.32	n
VVVv568	VVV J145518.57-582232.03	14:55:18.57	-58:22:32.03	318.58586	0.68028976	18.79(0.05)	17.77(0.03)	16.76(0.02)	15.85(0.02)	15.28(0.03)	1.20	–	y
VVVv569	VVV J145617.26-581944.66	14:56:17.26	-58:19:44.66	318.72119	0.66261086	–	–	–	15.44(0.02)	13.15(0.01)	1.21	0.29	y
VVVv570	VVV J145847.00-575924.03	14:58:47.00	-57:59:24.03	319.17035	0.80953676	–	–	–	–	16.33(0.07)	1.18	1.50	y
VVVv571	VVV J145810.12-574249.73	14:58:10.12	-57:42:49.73	319.22752	1.0918495	19.17(0.06)	18.54(0.06)	17.62(0.05)	16.47(0.04)	15.87(0.05)	1.01	–	n
VVVv572	VVV J145912.95-575224.81	14:59:12.95	-57:52:24.81	319.27580	0.88530680	–	–	–	18.52(0.29)	13.74(0.01)	1.47	0.98	y
VVVv573	VVV J150235.15-580550.76	15:02:35.15	-58:05:50.76	319.56183	0.47568088	–	19.49(0.16)	18.08(0.08)	16.92(0.06)	16.29(0.07)	1.04	–	n
VVVv574	VVV J150443.18-580654.81	15:04:43.18	-58:06:54.81	319.79961	0.32330840	15.81(0.01)	15.11(0.01)	15.02(0.01)	14.24(0.01)	13.76(0.01)	1.11	-1.60	n
VVVv575	VVV J150522.47-574002.48	15:05:22.47	-57:40:02.48	320.09491	0.67109969	19.40(0.09)	18.30(0.05)	16.95(0.03)	15.54(0.02)	14.72(0.02)	1.24	-0.44	y
VVVv576	VVV J150446.21-573111.93	15:04:46.21	-57:31:11.93	320.09657	0.83923684	17.57(0.02)	16.65(0.01)	15.68(0.01)	14.83(0.01)	14.37(0.01)	1.04	-2.14	y
VVVv577	VVV J150523.60-573105.93	15:05:23.60	-57:31:05.93	320.17031	0.79969078	–	–	–	17.92(0.16)	16.13(0.07)	1.96	–	y
VVVv578	VVV J150813.34-575523.33	15:08:13.34	-57:55:23.33	320.29770	0.26087960	–	–	18.39(0.10)	16.76(0.05)	15.95(0.05)	1.03	–	y
VVVv579	VVV J150813.36-573053.59	15:08:13.36	-57:30:53.59	320.50196	0.61437168	16.03(0.01)	14.44(0.01)	12.82(0.01)	12.22(0.01)	11.60(0.01)	1.21	-0.89	n
VVVv580	VVV J150935.66-573522.61	15:09:35.66	-57:35:22.61	320.62350	0.45731793	–	–	18.51(0.11)	15.75(0.02)	13.70(0.01)	3.53	0.75	y
VVVv581	VVV J151047.12-574616.64	15:10:47.12	-57:46:16.64	320.66875	0.22003922	–	–	17.89(0.07)	15.91(0.02)	14.43(0.01)	1.15	-0.31	y
VVVv582	VVV J151113.18-574843.98	15:11:13.18	-57:48:43.98	320.69772	0.15534864	19.74(0.12)	18.45(0.07)	17.00(0.03)	15.85(0.02)	15.24(0.03)	1.14	–	y
VVVv583	VVV J151051.98-574337.14	15:10:51.98	-57:43:37.14	320.70057	0.25269945	–	–	–	16.96(0.06)	15.24(0.03)	1.06	0.50	y
VVVv584	VVV J150936.37-571712.15	15:09:36.37	-57:17:12.15	320.77775	0.71801952	–	19.42(0.16)	16.89(0.03)	14.56(0.01)	12.79(0.01)	1.86	0.61	y
VVVv585	VVV J151136.89-565833.71	15:11:36.89	-56:58:33.71	321.17033	0.84723046	18.33(0.03)	17.52(0.02)	16.58(0.02)	15.75(0.02)	15.26(0.03)	1.06	–	n
VVVv586	VVV J151319.74-565132.86	15:13:19.74	-56:51:32.86	321.43110	0.82733508	–	–	–	18.01(0.17)	14.98(0.02)	2.08	1.78	y
VVVv587	VVV J151430.53-564509.59	15:14:30.53	-56:45:09.59	321.62440	0.83466418	–	–	18.72(0.12)	16.97(0.06)	15.77(0.04)	1.23	-0.80	n

Continued on next page

Table A.1 – *Continued from previous page*

Object ID	VVV Designation	α (J2000)	δ (J2000)	l	b	Z (mag)	Y (mag)	J (mag)	H (mag)	K_s (mag)	ΔK_s^a (mag)	α_{class}	SFR
VVVv588	VVV J151728.78-572026.38	15:17:28.78	-57:20:26.38	321.65964	0.12213421	–	–	–	–	14.03(0.01)	2.84	1.71	y
VVVv589	VVV J151802.91-571449.28	15:18:02.91	-57:14:49.28	321.77446	0.16075340	20.54(0.25)	18.63(0.07)	16.84(0.02)	15.52(0.02)	14.84(0.02)	1.01	-1.71	n
VVVv590	VVV J151817.23-571140.67	15:18:17.23	-57:11:40.67	321.82968	0.18795120	18.94(0.06)	18.12(0.04)	17.31(0.04)	16.12(0.03)	15.31(0.03)	1.07	-0.40	n
VVVv591	VVV J152050.24-563327.63	15:20:50.24	-56:33:27.63	322.46519	0.53895047	18.69(0.05)	18.11(0.04)	17.40(0.04)	16.71(0.05)	16.35(0.07)	1.08	–	n
VVVv592	VVV J152032.05-562731.91	15:20:32.05	-56:27:31.91	322.48330	0.64470282	–	–	–	–	16.24(0.07)	1.45	1.06	y
VVVv593	VVV J152034.71-562800.83	15:20:34.71	-56:28:00.83	322.48413	0.63463177	–	–	17.44(0.04)	16.51(0.04)	15.69(0.04)	1.31	-0.14	y
VVVv594	VVV J152235.73-565108.49	15:22:35.73	-56:51:08.49	322.50796	0.16049063	19.10(0.07)	17.23(0.02)	15.77(0.01)	13.60(0.01)	12.14(0.01)	1.03	-0.02	y
VVVv595	VVV J152015.17-560443.04	15:20:15.17	-56:04:43.04	322.65521	0.98611449	18.79(0.05)	17.91(0.03)	16.00(0.01)	13.20(0.01)	11.64(0.01)	1.50	0.64	n
VVVv596	VVV J152203.45-560904.17	15:22:03.45	-56:09:04.17	322.82754	0.78902942	–	–	–	17.32(0.08)	14.85(0.02)	1.34	0.49	y
VVVv597	VVV J152535.77-562026.67	15:25:35.77	-56:20:26.67	323.13425	0.36066323	–	–	19.84(0.33)	18.03(0.16)	17.05(0.14)	1.25	–	n
VVVv598	VVV J152332.89-553918.20	15:23:32.89	-55:39:18.20	323.27351	1.0905615	–	–	18.75(0.13)	17.02(0.07)	16.31(0.07)	1.04	–	n
VVVv599	VVV J152842.74-563040.60	15:28:42.74	-56:30:40.60	323.39604	-0.021641572	19.04(0.06)	18.18(0.04)	17.10(0.03)	16.16(0.03)	15.74(0.04)	1.03	–	y
VVVv600	VVV J152949.95-562243.27	15:29:49.95	-56:22:43.27	323.59868	0.00015428900	–	18.89(0.08)	16.92(0.02)	14.72(0.01)	13.09(0.01)	1.00	0.78	y
VVVv601	VVV J153113.73-560956.68	15:31:13.73	-56:09:56.68	323.87925	0.064860691	17.67(0.02)	16.49(0.01)	15.47(0.01)	14.43(0.01)	13.94(0.01)	1.09	-2.91	y
VVVv602	VVV J153035.84-555119.45	15:30:35.84	-55:51:19.45	323.98383	0.37008867	–	–	18.86(0.13)	16.30(0.04)	15.04(0.02)	1.11	-0.85	y
VVVv603	VVV J152919.69-552605.15	15:29:19.69	-55:26:05.15	324.07524	0.81801346	–	–	–	13.27(0.01)	11.54(0.01)	1.47	-0.01	n
VVVv604	VVV J153128.64-554206.72	15:31:28.64	-55:42:06.72	324.17308	0.42550626	–	–	19.83(0.32)	17.23(0.09)	15.33(0.03)	1.48	0.44	y
VVVv605	VVV J153126.10-554107.36	15:31:26.10	-55:41:07.36	324.17761	0.44244744	–	–	–	16.71(0.05)	14.93(0.02)	1.09	-0.04	y
VVVv606	VVV J153331.64-560322.81	15:33:31.64	-56:03:22.81	324.20432	-0.029807471	15.66(0.01)	14.13(0.01)	12.63(0.01)	12.22(0.01)	11.51(0.01)	1.45	-2.39	n
VVVv607	VVV J153300.09-553308.87	15:33:00.09	-55:33:08.87	324.43498	0.42422129	–	–	19.08(0.16)	16.94(0.07)	15.56(0.04)	1.04	-0.36	n
VVVv608	VVV J153358.87-553908.22	15:33:58.87	-55:39:08.22	324.49017	0.26277663	–	–	–	18.48(0.27)	16.57(0.09)	1.01	0.94	n
VVVv609	VVV J153341.12-551826.98	15:33:41.12	-55:18:26.98	324.65570	0.56812124	17.90(0.02)	16.59(0.01)	15.28(0.01)	14.22(0.01)	13.60(0.01)	1.14	-2.20	n
VVVv610	VVV J153445.56-552709.77	15:34:45.56	-55:27:09.77	324.69566	0.36132901	–	20.20(0.27)	17.34(0.03)	15.12(0.01)	13.56(0.01)	1.38	-0.54	y
VVVv611	VVV J153728.01-552400.62	15:37:28.01	-55:24:00.62	325.03772	0.17887791	–	–	20.03(0.39)	17.14(0.08)	15.10(0.02)	1.53	0.45	y
VVVv612	VVV J153547.48-550202.45	15:35:47.48	-55:02:02.45	325.05941	0.61557206	–	–	18.16(0.07)	16.05(0.03)	14.87(0.02)	1.05	-1.19	n
VVVv613	VVV J153517.84-543929.11	15:35:17.84	-54:39:29.11	325.22134	0.96221442	19.95(0.14)	18.76(0.08)	16.90(0.02)	14.88(0.01)	13.36(0.01)	1.67	0.02	n
VVVv614	VVV J153510.45-543257.45	15:35:10.45	-54:32:57.45	325.27035	1.0609729	17.57(0.02)	17.11(0.02)	16.36(0.01)	15.56(0.02)	15.17(0.03)	1.05	–	n
VVVv615	VVV J153856.83-550740.23	15:38:56.83	-55:07:40.23	325.36889	0.27353697	–	–	18.87(0.12)	16.90(0.05)	15.59(0.04)	1.15	0.46	y
VVVv616	VVV J154024.96-545754.32	15:40:24.96	-54:57:54.32	325.63482	0.27877063	–	–	–	16.62(0.04)	12.63(0.01)	2.04	1.14	n
VVVv617	VVV J154017.25-544511.18	15:40:17.25	-54:45:11.18	325.74680	0.45971181	–	20.75(0.33)	18.65(0.09)	16.51(0.04)	15.32(0.03)	1.21	–	y
VVVv618	VVV J154254.67-550052.84	15:42:54.67	-55:00:52.84	325.89076	0.023760632	20.01(0.10)	18.65(0.05)	15.74(0.01)	13.67(0.01)	12.11(0.01)	1.14	-0.04	y
VVVv619	VVV J154228.33-541935.97	15:42:28.33	-54:19:35.97	326.25638	0.61003782	–	–	–	13.96(0.01)	12.08(0.01)	1.07	-0.68	y
VVVv620	VVV J154157.90-541046.98	15:41:57.90	-54:10:46.98	326.28601	0.77190631	–	–	19.17(0.15)	17.36(0.08)	15.98(0.05)	2.52	–	y
VVVv621	VVV J154312.04-542308.80	15:43:12.04	-54:23:08.80	326.30508	0.49874086	–	–	–	17.12(0.06)	15.49(0.03)	1.38	-0.70	y
VVVv622	VVV J154110.25-535422.49	15:41:10.25	-53:54:22.49	326.35747	1.0604666	–	17.94(0.03)	15.88(0.01)	13.83(0.01)	12.46(0.01)	1.25	-0.28	y
VVVv623	VVV J154225.31-540519.18	15:42:25.31	-54:05:19.18	326.39433	0.80412405	19.92(0.09)	18.94(0.06)	17.47(0.03)	16.10(0.02)	15.29(0.03)	1.04	-1.07	y
VVVv624	VVV J154257.11-540416.99	15:42:57.11	-54:04:16.99	326.46668	0.77086815	–	–	19.11(0.15)	17.20(0.07)	15.77(0.04)	1.29	0.32	y
VVVv625	VVV J154317.95-540647.29	15:43:17.95	-54:06:47.29	326.48189	0.70678679	–	–	–	18.08(0.15)	14.49(0.01)	1.22	0.33	y
VVVv626	VVV J154359.60-541135.69	15:43:59.60	-54:11:35.69	326.51393	0.58140953	18.54(0.03)	18.03(0.03)	17.31(0.03)	15.40(0.01)	11.90(0.01)	1.08	-0.10	y
VVVv627	VVV J154435.13-540903.57	15:44:35.13	-54:09:03.57	326.60840	0.56209811	–	20.36(0.23)	18.07(0.06)	16.24(0.03)	15.00(0.02)	1.33	–	y
VVVv628	VVV J154449.54-540752.08	15:44:49.54	-54:07:52.08	326.64837	0.55635647	–	20.46(0.26)	17.42(0.03)	15.30(0.01)	13.76(0.01)	1.45	-0.51	y
VVVv629	VVV J154505.60-540947.91	15:45:05.60	-54:09:47.91	326.65972	0.50693781	–	20.21(0.21)	18.68(0.10)	16.48(0.04)	15.11(0.02)	1.38	-0.25	y
VVVv630	VVV J154456.13-540703.18	15:44:56.13	-54:07:03.18	326.66942	0.55726717	–	–	–	18.83(0.31)	15.76(0.04)	1.68	2.70	y
VVVv631	VVV J154518.36-541036.87	15:45:18.36	-54:10:36.87	326.67601	0.47713654	20.94(0.24)	19.53(0.11)	17.39(0.03)	15.13(0.01)	13.41(0.01)	1.82	-0.14	y
VVVv632	VVV J154409.80-535627.78	15:44:09.80	-53:56:27.78	326.68727	0.76629975	16.52(0.01)	15.71(0.01)	14.35(0.01)	12.95(0.01)	11.87(0.01)	1.51	0.29	y
VVVv633	VVV J154503.52-540248.79	15:45:03.52	-54:02:48.79	326.72692	0.60213885	–	–	–	18.02(0.15)	15.93(0.05)	1.53	–	y
VVVv634	VVV J154616.79-541206.67	15:46:16.79	-54:12:06.67	326.77318	0.37002715	–	–	–	–	16.88(0.12)	1.34	1.70	y
VVVv635	VVV J155022.57-535906.72	15:50:22.57	-53:59:06.72	327.37855	0.16707794	–	0.00(0.01)	–	16.93(0.05)	12.94(0.01)	1.31	-0.36	y
VVVv636	VVV J155146.28-532557.31	15:51:46.28	-53:25:57.31	327.88638	0.46727321	–	0.00(0.01)	19.47(0.19)	16.15(0.02)	13.57(0.01)	1.31	0.37	y

Continued on next page

Table A.1 – *Continued from previous page*

Object ID	VVV Designation	α (J2000)	δ (J2000)	l	b	Z (mag)	Y (mag)	J (mag)	H (mag)	K_s (mag)	ΔK_s^a (mag)	α_{class}	SFR
VVVv637	VVV J155206.86-532019.10	15:52:06.86	-53:20:19.10	327.98532	0.50792763	–	0.00(0.01)	–	17.89(0.12)	13.68(0.01)	1.84	0.64	y
VVVv638	VVV J155319.21-532538.36	15:53:19.21	-53:25:38.36	328.06843	0.32546250	–	0.00(0.01)	19.32(0.17)	15.33(0.01)	12.81(0.01)	1.02	0.02	y
VVVv639	VVV J155352.73-532223.92	15:53:52.73	-53:22:23.92	328.16705	0.31427970	–	0.00(0.01)	–	17.03(0.05)	11.99(0.01)	1.27	0.55	y
VVVv640	VVV J155303.38-531108.92	15:53:03.38	-53:11:08.92	328.19111	0.53719519	–	0.00(0.01)	–	17.90(0.12)	13.79(0.01)	2.08	0.84	y
VVVv641	VVV J155339.20-530511.82	15:53:39.20	-53:05:11.82	328.32325	0.55704821	15.57(0.01)	16.00(0.01)	16.06(0.01)	15.12(0.01)	14.85(0.03)	1.10	–	y
VVVv642	VVV J155510.51-531104.03	15:55:10.51	-53:11:04.03	328.43675	0.33616676	–	–	–	12.91(0.01)	10.37(0.01)	1.31	0.09	n
VVVv643	VVV J155543.20-531025.97	15:55:43.20	-53:10:25.97	328.50623	0.29203048	–	–	–	17.47(0.12)	16.22(0.11)	1.14	0.64	y
VVVv644	VVV J155508.35-530130.78	15:55:08.35	-53:01:30.78	328.53443	0.46204156	–	–	–	–	14.64(0.03)	1.13	-0.16	y
VVVv645	VVV J155555.56-525446.51	15:55:55.56	-52:54:46.51	328.69733	0.47241817	–	–	–	–	16.96(0.22)	1.43	3.85	y
VVVv646	VVV J155806.68-531630.20	15:58:06.68	-53:16:30.20	328.71482	-0.015923297	–	–	–	17.16(0.09)	15.47(0.06)	1.52	0.26	y
VVVv647	VVV J155412.81-522943.33	15:54:12.81	-52:29:43.33	328.76478	0.95933739	–	–	–	14.62(0.01)	12.01(0.01)	1.65	-0.12	n
VVVv648	VVV J155542.57-524230.82	15:55:42.57	-52:42:30.82	328.80328	0.65020641	–	–	–	–	14.76(0.03)	1.00	2.97	y
VVVv649	VVV J155643.04-524815.52	15:56:43.04	-52:48:15.52	328.85865	0.47887614	–	–	–	18.31(0.26)	14.99(0.04)	2.19	0.65	y
VVVv650	VVV J155734.78-525307.67	15:57:34.78	-52:53:07.67	328.90584	0.33288637	–	–	–	–	13.50(0.01)	1.81	0.79	y
VVVv651	VVV J155647.56-521908.67	15:56:47.56	-52:19:08.67	329.17983	0.84280263	–	–	17.68(0.05)	15.97(0.03)	14.76(0.03)	1.08	-0.78	n
VVVv652	VVV J155929.70-524223.17	15:59:29.70	-52:42:23.17	329.24234	0.28140468	–	–	–	17.88(0.17)	14.44(0.02)	2.84	1.83	n
VVVv653	VVV J155653.63-521254.18	15:56:53.63	-52:12:54.18	329.25868	0.91240690	–	–	–	13.85(0.01)	10.77(0.01)	1.40	-0.38	n
VVVv654	VVV J155730.34-520227.10	15:57:30.34	-52:02:27.10	329.44281	0.98495433	–	–	–	15.26(0.02)	11.50(0.01)	1.35	0.45	n
VVVv655	VVV J155842.66-515029.54	15:58:42.66	-51:50:29.54	329.71348	1.0165768	–	–	–	16.72(0.06)	15.00(0.04)	1.21	-1.23	y
VVVv656	VVV J160352.97-514258.66	16:03:52.97	-51:42:58.66	330.39955	0.58647377	–	19.03(0.12)	17.46(0.04)	16.22(0.03)	15.56(0.04)	1.01	-1.40	y
VVVv657	VVV J160501.51-515346.89	16:05:01.51	-51:53:46.89	330.41201	0.33458293	–	19.28(0.16)	17.93(0.06)	16.66(0.05)	14.72(0.02)	1.08	0.60	y
VVVv658	VVV J160614.37-515406.13	16:06:14.37	-51:54:06.13	330.54800	0.20564008	17.17(0.01)	16.18(0.01)	14.68(0.01)	13.21(0.01)	12.37(0.01)	1.03	-1.67	y
VVVv659	VVV J160436.86-512626.49	16:04:36.86	-51:26:26.49	330.66746	0.71725169	–	–	–	14.36(0.01)	11.88(0.01)	1.65	0.45	n
VVVv660	VVV J160558.60-513250.32	16:05:58.60	-51:32:50.32	330.75457	0.49647084	–	–	–	16.39(0.04)	12.62(0.01)	1.54	0.86	n
VVVv661	VVV J160553.34-504722.43	16:05:53.34	-50:47:22.43	331.25047	1.0696144	–	–	17.74(0.05)	14.74(0.01)	12.40(0.01)	1.06	1.25	y
VVVv662	VVV J161026.82-512234.13	16:10:26.82	-51:22:34.13	331.38447	0.15390492	–	–	–	18.55(0.24)	15.30(0.03)	1.56	0.81	y
VVVv663	VVV J161031.85-510602.50	16:10:31.85	-51:06:02.50	331.58124	0.34710876	–	–	–	15.82(0.02)	12.26(0.01)	1.27	0.30	n
VVVv664	VVV J160930.62-504822.40	16:09:30.62	-50:48:22.40	331.66287	0.67250054	–	–	–	17.12(0.06)	14.78(0.02)	1.44	-0.11	y
VVVv665	VVV J160957.70-504809.42	16:09:57.70	-50:48:09.42	331.71775	0.62685006	–	–	–	16.57(0.04)	14.09(0.01)	1.63	0.95	y
VVVv666	VVV J160917.91-503723.65	16:09:17.91	-50:37:23.65	331.76201	0.82992121	–	–	17.91(0.06)	16.28(0.03)	15.30(0.03)	1.08	-1.42	n
VVVv667	VVV J161200.30-505043.44	16:12:00.30	-50:50:43.44	331.92505	0.37585735	–	–	–	17.71(0.11)	15.84(0.05)	1.12	–	n
VVVv668	VVV J161146.40-500735.22	16:11:46.40	-50:07:35.22	332.38916	0.92619791	18.27(0.03)	17.64(0.03)	16.52(0.02)	15.33(0.01)	14.39(0.01)	1.17	-1.12	y
VVVv669	VVV J161155.45-500827.40	16:11:55.45	-50:08:27.40	332.39693	0.89909425	18.91(0.06)	18.12(0.05)	17.55(0.04)	16.58(0.04)	15.94(0.05)	1.06	–	y
VVVv670	VVV J161543.48-503433.61	16:15:43.48	-50:34:33.61	332.53779	0.16640011	20.08(0.17)	–	17.70(0.05)	15.90(0.02)	14.73(0.02)	1.42	-0.07	y
VVVv671	VVV J161238.40-500318.59	16:12:38.40	-50:03:18.59	332.53936	0.88316054	–	–	–	17.39(0.08)	15.39(0.03)	1.06	0.96	y
VVVv672	VVV J161303.16-500721.93	16:13:03.16	-50:07:21.93	332.54124	0.78857388	19.52(0.10)	18.87(0.10)	17.17(0.03)	16.12(0.03)	15.49(0.04)	1.07	-0.95	y
VVVv673	VVV J161644.12-504321.62	16:16:44.12	-50:43:21.62	332.55147	-0.050370517	–	–	–	14.62(0.01)	11.37(0.01)	1.03	0.12	y
VVVv674	VVV J161333.07-500522.46	16:13:33.07	-50:05:22.46	332.62215	0.75783258	–	–	–	16.30(0.03)	15.24(0.03)	1.08	–	n
VVVv675	VVV J161646.80-503408.73	16:16:46.80	-50:34:08.73	332.66328	0.055151209	15.78(0.01)	15.08(0.01)	14.32(0.01)	13.67(0.01)	13.46(0.01)	1.09	-0.62	y
VVVv676	VVV J161327.72-494925.09	16:13:27.72	-49:49:25.09	332.79443	0.96094652	–	–	18.80(0.12)	16.43(0.04)	15.07(0.03)	1.11	-0.81	y
VVVv677	VVV J161708.10-502456.26	16:17:08.10	-50:24:56.26	332.81058	0.12617463	–	–	–	16.97(0.07)	12.55(0.01)	1.20	-0.17	n
VVVv678	VVV J161741.28-502718.42	16:17:41.28	-50:27:18.42	332.84627	0.036513070	19.39(0.08)	19.00(0.09)	18.20(0.07)	16.95(0.07)	12.61(0.01)	1.77	0.23	n
VVVv679	VVV J161455.50-495908.92	16:14:55.50	-49:59:08.92	332.85355	0.68113407	–	–	–	17.44(0.11)	13.14(0.01)	1.63	1.92	n
VVVv680	VVV J161830.18-501930.00	16:18:30.18	-50:19:30.00	333.03010	0.038999545	–	–	19.06(0.15)	17.12(0.08)	15.88(0.06)	1.14	-0.78	y
VVVv681	VVV J161610.85-494746.21	16:16:10.85	-49:47:46.21	333.13083	0.67805818	–	–	–	16.97(0.07)	14.23(0.01)	2.68	0.96	y
VVVv682	VVV J161854.71-501158.83	16:18:54.71	-50:11:58.83	333.16448	0.082832989	19.55(0.10)	18.65(0.06)	17.49(0.04)	16.33(0.04)	15.51(0.04)	1.56	–	y
VVVv683	VVV J161533.66-493810.79	16:15:33.66	-49:38:10.79	333.16930	0.86275211	–	–	–	16.53(0.05)	14.00(0.01)	1.31	0.42	y
VVVv684	VVV J161854.96-500838.21	16:18:54.96	-50:08:38.21	333.20395	0.12217380	19.35(0.08)	18.82(0.07)	18.00(0.06)	16.41(0.04)	13.17(0.01)	1.03	0.90	y
VVVv685	VVV J161615.48-493458.37	16:16:15.48	-49:34:58.37	333.28778	0.82304445	–	–	–	17.16(0.08)	15.27(0.03)	1.56	-0.37	y

Continued on next page

Table A.1 – *Continued from previous page*

Object ID	VVV Designation	α (J2000)	δ (J2000)	l	b	Z (mag)	Y (mag)	J (mag)	H (mag)	K_s (mag)	ΔK_s^a (mag)	α_{class}	SFR
VVVv686	VVV J161916.95-500243.18	16:19:16.95	-50:02:43.18	333.31499	0.15137133	–	–	–	–	16.11(0.07)	1.28	1.42	y
VVVv687	VVV J161650.93-491901.77	16:16:50.93	-49:19:01.77	333.54143	0.94756164	19.24(0.07)	18.70(0.07)	17.52(0.04)	16.77(0.06)	15.45(0.04)	1.00	–	n
VVVv688	VVV J161950.92-493821.50	16:19:50.92	-49:38:21.50	333.66491	0.37663182	–	–	18.92(0.14)	–	14.57(0.02)	1.82	1.64	n
VVVv689	VVV J162006.05-493656.76	16:20:06.05	-49:36:56.76	333.71051	0.36468141	19.64(0.10)	18.61(0.06)	17.26(0.03)	15.70(0.02)	14.76(0.02)	2.01	-0.39	y
VVVv690	VVV J161916.31-491409.71	16:19:16.31	-49:14:09.71	333.88107	0.72976787	17.18(0.01)	16.80(0.01)	16.16(0.01)	15.39(0.02)	15.02(0.03)	1.07	–	n
VVVv691	VVV J162051.36-492535.05	16:20:51.36	-49:25:35.05	333.93086	0.41294680	17.50(0.02)	17.08(0.02)	16.20(0.01)	15.26(0.01)	14.55(0.02)	1.06	-1.39	n
VVVv692	VVV J162059.45-491908.03	16:20:59.45	-49:19:08.03	334.02221	0.47373084	18.95(0.06)	17.98(0.04)	16.66(0.02)	15.79(0.02)	15.13(0.03)	1.00	–	n
VVVv693	VVV J162028.12-490800.03	16:20:28.12	-49:08:00.03	334.09242	0.66548708	17.35(0.01)	16.53(0.01)	–	14.86(0.01)	14.28(0.01)	1.01	-2.86	n
VVVv694	VVV J162138.12-491021.21	16:21:38.12	-49:10:21.21	334.20001	0.50316584	21.04(0.31)	19.13(0.11)	17.63(0.06)	15.70(0.03)	14.34(0.02)	1.42	0.09	y
VVVv695	VVV J162337.14-491149.89	16:23:37.14	-49:11:49.89	334.41118	0.25600461	17.66(0.02)	16.54(0.01)	15.48(0.01)	14.36(0.01)	13.39(0.01)	1.66	-0.59	y
VVVv696	VVV J162050.35-483843.24	16:20:50.35	-48:38:43.24	334.47938	0.96903201	18.29(0.03)	17.30(0.02)	16.10(0.02)	15.38(0.02)	14.94(0.03)	1.04	-2.23	n
VVVv697	VVV J162327.18-490255.08	16:23:27.18	-49:02:55.08	334.49771	0.37977898	–	–	–	14.25(0.01)	11.59(0.01)	2.25	0.86	n
VVVv698	VVV J162507.05-491128.22	16:25:07.05	-49:11:28.22	334.58714	0.085686548	–	–	–	15.27(0.02)	11.85(0.01)	1.18	-0.36	y
VVVv699	VVV J162344.34-485455.29	16:23:44.34	-48:54:55.29	334.62548	0.44010368	–	–	–	–	16.19(0.09)	2.08	2.78	y
VVVv700	VVV J162708.19-484400.79	16:27:08.19	-48:44:00.79	335.14625	0.16707254	–	–	–	–	14.75(0.03)	2.84	1.73	n
VVVv701	VVV J162440.71-475426.69	16:24:40.71	-47:54:26.69	335.45321	1.0361210	20.88(0.28)	18.99(0.10)	17.90(0.08)	16.15(0.04)	15.41(0.05)	1.09	-1.49	n
VVVv702	VVV J162850.16-481432.68	16:28:50.16	-48:14:32.68	335.69555	0.30414709	20.22(0.19)	18.96(0.10)	17.41(0.05)	16.13(0.05)	15.31(0.05)	1.04	–	y
VVVv703	VVV J162726.01-475931.65	16:27:26.01	-47:59:31.65	335.71411	0.64633748	–	–	–	15.58(0.03)	12.12(0.01)	1.64	0.89	n
VVVv704	VVV J163001.64-481530.95	16:30:01.64	-48:15:30.95	335.82052	0.14929293	–	–	–	16.29(0.06)	11.86(0.01)	1.03	-0.06	y
VVVv705	VVV J162906.01-480536.96	16:29:06.01	-48:05:36.96	335.83362	0.37501161	–	–	17.84(0.08)	15.69(0.03)	14.19(0.02)	1.03	-0.29	y
VVVv706	VVV J163101.05-481842.45	16:31:01.05	-48:18:42.45	335.89495	-0.0069767210	19.30(0.08)	17.03(0.02)	14.78(0.01)	13.01(0.01)	11.90(0.01)	1.44	-3.26	y
VVVv707	VVV J162943.72-475759.56	16:29:43.72	-47:57:59.56	335.99810	0.38645778	–	–	–	17.97(0.27)	13.80(0.01)	2.26	1.49	n
VVVv708	VVV J162939.42-475032.13	16:29:39.42	-47:50:32.13	336.07996	0.48075245	–	–	–	17.79(0.22)	14.37(0.02)	1.95	1.15	n
VVVv709	VVV J163035.64-474559.55	16:30:35.64	-47:45:59.55	336.24313	0.41855408	–	–	–	–	16.71(0.17)	3.21	3.43	y
VVVv710	VVV J163225.37-475338.29	16:32:25.37	-47:53:38.29	336.36024	0.10754899	–	19.56(0.18)	17.85(0.08)	16.15(0.05)	15.37(0.05)	1.56	–	y
VVVv711	VVV J163438.61-472001.77	16:34:38.61	-47:20:01.77	337.02552	0.21358026	20.31(0.20)	18.49(0.07)	16.72(0.03)	14.68(0.01)	11.37(0.01)	1.29	0.17	n
VVVv712	VVV J163550.53-472231.49	16:35:50.53	-47:22:31.49	337.13198	0.035779233	–	–	–	14.82(0.02)	12.56(0.01)	1.61	-0.92	y
VVVv713	VVV J163352.79-465218.51	16:33:52.79	-46:52:18.51	337.27716	0.62226804	16.91(0.01)	16.04(0.01)	13.99(0.01)	12.61(0.01)	11.47(0.01)	1.81	-0.08	y
VVVv714	VVV J163353.64-465134.78	16:33:53.64	-46:51:34.78	337.28772	0.62874170	–	–	–	–	15.08(0.04)	1.65	0.76	y
VVVv715	VVV J163702.59-470039.76	16:37:02.59	-47:00:39.76	337.53883	0.12988208	–	–	–	–	12.34(0.01)	1.03	2.23	n
VVVv716	VVV J163555.14-464920.63	16:35:55.14	-46:49:20.63	337.54935	0.39882568	–	–	17.14(0.05)	15.16(0.02)	13.92(0.01)	1.02	-1.06	y
VVVv717	VVV J163605.56-464040.61	16:36:05.56	-46:40:40.61	337.67616	0.47413121	–	–	–	–	14.37(0.02)	2.09	0.80	y
VVVv718	VVV J163854.24-465446.26	16:38:54.24	-46:54:46.26	337.82422	-0.040427091	–	–	–	16.35(0.07)	14.73(0.03)	1.09	-1.37	y
VVVv719	VVV J163907.18-464958.72	16:39:07.18	-46:49:58.72	337.90832	-0.014663955	–	–	–	14.63(0.01)	11.61(0.01)	1.31	0.02	y
VVVv720	VVV J163722.54-461329.11	16:37:22.54	-46:13:29.11	338.16032	0.61494209	–	–	–	–	14.97(0.04)	2.04	1.50	y
VVVv721	VVV J163948.77-454847.96	16:39:48.77	-45:48:47.96	338.74912	0.57448974	–	–	18.49(0.16)	15.96(0.05)	13.98(0.01)	1.21	0.87	y
VVVv722	VVV J164042.44-453905.82	16:40:42.44	-45:39:05.82	338.97368	0.56499826	–	–	–	17.90(0.27)	13.53(0.01)	1.04	0.06	y
VVVv723	VVV J164231.97-454048.90	16:42:31.97	-45:40:48.90	339.16278	0.30656144	–	–	15.32(0.01)	12.99(0.01)	11.94(0.01)	1.26	-0.21	y
VVVv724	VVV J164257.47-444743.95	16:42:57.47	-44:47:43.95	339.87852	0.83198489	20.17(0.17)	18.37(0.06)	16.54(0.03)	14.92(0.02)	14.19(0.02)	1.51	-2.13	n
VVVv725	VVV J164624.86-451206.07	16:46:24.86	-45:12:06.07	339.96997	0.10400385	18.27(0.03)	17.77(0.03)	17.13(0.04)	16.40(0.05)	16.07(0.09)	1.16	–	n
VVVv726	VVV J164359.99-444504.52	16:43:59.99	-44:45:04.52	340.03324	0.72143937	–	–	–	–	16.54(0.13)	2.07	1.45	n
VVVv727	VVV J164622.25-445953.10	16:46:22.25	-44:59:53.10	340.11987	0.24199984	–	–	–	14.45(0.01)	11.91(0.01)	1.24	0.13	n
VVVv728	VVV J164734.30-445638.46	16:47:34.30	-44:56:38.46	340.29861	0.11519407	–	–	–	15.35(0.02)	11.54(0.01)	1.45	0.65	y
VVVv729	VVV J164803.79-444359.42	16:48:03.79	-44:43:59.42	340.51590	0.18477007	–	–	–	16.00(0.04)	12.34(0.01)	1.20	0.27	y
VVVv730	VVV J164639.49-443044.62	16:46:39.49	-44:30:44.62	340.52261	0.51824117	20.78(0.28)	19.00(0.10)	17.41(0.05)	15.88(0.03)	15.03(0.03)	1.30	-1.95	y
VVVv731	VVV J164634.32-442531.34	16:46:34.32	-44:25:31.34	340.57888	0.58638202	–	–	18.30(0.11)	15.97(0.04)	14.97(0.03)	3.70	–	n
VVVv732	VVV J164622.42-441634.06	16:46:22.42	-44:16:34.06	340.66946	0.71017554	–	–	17.77(0.07)	15.99(0.04)	15.29(0.04)	1.03	–	n
VVVv733	VVV J164620.85-441447.50	16:46:20.85	-44:14:47.50	340.68894	0.73295855	18.92(0.05)	17.94(0.04)	16.84(0.03)	15.81(0.03)	15.32(0.04)	1.55	–	n
VVVv734	VVV J164752.96-442816.11	16:47:52.96	-44:28:16.11	340.69533	0.37841721	–	–	–	16.78(0.07)	15.26(0.04)	1.13	–	y

Continued on next page

Table A.1 – *Continued from previous page*

Object ID	VVV Designation	α (J2000)	δ (J2000)	l	b	Z (mag)	Y (mag)	J (mag)	H (mag)	K_s (mag)	ΔK_s^a (mag)	α_{class}	SFR
VVVv735	VVV J165029.33-441952.02	16:50:29.33	-44:19:52.02	341.10170	0.11162264	–	–	–	17.10(0.10)	15.35(0.04)	1.06	-0.47	y
VVVv736	VVV J165055.45-440659.40	16:50:55.45	-44:06:59.40	341.31663	0.18873828	–	–	–	–	15.02(0.03)	1.08	1.60	y
VVVv737	VVV J165131.99-440044.27	16:51:31.99	-44:00:44.27	341.46665	0.17091321	–	–	–	15.57(0.02)	11.95(0.01)	1.66	0.20	y
VVVv738	VVV J165046.51-435041.49	16:50:46.51	-43:50:41.49	341.50858	0.38280417	–	–	–	17.58(0.12)	16.30(0.09)	1.08	–	y
VVVv739	VVV J164822.88-432206.16	16:48:22.88	-43:22:06.16	341.59616	1.0208969	18.03(0.02)	17.35(0.02)	16.60(0.02)	15.92(0.03)	15.64(0.05)	1.02	–	n
VVVv740	VVV J165259.55-440203.79	16:52:59.55	-44:02:03.79	341.61623	-0.045736852	–	–	–	16.96(0.07)	15.44(0.04)	1.25	-0.93	y
VVVv741	VVV J165005.32-432227.21	16:50:05.32	-43:22:27.21	341.79097	0.77929297	18.95(0.05)	17.98(0.04)	17.17(0.03)	16.18(0.03)	15.84(0.06)	1.61	–	n
VVVv742	VVV J165053.55-432707.55	16:50:53.55	-43:27:07.55	341.82441	0.61726592	19.01(0.05)	18.15(0.04)	17.20(0.03)	16.33(0.04)	15.88(0.06)	1.06	–	n
VVVv743	VVV J165251.56-433950.49	16:52:51.56	-43:39:50.49	341.88755	0.20750513	–	–	19.31(0.21)	15.04(0.01)	12.42(0.01)	1.41	0.93	y
VVVv744	VVV J165354.84-433809.08	16:53:54.84	-43:38:09.08	342.03005	0.077559552	19.36(0.06)	18.67(0.06)	17.87(0.06)	16.56(0.05)	13.13(0.01)	1.04	-0.05	y
VVVv745	VVV J165144.08-431111.91	16:51:44.08	-43:11:11.91	342.12662	0.66841562	–	–	18.90(0.15)	16.84(0.06)	15.51(0.04)	1.20	0.08	n
VVVv746	VVV J165344.38-432819.36	16:53:44.38	-43:28:19.36	342.13710	0.20551300	–	–	–	18.07(0.19)	15.74(0.05)	1.22	0.91	y
VVVv747	VVV J165205.49-430449.43	16:52:05.49	-43:04:49.43	342.25001	0.68576070	–	–	18.52(0.11)	13.76(0.01)	11.73(0.01)	2.40	0.83	n
VVVv748	VVV J165331.07-431512.35	16:53:31.07	-43:15:12.35	342.28104	0.37492197	–	–	–	17.05(0.08)	15.29(0.03)	1.15	0.19	y
VVVv749	VVV J165448.52-432409.89	16:54:48.52	-43:24:09.89	342.31324	0.098575043	–	–	–	18.58(0.31)	15.33(0.04)	1.11	1.69	y
VVVv750	VVV J165244.59-430520.02	16:52:44.59	-43:05:20.02	342.31899	0.58841402	–	–	–	–	16.28(0.08)	2.28	2.55	y
VVVv751	VVV J165249.10-430236.21	16:52:49.10	-43:02:36.21	342.36287	0.60665463	18.37(0.03)	17.69(0.03)	16.19(0.01)	14.53(0.01)	13.08(0.01)	1.22	-0.01	y
VVVv752	VVV J165507.68-431244.47	16:55:07.68	-43:12:44.47	342.49782	0.17312413	–	–	–	17.55(0.12)	15.70(0.05)	1.03	0.83	y
VVVv753	VVV J165452.75-430321.11	16:54:52.75	-43:03:21.11	342.59096	0.30682127	–	–	–	16.20(0.03)	12.68(0.01)	1.49	0.21	n
VVVv754	VVV J165528.31-430602.58	16:55:28.31	-43:06:02.58	342.62406	0.19446658	–	–	–	18.57(0.32)	12.70(0.01)	1.69	0.94	n
VVVv755	VVV J165504.79-425847.58	16:55:04.79	-42:58:47.58	342.67309	0.32609823	–	–	–	17.82(0.16)	13.62(0.01)	1.50	0.85	n
VVVv756	VVV J165225.39-423432.39	16:52:25.39	-42:34:32.39	342.67855	0.95933654	21.01(0.29)	19.61(0.16)	17.16(0.03)	15.27(0.02)	13.63(0.01)	1.94	0.27	y
VVVv757	VVV J165231.55-423049.66	16:52:31.55	-42:30:49.66	342.73837	0.98398831	–	–	18.79(0.14)	16.63(0.05)	15.61(0.05)	1.00	–	n
VVVv758	VVV J165625.48-425554.23	16:56:25.48	-42:55:54.23	342.86490	0.16459184	19.15(0.15)	18.95(0.13)	17.80(0.06)	14.94(0.01)	10.61(0.01)	1.18	-0.16	n
VVVv759	VVV J165330.26-422615.00	16:53:30.26	-42:26:15.00	342.91171	0.89267240	–	–	–	17.49(0.11)	16.30(0.12)	2.31	1.75	y
VVVv760	VVV J165514.44-424026.62	16:55:14.44	-42:40:26.62	342.92954	0.49531414	17.09(0.03)	16.54(0.02)	16.11(0.01)	15.16(0.01)	14.79(0.03)	1.12	-1.77	y
VVVv761	VVV J165639.54-423813.91	16:56:39.54	-42:38:13.91	343.12166	0.31517808	–	–	18.32(0.09)	16.46(0.04)	15.51(0.06)	1.04	-1.04	n
VVVv762	VVV J165704.45-423124.12	16:57:04.45	-42:31:24.12	343.25829	0.32656064	17.31(0.03)	17.13(0.03)	16.58(0.02)	15.85(0.02)	15.28(0.05)	1.01	-1.10	n
VVVv763	VVV J165657.89-422955.09	16:56:57.89	-42:29:55.09	343.26505	0.35773152	–	–	18.28(0.09)	15.27(0.01)	13.63(0.01)	2.89	-1.34	n
VVVv764	VVV J165410.03-415356.82	16:54:10.03	-41:53:56.82	343.40683	1.1373473	–	18.76(0.10)	–	–	11.94(0.01)	1.02	0.12	y
VVVv765	VVV J165452.35-415132.72	16:54:52.35	-41:51:32.72	343.52064	1.0605548	–	–	18.91(0.16)	16.97(0.07)	14.58(0.03)	1.35	-0.52	y
VVVv766	VVV J165959.76-422759.67	16:59:59.76	-42:27:59.67	343.63706	-0.060548504	–	–	–	17.87(0.15)	15.78(0.08)	1.06	-0.27	y
VVVv767	VVV J165646.93-415231.10	16:56:46.93	-41:52:31.10	343.73084	0.77335930	14.05(0.01)	13.79(0.01)	13.46(0.01)	–	12.25(0.01)	1.07	-2.38	n
VVVv768	VVV J170030.35-421248.67	17:00:30.35	-42:12:48.67	343.89438	0.021313034	18.53(0.09)	18.04(0.05)	18.55(0.11)	16.73(0.05)	14.95(0.04)	1.07	-0.39	y
VVVv769	VVV J165846.96-414317.51	16:58:46.96	-41:43:17.51	344.08324	0.57716965	–	–	18.30(0.09)	14.37(0.01)	12.30(0.01)	1.81	0.47	n
VVVv770	VVV J170129.39-413942.90	17:01:29.39	-41:39:42.90	344.44189	0.21617262	–	–	–	–	15.07(0.03)	1.35	0.67	y
VVVv771	VVV J165759.50-410834.91	16:57:59.50	-41:08:34.91	344.44477	1.0525317	–	–	16.24(0.01)	12.90(0.01)	11.63(0.01)	1.27	-0.00	n
VVVv772	VVV J165827.14-405409.28	16:58:27.14	-40:54:09.28	344.68722	1.1337881	–	–	17.26(0.03)	13.61(0.01)	11.74(0.01)	1.89	0.44	n
VVVv773	VVV J170129.82-411022.03	17:01:29.82	-41:10:22.03	344.82892	0.51528056	–	–	–	15.49(0.02)	12.30(0.01)	1.19	0.64	n
VVVv774	VVV J170028.83-403311.02	17:00:28.83	-40:33:11.02	345.19957	1.0478620	18.41(0.03)	17.50(0.02)	16.48(0.01)	15.20(0.01)	14.43(0.02)	1.17	-0.67	y
VVVv775	VVV J170036.85-403207.80	17:00:36.85	-40:32:07.80	345.22906	1.0386520	–	20.27(0.26)	19.17(0.15)	17.42(0.09)	15.67(0.05)	1.03	1.52	y
VVVv776	VVV J170041.05-403228.55	17:00:41.05	-40:32:28.55	345.23270	1.0246302	–	–	18.95(0.12)	16.23(0.03)	14.61(0.02)	1.11	-0.09	y
VVVv777	VVV J170050.17-403217.91	17:00:50.17	-40:32:17.91	345.25280	1.0036820	–	–	17.52(0.03)	15.93(0.02)	14.91(0.02)	1.38	-0.78	y
VVVv778	VVV J170038.73-402958.86	17:00:38.73	-40:29:58.86	345.26095	1.0560172	–	–	18.78(0.11)	14.92(0.01)	12.17(0.01)	1.51	1.09	y
VVVv779	VVV J170202.20-404118.61	17:02:02.20	-40:41:18.61	345.27405	0.73163157	–	–	–	15.53(0.02)	12.25(0.01)	1.17	0.91	y
VVVv780	VVV J170104.38-402659.86	17:01:04.38	-40:26:59.86	345.35017	1.0224882	19.90(0.11)	18.63(0.06)	16.85(0.02)	15.20(0.01)	14.15(0.01)	1.08	-0.52	y
VVVv781	VVV J170103.96-402640.28	17:01:03.96	-40:26:40.28	345.35366	1.0268645	–	–	18.61(0.09)	15.73(0.02)	13.90(0.01)	1.28	1.51	y
VVVv782	VVV J170558.41-405720.74	17:05:58.41	-40:57:20.74	345.51464	-0.022210888	–	–	–	16.64(0.05)	14.82(0.02)	1.04	-1.07	y
VVVv783	VVV J170215.24-395854.81	17:02:15.24	-39:58:54.81	345.85827	1.1313735	18.74(0.04)	18.00(0.04)	16.38(0.02)	15.12(0.02)	14.26(0.02)	1.31	-1.01	y

Continued on next page

Table A.1 – *Continued from previous page*

Object ID	VVV Designation	α (J2000)	δ (J2000)	l	b	Z (mag)	Y (mag)	J (mag)	H (mag)	K_s (mag)	ΔK_s^a (mag)	α_{class}	SFR
VVVv784	VVV J170450.47-401830.72	17:04:50.47	-40:18:30.72	345.90020	0.54029024	–	–	–	15.58(0.02)	13.34(0.01)	1.36	0.16	y
VVVv785	VVV J170601.51-402746.57	17:06:01.51	-40:27:46.57	345.91354	0.26735575	–	–	–	16.55(0.06)	12.51(0.01)	1.97	0.77	y
VVVv786	VVV J170448.34-401326.37	17:04:48.34	-40:13:26.37	345.96334	0.59691276	–	–	18.23(0.09)	15.30(0.02)	13.69(0.01)	1.63	0.27	y
VVVv787	VVV J170648.69-402635.41	17:06:48.69	-40:26:35.41	346.01944	0.15985572	–	–	–	–	13.75(0.01)	1.88	0.91	n
VVVv788	VVV J170711.21-400902.64	17:07:11.21	-40:09:02.64	346.29617	0.27843602	18.59(0.03)	17.82(0.03)	16.92(0.03)	16.04(0.04)	15.70(0.06)	1.04	–	n
VVVv789	VVV J170811.64-392444.91	17:08:11.64	-39:24:44.91	347.00307	0.56616179	20.30(0.15)	18.79(0.07)	17.37(0.04)	16.29(0.04)	15.52(0.05)	1.30	-1.27	n
VVVv790	VVV J170810.22-391409.92	17:08:10.22	-39:14:09.92	347.14166	0.67537939	–	–	–	17.81(0.19)	16.60(0.13)	1.58	–	n
VVVv791	VVV J170806.33-385911.97	17:08:06.33	-38:59:11.97	347.33399	0.83471887	–	–	–	–	13.13(0.01)	2.15	1.36	n
VVVv792	VVV J170919.43-390259.83	17:09:19.43	-39:02:59.83	347.42453	0.60710796	–	–	–	–	12.76(0.01)	1.72	1.42	n
VVVv793	VVV J170856.29-385848.19	17:08:56.29	-38:58:48.19	347.43599	0.70892496	–	–	–	16.24(0.05)	12.72(0.01)	2.83	1.16	n
VVVv794	VVV J171250.14-391027.51	17:12:50.14	-39:10:27.51	347.72752	-0.015583892	20.24(0.19)	18.85(0.11)	17.07(0.04)	15.98(0.04)	15.40(0.05)	1.01	–	y
VVVv795	VVV J171312.64-385041.41	17:13:12.64	-38:50:41.41	348.03690	0.11907653	–	–	19.32(0.29)	17.47(0.16)	16.61(0.15)	1.14	–	y
VVVv796	VVV J171207.43-384126.86	17:12:07.43	-38:41:26.86	348.03683	0.38100590	–	–	–	16.87(0.09)	12.45(0.01)	2.61	1.10	y
VVVv797	VVV J171219.10-382941.67	17:12:19.10	-38:29:41.67	348.21749	0.46573558	–	18.89(0.11)	17.89(0.08)	16.78(0.09)	15.90(0.08)	1.24	–	y
VVVv798	VVV J171244.16-382639.53	17:12:44.16	-38:26:39.53	348.30653	0.42940932	–	–	–	–	14.05(0.01)	1.03	1.60	y
VVVv799	VVV J171316.81-383051.00	17:13:16.81	-38:30:51.00	348.31258	0.30219850	–	–	16.25(0.02)	13.10(0.01)	11.73(0.01)	1.33	-1.33	y
VVVv800	VVV J171246.04-382524.63	17:12:46.04	-38:25:24.63	348.32696	0.43669491	–	–	18.89(0.20)	15.80(0.04)	12.89(0.01)	1.20	1.44	y
VVVv801	VVV J171222.63-381837.43	17:12:22.63	-38:18:37.43	348.37339	0.56510648	–	–	–	14.13(0.01)	11.43(0.01)	1.51	0.07	y
VVVv802	VVV J171410.63-383011.83	17:14:10.63	-38:30:11.83	348.42421	0.16639652	19.70(0.12)	–	18.13(0.10)	16.31(0.06)	13.30(0.01)	1.12	1.38	y
VVVv803	VVV J171343.94-381016.01	17:13:43.94	-38:10:16.01	348.64244	0.43158102	–	–	–	–	13.58(0.01)	2.36	1.35	n
VVVv804	VVV J171504.10-380938.79	17:15:04.10	-38:09:38.79	348.80431	0.22454961	–	–	18.45(0.13)	14.38(0.01)	11.87(0.01)	1.29	0.08	y
VVVv805	VVV J171524.97-380818.55	17:15:24.97	-38:08:18.55	348.86227	0.18195621	–	–	–	16.75(0.10)	13.00(0.01)	1.08	0.17	y
VVVv806	VVV J171406.87-374640.84	17:14:06.87	-37:46:40.84	349.00522	0.60069041	–	–	–	–	14.46(0.02)	1.81	1.39	n
VVVv807	VVV J171643.72-374852.74	17:16:43.72	-37:48:52.74	349.27611	0.15949058	–	–	–	–	15.52(0.06)	1.39	1.29	y
VVVv808	VVV J171632.78-374609.27	17:16:32.78	-37:46:09.27	349.29224	0.21515387	–	–	–	–	16.45(0.14)	2.03	–	y
VVVv809	VVV J171713.14-373941.72	17:17:13.14	-37:39:41.72	349.45704	0.16903153	–	–	–	–	16.66(0.17)	1.71	2.72	y
VVVv810	VVV J171707.96-373320.37	17:17:07.96	-37:33:20.37	349.53356	0.24424625	–	–	–	–	14.70(0.03)	2.34	1.78	n
VVVv811	VVV J171714.07-372347.84	17:17:14.07	-37:23:47.84	349.67499	0.31974102	–	–	–	17.32(0.16)	12.53(0.01)	1.61	0.98	n
VVVv812	VVV J171726.31-372352.20	17:17:26.31	-37:23:52.20	349.69743	0.28597331	–	–	–	–	14.55(0.02)	3.36	1.86	n
VVVv813	VVV J171525.93-364642.02	17:15:25.93	-36:46:42.02	349.97008	0.97119498	–	–	18.06(0.09)	14.50(0.01)	11.61(0.01)	1.42	-0.20	n
VVVv814	VVV J171810.35-370848.64	17:18:10.35	-37:08:48.64	349.98669	0.31151801	–	–	–	17.59(0.21)	15.82(0.08)	1.09	0.19	n
VVVv815	VVV J142604.9-604116.8	14:26:04.95	-60:41:16.81	314.26287	0.084603	–	–	–	–	15.29(0.06)	1.71	1.58	y
VVVv816	VVV J130950.1-624631.7	13:09:50.13	-62:46:31.76	305.03426	0.021138	–	–	–	–	15.00(0.03)	1.4	2.29	y

Appendix B

FIRE Spectra of VVV Objects.

In here we show the spectra of 21 objects from the VVV spectroscopic sample which are not discussed in more detail in chapter 6. We mark some of the most prominent features observed in their spectra. The line identification for some objects might not be complete.

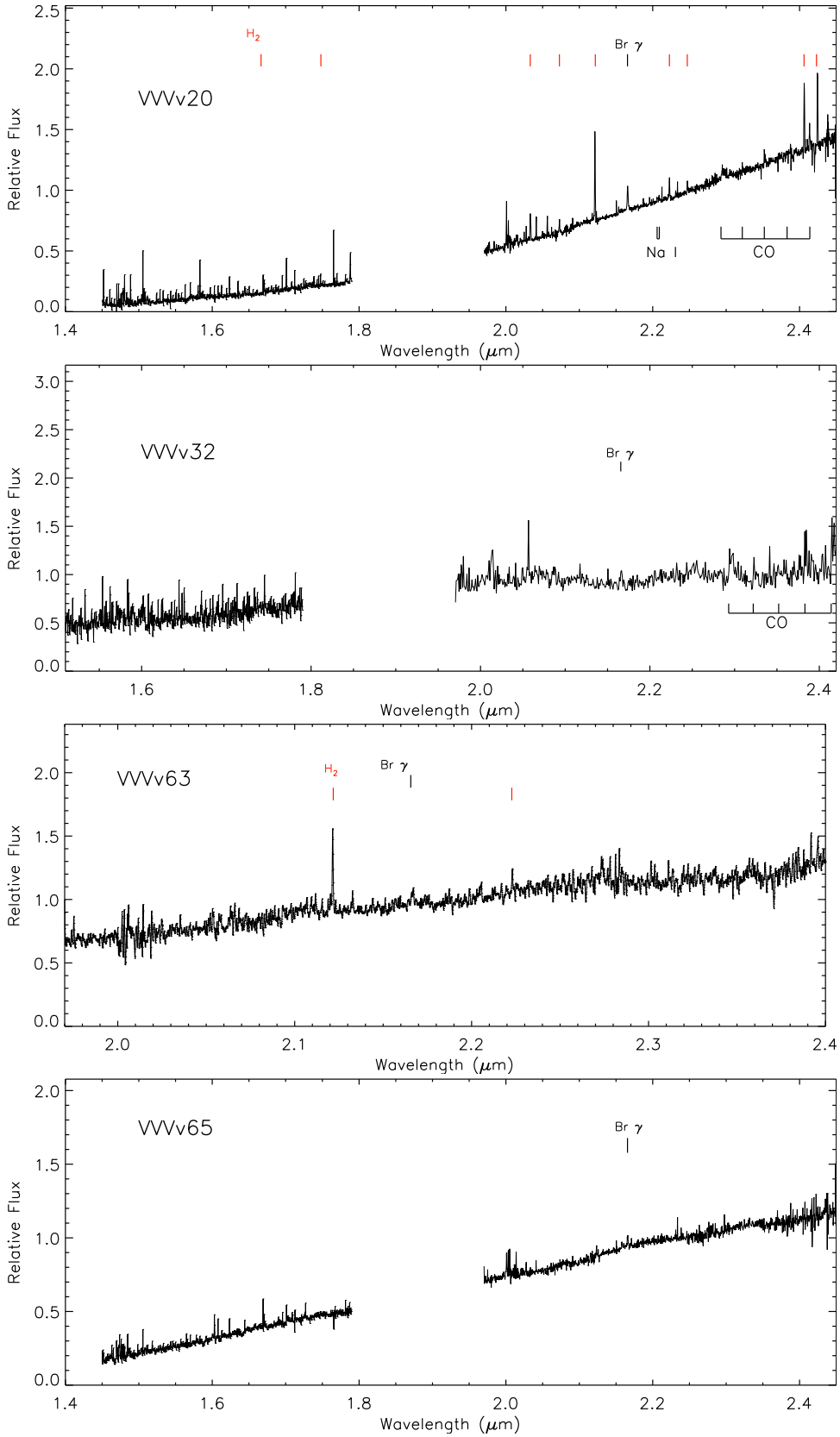

Figure B.1: FIRE spectra of objects not discussed in detail in Chapter 6.

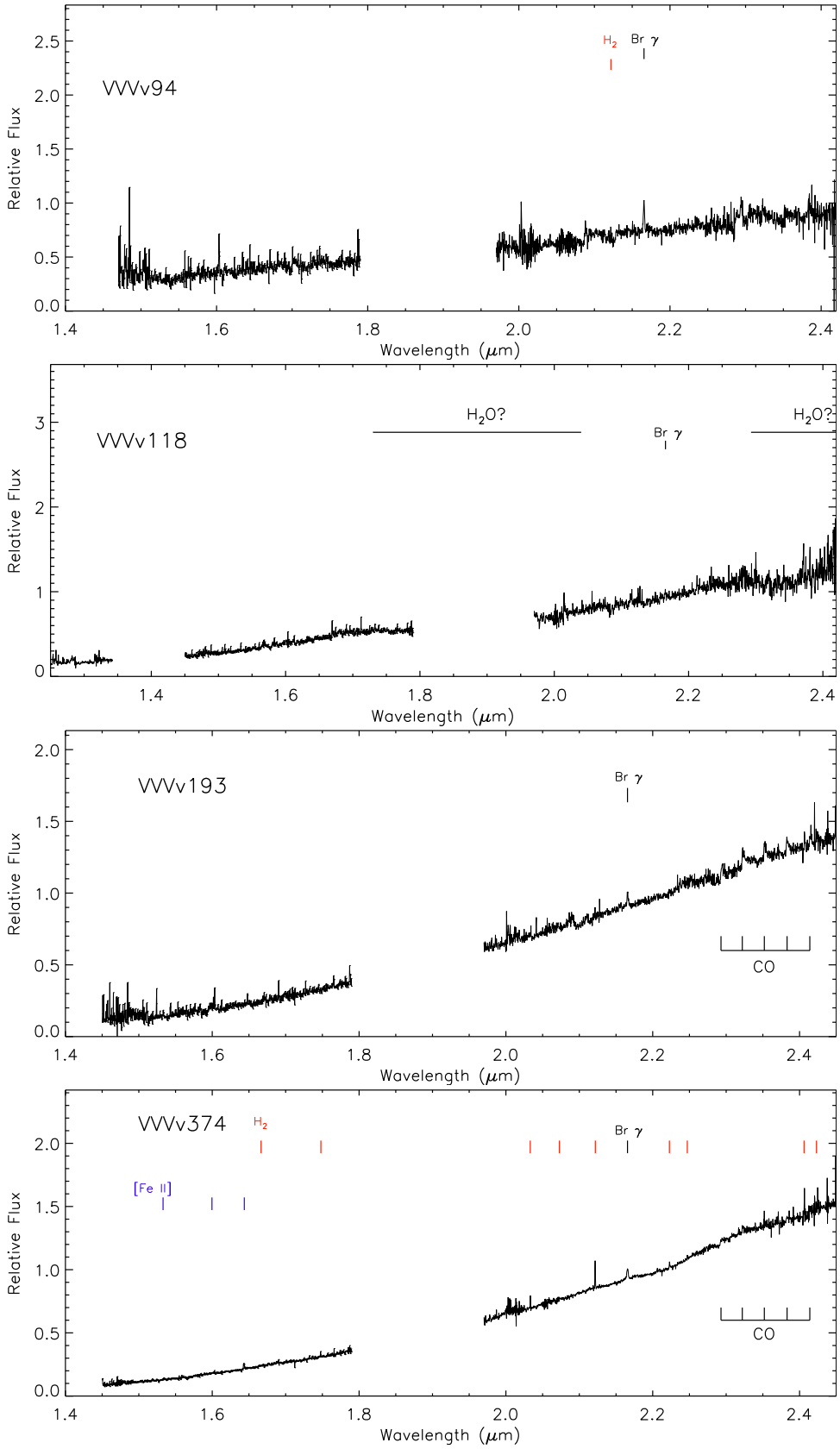

Figure B.2: FIRE spectra of objects not discussed in detail in Chapter 6.

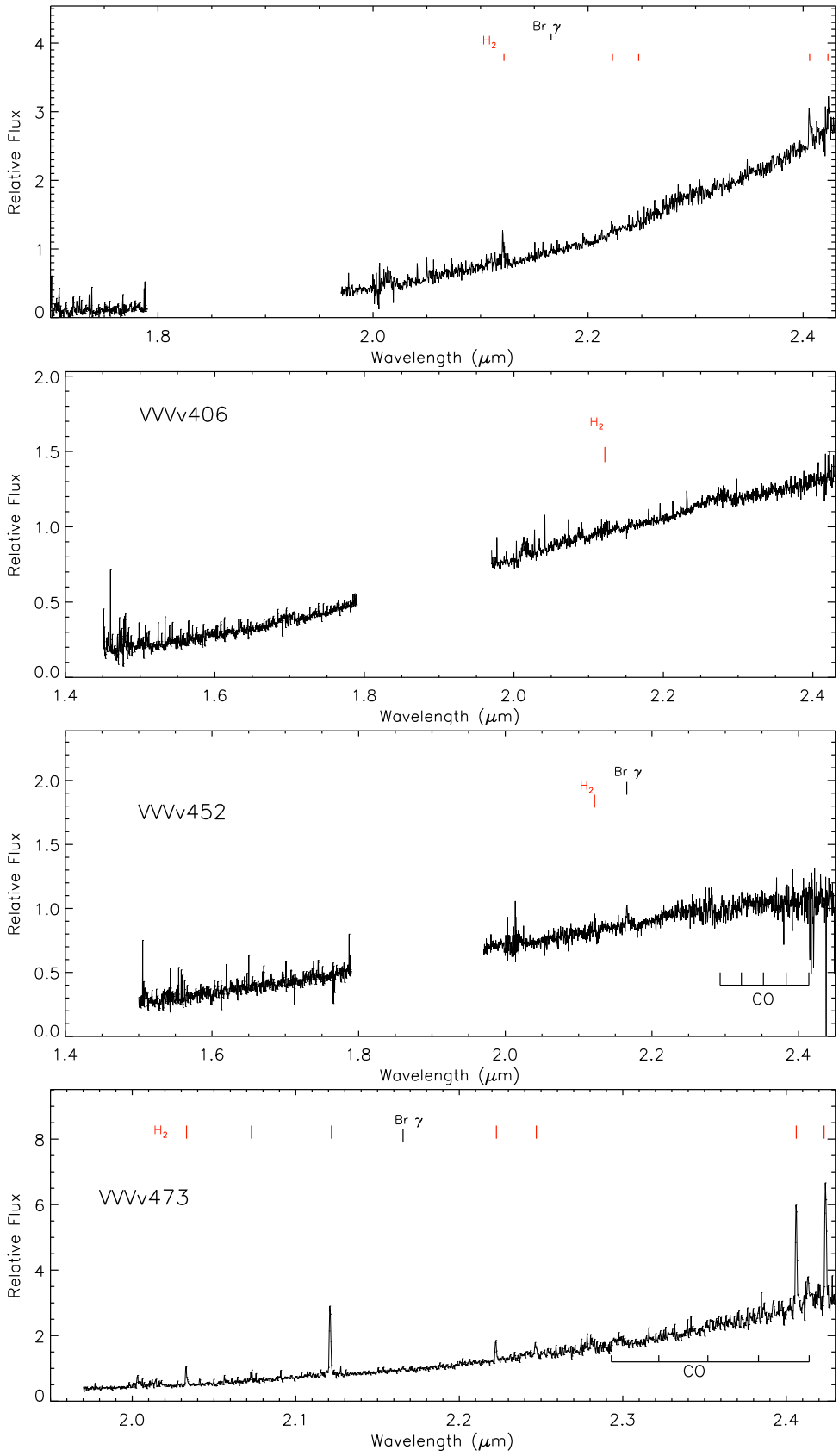

Figure B.3: FIRE spectra of objects not discussed in detail in Chapter 6.

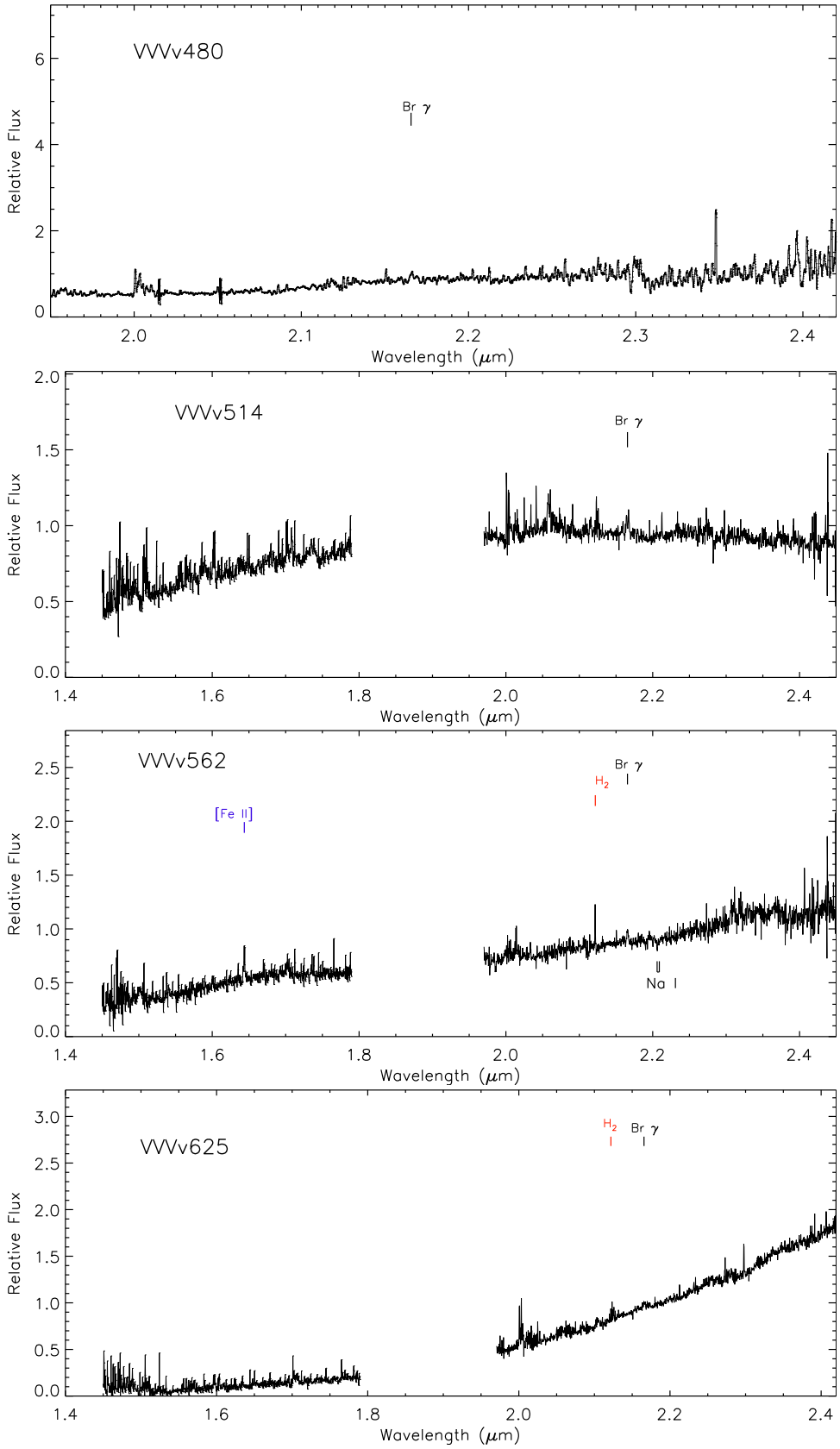

Figure B.4: FIRE spectra of objects not discussed in detail in Chapter 6.

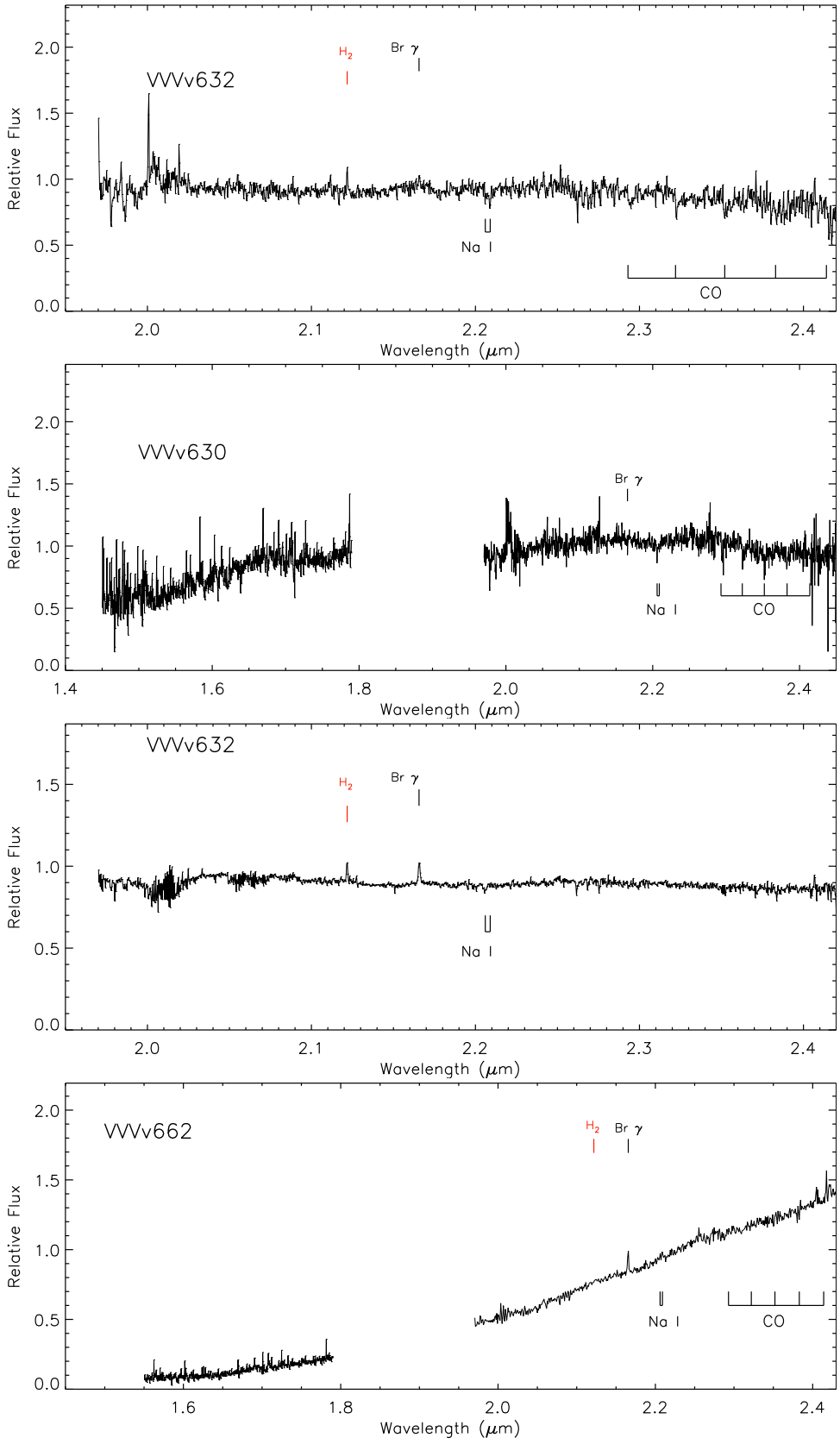

Figure B.5: FIRE spectra of objects not discussed in detail in Chapter 6.

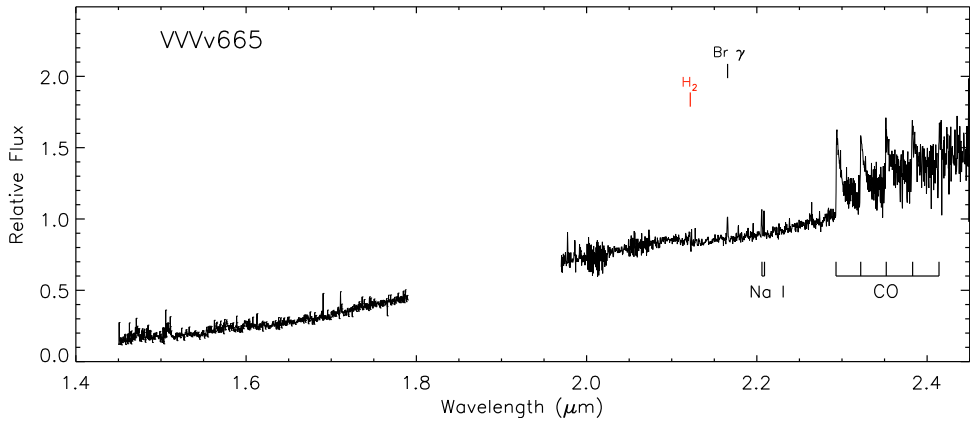

Figure B.6: FIRE spectra of objects not discussed in detail in Chapter 6.